*In Memory*

*Margaret (Mum) and Suzanne*

# The essence of FIA: A study of the distribution of Foliation Intersection Axes data and its significance from hand sample to regional scales.

Volume 1: Text.

Thesis submitted by

Cameron Russell Huddlestone-Holmes BSc(Hons) *JCU*

in October 2005

for the degree of Doctor of Philosophy

in the School of Earth Sciences

James Cook University

# STATEMENT OF ACCESS

I, the undersigned, author of this work, understand the James Cook University will make this thesis available for use within the University Library and, via the Australian Digital Thesis network, for use elsewhere.

I understand that, as an unpublished work, a thesis has significant protection under the Copyright Act and I do not wish to place further restriction on access to this work.

Cameron Huddlestone-Holmes Date

# ELECTRONIC COPY

I, the undersigned, the author of this work, declare that the electronic copy of this thesis provided to the James Cook University Library is an accurate copy of the print thesis submitted, within the limits of the technology available.

Cameron Huddlestone-Holmes Date

# STATEMENT OF SOURCES

## DECLARATION

I declare that this thesis is my own work and has not been submitted in any other form for another degree or diploma at any university of other institution of tertiary education. Information derived from published or unpublished work of others has been acknowledged in the text and a list of references is given.

Cameron Huddlestone-Holmes Date

# Statement on the Contribution of Others

T.H. Bell provided supervision and inspiration for these studies. He also provided editorial assistance. Funding for fieldwork and analyses was provided from an ARC Large grant to T.H. Bell, and a JCU Doctoral Merit Research Scheme grant to Huddlestone-Holmes. Stipend support was received from a JCU School of Earth Sciences Scholarship.

Funding for the high resolution X-ray computed tomography (HRXCT) analysis for chapters 1 and 2 was provided in part by a Large ARC grant to T.H. Bell and NSF grant EAR-0113480 to R. Ketcham. Operation of the University of Texas High-Resolution X-ray CT Facility is supported by NSF grants EAR-0004082 and EAR-0345710.

R. Ketcham, University of Texas CT Facility, acquired the HRXCT data (including fine tuning the process for this application), and contributed to the description of the HRXCT technique and some aspects of the discussions in chapters 1 and 2. David Donald, James Cook University, collaborated on chapters 3 and 4 with particular regard to the development of the bootstrap statistical techniques.

Ian Atkinson, Wayne Mallett and Dominique Morel from James Cook University High Performance Computing provided computational support for the analysis of the HRXCT data. Much of the analysis of this data was done using their facilities. Kevin Blake is acknowledged for assisting with electron microprobe analyses. Nick Fisher, Valuemetrics Australia, provided advice on directional statistics. Nick Timms provided some of the data used in chapter 4.

Carl Merschat and Mark Carter at the North Carolina Geological Survey provided assistance with field work.

Critical reviews by F.S. Spear, S.E. Johnson and T. Foster greatly improved chapter 1 which has been accepted for publication in American Mineralogist.

George Ridgway and Gina Curro performed the difficult task of editing chapters 2, 3 and 4. Their assistance greatly improved the readability of these chapters. Any errors remaining are mine.

# Acknowledgements

Firstly and most importantly I would like to thank Laurene for her love and support. These last years have been stressful and I am grateful that they have brought us closer. You have helped me to understand what is important in life. You have done more to help me on this journey than anyone. I am looking forward to being able to put more time into being a good husband to you and father to Amélie and Imogen.

I would also like to thank my family for their love, support and encouragement. Your belief in me helped me to keep going when times got tough.

Tim Bell's support and enthusiasm were greatly appreciated, as was his cheap red wine (with an occasional decent bottle thrown in). Tim's creativity is inspirational, and I would not have started a PhD, let alone finished it, without his encouragement.

Towards the end of the write up of this thesis, George Ridgway provided great support in helping me to stay on task. Aside from the editorial assistance, George's encouragement and advice were greatly motivating.

Finally, I would like to acknowledge my fellow students, past and present, and the general and academic staff of the School of Earth Sciences at James Cook University. It has been a very memorable time, largely because of the people I shared it with.

# Table of Contents

# Table of Tables

# Table of Figures

# Introduction and Thesis Outline

The study of orogenic belts is fundamental to understanding many of the crustal scale processes that control the formation and behaviour of continents. However, the history of orogenic belts is commonly very complicated, with overprinting pulses of metamorphism and deformation that can be diachronous along the length of an orogen. Repeated deformation events overprint or remove the effects of earlier ones. Consequently structures preserved in the rock matrix do not preserve evidence of all the deformation events that the rock has gone through. Combined with deformation partitioning that causes strain to be heterogeneously distributed at all scales, matrix structures cannot be used as a framework for correlating metamorphic events across an orogen.

FIAs are a structure that appears to provide a consistent record through time, allowing the effects of deformation events that may have been destroyed or redistributed in the matrix to be preserved. FIAs are the foliation inflection/intersection axis preserved in porphyroblasts. They are interpreted as being the intersection of successive foliations, or the curvature of one into the next, which have been overgrown by a porphyroblast. They can be equated with the intersection lineation between these two foliations or the fold axis of the second event. An alternative interpretation is that they represent the axis of rotation of a porphyroblast while it was growing. However they are interpreted, they can be routinely measured and used to investigate structural, metamorphic, and tectonic processes

FIAs are most commonly measured using the asymmetry method. This method finds the average FIA orientation for a sample using a series of spatially oriented thin sections. It relies on the fact that a simple asymmetrically folded surface with a sub-horizontal axis will appear to have opposite asymmetries when cut by two vertical planes that strike either side of the fold axis; curved inclusion trails preserved in porphyroblasts are analogous to such a fold.

Questions have been raised about the accuracy of FIA measurements because they are not measured directly. What is the intra sample variation of FIAs, and how reliable are FIA orientations determined by the asymmetry method? Data suggesting that they most likely remain consistently oriented, in spite of the overprinting effects of younger deformations, are difficult for many to accept. These questions have lead to doubt as to the significance of FIAs, and whether they can be correlated between samples and along orogens. This thesis takes a detailed look at FIAs using newly developed techniques in an attempt to address these issues, and to provide an insight into their significance. The four chapters have been written as manuscripts and the first has been accepted for publication as an electronic article in American Mineralogist.

Finding the orientation of a FIA in a single porphyroblast requires the inclusion trails to be viewed in three dimensions, or sectioned in multiple orientations. This is rarely possible in rocks and not possible using two-dimensional thin sections. Virtual models of the inclusion trails can be made using serial grinding or serial thin sectioning. These techniques are time

intensive and the orientation of the axes need to be at a high angle to the sections or grinding plane for the geometry of the curved trails to be captured. High resolution X-ray computed tomography (HRXCT) provides an alternate means by which the inclusion trails inside porphyroblasts can be imaged. It enables the internal structure of solid objects to be visualized in three-dimensions. HRXCT is a development of X-ray computed tomography technology developed for medical applications. It measures the attenuation of X-rays as they pass through an object; the amount of X-ray energy attenuated is proportional to its energy, and the density and average atomic mass of the material being analysed. HRXCT is capable of resolutions of less than 10μm. Chapter 1 demonstrates the application of HRXCT to the analysis of the geometry of inclusion trails in garnet porphyroblasts. A background for this technique is provided along with operating parameters suitable for imaging garnet inclusion trails. Techniques for the analysis of the data are also discussed.

The HRXCT technique described in Chapter 1 was used to generate a three-dimensional dataset for a sample of garnet schist from Vermont. This dataset was used to investigate the orientations of FIAs in multiple porphyroblasts from the same sample in Chapter 2. This study allows the intra sample variation of FIA orientations to be determined. This is the first time that FIAs in individual porphyroblasts have been measured.

The asymmetry method does not provide an estimate of the error in the measured FIA orientation. Determining FIA orientations using HRXCT allows the distribution within a sample to be determined, but it is not practical for large numbers of samples because of cost and time issues. Chapter 3 investigates the use of maximum likelihood estimation (MLE) to fit a cyclic logistic regression to asymmetry data, which allows a confidence interval to be determined for the FIA. A resampling method known as bootstrapping is used to obtain more robust estimates of the variability of the model parameters, and the goodness-of-fit, than are achieved using currently available techniques.

The 4$^{th}$ chapter of the thesis looks at how FIA can be correlated between samples and their significance to orogenic processes. Examples of the application of the bootstrapped MLE approach and the correlation of FIA are given for both regional and sample scale problems. The causes of variation of FIA at hand sample and regional scales are discussed in this context. Guidelines for the use of FIA are presented along with a discussion of their significance.

# Chapter 1. Getting the Inside Story: using computed X-ray tomography to study inclusion trails in garnet porphyroblasts

This chapter has been accepted for publication by The American Mineralogist as an electronic article. It is best viewed as an interactive Adobe Acrobat document, which can be found on the CD in appendix A of this thesis.

Huddlestone-Holmes, C. R. & Ketcham, R. A. 2005. Getting the inside story: using computed X-ray tomography to study inclusion trails in garnet porphyroblasts. *American Mineralogist*, **90**, ea1-ea17.

# Abstract

This study demonstrates how high-resolution X-ray computed tomography can be used to determine the geometry of curved inclusion trails in garnet porphyroblasts. For the first time, the three-dimensional geometry of these features is shown as an animation, a stereo pair, a VRML model and two-dimensional sections. The spatial resolution of the data in this study, approximately 10 μm, is high enough to resolve inclusions, and finer resolutions are possible. Comparisons of scan imagery to thin section and microprobe data demonstrate that many typical inclusion phases in garnet porphyroblasts can be clearly distinguished, including quartz, ilmenite and monazite. A sodium metatungstate solution with a density of 1.19 g/cm$^3$ was used for a wedge calibration during scanning, reducing artifacts to a minimum and allowing maximum image contrast. The overall conclusion of this study is that high-resolution X-ray computed tomography is a quick, non-destructive technique that is invaluable in the study of porphyroblast microstructure. The three-dimensional data generated by this technique can be compared with geometries predicted by the varying theoretical models for the formation of curved inclusion trails in garnet porphyroblasts. They can also be analyzed to determine the three-dimensional orientation of curvature axes in individual porphyroblasts, which has not been possible until now.

# 1 Introduction

This paper describes a technique that allows the geometry of curved inclusion trails in garnet porphyroblasts to be studied in three-dimensions. Curved inclusion trails are a common feature of porphyroblastic minerals in rocks from deformed metamorphic terrains. They have been a source of intrigue for nearly a century and have the potential to provide insights into the structural and metamorphic processes that occur during orogenesis. Johnson (1999) provides a good review of the current literature on porphyroblast inclusion trails. He points out one of the remaining obstacles to getting the most from these structures is the lingering uncertainty over how these features are formed. This debate centers on whether or not the porphyroblasts rotate relative to fixed geographical coordinates. In the rotational model the curved trails are the result of syn-growth rotation of the porphyroblast with respect to a foliation that is parallel to the plane of shear during simple shear or non-coaxial flow (e.g. Passchier et al. 1992, Rosenfeld 1970, Schoneveld 1977, Williams & Jiang 1999). The non-rotational model has the porphyroblast preserving the rotation of the matrix foliation about it during multiple foliation forming events (Aerden 1995, Bell et al. 1992b, Bell et al. 1992c, Ramsay 1962, Stallard & Hickey 2001). How inclusion trails are interpreted in micro-structural studies is largely dependant on which of these contradictory models for their formation is favored.

There have been many theoretical studies done attempting to predict the geometry of inclusion trails based on the mechanism of formation (e.g. Masuda & Mochizuki 1989, Samanta et al. 2002b, Schoneveld 1977, Stallard et al. 2002, Williams & Jiang 1999). Conversely, the number of studies of the three-dimensional geometry of inclusion trails in rocks is small. This is because of the difficulty of doing such a study. The traditional approach to studying these geometries has been to cut serial thin sections (Johnson 1993b, Johnson & Moore 1996), do universal stage studies (Powell & Treagus 1967, 1970) or do serial grinding/microprobe studies (e.g. Marschallinger 1998, Spear & Daniel 1998). These techniques are destructive, time consuming and sections can only be cut in one direction. Serial thin sections have a minimum interval of one to two millimeters, serial grinding is time consuming and universal stage studies deal with only a thin slice of rock. It can be difficult to correlate trails between sections and impossible to re-section the porphyroblast in different orientations. To be able to get a full appreciation of the geometry of inclusion trails a new technique is needed that allows these features to be studied in more detail.

Recently Ikeda et al. (2002) used high-resolution X-ray computed tomography (HRXCT) to look at the geometry of inclusion trails in garnet porphyroblasts in three-dimensions. X-ray computed tomography, or X-ray CT, is a technique that enables the internal structure of solid objects to be visualized in three-dimensions. It has found an ever increasing number of applications in the study of geological problems (Ketcham & Carlson 2001, Mees et al. 2003). Some of the tasks that HRXCT systems have been used for over the last ten years include palaeontological studies (e.g. Cifelli et al. 1996, Rowe 1996), non-destructive studies of meteorites (Tsuchiyama et al. 2002) and quantitative analysis of porphyroblast crystallization in metamorphic rocks (Carlson & Denison 1992, Denison et al. 1997).

X-ray CT was originally developed for medical imaging in the late 1960's and early 1970's (Natterer & Ritman 2002). The technique allows an image to be constructed that shows a thin slice through a three-dimensional object based on how it attenuates X-ray energy. Stacks of these slices make a three-dimensional representation of the object. This attenuation is closely related to the energy of the X-rays, and the average atomic number and density of the material that the X-rays are passing through. In medical CT systems the variation in density and composition of bones and other organs allow imaging of the human body. Similarly, variations in mineral density and composition allow the three-dimensional textures within a rock to be revealed. The resulting data can then cut into an infinite number of sections in any given orientation, or viewed with various three-dimensional techniques. Another advantage of the technique is that the material is not destroyed in the process. Recent developments in the production of higher resolution industrial X-ray CT systems have resulted in increased spatial resolution, which coupled with the high density contrast between garnet and the minerals that typically form inclusion trails makes X-ray CT well suited to the study of the three-dimensional

morphology of these microstructures. The aim of this paper is to provide the reader with a background into this technique and a demonstration of its application. Parameters that can be controlled by the researcher are discussed from the point of view of obtaining optimal results.

## 1.1 An Introduction to Computed X-ray tomography

HRXCT, as applied in this study, is the evolution of the X-ray CT technique originally developed for medical imaging which is capable of imaging at spatial resolution 1-3 orders of magnitude greater than medical scanners in a wide range of materials. The resulting HRXCT technique has great potential for geological applications. The reader is referred to Ketcham and Carlson (2001) who give a thorough account of the current technology and its applications in the geological sciences. The key aspects of X-ray CT as related to this study are provided here.

X-ray CT works on the principal that the energy of X-rays will be attenuated as they pass through a sample, and that the amount of attenuation is related to certain properties of the material. The change in intensities of X-rays from before they enter the sample to after they have passed through it are measured. Beer's law relates this change in intensity between the incident intensity ($I_0$) and the final intensity ($I$) to the linear attenuation coefficient (μ):

$$I = I_0 \exp\left[-\sum_i (\mu_i x_i)\right], \tag{1}$$

where each increment $i$ represents a single material that has an attenuation coefficient $\mu_i$ and $x_i$ is the length of that material that the X-rays travel through.

For a single material, μ is related to the electron density of the phase ($\rho$), its atomic number (Z) and the energy of the X-rays (E). Figure 1 shows μ for different minerals as a function of X-ray energy. These have been calculated by multiplying mass attenuation coefficients obtained from the XCOM online database (Berger et al. 1999) by the mass density of the phase. In general, values of μ decrease as X-ray energy increases. This is a result of the increasing importance of Compton scattering at X-ray energies over 50-100kV, where the amount of attenuation is proportional to Z. Below these levels photoelectric absorption dominates, and the amount of attenuation is proportional to $Z^{4-5}$ resulting in greater sensitivity. While lower energy X-rays provide greater sensitivity, there is a trade-off in terms of the signal-to-noise ratio and penetration with higher X-ray energies fairing better on both accounts. Typically, X-ray sources used in X-ray CT are not monochromatic and for a tungsten tube with a voltage of 160kV, the average X-ray energy will be approximately 64 kV. Equation 1 is for a single X-ray energy, and it is this equation that is solved to define μ. This is not considered a problem as the reconstructions assign a single value per pixel that represents the relative level of absorption of the X-ray energy spectra at that point. As discussed above, the ability of X-ray CT to differentiate between different minerals is dependent on several factors; however, the

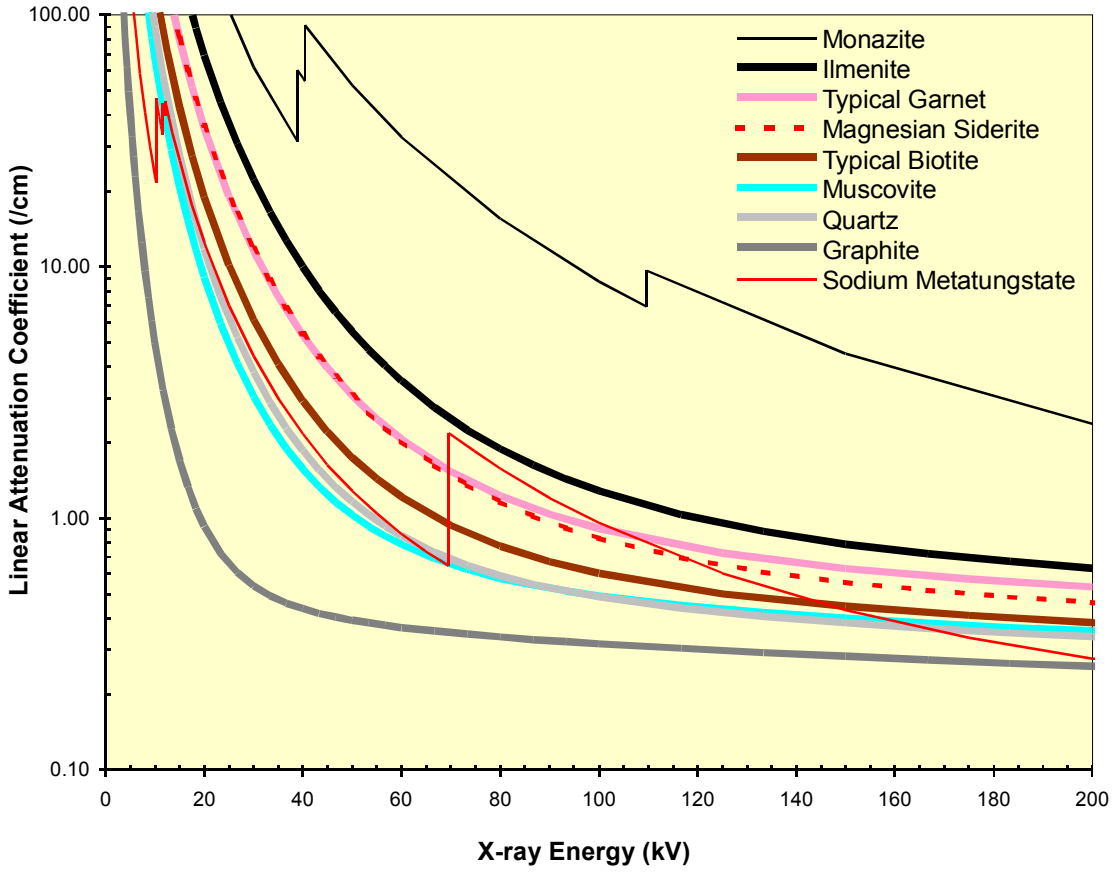


**Figure 1.** Linear attenuation coefficients (μ) as a function of X-ray energy for minerals typical of a garnet-bearing schist. This plot shows that garnet has a μ that is significantly higher than those matrix minerals typically found in pelitic schists, and significantly lower than those of the iron/titanium oxides. These minerals are also found as inclusions in garnet porphyroblasts and this contrast in μ values is what enables the imaging inclusion trails using X-ray CT. Note that magnesian siderite has a very similar μ to garnet, particularly at low X-ray energies. This is because the average Z-values are very similar for the two minerals. At higher X-ray energies the μ of these two minerals diverge due to the higher density of garnet. At the X-ray energies used for this study (150keV), these minerals cannot be differentiated. Muscovite and quartz show a similar trend. The spikes on the curves for sodium metatungstate (SMT) and monazite reflect the X-ray absorption edges of high-atomic-number elements. The data was generated by multiplying mass attenuation coefficients generated by the XCOM online database (Berger et al. 1999) by the mass density of the phase.

technique is sensitive enough to differentiate between minerals with as little as a 0.1% difference in attenuation coefficients (Wellington & Vinegar 1987).

The three-dimensional representations generated by X-ray CT are actually a stack of cross-sectional slices through the object of interest. Each slice is a two-dimensional image reconstructed from a series of projections or views (up to several thousand) on the same plane, with the sample being rotated relative to the source-detector pair between each view. The majority of scanning machines have what is known as a third generation geometry. This geometry consists of a fan beam X-ray source and a detector array that is wide enough to allow the whole object to fit within the fan (fig. 2b). This means that the sample only needs to rotate relative to the source-detector pair between views. The data collected in a single view is output as levels of attenuation and a profile is shown in figure 2c. Note the dome shape that is the

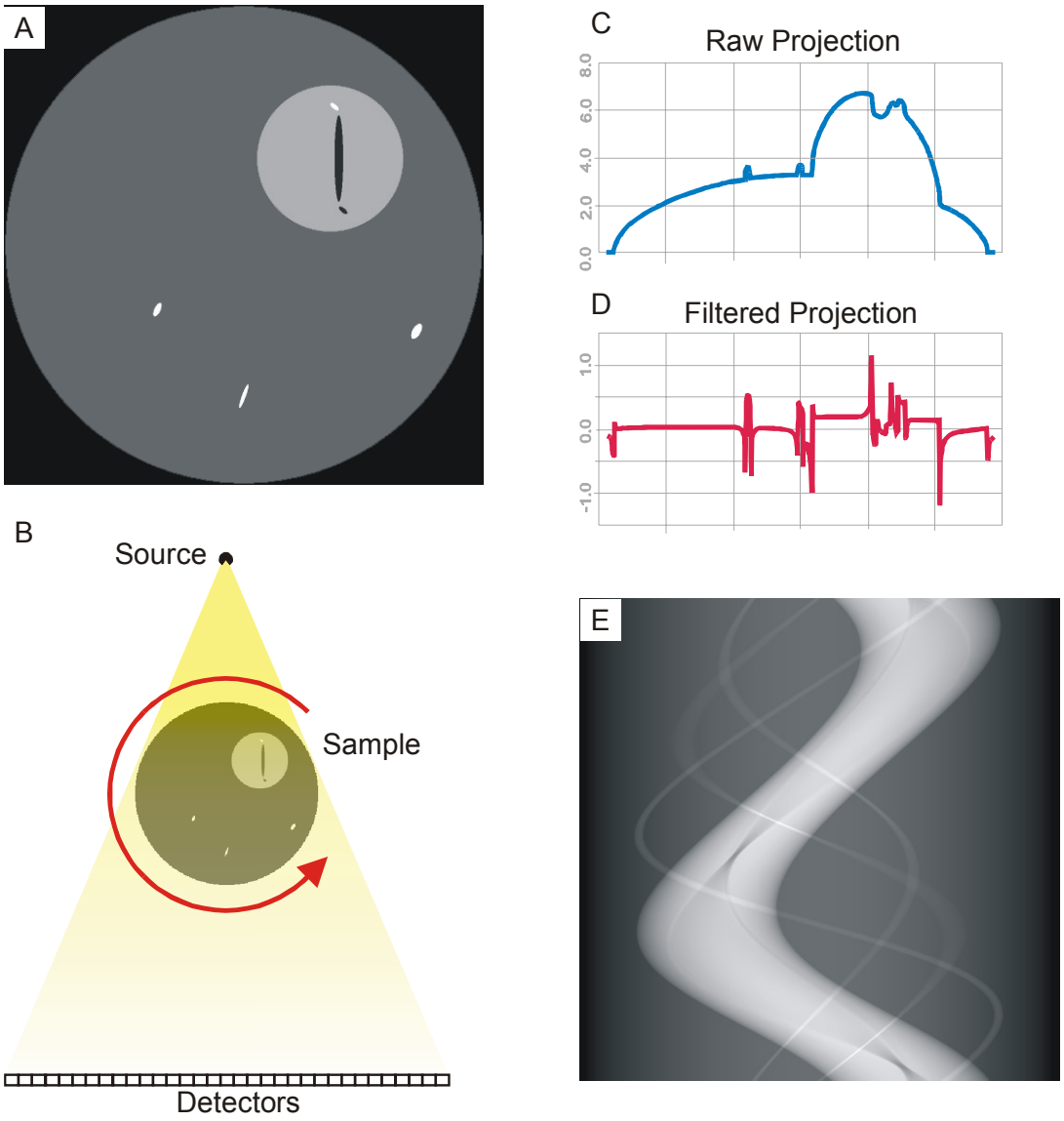


**Figure 2.** This figure shows how computed tomography works. A virtual phantom is shown in (A), representing a slice through a core of matrix material (dark grey), with a garnet porphyroblast (mid grey) and several iron oxide grains. The garnet has inclusions of matrix material and an iron oxide. Third generation scan geometry is shown in (B). (C) is the raw data profile for the view in (B). (D) shows the data from (B) after filtering to enhance edges before reconstruction. (E) is a sinogram of all the data from 512 detectors (columns) and 512 views (rows) for the phantom in (A). Zones of higher attenuation (garnet, iron oxides) are represented by lighter shades of grey. All of these simulations where made using CTSim (http://www.ctsim.org).

result of X-rays having to travel through a greater volume of rock at the center of the profile. The raw data for all views in a slice can be displayed as a sinogram (fig 2e), with each line representing the data from a single viewing angle and the columns showing values for individual detectors. Traditionally, a grey scale from dark to light is used to represent low to high attenuation levels, in keeping with conventional X-ray radiography.

The two-dimensional slice images are generated from the raw data via a mathematical process called reconstruction. There are several algorithms that can be used to reconstruct

images with a balance between computational expense, noise reduction and spatial accuracy required. The most commonly used algorithm is filtered back-projection (Kak & Slaney 1988, Natterer & Ritman 2002), in which a filter is applied to the data before the image is reconstructed. A combination between a ramp filter that accentuates contrast and reduces blurring and star patterns in the final image and a noise filter is used. This combination maintains good spatial accuracy without significantly diminishing the sensitivity of the scan. The range of filters and filter parameters provide scope for fine-tuning the image, dependent on the goals of the project and the nature of the material. Figure 2d shows the data from figure 2c after the application of a filter. The dome shape has been removed and the boundaries of the different materials have been sharpened. The final step in this process of reconstructing a tomographic image is back-projection, where the filtered data from each view is smeared across the image, as shown by the animation in figure 3. Prior to reconstruction it may be necessary to correct for drift. One way this is done is to trace the values for attenuation in air over time, equalizing them if there is a significant variation.

The resulting two-dimensional images have pixel values that correspond to the raw CT values that are scaled from low attenuation to high. This scaling has traditionally been a 12-bit range with 4096 values possible, although most modern equipment provides 16-bit (65,536 values) data. These values show the relative difference in X-ray attenuation between regions represented by each pixel. This scale is arbitrary with the key concern being to maximize the contrast between minerals in the sample. It is difficult to calibrate the system to correlate the CT values with a reference scale such as density when working with geological materials. This is because the CT values are dependent on the density and composition of the sample, the size of the sample, the energy of the X-rays and the geometry of the scan. The fact that scans are done with polychromatic X-ray sources is the biggest hindrance to a more quantitative determination of CT values. Tsuchiyama et al (2002) provide an example of the complexities in using X-ray CT for quantitative analysis of mineral compositions. This is not considered to be a necessary step for textural analysis where identification of minerals is less important or can be done by correlation with thin sections. It must be pointed out that each pixel (picture element) in a slice is more correctly a voxel (volume element), in that it has a depth equal to the thickness of the slice. The final three-dimensional volume for visualization is constructed by stacking these slices together.

The spatial resolution that can be achieved by X-ray CT is controlled by the size of the X-ray focal spot and detectors, and the ability to get satisfactory counting statistics in the measurement of the intensity of X-rays that have passed through the sample. These two factors work against each other, as a small focal spot will have lower intensity and small detectors will record fewer counts. A balance must be reached between X-ray energy, the size of the source and the detectors and of the apertures used on them, scan times and sample size. Typically, the

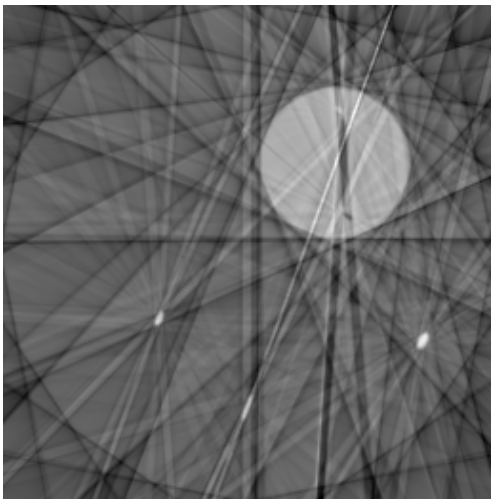

**Figure 3.** The animation shows the back-projection process, where the filtered data from each view is smeared over each other creating the final image. This animation was created using CTSim (http://www.ctsim.org) and is a reconstruction of the virtual phantom in figure 2A. The animation can be paused and stepped backward and forward one frame at a time. The frames represent 1, 2, 4, 8, 12, 16, 20, 24, 32, 48, 64, 128, 256, 512 and 1024 views respectively. The divergent nature of the material boundaries in each view is a result of the third generation scan geometry. Note the sharpness of the boundaries between the different materials, which are due to the filtering of the data before reconstruction. To view this animation, see the interactive Adobe Acrobat document on the CD in appendix A of this thesis.

two-dimensional slices are constructed as images at either a 512 x 512 or 1024 x 1024 resolution. The minimum resolution of a system therefore is one where each voxel in the reconstructed slice is of the same physical dimension as the minimum area that can be resolved when constructing the image. For modern industrial scanning systems this is roughly 3 μm for a sample 3 mm in maximum dimension. The current limitations in tube-based X-ray sources that complicate obtaining better resolution are the minimum focal spot size (~10 μm in most systems) and focal spot drift. Better resolution may be obtained with synchrotron-based CT systems, with Jones et al (2003) reporting resolutions as low as 2 μm.

Each CT voxel value represents the average attenuation within the corresponding volume of material. When that volume encompasses two or more materials of differing properties partial volume effects occur where the CT value is the volume weighted average of these different materials. In addition, because of the finite resolution of X-ray CT, voxel values are also influenced somewhat by surrounding material. These factors lead to blurring of material boundaries, and can complicate straightforward interpretation of grey level values. Conversely, this aspect of the data also allows some features that are finer than the voxel size to be detectable and even measurable. This is particularly the case for planar features such as fractures (see figure 6 of Ketcham & Carlson, 2001; Van Geet & Swennen, 2001) and high-attenuation trace phases (Kyle & Ketcham 2003). In application the minimum size of a grain that can be imaged in a rock will depend largely on the contrast in attenuation between adjacent

minerals, and the voxel size. For example, individual quartz grains in a quartzite would not be distinguishable regardless of their size whereas an ilmenite grain with dimensions close to that of a voxel may stand out from the quartz, although its attenuation signal would be smeared over several voxels. In such instances specialized calculations are required to extract reliable dimensional information. In order for a grain to be accurately measurable in a straightforward fashion, such as thresholding, as a rule it must be at least four voxels wide in each dimension.

X-ray CT scanners require offset and gain calibrations as a minimum. An additional form of calibration is a wedge calibration. In this technique a wedge of material with attenuation properties approaching those of the sample is scanned through a full rotation. This procedure provides an offset-corrected average detector reading from which all data are subtracted. Wedges are actually cylinders of material, such as garnet powder, or a solution of sodium metatungstate (SMT) in water. The advantage of an SMT solution is that it can be easily mixed to produce whatever density is desired (Krukowski 1988) it is non-toxic and as a liquid is uniform in physical properties. Because of the high attenuation coefficient of tungsten, very low concentrations can produce net attenuation coefficients similar to solid rock. The linear attenuation coefficient of a solution of SMT mixed to a density of 1.19g/cm$^3$ is shown on figure 1 for comparison with a range of pelitic minerals.

The two main artifacts that can occur in X-ray CT are beam hardening and ring artifacts. Beam hardening is caused by the preferential attenuation of lower energy X-rays as they pass through the object being scanned. The result is that the material closer to the source has a different X-ray spectrum passing through it than that further along the X-ray path. In the final image this results in the center of the image appearing to cause less attenuation than the edges. Star patterns and streaks emanating from highly attenuating objects in the final image are also due to beam hardening. Steps can be taken during sample preparation, scanning, data filtering and image reconstruction to remove the effects of beam hardening. The most successful is the wedge calibration that effectively removes the lower-energy X-rays from consideration. Ring artifacts are the result of anomalous responses from individual or sets of detectors. They result in circular features centered on the rotation axis in the final image. Again a variety of techniques can be employed to correct for this artifact with wedge calibration and data filtering being the most effective.

## *1.2 Sample Description*

The oriented sample selected for this study, V209, was collected from the Cram Hill Formation in southeastern Vermont. This rock was chosen because it has a high density of garnet porphyroblasts, most with well developed inclusion trails (fig. 4) and previous work (Bell et al. 1998) has shown that two distinct foliation curvature axes are preserved from core to rim. It is a carbonaceous pelite that has been metamorphosed to amphibolite facies and contains

quartz, muscovite, garnet, biotite, calcite, ilmenite and trace epidote. Grain sizes of matrix minerals are shown in table 1. The sample is compositionally banded with mica rich and quartz rich bands at a sub-centimeter scale. The mica rich bands have a slightly higher garnet density than the quartz rich areas. Fine graphite is present throughout the rock as a fine dusting of grains that in places form density bands.

Almandine-rich garnet and biotite are present as porphyroblastic phases with the latter restricted to the quartz-rich bands in the matrix. Garnet porphyroblasts have only partially developed crystal face,s and inclusion trails composed of elongate quartz, ilmenite grains, fine graphite, magnesian siderite and bands of hydrated Fe-oxide with pyrophyllite and quartz. The hydrated Fe-oxide/clay bands are the result of alteration along inclusion rich bands that probably represented some form of compositional layering in the rock prior to garnet growth. The composition of these precursor inclusions cannot be determined. The orientation of these bands does not appear to have been changed by the alteration process. Inclusion trail density is higher in porphyroblasts that are in the quartz rich bands. The grain sizes of the inclusions are given in table 1. A texturally distinct core and rim is preserved within the garnet porphyroblasts with the latter having few inclusions other than graphite. The core-rim transition is coincident with a drop in Ca content seen in X-ray compositional maps (fig. 5) that also show weak compositional zoning. Iron stained micro-fractures in garnet porphyroblasts are visible in the photomicrographs. Some biotite porphyroblasts have inclusion trails defined by graphitic bands and rare elongate quartz grains.

| **Phase** | **Matrix (mm)** | **Inclusions (mm)** |
|---|---|---|
| Garnet* | 1.0 – 4.0 | not applicable |
| Biotite* | 0.2 – 0.6 | not applicable |
| Quartz | 0.060 – 0.150 | < 0.100 |
| Micas | <0.015 | not present |
| Ilmenite | 0.1 – 0.25 | 0.1 – 0.25 |
| Magnesian Siderite | not present | < 0.050 |
| Graphite | < 0.004 | < 0.004 |

* Porphyroblastic phases.

**Table 1.** Grain sizes of porphyroblastic, matrix and inclusion phases. Many of the grains are elongate and the long axis dimensions only are given here. Where a definite minimum grain size is observed a range is given. Matrix quartz has two distinct domains with quartz in mica rich areas having a maximum grain size of 0.080 mm.

# 2 Methodology

## 2.1 Sample preparation

Sample preparation for X-ray CT began with cutting a 30mm thick, horizontal slab from the specimen. Samples were then prepared by drilling a vertical core 11mm in diameter through the slab. In order to preserve the orientation information, a north-south groove was made in the top surface of the specimen before coring, and a piece of wire with a notch at the northern end was glued into the groove after coring. This provided an orientation marker that could be clearly imaged by X-ray CT. A core is used because a cylinder is the ideal shape for X-ray CT analysis as it images a circular field of view. No other sample preparation was necessary.

## 2.2 Computed X-ray tomography

The scanner used for this study is at the University of Texas (UT) HRXCT Facility (Ketcham & Carlson 2001). Table 2 shows the scan parameters used in this study. Because of the wide range of material types and imaging requirements for geological research, data acquisition parameters must typically be customized for any given project. The principal aim of the scans in this study was to be able to discriminate between garnet and the material that makes up inclusion trails within the garnet. A balance was required between the volume of rock scanned to get enough garnets imaged, the spatial resolution of the scans, and the amount of contrast between CT values for the different materials.

| Parameter | Value | Parameter | Value |
|---|---|---|---|
| Source Voltage (keV) | 150 | Voxel size (μm x μm x μm) | 10.7 x 10.7 x 13.1 |
| Beam Current (mA) | 0.2 | | |
| Spot size (μm) | 30 | Image scale | 16-bit |
| Slice thickness (mm) | 0.0131 | Views per 360˚ | 1600 |
| Spacing of slices (mm) | 0.0131 | Time per view (ms) | 133 |
| Number of slices | 918 | Time per slice* (min) | 1.3 |
| Scanned height (mm) | 12.0 | Wedge | SMT** |
| Field of view (mm) | 11.0 | Offset | none |
| Slice resolution (pixels x pixels) | 1024 x 1024 | Source to Object Distance (mm) | 38 |

* Data for 27 slices acquired simultaneously
** SMT – sodium metatungstate solution mixed to a density of 1.19g/cm$^3$

**Table 2.** X-ray CT scan parameters used. See text for discussion.

An X-ray energy of 150 keV was used to provide good material penetration while avoiding beam fluctuations that occasionally occur at higher energies on the UTCT system. The current was set to 0.2 mA, resulting in a focal spot size of roughly 35 μm; the corresponding loss in sharpness was more than offset in this case by the increase in X-ray intensity and signal to noise ratio. A 1.19 g/cm$^3$ SMT solution was used for the wedge calibration. A total of 1600 views were acquired per rotation, with a sampling time of 133 ms per view, resulting in a per-rotation time of ~3.5 minutes for data acquisition plus ~0.5 minutes for preliminary data processing. Data for 27 slices were gathered during each rotation, resulting in a per-slice acquisition time of approximately 9 seconds. A total of 918 slices were acquired for each of four cores, and total acquisition time was about 2.5 hours per core. The sinogram data were reconstructed into images on a separate computer after all scan data were acquired, as the acquisition rate outstrips the processing rate. The reconstruction algorithm features re-sampling of the data to a parallel-beam configuration, followed by back-projection using the Laks filter.

## 2.3 Comparative techniques

A polished thin-section was prepared from the sample analysed by HRXCT in this study. This was done to allow comparison of the images generated with more traditional methods of analysis. Optical microscope images were taken on a Leica DMRXP microscope using a Leica DC300 digital camera. Electron microprobe analyses were made using two machines, a JEOL JX-840 electron probe microanalyser and a JEOL JX-8200 Superprobe. Back-scattered electron (BSE) images and point analyses were made on the JX-840 and X-ray compositional maps were made on the Superprobe. Qualitative point analyses were done using the energy dispersive technique with an accelerating voltage of 15kV, a beam current of 10nA and a count time of 40s on the JX-8200. Fe, Ca, Mg, Mn were mapped using the wavelength dispersive technique with other elements collected simultaneously using the energy dispersive technique. Mapping conditions were an accelerating voltage of 15kV, beam current of 100nA, spot size of 7μm, step size of 7μm and count time of 180mS.

## 2.4 Data analysis

All image analysis and processing was carried out on either James Cook University's high performance computer, Hydra, which is an SGI Origin 3800 with 84 processors, 42 Gigabytes of RAM and 1.5 Terabytes of storage or a Sunblade 2000 with dual processors and 4 Gigabytes of RAM. The images generated by the UT HRXCT facility are 1024 x 1024 pixel, 16-bit images written in a modified tiff format, with one image for each slice. One of the main challenges in working with data derived from X-ray CT is its size, with the volume of data collected for a 12mm length of core in this study being over 1.8 Gb. It is for this reason that a high performance computer was used to analyse the data. Currently available high-end desktop

computers with a large amount of RAM would be sufficient for working with subsets or down sampled versions of the data.

Three-dimensional rendering and slicing were performed using OpenDX (DX), an open source date visualisation program based on IBM, Inc.'s Data Explorer. DX is freely available on the Internet at http://www.opendx.org/. ImageMagick, an open source image-handling program available at http://www.imagemagick.org/, was used to prepare the data for importing into DX. The tiff files were converted into raw greyscale images that were concatenated into a single file that was then imported into DX and saved in native DX format as positions dependent data. Two versions of the data were imported into DX, one leaving the data intact, the other down sampling the images to 8-bit data at a resolution of 256 x 256 pixels using every third slice. Before down sampling, the image values were rescaled to spread the data over the full 8-bit range. ImageMagick uses the Lanczos sampling algorithm to resample the image by default. The lower resolution version of the data was used for imaging the whole core and locating garnets within the core, with the full resolution data used for detailed analysis of individual porphyroblasts.

The location of the centers of the garnet porphyroblasts was measured using the low-resolution dataset. A subset was then made of the full resolution dataset centered on each porphyroblast with a maximum dimension slightly greater than the maximum dimension of that garnet. This was done to allow the features of individual porphyroblast to be studied in detail and reduce processing time. To visualize inclusion trails in three-dimensions, the matrix material outside the garnets had to be removed (actually assigned a dummy value) because it has similar CT values to the inclusions themselves.

Using DX the data can be viewed as a volume rendering, a slice through the data, as contoured isosurfaces in three-dimensions or as contour lines on a slice through the data. Two-dimensional slices can be made at any orientation through any point in the data volume. When visualizing the data using DX, a color map is used to assign colors (or greyscales) to the data. This allows enhancement of the features of interest, such as inclusion trails in garnet. The 16-bit data depth allows high contrast color maps to be assigned over any given data interval. Aside from DX, there are many commercially available software packages that are suitable for analyzing X-ray CT data thanks largely to medical imaging. Amira http://www.tgs.com/ and IDL (http://www.rsinc.com/idl) are used at the UTCT facility.

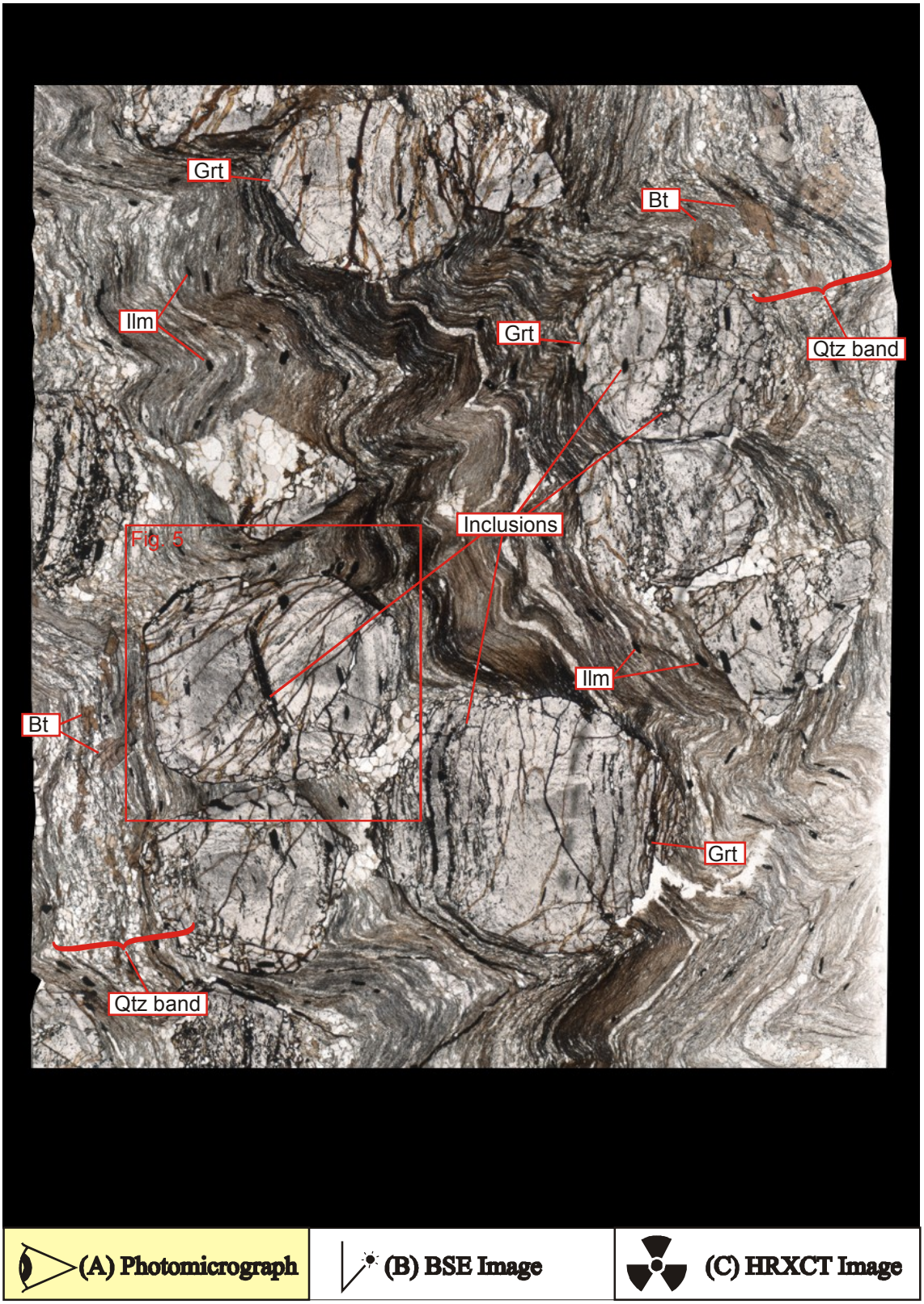


**Figure 4**. (A) is a photomicrograph of a thin section in plane polarized light through a core analyzed by HRXCT. The section is vertical and oriented west-east, looking north. The images are all of an 11 mm diameter core, 12 mm high, cut parallel to its axis. Mineral name abbreviations are from Kretz (1983). Click on the buttons below the image to select A, B or C. To view this interactive figure, see the interactive Adobe Acrobat document on the CD in appendix A of this thesis.

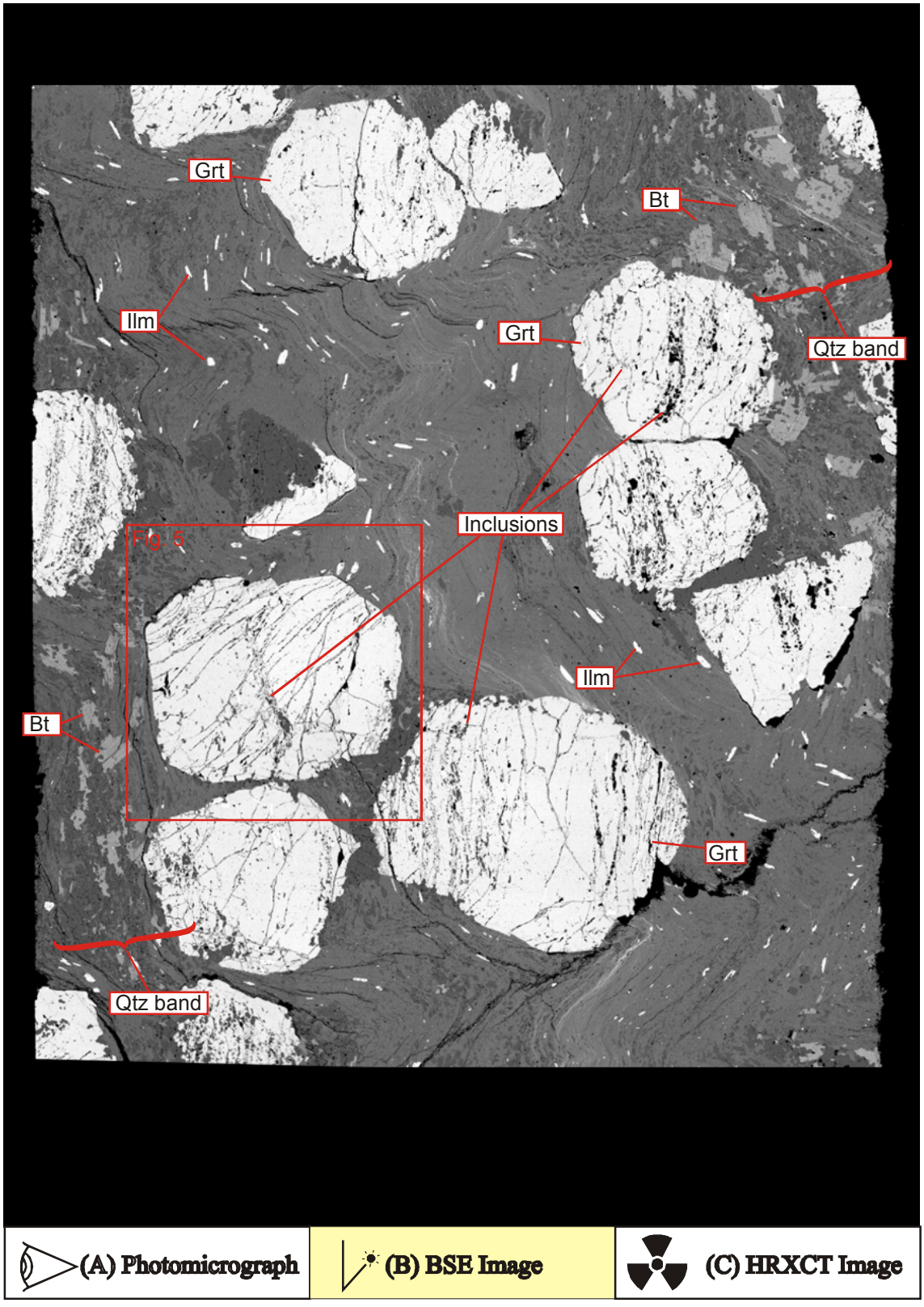


**Figure 4 cont…** (B) is an electron backscatter image of the thin section shown in (A). The images are all of an 11 mm diameter core, 12 mm high, cut parallel to its axis. Mineral name abbreviations are from Kretz (1983).

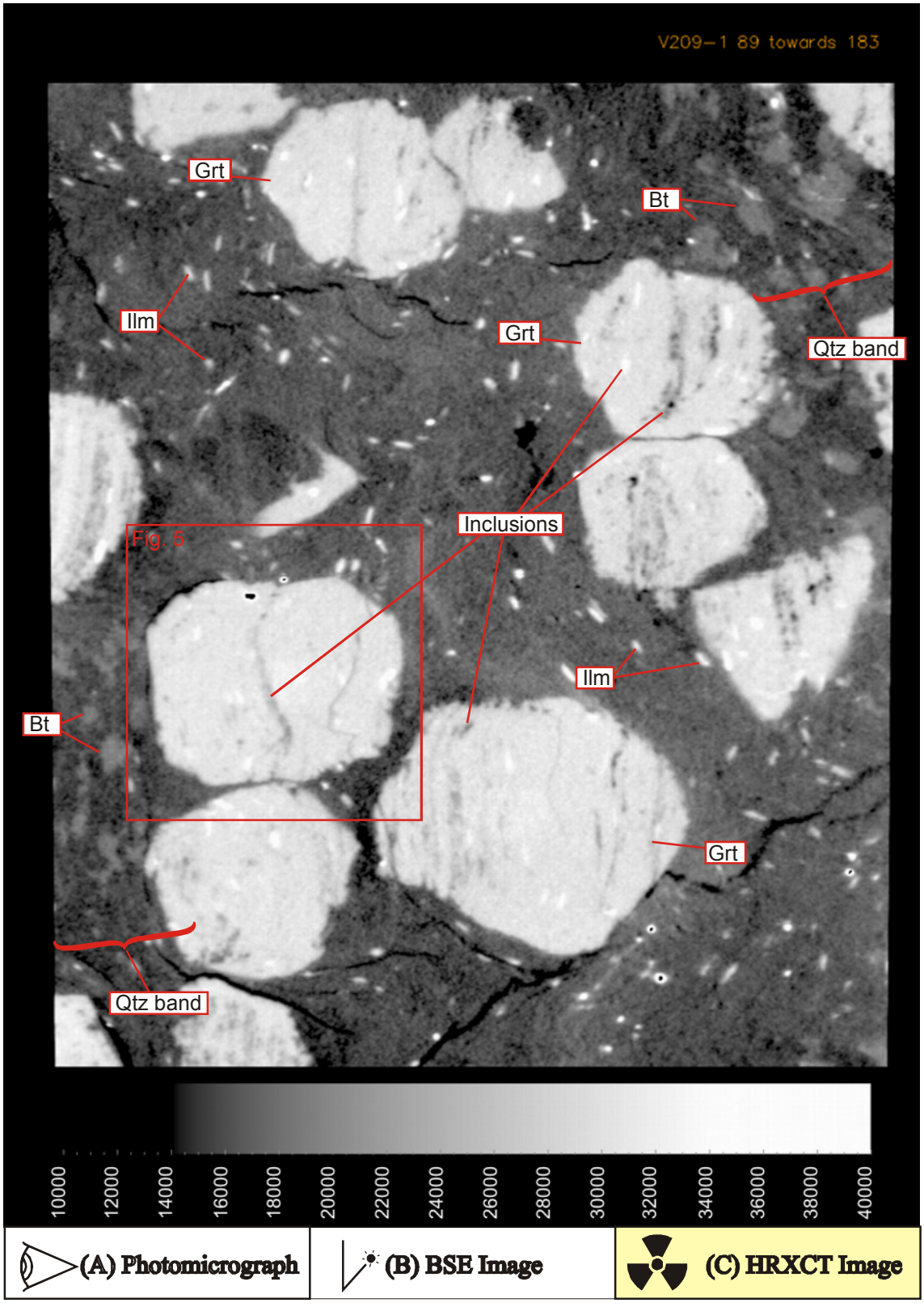


**Figure 4 cont…** (C) is a slice through the HRXCT data for the core along the plane of the thin section. A gray scale has been applied to the data with lighter levels representing more highly attenuating material. The images are all of an 11 mm diameter core, 12 mm high, cut parallel to its axis. Mineral name abbreviations are from Kretz (1983).

# 3 Discussion

Figure 4 shows a transmitted light photomicrograph of a thin section made parallel to the axis of a sample core (a), an electron backscatter image of the thin section (b) and a slice through the HRXCT data for that core in the same orientation and position as the thin section (c). This allows comparison between the three techniques. The image produced by HRXCT is similar to that collected by electron backscatter because the two techniques are both imaging similar properties of the sample (the average atomic number). The matrix displays compositional banding at the scale of the thin section with quartz rich bands pitching at 80° to the right in the lower left and upper right corners of the image. This is also apparent in the HRXCT image as darker areas within the matrix, a result of the relatively low attenuation value of quartz (fig. 4c). Biotite porphyroblasts with fine graphitic inclusion trails can also be seen in these parts of the images although the trails are only visible in the photomicrograph. The HRXCT image shows lower resolution for the matrix because of the similarity in attenuation values of quartz and muscovite (fig. 1) and its fine grain size. Fine biotite, which has an attenuation value slightly higher than the other matrix minerals is also present, but partial volume effects due to its fine grain size result in their blending in to the rest of the matrix. Slightly coarser rutile grains are well imaged and provide markers for the matrix foliations. The garnet porphyroblasts stand out clearly in all images, as do their inclusion trails. In this set of figures nothing has been done to enhance any of the features, except to compress the greyscale values for the HRXCT image to a range of 14,000 to 38,000 (instead of 0 to 65,536) to enhance contrast.

Figure 5 shows a series of images of the garnet porphyroblast highlighted in the lower left of figure 4. These include photomicrographs (figs. 5a,b) and compositional maps (figs. 5d-h) as well as a false color HRXCT (fig. 5i) image for comparison. Looking at the photomicrographs a band of hydrated iron oxide with pyrophyllite and quartz can be seen running through the center of the garnet. This band shows clockwise asymmetry with an anti-clockwise flick towards its ends. Fine elongate magnesian siderite grains are also present and show typically high-birefringence in crossed polars (fig. 5b), with iron content similar to garnet, magnesium content higher than garnet (particularly near the centre of the garnet) but no silicon (fig. 5d,e,h). Elongate ilmenite grains are the coarsest inclusions preserved and are generally elongate parallel to the central band. Quartz inclusions (white on the silicon map, fig. 5h) are present as fine grains or clusters that are also elongate. Fine calcium rich inclusions (fig. 5g) are apatite. The porphyroblast has a fine dusting of graphite that is clearly visible in the plane polarized light photomicrograph (fig. 5a) and a weak form of sector zoning is present. At the left and right ends of the porphyroblast, graphite defines more or less vertical bands in the outer 0.2mm of the grain that appear to be continuous with banding in the matrix. This corresponds

with a rim overgrowth and zoning in the magnesium, manganese and calcium composition. A feature that stands out in the photomicrographs is the top-right to bottom-left running iron stained fractures. They appear to have a significant thickness (~50µm) but this results from their low angle to the section (east-west, vertical) that has a thickness of approximately 30µm. They majority of fractures dip at approximately 70° towards 235° and are generally only a few microns thick.

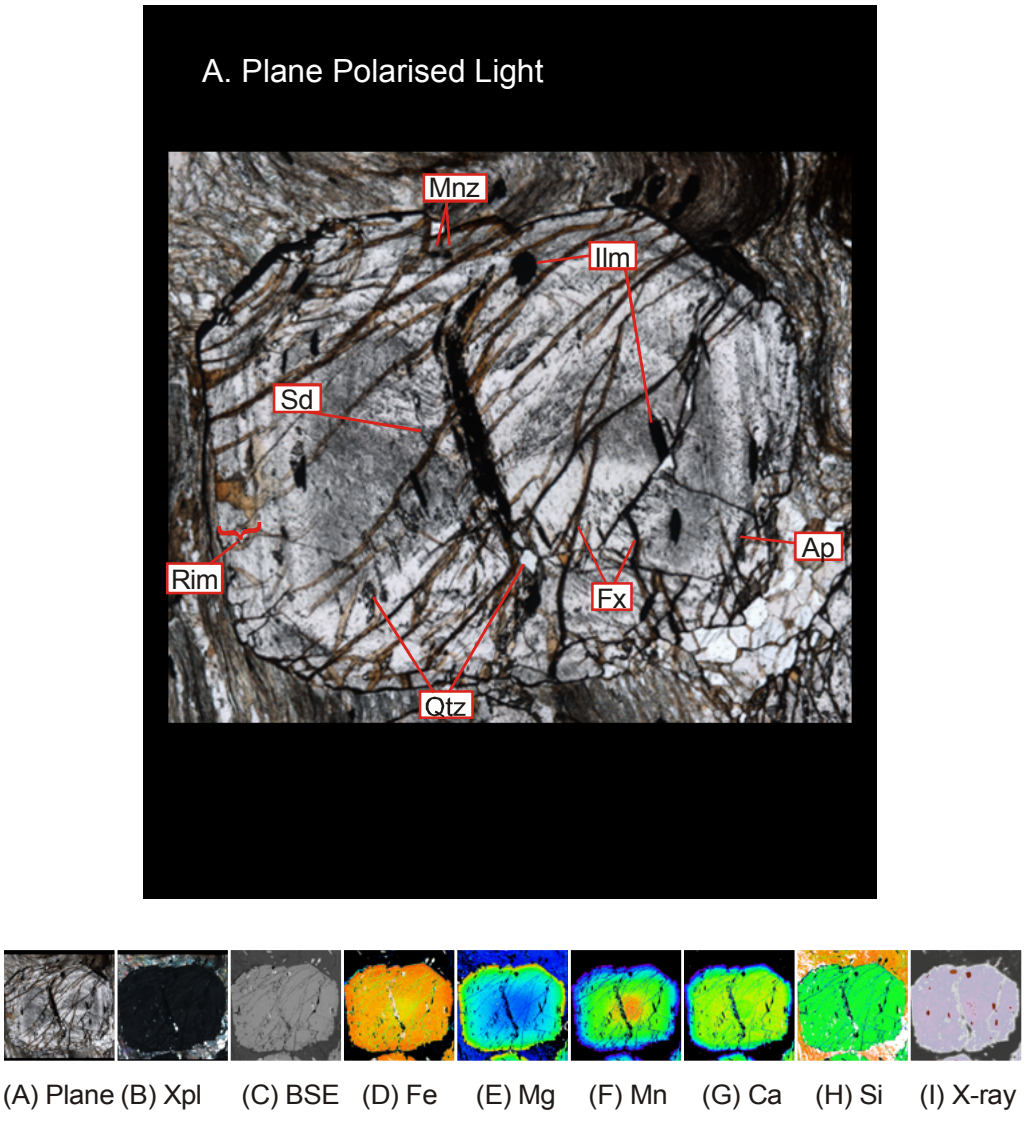


**Figure 5.** This series of images shows the garnet indicated in figure 4 for detailed examination. (A) and (B) are photomicrographs in plane polarized and crossed polar transmitted light respectively. A BSE image is shown in (C) along with compositional maps for Fe (D), Mg (E), Mn (F), Ca (G), and Si (H). A HRXCT image, which has been assigned a false color scale to highlight features, is shown in (I). All images show a region approximately 3.5mm across. Mineral name abbreviations are from Kretz (1983). Fractures have been labeled Fx. Switch between images by clicking on the thumbnails. See text for further discussion. To view this interactive figure, see the interactive Adobe Acrobat document on the CD in appendix A of this thesis.

The HRXCT image of this porphyroblast (fig 5i) clearly shows the central band and ilmenite grains. In this image a color map has been used to enhance the inclusions, rendering material with CT values lower than garnet shades of grey (hydrated iron oxides, quartz, clay) and material with higher values red-brown (ilmenite). The overall asymmetry of the inclusion trails is clear in this image, including the reversal at the ends of the central band. In this case individual quartz grains in the garnet are generally too fine to image well and only larger grains or accumulations of grains are visible in the HRXCT image. Where these grains or accumulations are elongate they help to define the inclusion trail geometry. Ilmenite grains are generally coarser in this specimen and their elongate nature can be readily seen. Magnesian siderite inclusions cannot be distinguished from garnet because these two phases have very similar attenuation characteristics (fig.1) at the X-ray energies used for this study. The majority of the fractures seen in the photomicrographs (figs. 5a,b) and compositional maps (figs 5d-h) are not visible in the HRXCT image (fig. 5i), because they are generally very fine and not filled by a material with significantly different attenuation characteristics to the garnet. Only coarse fractures are imaged. Similarly, graphite dusting is also too fine and sparse to make an impact on the CT values for the garnet. The two small grains (red spots in figure 5i) at the top of the porphyroblast are monazite, which is very highly attenuating because of its high average atomic weight (they also stand out as two bright spots in the BSE image, fig. 5c). Although these grains are less than 60 μm in diameter, they stand out in the image because they have a much higher attenuation coefficient than the material they are in (fig. 1). The halo-like artifact is a result of smearing in the reconstruction of the image. What appears to be a speckling of ilmenite in the center of the garnet porphyroblast is probably the result of compositional zoning in the garnet. In addition to the major-element zoning shown in Figure 5, qualitative electron microprobe analysis indicates that the core of the garnet is relatively high in yttrium. Estimation of the effects of zoning in both major elements and Y, based on profiles of garnets from the Picuris Mountains by Chernoff and Carlson (1997, 1999), suggest that either may cause a shift in attenuation coefficient on the order of 0.5% with X-rays in the 20-100 keV energy range. This shift is slightly above the lower limit of detectability in CT with a polychromatic X-ray source

This study demonstrates that HRXCT is capable of imaging inclusion trails in garnet porphyroblasts where the inclusions are of suitable size, composition and abundance. The data presented here suggest some guidelines for the selection of the most suitable samples for this technique. Firstly, the spatial resolution of the images is largely controlled by the sample size. The image size is constrained by the number of detectors, in this case 1024, resulting in an image size of 1024 x 1024 for each slice. The smaller the sample, the higher the achievable spatial resolution. Although the theoretical minimum resolution for modern HRXCT systems is around three microns for a sample two to three millimeters in diameter this is really pushing the equipment to its limits. At this scale data acquisition would be more time-intensive (and money-

expensive) in order to obtain relatively noise-free images, as there is much less differential attenuation across small samples. In addition, a smaller focal spot would be required, decreasing X-ray intensity and increasing problems associated with drift in the focal spot position. As a result a study of inclusion trail geometry would ideally involve a sample with five-ten mm diameter garnets that could be scanned individually or in cores drilled from the sample providing a voxel size of five to ten microns. Scanning a larger sample at low resolution would allow the garnets within it to be located for extraction.

The mineralogy, size, density and distribution of inclusions within porphyroblasts dictate which samples are most suitable for the analysis of inclusion trails using CT. Minerals with significantly different attenuation coefficients to garnet provide the best contrast and both quartz and iron/titanium oxides are ideal. It is a happy coincidence that these minerals are the most common inclusions seen in garnet porphyroblasts. Given the voxel size described above, an inclusion size ranging from fifty microns to 0.2 mm in maximum dimension would be ideal, allowing the shape of individual inclusions to be clearly imaged.

An appropriate range for the density of inclusions is from ten to thirty percent. If the density is too high images are confusing, while if it is too low the trails aren't adequately defined. Inclusions that are evenly distributed throughout the porphyroblast provide a clear picture of the overall geometry of the trails. Where they are restricted to bands, either as a relict of primary layering of the rock or as the result of a differentiated crenulation cleavage, they provide marker bands that are continuous through the porphyroblast and allow comparison with geometries predicted from models for the formation of curved inclusion trails (e.g. Stallard et al. 2002, Williams & Jiang 1999). The garnet in figures 5 is a good example of this type of inclusion distribution. The size of the inclusions is less important if they define bands as the bands as a whole would define the inclusion trails.

A powerful advantage of HRXCT is that a true three-dimensional dataset is created and the data can be viewed in a large number of ways. A single porphyroblast can be viewed in three-dimensions, made transparent to highlight the inclusion trails or removed altogether leaving just the inclusions. Intersecting or parallel slices can be made with an infinite range of orientations and through any point in the porphyroblast. Figure 6 demonstrates a range of viewing techniques of the trails from the garnet featured in figure 5. An animation makes the three-dimensional geometry of the trails clearer in figure 7, as does a VRML model that is available for download through appendix 1. These data can also be viewed as stereographic projections allowing the trails to be studied in three-dimensions. Figure 8 is a stereo pair that can be printed to hard copy and viewed using a standard stereo viewer.

Figures 6a-d and 7 are looking south and the asymmetry of the inclusion trails can be clearly seen in three-dimensions. The central band shows a central section that is approximately vertical, with a subtle doubly curving non-cylindrical geometry. Towards the top and bottom

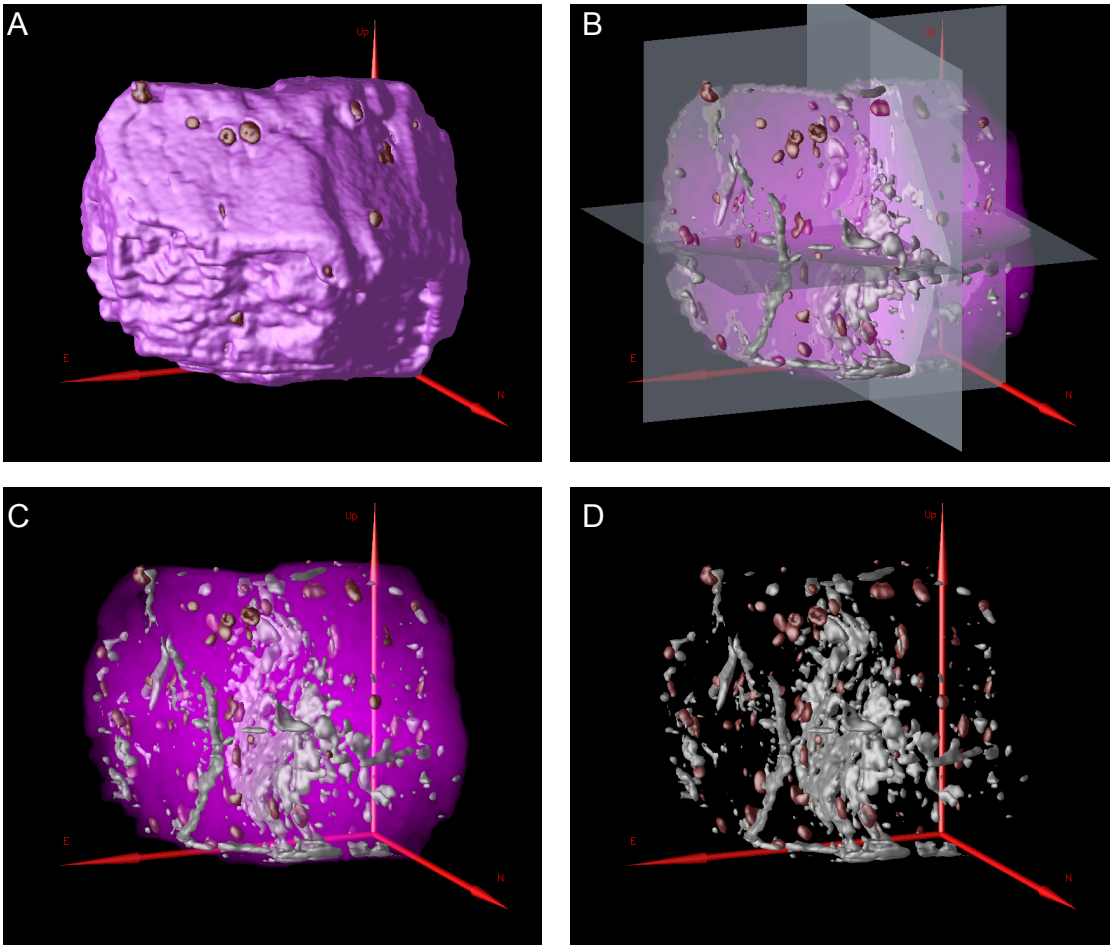


**Figure 6.** This figure shows different ways of viewing the HRXCT data. All images show the garnet in figure 5, with a field of view of 4.5 cm. (A) shows the garnet rendered as a solid, opaque object. (B) shows the garnet rendered as a transparent object, with the inclusions rendered solid (gray for low attenuation, red-brown for high attenuation), with sections cut horizontally, east-west vertical and north-south vertical. The same image without the sections is shown in (C) and without the sections or garnet in (D).

edges of this band the curvature tightens with the same anti-clockwise, or top to the east, asymmetry. The axis about which this curvature occurs plunges at 2.5° towards 187.5°. This was measured to a 5° interval using a similar technique to that used to measure FIAs in thin section, making many slices through the garnet. This proved to be more reliable than attempting to fit an axis to the three-dimensional data because of the irregular distribution of inclusions. The geometry seen here is referred to as being sigmoidal (as opposed to spiral) and represents approximately 75° of curvature. The flick back at the end of the trails seen in the photomicrographs in figure 5 is also apparent. The axis about which this flick occurs has a trend of 122.5°. It was not possible to accurately measure its plunge of because it occurs over too small a region. As mentioned earlier, fine graphite dusting cannot be imaged by HRXCT so the orientation of trails in the very rim of the garnet could not be measured.

When studying the VRML model in appendix 1 a sub-vertical axis of curvature is also apparent with a south to the east asymmetry. See the Applications section below for a discussion of the measurement of FIAs. It is interesting to note that the ilmenite grains range in shape from fat discs to short rods, all plunging steeply and parallel to the central band. This probably represents the stretching lineation for the foliation defined by the central band.

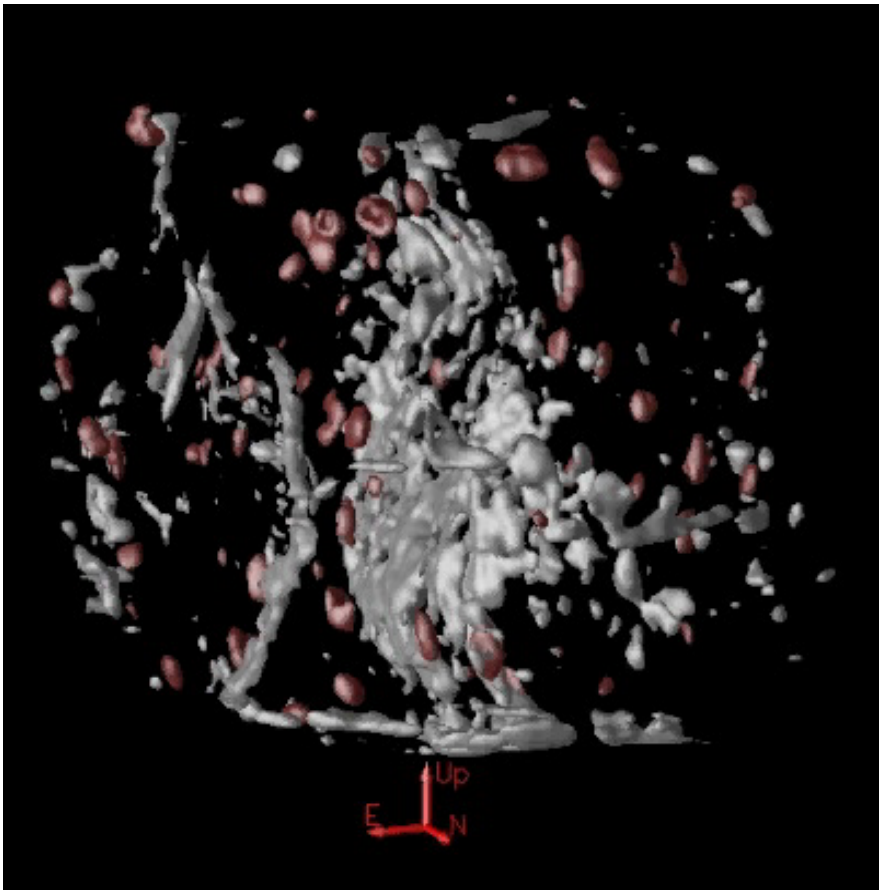


**Figure 7.** This is an animation that shows the inclusion trails from the garnet featured in figure 5 and 6a-d being rotated through a 40° range about a vertical axis. This allows the three-dimensional geometry of the inclusion trails to be seen more clearly. Note the doubly curving non-cylindrical geometry shown by the central band, which curves about a sub-horizontal, north-south trending axis. A fracture crosses the northeast part of the garnet and is distinguishable from the inclusion trails by its irregular nature and discordance with the rest of the trails. The field of view is approximately 4.5 cm. The animation can be paused and stepped through frame by frame if desired. To view this animation, see the interactive Adobe Acrobat document on the CD in appendix A of this thesis.

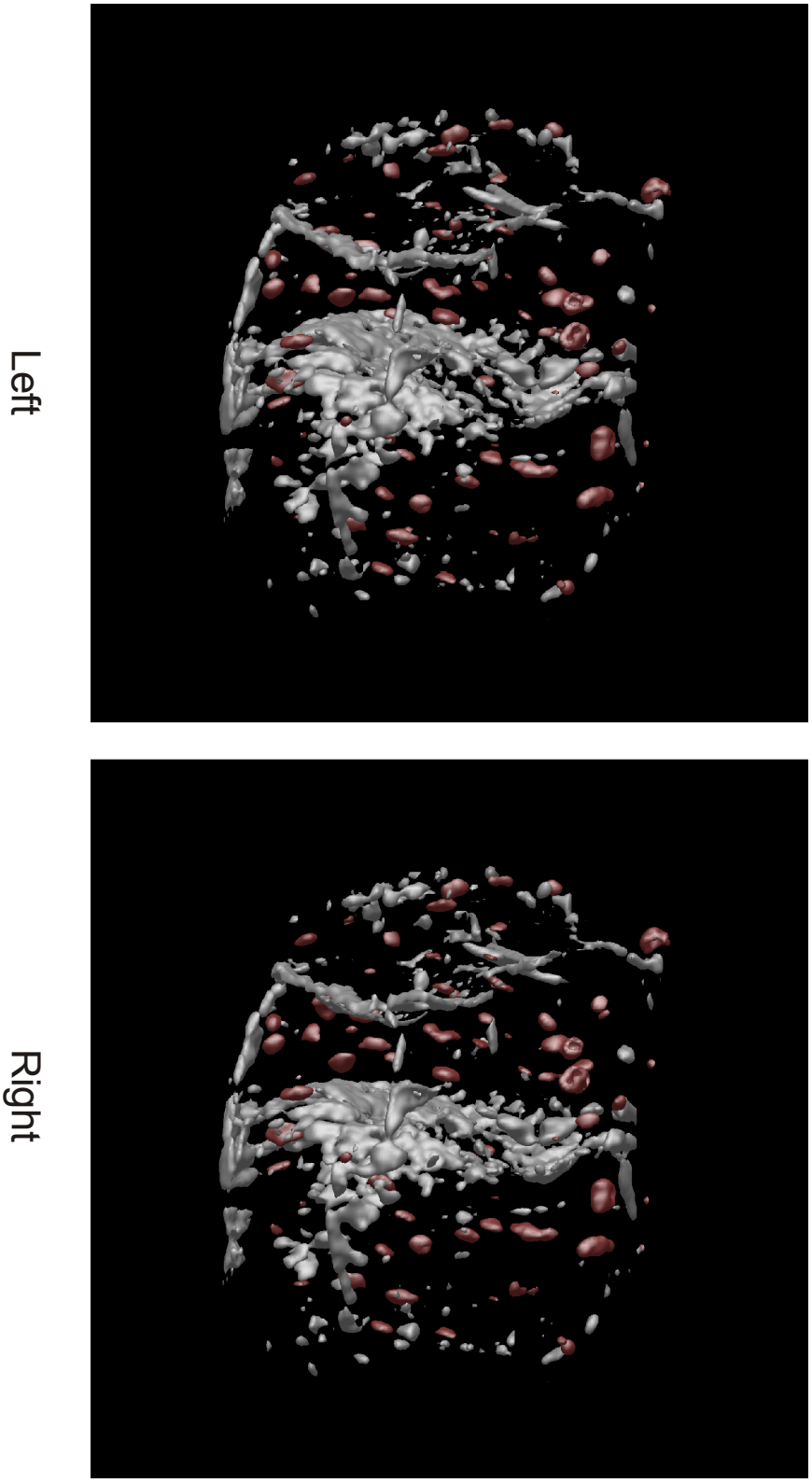


**Figure 8.** A stereo pair of the three-dimensional image of the inclusion trails in the garnet in figures 5, 6 and 7. This allows the true three-dimensional geometry of these microstructures to be viewed using a standard stereo viewer. Images have a resolution of 375dpi and can be printed in color or greyscale. The field of view is approximately 4.5 cm To print these images, see the interactive Adobe Acrobat document on the CD in appendix A of this thesis.

## 3.1 Applications

### 3.1.1 Investigating the three-dimensional geometry of inclusion trails

The most obvious application of this technique is in attempting to answer the question of whether or not curved inclusion trails form as the result of the porphyroblast rotating relative to fixed geographic reference frame or by the overgrowth of a series of foliations. This technique allows detailed three-dimensional study of inclusion trails enabling their geometry to be compared with those predicted from models. Williams and Jiang (1999) provide a criterion with which that the three-dimensional geometry of spiral inclusion trails (as opposed to the two-dimensional geometry) can be used to determine whether rotational or non-rotational models apply. Conversely, Stallard et al (2002) predict that the different processes hypothesized for the formation of inclusion trails may not produce inclusion trail geometries that are significantly different. Unfortunatley, the garnets imaged in this study do not contain spirals so no conclusions can be drawn here. However, the data here demonstrate how HRXCT data could be used. The inclusion pattern in figure 9a is similar to the closed loop structures predicted by Stallard et al (fig. 4, 2002), for instance, which they predict will be a feature regardless of how the curved trails form. This geometry is the result of the subtle doubly curving geometry of the trails that demonstrate that if the non-rotation model is correct then the crenulation hinges they grow in are non-cylindrical. This is an example of how HRXCT data can be sectioned at any orientation and the geometry in the section compared with that predicted by a model.

Most of the literature on numerical simulations or theoretical models of inclusion trail development in porphyroblasts are concerned with spiral shaped trails (e.g. Samanta et al. 2002b, Stallard et al. 2002, Williams & Jiang 1999). In reality, sigmoidal trails, as in the data presented here, are much more common than spiral trails. Sigmoidal trails have a simple S or Z shape and a maximum of 90º to 120º of apparent rotation. It is interesting to note that close to the axis of curvature these sigmoidal trails looked like a 180° spiral (figure 9b). This observation reinforces the idea that if three-dimensional data such as presented here are not available then multiple thin sections of differing orientations are needed to see the full complexity of structures preserved in inclusion trails (Cihan 2004). To compare models against reality a selection of samples with inclusion trails that range from true spiral shapes to simple sigmoids is needed. At present, there are only two publications on the three-dimensional geometry of real inclusion trails, one on spirals (Johnson 1993b) and one on millipede structures (Johnson & Moore 1996) and these data need to be added to if our understanding is to be advanced. Aspects of deformation mechanisms themselves revealed from this type of study may be supportive of one model or the other. A key concept of the argument for non-rotation of porphyroblasts is that of deformation partitioning (see Bell 1985) while most rotational arguments are based on simple and pure shear (e.g. Samanta et al. 2002b, Stallard et al. 2002).

How features such as truncation surfaces and millipede structures relate to these processes will be better understood once they have been studied in three-dimensions. For instance, figure 9c shows a truncation surface in a garnet imaged by HRXCT. Study of these features in the sample revealed them to be sub-planar features that curve only slightly around the core of the garnet. The near vertical trails in the core of the garnet curve into these truncation surfaces with an apparent rotation of 90°. This geometry supports the hypothesis that truncations in porphyroblasts are evidence for episodic deformation and metamorphism (Bell et al. 1992c). A full discussion of the three-dimensional geometry of inclusion trails with respect to models for their formation warrants a paper of its own and will not be pursued further here.

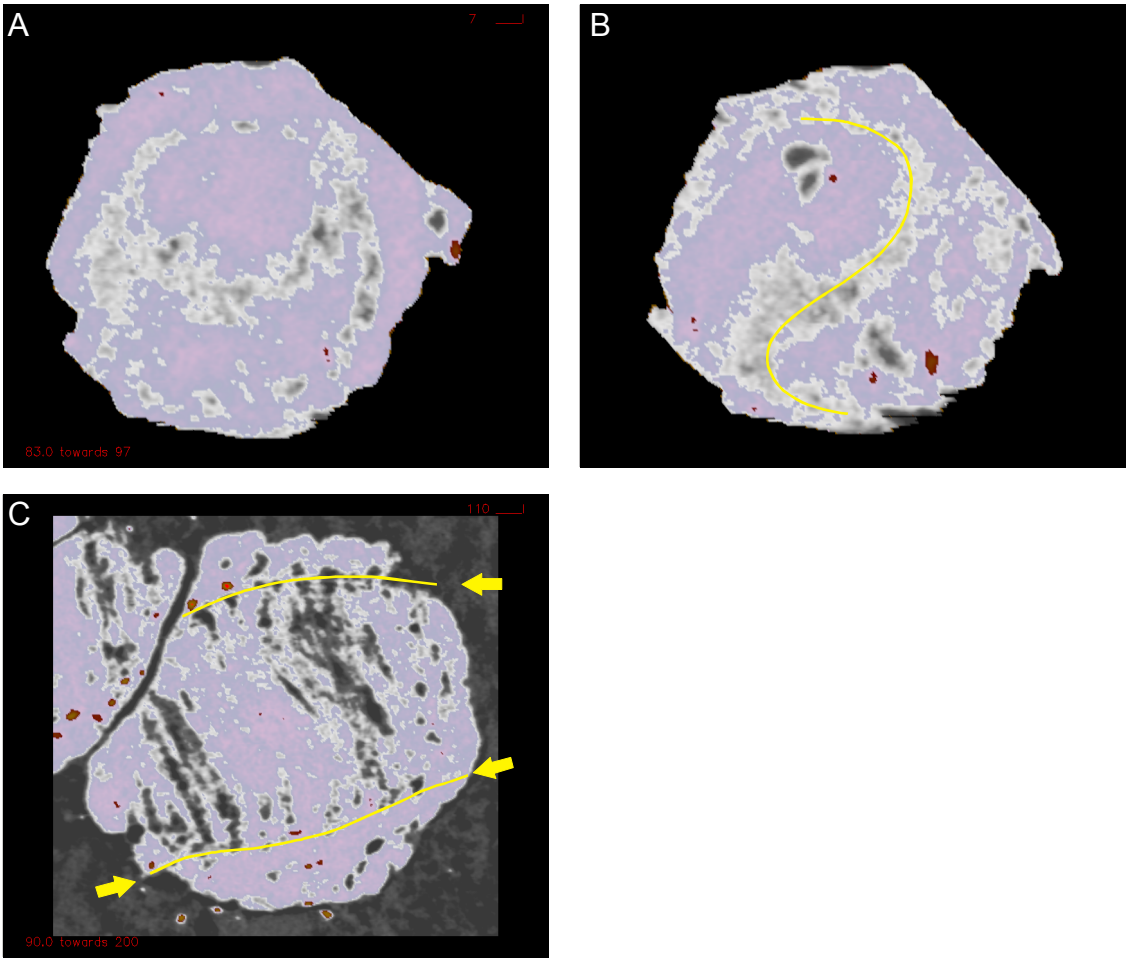


**Figure 9.** (A) is a section through the garnet in figures 5 through 8 parallel to the axis of curvature showing closed loop structures predicted by Stallard et al (2002). (B) shows a section through the same garnet oriented slightly oblique to the axis of curvature. The apparent 180° spiral geometry (mouse over to highlight) could give a false sense of the amount of curvature if seen only in thin section. A flat truncation (yellow arrows, mouse over to highlight) of a steep foliation with clockwise asymmetry is shown in (C). Field of view 5.5cm. To view this interactive figure, see the interactive Adobe Acrobat document on the CD in appendix A of this thesis.

### 3.1.2 Assessing the distribution of FIA in a single sample

A concept that has had recent exposure in the literature is that of the FIA (foliation intersection/inflection axis preserved in porphyroblasts), which measures the axis of curvature of curved inclusion trails (Bell et al. 1995, Bell et al. 1998, Hayward 1990). In a review of the uses of porphyroblast microstructures, Johnson (1999) raised some important questions regarding FIA, mostly regarding the spread of orientations obtained for a single sample and the error therein. The main problem in addressing these questions is that the technique for determining FIA only allows the trend to be determined for a sample, rather than for individual porphyroblasts. As a result, it is impossible to know what their porphyroblast to porphyroblast variation is and following on from this, what the true statistical spread of trends for a sample is. To allow FIA to be used to their full potential, questions about the statistical confidence that can be assigned to determined trends need to be addressed.

The HRXCT technique provides a method for measuring the FIA of individual porphyroblasts, thus allowing the range of their orientations to be determined. This is the subject of the study for which the data presented here were collected and a paper discussing the results is in preparation. Two FIA could be measured in this sample. The first is for the broad central or core part of the trail, which was measured in 58 garnets and has a mean orientation plunging at 10.6° towards 200.7°. The data are symmetrical and forms a clustered distribution (figure 10b) with a 95% confidence cone semi-angle of 4.1°. The second is in the median part of the garnet (the flick back in figure 5) for which only the trend could be measured reliably. It was measured in 17 porphyroblasts and a mean value of 116.9° was obtained, with a 95% confidence interval of ± 2.7° (figure 10c). The sub-planar part of the trails was also measured in 55 of the garnets for which core FIA were measured (the other three either had too few inclusions in the central part or were too smoothly curved) and while they are more dispersed than the FIA data they have a similar distribution pattern with a mean orientation plunging at 18.0° towards 292.8° (figure 10a). There is a strong correlation between the trend of the core foliation and core FIA. There is no evidence in the data to suggest that the event that formed the median FIA in anyway modified (i.e. rotated) the distribution of structures already preserved in the cores of the garnet. This observation, along with the clustered nature of the FIA data from the core of the garnets, suggests that the prophyroblasts in this sample have not rotated. The non-rotation interpretation of the history preserved here is that a steep foliation trending 30°-210° is overprinted by a flat lying crenulation cleavage. The garnet nucleates and grows during this event and preserves the curvature of the steep foliation into the flat. The core FIA orientation is that of the intersection between the earlier steep and following flat foliation. Another steep 115°-295° trending foliation then forms and is overgrown by a small radial increment that forms the median part of the garnet. A final increment of growth forms the rim of the garnet, most likely in a flat foliation. The steep FIA seen in the VRML model (appendix 1)

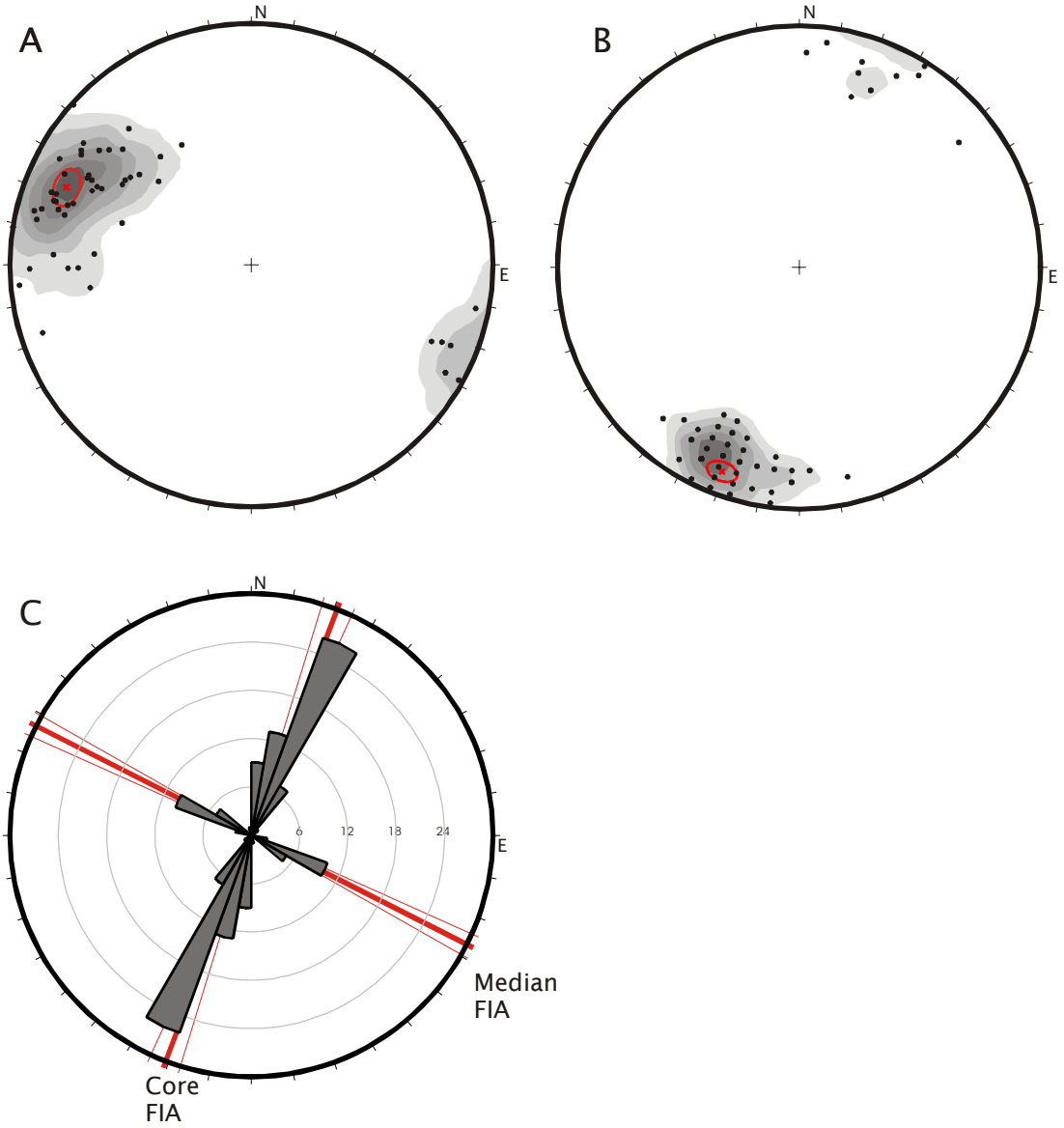


**Figure 10.** This figure shows preliminary data from a study of the distribution of FIA in individual porphyroblasts from a single sample. (A) and (B) are equal area stereo nets showing the orientations of inclusion trails measured in the cores of 55 garnets (plotted as poles) and the orientations of FIA from the core of 58 garnets respectively. These data are plotted as points and density contours as the FIA data have some repeat readings. The mean orientations are marked with a red cross and the 95% confidence cone as a red circle. The regular spacing in the core FIA data is a result of them being measured in 5° intervals. (C) is a rose diagram showing the FIA data from the garnet cores and an additional 17 measurements from their medians. See text for further discussion.

is most likely the result of the intersection between relicts of the original steep foliation (that has been protected from the effects of the flat foliation in the strain shadow immediately adjacent the garnet) and the later steep foliation that formed the median FIA.

Previously, three-dimensional datasets have been created by indirect construction from a series of two-dimensional thin-sections through a porphyroblast (e.g. Johnson 1993b, Johnson & Moore 1996) or serial lapping (e.g. Daniel & Spear 1998, Daniel & Spear 1999,

Marschallinger 1998, Spear & Yao 2001, Spear & Daniel 1998, Spear & Daniel 2001). These methods are time consuming – to achieve a similar resolution of data to that gathered by HRXCT in this study, Marschallinger's (1998) technique would require 300 cycles of lapping and image collection for a 3mm diameter garnet. The HRXCT data presented here, representing approximately four cubic centimeters of rock, was gathered in about a day and a half. There are two advantages of serial lapping over HRXCT. Firstly, the resolution in the two-dimensional slices being mapped can be significantly higher. Secondly, a range of images can be collected for each slice, such as optical photographs, back-scattered electron images, secondary electron images and compositional maps, providing compositional data in three-dimensions. However, for textural analysis on a truly three-dimensional basis, HRXCT is an invaluable tool. Furthermore, these approaches are not exclusive of each other: because HRXCT is non-destructive, the samples are preserved for future compositional analysis, which can be targeted at the most potentially informative porphyroblasts.

## 3.2 Future Directions in HRXCT

While this technique is readily available now and provides an excellent tool for the study of geological textures, it continues to be refined. Research into improved reconstruction algorithms that reduce artifacts or improve processing time continues (e.g. De Man et al. 2001, Elbakri & Fessler 2003, Kalukin et al. 2000, Yamaya et al. 2000). This, along with the steady increase in computing power and advances in detector technology, will allow ultra-high resolution studies with improved differentiation of materials. The currently available X-ray CT technology is limited by the use of polychromatic X-ray sources. This means that the X-ray attenuation coefficients can not be determined quantitatively. Tsuchiyama et al. (2002) described a technique for quantifying the relationship between CT values and linear attenuation coefficients by normalizing the CT values to a known standard. Another possibility is the use of monochromatic X-ray sources which allow quantitative determination of the X-ray coefficients of the material being scanned(e.g. Bonse & Busch 1996). This can only be done with synchrotron radiation as an X-ray source (Dilmanian 1992, Natterer & Ritman 2002) at this time, which limits its availability. The HRXCT technique described here relies on the absorption of X-rays. The use of synchrotron radiation sources have allowed other methods to be investigated including dual energy subtraction (Torikoshi et al. 2001, Torikoshi et al. 2003), fluorescence (Takeda et al. 2000) and phase shift contrast (Bonse & Beckmann 2001, Bronnikov 2002), all of which are more sensitive to variations in materials than conventional attenuation contrast methods.

In addition, specialized software tools for efficiently making geologically useful measurements in three-dimensional volumes are under continuous development. Examples include measuring the size and shape characteristics of multiple crystals, clasts or vesicles

(Ketcham 2004, Koeberl et al. 2002, Proussevitch et al. 1998) and three-dimensional fabric orientation and strength (Ketcham & Ryan 2004).

# 4 Conclusions

Computed X-ray tomography continues to find a broader range of application in the geological sciences. Here, its viability as a technique for the imaging of the three-dimensional geometry of inclusion trails in garnet porphyroblasts has been demonstrated. Preliminary studies have given the range of FIA orientations in a single sample for the first time and given support to the non-rotational argument for the formation of curved inclusion trails. With the selection of samples following the guidelines given here, the study of the three-dimensional geometry of curved inclusion trails in garnet can be furthered. This will help to address the ongoing controversy of the mode of formation of these features. The FIA concept can be tested further allowing their significance to be better understood.

# References

Aerden, D. G. A. M. 1995. Porphyroblast non-rotation during crustal extension in the Variscan Lys-Caillaouas Massif, Pyrenees. *Journal of Structural Geology* **17**, 709-725.

Bell, T. H. 1985. Deformation partitioning and porphyroblast rotation in metamorphic rocks: a radical reinterpretation. *Journal of Metamorphic Geology* **3**, 109-118.

Bell, T. H., Forde, A. & Hayward, N. 1992a. Do smoothly curved, spiral-shaped inclusion trails signify porphyroblast rotation?: Reply. *Geology* **20**(11), 1055-1056.

Bell, T. H., Forde, A. & Wang, J. 1995. A new indicator of movement direction during orogenesis: measurement technique and application to the Alps. *Terra Nova* **V. 7**, 500-508.

Bell, T. H., Hickey, K. A. & Upton, G. J. G. 1998. Distinguishing and correlating multiple phases of metamorphism across a multiply deformed region using the axes of spiral, staircase and sigmoidal inclusion trails in garnet. *Journal of Metamorphic Geology* **16**(6), 767-794.

Bell, T. H., Johnson, S. E., Davis, B., Forde, A., Hayward, N. & Witkins, C. 1992b. Porphyroblast inclusion-trail orientation data; eppure non son girate! *Journal of Metamorphic Geology* **10**(3), 295-307.

Berger, M. J., Hubbell, J. H., Seltzer, S. M., Coursey, J. S. & Zucker, D. S. 1999. XCOM: Photon Cross Section Database (version 1.2), [Online]. **2002**. National Institute of Standards and Technology, Gaithersburg, MD.

Bonse, U. & Beckmann, F. 2001. Multiple-beam X-ray interferometry for phase-contrast microtomography. *Journal of Synchrotron Radiation* **8**(Part 1), 1-5.

Bonse, U. & Busch, F. 1996. X-ray computed microtomography (μCT) using synchrotron radiation (SR). *Progress in biophysics and molecular biology* **65**, 133-169.

Bronnikov, A. V. 2002. Theory of quantitative phase-contrast computed tomography. *Journal of the Optical Society of America A-Optics & Image Science* **19**(3), 472-480.

Carlson, W. D. & Denison, C. 1992. Mechanisms of porphyroblast crystallization; results from high-resolution computed X-ray tomography. *Science* **257**(5074), 1236-1239.

Chernoff, C. B. & Carlson, W. 1997. Disequilibrium for Ca during growth of pelitic garnet. *Journal of Metamorphic Geology* **15**(4), 421-438.

Chernoff, C. B. & Carlson, W. 1999. Trace element zoning as a record of chemical disequilibrium during garnet growth. *Geology* **27**(6), 555-558.

Cifelli, R. L., Rowe, T. B., Luckett, W. P., Banta, J., Reyes, R. & Howes, H. I. 1996. Fossil evidence for the origin of the marsupial pattern of tooth replacement. *Nature* **379**, 715-718.

Cihan, M. 2004. The drawbacks of sectioning rocks relative to fabric orientations in the matrix: A case study from the Robertson River Metamorphics (Northern Queensland, Australia). *Journal of Structural Geology* **26**, 2157 -2174.

Daniel, C. G. & Spear, F. S. 1998. Three-dimensional patterns of garnet nucleation and growth. *Geology* **v.26**, 503-506.

Daniel, C. G. & Spear, F. S. 1999. The clustered nucleation and growth processes of garnet in regional metamorphic rocks from north-west Connecticut, USA. *Journal of Metamorphic Geology* **17**(5), 503.

De Man, B., Nuyts, J., Dupont, P., Marchal, G. & Suetens, P. 2001. An iterative maximum-likelihood polychromatic algorithm for CT. *IEEE Transactions on Medical Imaging* **20**(10), 999-1008.

Denison, C., Carlson, W. D. & Ketcham, R. A. 1997. Three-dimensional quantitaitve textural analysis of metamorphic rocks using high-resolution computed X-ray tomography: Part I. Methods and techniques. *Journal of Metamorphic Geology* **15**(1), 29-44.

Dilmanian, F. A. 1992. Computed tomography with monochromatic X-rays. *American Journal of Physiological Imaging* **7**, 175-193.

Elbakri, I. A. & Fessler, J. A. 2003. Segmentation-free statistical image reconstruction for polyenergetic x-ray computed tomography with experimental validation. *Physics in Medicine & Biology* **48**(15), 2453-2477.

Hayward, N. 1990. Determination of early fold axis orientations in multiply deformed rocks using porphyroblast inclusion trails. *Tectonophysics* **V. 179**, 353-369.

Ikeda, T., Shimobayashi, N., Wallis, S. R. & Tsuchiyama, A. 2002. Crystallographic orientation, chemical composition and three dimensional geometry pf sigmoidal garnet: evidence for rotation. *Journal of Structural Geology* **24**, 1633-1646.

Johnson, S. E. 1993. Unravelling the spirals: a serial thin-section study and three dimensional computer-aided reconstruction of spiral-shaped inclusion trails in garnet porphyroblasts. *Journal of Metamorphic Geology* **11**, 621-634.

Johnson, S. E. 1999. Porphyroblast microstructures: A review of current and future trends. *American Mineralogist* **V.84**, 1711-1726.

Johnson, S. E. & Moore, R. R. 1996. De-bugging the 'millipede' porphyroblast microstructure: a serial thin-section study and 3-D computer animation. *Journal of Metamorphic Geology* **14**, 3-14.

Jones, K. W., Feng, H., Lindquist, W. B., Adler, P. M., Thovert, J. F., Vekemans, B., Vincze, L., Szaloki, I., Van Grieken, R., Adams, F. & Riekel, C. 2003. Study of the microgeometry of porous materials using synchrotron computed microtomography. In: *Applications of X-Ray Computed Tomography in the Geosciences* (edited by Mees, F., Swennen, R., Van Geet, M. & Jacobs, P.). *Geological Society Special Publication (215)* **215**. Geological Society of London, London, 39-49.

Kak, A. C. & Slaney, M. 1988. *Principles of Computerized Tomographic Imaging*. The Institute of Electrical and Electronics Engineers, Inc., New York.

Kalukin, A. R., Van Geet, M. & Swennen, R. 2000. Principal components analysis of multienergy X-ray computed tomography of mineral samples. *IEEE Transactions on Nuclear Science* **47**(5), 1729-1736.

Ketcham, R. A. 2004. Efficient and flexible three-dimensional measurement of features in CT data volumes: implications for quantitative analysis of metamorphic textures. In: *32nd International Geological Congress* **Abstract Volume, Part 1**, Florence, Italy, Abstract 93-4, 445.

Ketcham, R. A. & Carlson, W. D. 2001. Acquisition, optimization and interpretation of X-ray computed tomographic imagery: applications to the geosciences. *Computers and Geosciences* **27**, 381-400.

Ketcham, R. A. & Ryan, T. 2004. Quantification and visualization of anisotropy in trabecular bone. *Journal of Microscopy* **213**, 158-171.

Koeberl, C., Denison, C., Ketcham, R. A. & Reimold, W. U. 2002. High resolution X-ray computed tomography of impactites. *Journal of Geophysical Research - Planets* **107(E10)**, 5089.

Krukowski, S. T. 1988. Sodium metatungstate: a new heavy-mineral separation medium for the extraction of conodonts from insoluble residues. *Journal of Paleontology* **62**(2), 314-316.

Kyle, J. R. & Ketcham, R. A. 2003. In-situ distribution of gold in ores using high-resolution X-ray computed tomography. *Economic Geology* **98**, 1697-1701.

Marschallinger, R. 1998. Three-dimensional reconstruction and modelling of microstructures and microchemistry in geological materials. *Scanning* **20**, 65-73.

Masuda, T. & Mochizuki, S. 1989. Development of snowball structure: numerical simulation of inclusion trails during synkinematic porphyroblast growth in metamorphic rocks. *Tectonophysics* **170**, 141-150.

Mees, F., Swennen, R., van Geet, M. & Jacobs, P. 2003. *Applications of X-ray computed tomography in the geosciences*. Geological Society of London, London.

Natterer, F. & Ritman, E. L. 2002. Past and Future Directions in X-Ray Computed Tomography (CT). *International Journal of Imaging Systems and Technology* **12**, 175-187.

Passchier, C. W., Trouw, R. A. J., Zwart, H. J. & Vissers, R. L. M. 1992. Porphyroblast rotation: eppur si muove? *Journal of Metamorphic Geology* **10**, 283-294.

Powell, D. & Treagus, J. E. 1967. On the geometry of S-shaped inclusion trails in garnet porphyroblasts. *Mineralogical Magazine* **36**, 453-456.

Powell, D. & Treagus, J. E. 1970. Rotational fabrics in metamorphic minerals. *Mineralogical Magazine* **37**(No. 291), 801-813.

Proussevitch, A., Ketcham, R. A., Carlson, W. & Sahagian, D. 1998. Preliminary results of X-ray CT analysis of Hawaiian vesicular basalts. In: *American Geophysical Union 1998 spring meeting* (edited by Anonymous) **79**. American Geophysical Union, 360.

Ramsay, J. G. 1962. The geometry and mechanics of formation of 'similar' type folds. *Journal of Geology* **70**, 309-327.

Rosenfeld, J. L. 1970. *Rotated Garnets in Metamorphic Rocks. Geological Society of America Special Paper, 129*. Geological Society of America, Boulder, Colarado.

Rowe, T. 1996. Coevolution of the mammalian middle ear and neocortex. *Science* **273**, 651-654.

Samanta, S. K., Mandal, N., Chakraboty, C. & Majumder, K. 2002. Simulation of inclusion trail patterns within rotating synkinematic porphyroblasts. *Computers and Geosciences* **28**, 297-308.

Schoneveld, C. 1977. A study of some typical inclusion patterns in strongly paracrystalline-rotated garnets. *Tectonophysics* **39**, 453-471.

Spear, F. & Yao, K. 2001. The three dimensional geometry of garnet growth, Harpswell Neck, Maine, USA. In: *Eleventh Annual V.M. Goldschmidt Conference, Hot Springs, VA, USA. Abstract number, 3693.* (edited by Bodnar, R. J. & Hochella, M. F.). Lunar and Planetary Institute, Houston, Texas.

Spear, F. S. & Daniel, C. G. 1998. Three-dimensional imaging of garnet porphyroblast sizes and chemical zoning: Nucleation and growth history in the garnet zone. *Geological Materials Research* **1**(1), 1-43.

Spear, F. S. & Daniel, C. G. 2001. Diffusion control of garnet growth, Harpswell Neck, Maine, USA. *Journal of Metamorphic Geology* **19**(2), 179.

Stallard, A. & Hickey, K. A. 2001. Shear zone vs folding for spiral inclusion trails in the Canton Schist. *Journal of Structural Geology* **23**, 1845-1864.

Stallard, A., Ikei, H. & Masuda, T. 2002. Numerical simulations of spiral-shaped inclusion trails: can 3D geometry distinguish between end-member models of spiral formation? *Journal of Metamorphic Geology* **20**, 801-812.

Takeda, T., Momose, A., Yu, Q. W., Yuasa, T., Dilmanian, F. A., Akatsuka, T. & Itai, Y. 2000. New types of X-ray computed tomography (CT) with synchrotron radiation: Fluorescent X-ray CT and phase-contrast X-ray CT using interferometer. *Cellular & Molecular Biology* **46**(6), 1077-1088.

Torikoshi, M., Tsunoo, T., Endo, M., Noda, K., Kumada, M., Yamada, S., Soga, F. & Hyodo, K. 2001. Design of synchrotron light source and its beamline dedicated to dual-energy x-ray computed tomography. *Journal of Biomedical Optics* **6**(3), 371-377.

Torikoshi, M., Tsunoo, T., Sasaki, M., Endo, M., Noda, Y., Ohno, Y., Kohno, T., Hyodo, K., Uesugi, K. & Yagi, N. 2003. Electron density measurement with dual-energy x-ray CT using synchrotron radiation. *Physics in Medicine & Biology* **48**(5), 673-685.

Tsuchiyama, A., Nakamura, T., Nakano, T. & Nakamura, N. 2002. Three-dimensional description of the Kobe meteorite by micro X-ray CT method: Possibility of three-dimensional curation of meteorite samples. *Geochemical Journal* **36**, 369-390.

Wellington, S. L. & Vinegar, H. J. 1987. X-ray computerized tomography. *Journal of Petroleum Technology*(August 1987), 885-898.

Williams, P. F. & Jiang, D. 1999. Rotating garnets. *Journal of Metamorphic Geology* **17**, 367-378.

Yamaya, T., Obi, T., Yamaguchi, M. & Ohyama, N. 2000. An acceleration algorithm for image reconstruction based on continuous-discrete mapping model. *Optical Review* **7**(2), 132-137.

# Appendix 1. VRML Files

A vrml model of the data shown in figure 7 is available on the attached CD in \\chapter1\vrml. There are two versions of this model, a low res version (3.3MB) or a high re version (7.5MB). Some of the inclusions around the edge of the garnet and fractures have been removed from the original dataset to allow the trails to be seen more clearly.

These models are best viewed using the freely available Cortona® VRML Client which works as a plug-in for most internet browsers. Cortona is available on the attached CD or at http://www.parallelgraphics.com/products/cortona/ (Mac users see links on right side of page). Cortona is available for Windows, Mac OS X and Mac OS 9 operating systems.

### Viewing VRML files in Cortona VRML Client

To view one of the vrml files, download it to your local hard drive. Open the web browser for which you have installed the Cortona VRML Client and go to File, Open and browse to the vrml file and open it. This will launch the Cortona VRML Client within a browser window, which should look something like this

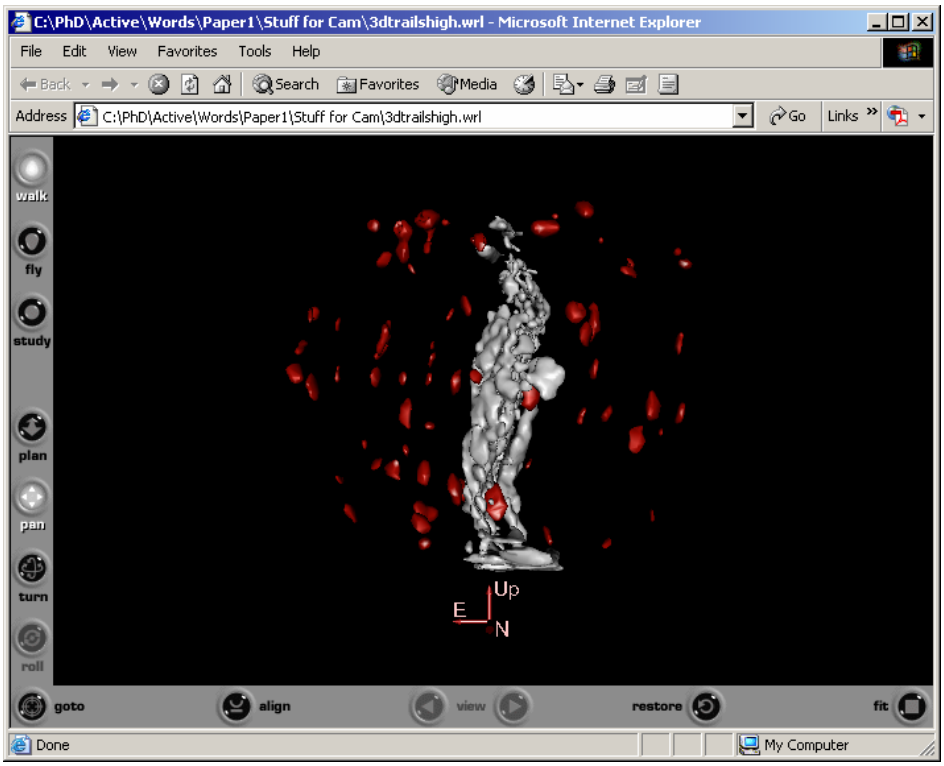


Viewing a scene in Cortona VRML Client is a lot like looking at an object through a camera. You can move (navigate) the camera around so that you can look at different views. There are three different navigation modes available – Walk, Fly and Study. The study mode is recommended for viewing the vrml models presented here.

Clicking on the *study* and *plan* buttons allows you to zoom in and out by clicking and dragging the mouse up and down and to rotate the object by clicking and dragging to the left or right.

Clicking on the *study* and *pan* buttons lets you pan left, right, up or down by clicking and dragging the mouse in the direction you want to go.

# Chapter 2. An X-ray computed tomography study of inclusion trail orientations in multiple porphyroblasts from a single sample

# Abstract

Inclusion trails in 58 garnet porphyroblasts in a single sample from the Cram Hill Formation in southeast Vermont were imaged using high resolution X-ray computed tomography. The resulting 3D dataset, with an 11μm voxel size, was analysed to determine the distribution of microstructures preserved in the porphyroblasts. Texturally the porphyroblasts have a large core with a sub-vertical foliation that has a clustered distribution. The mean orientation has a plunge of 18° towards 292.8° and a 95% confidence cone semi-angle of 5.3°. This steep foliation curves into a sub-horizontal foliation. The foliation intersection/inflection axes (FIAs) defined by this curvature have a more tightly clustered distribution. Their orientation has a plunge of 10.6° towards 200.5° and a 95% confidence cone semi-angle of 4.1°. The trend of a second FIA was measured in the median of 17 of the garnets. These axes had a mean orientation of 116.9° with a 95% confidence interval of 114.2° to 119.6°. The clustered distribution of the foliation and FIA data from the core of the porphyroblasts, despite the presence of several later foliation forming events, provide strong evidence that the porphyroblasts have not rotated relative to a fixed geographic reference frame in this sample. The data distribution can be readily explained as variations in the primary fabrics that have been overgrown by irrotational porphyroblasts.

The lack of porphyroblast rotation is explained using the PBIS (progressive, bulk, inhomogeneous shortening) strain model in which deformation partitions into zones of shearing and zones of shortening or no strain. Porphyroblasts are effectively decoupled from the matrix and do not rotate. The FIA orientations are shown to reflect the trend of steep foliations, which is perpendicular to the direction of bulk shortening during horizontal compression, in a succession of steep and flat foliation forming events. An extended deformation history of four foliations is preserved in the porphyroblasts.


# 1 Introduction

In 1968 John Rosenfeld wrote on how curved inclusion trails trapped in garnet porphyroblasts had been underutilized due to a lack of adequate methods of study. He demonstrated how quantitative measurements of axes of curvature could be used in the interpretation of the structural history of the rocks that hosted them. Rosenfeld followed this with a more detailed investigation of these features complete with techniques for measuring them (Rosenfeld 1970). While there has been much debate as to what curved inclusion trails represent and how they formed (Bell 1985, Ikeda et al. 2002, Ilg & Karlstrom 2000, e.g. Schoneveld 1977, Stallard et al. 2002, Williams & Jiang 1999), there was a distinct hiatus in any attempts to apply these features to solving geological problems. Twenty years after Rosenfeld's last communication on the topic, Bell and co-workers introduced the concept of the

Foliation Intersection or Inflection Axis (Bell et al. 1995, FIA`; Hayward 1990). They provided a simplified technique for measuring the axis of curvature (which they call the FIA). This method has been applied to many geological problems including: investigating tectono-metamorphic histories and correlating multiple phases of metamorphism on local and orogenic scales (e.g. Bell et al. 1998, Bell & Mares 1999, Cihan & Parsons 2005, Lee et al. 2000, Sayab 2005, Yeh & Bell 2004); investigating foliation development and folding mechanisms (Bell & Hickey 1997, Timms 2003); arguing for the lack of porphyroblast rotation (Bell et al. 1997, Ham & Bell 2004, Hickey & Bell 1999); studying porphyroblast nucleation and growth relative to deformation (Bell et al. 2003, Bell et al. 2004); reconstructing plate motions (Bell et al. 1995); constraining age dates (Bell & Welch 2002); and investigating pluton emplacement mechanisms and timing (Davis 1993). Using FIAs, these authors have demonstrated that the porphyroblasts have not rotated. If this holds true for most rocks, the value of FIAs to geologists will exceed even Rosenfeld's expectations.

Johnson (1999) raised a series of questions about the measurement of FIAs, mostly regarding measurement errors and the spread of orientations in a single sample. The technique Hayward (1990) described for measuring FIAs yields the average orientation for a sample but cannot measure the orientation of a FIA in an individual porphyroblast. As a result it is difficult to know what the porphyroblast to porphyroblast variation in FIA orientations within a single sample is. The true statistical spread of trends for a sample is unknown. Upton et al. (2003) give a method to determine the spread of values in a single sample using a maximum likelihood approach. However, this technique provides only an indirect measure of the distribution. To allow FIAs to be used to their full potential, questions about the statistical confidence that can be assigned to the determined trends need to be answered. To do this the FIAs in individual prophyroblasts need to be measured in statistically significant quantities so that rigorous analysis can be done.

High resolution X-ray computed tomography (HRXCT) provides a technique that allows inclusion trails to be imaged in intact samples (Huddlestone-Holmes & Ketcham 2005). Previously, serial sectioning of individual porphyroblasts has been used to look at the morphology of the structures preserved inside porphyroblasts (e.g. Johnson 1993b, Johnson & Moore 1996). This is a laborious technique, unsuitable for collating statistically significant amounts of data. It is also difficult to correlate inclusion trail surfaces from section to section, which reduces the accuracy. Using HRXCT, the three-dimensional orientation of FIAs can be measured to a five-degree range in plunge and plunge direction. A large amount of data can be acquired relatively quickly without destroying the sample allowing the application of complimentary techniques if required.

This chapter examines the distribution of FIAs in 58 porphyroblasts from a single sample. The plunge and plunge direction of the FIAs have been measured. Statistical analyses

of the results were applied to describe these data and determine the confidence that can be placed in the measured orientations. By looking at the geometry of the inclusion trails in this sample, inferences can also be made as to what the FIA measurements actually represent, as well as the process that formed them.

## 1.1 What is a FIA?

Foliation inflection or intersection axes (FIAs) are interpreted to be the intersection of successive foliations, or the curvature of one into the next, that have been overgrown by a porphyroblast (Bell et al. 1995, Hayward 1990). Rosenfeld (1970) and others would argue that FIA are the result of the porphyroblast including an active foliation which is causing it to rotate (Fig. 1) and that the FIA is actually the axis of this rotation. Bell et al. (1995) argue that FIAs are the product of overprinting deformation events/foliations and that porphyroblast rotation is not necessary to produce them. The measurement of FIAs makes no inference whether the porphyroblast has rotated or not. If a porphyroblast has not rotated, FIAs within it will still be in their original orientation. If the porphyroblasts has rotated, subsequent foliation forming events will reorient the earlier FIAs. This study will examine whether there was evidence for redistribution in this sample.

FIAs formed by the porphyroblast rotation model will be perpendicular to the direction of movement in the foliation (i.e. the axis of principal strain). FIAs formed by the second of the above models will be perpendicular to the direction of bulk shortening. This is based on the observation that foliations form perpendicular to this direction (e.g. Hobbs et al. 1976, Passchier & Trouw 1996). Bell and Johnson (1989) have argued that foliations in orogenic belts alternate between vertical and horizontal as orogenesis progresses. It follows from this that the orientation of FIAs will be a reflection of the strike of vertical foliations.

## 1.2 The Rotation Debate

The accepted paradigm in the earth sciences until the mid-eighties was that porphyroblasts and other rigid objects rotate with respect to a geographical reference frame during non-coaxial deformation. The rotation is due to the vorticity created by the simple shearing component of the deformation (Lister & Williams 1983, Rosenfeld 1970). Bell and others (Bell 1985, Bell et al. 1989, Bell et al. 1992a, Bell & Johnson 1990, Bell et al. 1992c, Johnson 1993a, Steinhardt 1989) argue that porphyroblasts do not rotate due to the effects of deformation partitioning.

The debate concerns deformation mechanisms. Bell (1981) proposed the PBIS (progressive, bulk, inhomogeneous shortening) strain model, which is based on the concept that the deformation partitions into zones of progressive shearing (shearing) and zones of progressive shortening (shortening or no strain, Fig. 2). A pre-existing porphyroblast will

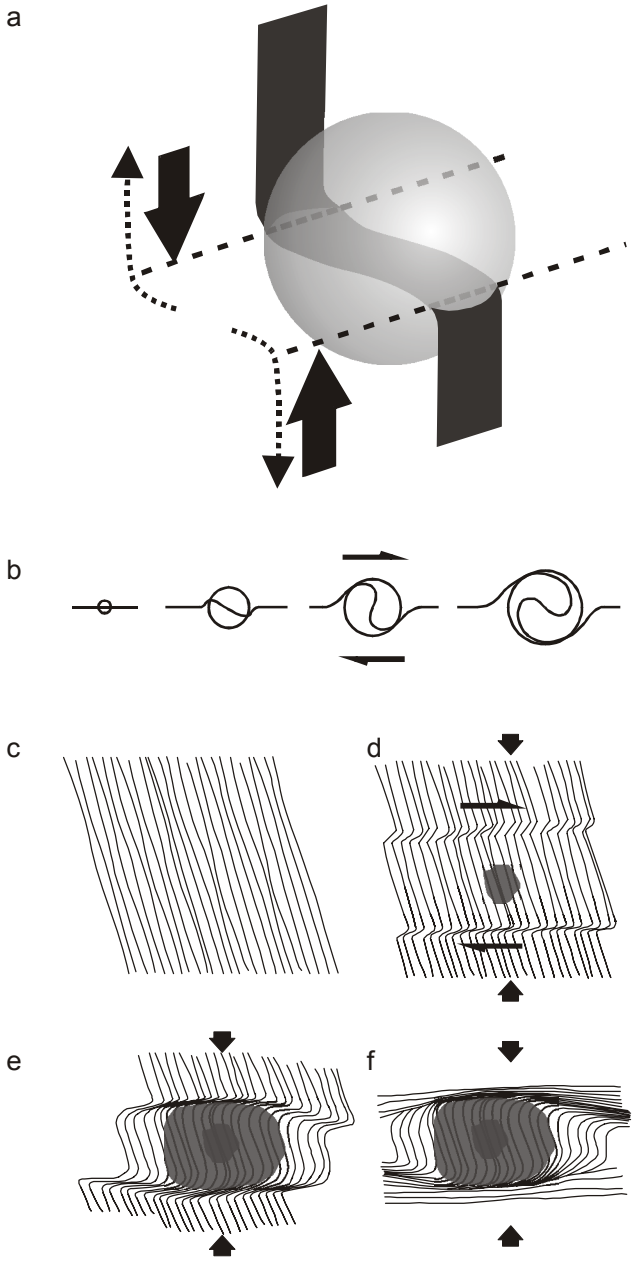


**Figure 1.** The two models for the formation of curved inclusion trails are shown here. In (a), a spherical porphyroblast is shown along with a curved foliation plane that it includes. The dashed lines show the axes of rotation of this foliation plane. The large solid arrows show the shear sense that would have been necessary to form this geometry via porphyroblast rotation, the dotted arrows show the shear sense that would have rotated a flat foliation to the vertical in an irrotational model. A cross section of the rotational model is shown in (b), where a porphyroblast grows while being rotated by shear on the foliation. (c) to (f) show the progressive development of curved trails in the deformation partitioning model. A porphyroblast (grey oval) grows in the crenulation hinge (d), eventually overgrowing the curvature of the sub vertical foliation into the flat foliation (e). The deformation intensifies against the edge of the porphyroblast which has stopped growing (f).

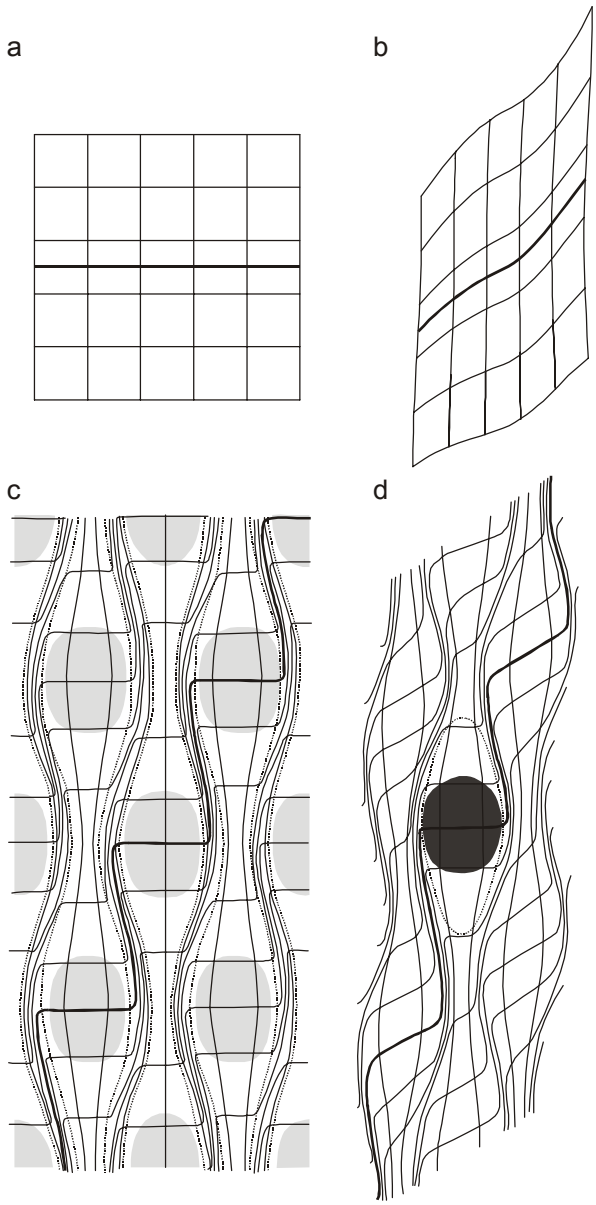


**Figure 2.** This series of strain field diagrams in the $\varepsilon_1\varepsilon_2$ plane demonstrates the development of non-coaxial Progressive Bulk Inhomogenous Shortening (PBIS, Bell 1981). A reference grid is shown in (a) along with a marker band (heavy line). Early in deformation the strain will not have partitioned (b) and coaxial shortening dominates. As deformation progresses (c), the strain partitions into zones of no strain (grey ellipses), zones of shortening (between the ellipses and the dotted lines) and zones of shearing (between the dotted lines). In (b) and (c) the dark grey ellipse represents a porphyroblast which causes strain to partitions around it throughout deformation.

partition the deformation so that it is in a zone of no strain (Fig. 2d). It is effectively decoupled from the matrix and does not rotate. This concept has formed the central plank of the non-rotation argument since first used in this way by Bell (1985). The majority of theoretical models for rigid body rotation are based in hydrodynamics theory (e.g. Samanta et al. 2002a) and, unsurprisingly, these models predict that a rigid body in a fluid undergoing a deformation with a simple shearing component will rotate. Significantly, the rotational models do not account for

the great wealth of data that suggests that porphyroblasts do not rotate (e.g. Aerden 2004, Aerden 1995, Bell & Chen 2002, Bell & Hickey 1999, Evins 2005, Hayward 1992, Johnson 1990, Jung et al. 1999, Steinhardt 1989).

Recently, several papers describing the results of analogue modeling cast doubt on the validity of hydrodynamic models (Aerden 2005, Ceriani et al. 2003, Mancktelow et al. 2002, Stewart 1997, ten Grotenhuis et al. 2002). Two problems have been identified, firstly the applicability of a viscous fluid as an analogue to rocks that are anisotropic and heterogeneous. Secondly, the nature of coupling between the matrix and porphyroblast appears to have a significant effect. It is clear from the literature that the scientific community still has no firm consensus as to whether or not curved inclusion trails form by rotation. How these data fit with both of these hypotheses will be investigated.

## 1.3 Geological Setting

The oriented sample selected for this study comes from southeast Vermont, where the pioneering work on curved inclusion trails by Rosenfeld (Rosenfeld 1968, Rosenfeld 1970) was done. Sample V209 was collected from the Cram Hill Formation in southeastern Vermont and is ideally suited to this kind of study because it has a high density of garnet porphyroblasts, most with well-developed inclusion trails (Fig. 3). It is a carbonaceous pelite that has been metamorphosed to amphibolite facies and contains quartz, muscovite, garnet, biotite, calcite, ilmenite and trace epidote. Fine graphite is present throughout the rock as a dusting of grains that, in places, form density bands. At hand sample scale quartz and mica rich bands are observed. Inclusion trails within garnet are composed of quartz, ilmenite, graphite, magnesian siderite, hydrated iron oxide and pyrophyllite.

## 1.4 Previous Work

Bell et al. (1998) document three separate FIAs for sample V209. Oldest to youngest (core, median and rim/matrix), these trend at 45˚, 110˚ and 30˚ respectively (relative to magnetic north, which is 14˚ west of true north at the sample locality) and are assigned to regional FIA sets 1, 2 and 4 respectively. In the same study Bell et al. (1998) reported FIAs for 88 samples from the region where sample V209 was collected. They distinguished four distinct FIA sets in the region, trending SW-NE, W-E, NNW-SSE and SSW-NNE (sets 1 to 4 respectively, 1 youngest, 4 oldest). Some examples of how these data have been used include distinguishing multiple phases of metamorphism (Bell et al. 1998), constraining age dates (Bell & Welch 2002) and investigating regional patterns of deformation partitioning (Bell et al. 2004).

**Figure 3.** Photomicrograph of sample V209 showing its garnet density and inclusion trails. Note that the bulk of the trails are steep in the core of the garnets, with a clockwise asymmetry. The section is oriented east-west looking north. The short edge of the image is approximately 11mm.

# 2 Methods

## *2.1 The Asymmetry Method*

Hayward (1990) introduced the asymmetry method for determining FIA orientations which was later refined by Bell et al. (1995). Using the horizontal plane as a reference, the strike of the FIA is determined first. Six vertical thin-sections striking at 30˚ increments are prepared for each sample. The asymmetry of curved inclusion trails are noted for porphyroblasts in each thin-section viewed in the same direction (clockwise about a vertical axis). The trend of the FIA is constrained to a 30˚ interval over which the observed asymmetry flips. Two additional vertical thin-sections are cut to further constrain the trend to a 10˚ interval (Figs. 4 and 6). A similar procedure is followed to obtain the plunge of a FIA; a series of thin-sections dipping in the vertical plane that contains the trend of the FIA are prepared, and again, the interval over which the asymmetries flip is determined.

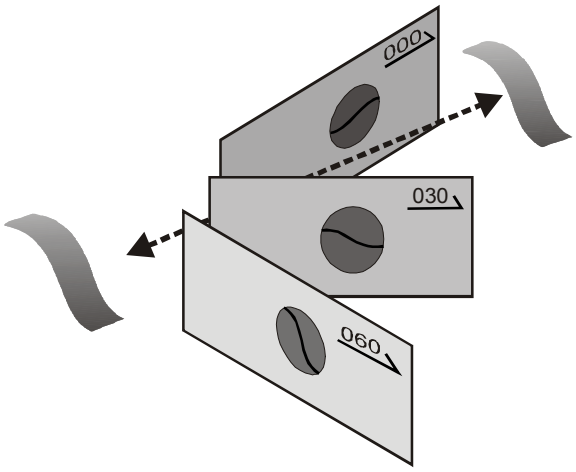


**Figure 4.** This figure illustrates the asymmetry method. In this case the FIA is oriented at approximately 015°. Vertical thinsections striking at 000°, 030° and 060° are shown – note the flip in asymmetry of the inclusion trails in the grey "porphyroblasts" from clockwise to anti-clockwise between 000° and 030°. Extra sections between these two would allow the FIA to be constrained further. A similar process can be used to define the plunge of the FIA.

### 2.1.1 Asymmetry Method Statistical Analysis

Some work has been published that discusses the statistical analysis of FIA data collected in a region (Bell et al. 1998, Yeh & Bell 2004). However, apart from reporting the range over which the flip in asymmetry occurs, there has been no way of describing the confidence of an individual FIA measurement until recently. Upton et al. (2003) developed a maximum likelihood estimation (MLE) approach to fit a cyclic logistic regression to asymmetry data allows the FIA orientation and a shape parameter to be determined. The shape parameter, β, describes how rapidly the asymmetry of inclusion trail curvature changes as the FIA orientation is approached. This allows a confidence interval to be calculated. This technique has been greatly improved in Chapter 3 using bootstrapped estimates of the model parameters. These methods have been applied in analysing the asymmetry data described.

## *2.2 High Resolution X-ray Computed Tomography*

High resolution X-ray computed tomography (HRXCT) is a technique that can be used to image the structures preserved within solid objects such as rocks. It is an adaptation of medical X-ray computed tomography (X-ray CT) with the benefits of increased resolution (<10μm cf. 2-3m), longer scan times and higher X-ray energies (up to 400 keV). Recently this technique has been applied to imaging inclusion trails in garnet posphyroblasts (Bauer et al. 1998, Ikeda et al. 2002). In chapter 1 of this thesis the technique is described in full, demonstrating the detail that can be seen in images produced by HRXCT and comparing them with more familiar polarizing microscope images and compositional maps collected on an electron microprobe.

In summary, HRXCT in geological materials measures the attenuation of X-rays as they pass through different minerals in the sample. Minerals with a higher average atomic number (Z) and higher density will attenuate more X-rays, and are traditionally assigned lighter shades in a greyscale image (like bones in an X-ray). The amount of attenuation is in part related to the energy of the X-rays. Because the X-ray sources are polychromatic, images constructed using HRXCT are qualitative. Phases such as quartz, the feldspars, calcite and micas have significantly lower attenuation coefficients (a measure of the level of X-ray attenuation) than garnet, while iron oxides and REE phases such as monazite are significantly more attenuating. As a result, HRXCT images provide clear differentiation between matrix, garnet and inclusions within the garnet. The three-dimensional datasets created by HRXCT are actually a stack of two-dimensional slices taken through the object of interest. The slices are typically scanned with a fan of X-rays passing through the object as it is turned through 360º and data is collected at rotational increments (views). An image for each slice is reconstructed from these data and they are stacked together to form the three-dimensional dataset.

### 2.2.1 HRXCT Scan Parameters

To prepare the sample for HRXCT, two horizontally oriented slabs 30mm thick were cut from the top and bottom of the specimen. Two vertical drill cores 11mm in diameter were taken from each slab (Fig. 5). To ensure that the orientation of the drill cores was preserved, a north-south groove was made in the top surface of the slabs before coring, and a piece of wire with a notch at the northern end was glued into the groove after coring. This provided an orientation marker that could be clearly imaged by X-ray CT. Cylindrical drill cores are ideal for X-ray CT analysis.

| Parameter | Value | Parameter | Value |
|---|---|---|---|
| Source Voltage (keV) | 150 | Voxel size (μm x μm x μm) | 10.7 x 10.7 x 13.1 |
| Beam Current (mA) | 0.2 | | |
| Spot size (μm) | 30 | Image scale | 16-bit |
| Slice thickness (mm) | 0.0131 | Views per 360˚ | 1600 |
| Spacing of slices (mm) | 0.0131 | Time per view (ms) | 133 |
| Number of slices | 918 | Time per slice* (min) | 1.3 |
| Scanned height (mm) | 12.0 | Wedge | SMT** |
| Field of view (mm) | 11.0 | Offset | none |
| Slice resolution (pixels x pixels) | 1024 x 1024 | Source to Object Distance (mm) | 38 |

* Data for 27 slices acquired simultaneously

** SMT – sodium metatungstate solution mixed to a density of 1.19g/cm$^3$

**Table 1.** X-ray CT scan parameters used for each of the four cores analysed. See text for further discussion.

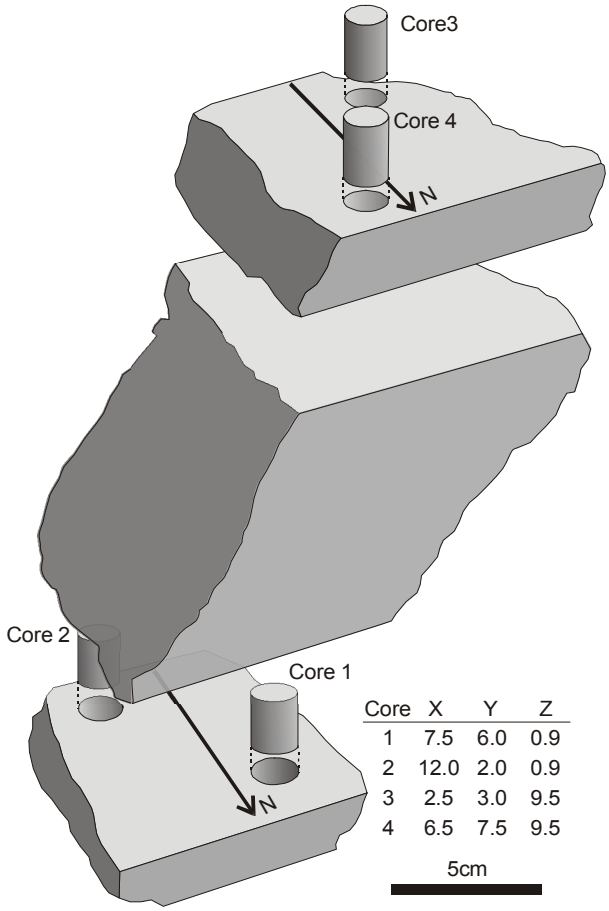


**Figure 5.** Schematic showing relative positions of the four drill cores analysed in this study. The table shows the coordinates of the centre of the drill cores in a coordinate system originating at the lower southwest corner of a box bounding the sample.

The scanner used for this study is housed in the University of Texas HRXCT Facility. Table 1 shows the scan parameters used in this study. Each drill core was scanned along a twelve millimetre axial length, with the data for all four drill cores collected in approximately ten hours. Image reconstruction was done as a separate process after acquisition by applying back-projection using a Laks filter. Each image is 1024 by 1024 pixels of 16-bit data, and there are 918 images or slices for each drill core making for a total dataset of over 7 GB.

### 2.2.2 FIAs and Foliations from HRXCT

The data were analysed using the OpenDX (www.opendx.org) software package. Firstly, a low resolution dataset was created by taking every fourth slice and downsampling it to 8-bits and 256 x 256 pixels. The locations of the centres of the garnet porphyroblasts were measured using this dataset. Subsets were then made of the full resolution dataset centred on each garnet with dimensions slightly greater than the garnets maximum. These subsets were used to reduce the computing time involved in analysing these data. The resulting volumes were

sliced vertically through individual porphyroblasts in the same manner that vertical thin-sections are taken for a rock using the asymmetry method. These slices could be made through any part of the garnet to ensure that they passed through inclusion rich zones from which the asymmetry of curvature could be determined. Once the trend of the FIA was identified, slices dipping in a plane parallel to this trend were made to determine its plunge.

To determine the trend of foliations preserved in the cores of the garnet, the strike of inclusion trails was first measured in a horizontal slice through the core of the garnet. The pitch of the trails was then measured in three vertical slices, one perpendicular to the strike and two at 40º to the strike. The plane of best fit for these data was then calculated. The reasons for following the approach of using 2-D slices of a 3-D dataset in preference to working directly with the 3-D data are explained in the discussion.

### 2.2.3 HRXCT Data Statistical Analysis

The statistical analysis of the three-dimensional distribution of data measured in this sample followed the techniques described in Fisher et al. (1987) for analysing circular data. FIA data and poles to foliations are considered to be undirected lines, or axial data, and must be treated as such. Initial investigations were made using graphical methods (stereoplots, colatitude and longitude plots) together with calculation of the eigenvalues and eigenvectors of the orientation matrix. The eigenvalue method provides the mean orientation as well as describing the shape of the distribution (Woodcock 1977, Woodcock & Naylor 1983). This is important in determining whether the data are clustered or have a girdle distribution. The next stage involved parametric analysis – if the data are clustered, a Watson bipolar model (the spherical equivalent of a normal distribution) can be fitted; if it has a girdle distribution, a Watson girdle model would be used. The advantages of applying a parametric model to the data are that tests for discordance can be done and, if appropriate, a conical confidence interval determined.

As well as a detailed analysis of the total dataset, exploratory analysis was done on data from each of the four drill cores to see if there was a significant difference between them. The data were tested, both graphically and formally, to see if each of the four drill cores samples the same population.

For trend data, the techniques described in Fisher (1993) for analysis of circular data were applied. A similar approach to that used for the spherical data was used with a graphical analysis using rose diagrams and calculation of a mean and confidence interval. Parametric tests were not performed.

Tests for correlation between the orientation of the FIAs, the orientations of foliations in the core of the garnets and the diameter of the porphyroblasts were also performed. For the spherical data, the techniques for testing for correlations between two random unit axes and between a random unit axis and another variable that are described in Fisher et al. (1987) were

employed. For the trend data (i.e. circular), the tests for a T-linear association outlined in Fisher and Lee (1983) and Fisher (1993) were used. These tests calculate a correlation coefficient "pt" that give an indication of the strength of any correlation. For the test to check for any dependency of FIA trends on garnet diameter, the diameter was first converted into a radial measurement by the equation $2 \times atan(diameter)$ which allows the standard T-linear test to be used.

Modification of the analysis of these data due to their grouped nature was not performed because the 5º interval is small enough that it is not necessary (Upton & Fingleton 1989). In reporting eigenvalues and eigenvectors, t1 is taken to be the smallest eigenvalue and t3 the largest, or principal axis, as in Fisher et al. (1987).

# 3 Results

## *3.1 General Description of Trails*

Sample V209 has almandine-rich garnet porphyroblasts with two distinct textural zones: firstly, a broad core with a moderate density of elongate quartz, ilmenite grains, fine graphite, magnesian siderite and bands of hydrated iron oxide with pyrophyllite and quartz inclusions; and secondly, a fine rim with very few inclusions except graphite. The hydrated iron oxide/clay bands are interpreted to be the result of alteration along inclusion rich bands that probably represent some form of compositional layering in the rock prior to garnet growth. The composition of the precursor inclusions cannot be determined. The orientation of these bands does not appear to have been changed by the alteration process. Inclusion trail density is higher in porphyroblasts that lie in the sample's quartz rich bands. The garnet porphyroblasts show well-developed crystal faces in the mica rich bands only.

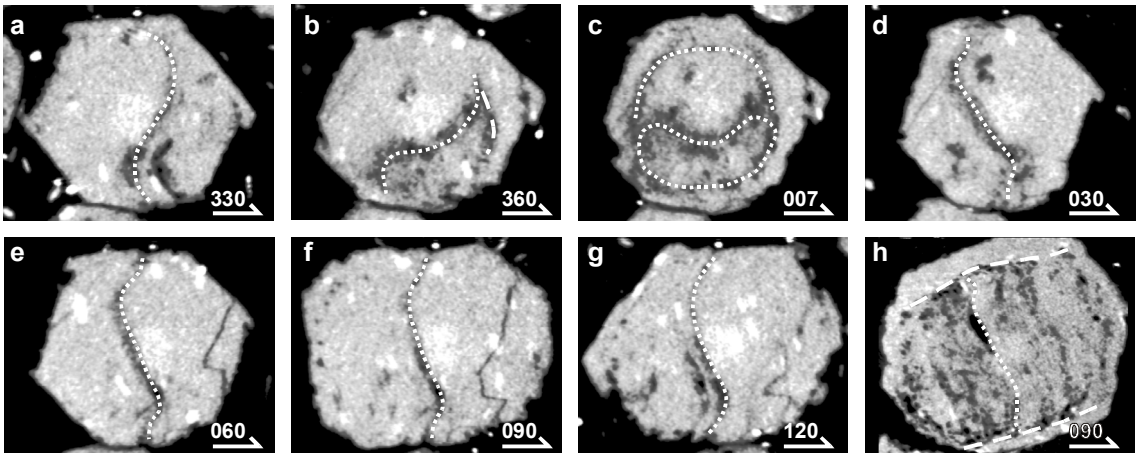


**Figure 6.** A series of vertical sections through the X-ray CT data for garnet 27 in drill core 1 (a-g) showing the asymmetry flip in the core at 007° from anticlockwise to clockwise. Note the closed loop pattern in (c), which is on the FIA. The flip in rim asymmetry is subtler and can be recognized by the change from "stair case" to "accumulating" trails between the 090° and 120° sections. The horizontal truncation in garnet 7 in drill core 3 is shown in (h).

Characteristically the inclusion trails in the core of the garnet porphyroblasts (which generally extends to 70 – 80% of the porphyroblasts' radius) are sub-vertical with an east-southeast dip direction. These trails curve smoothly in a top to the east sense by a maximum of 110º. They have a subtle doubly curving non-cylindrical geometry that results in closed loop structures in sections parallel to them (Fig. 6). Depending on the orientation of the section, a reversal in the asymmetry at the edge of the core trails is observed in some garnets. This flip occurs over a very short distance relative to the extent of the core and the trails are truncated at the transition to the rim in some garnets, whether there is a rim growth or not (Fig. 6). The graphitic inclusion trails in the rim are sub-horizontal and curve into the vertical matrix foliation. Distinct FIA orientations can be determined for the core, median and rim/matrix. However, as the rim trails are fine and graphitic, they could not be analysed using HRXCT and will not be considered further. All data are reported relative to magnetic north unless otherwise noted. The magnetic deviation at the sample locality was 14° west at the time that the sample was collected.

## 3.2 The Asymmetry Method

Eighteen sections were cut at 10° intervals from 000° to 170°. The asymmetry of curvature was recorded for every garnet where it was unambiguous (the data are presented in appendix 1). Ambiguities were due to millipeding, poor inclusion density, fracturing, alteration, off centre cuts or a combination of these factors. The core and median FIAs were determined to be at 25° and 115° respectively. For the core FIA, both asymmetries are observed in the 350° (170°), and 000° to 060° sections (see Fig. 7). Both asymmetries were observed in the 090° to 140° sections for the median FIA. Using the maximum likelihood estimation approach described in Chapter 3, the core FIA trend was determined to be 24.7º with a 95% confidence interval of 21.5° to 27.9° and the median FIA trend was determined to be 116.3°, with a 95% confidence interval of 112.8° to 119.8°.

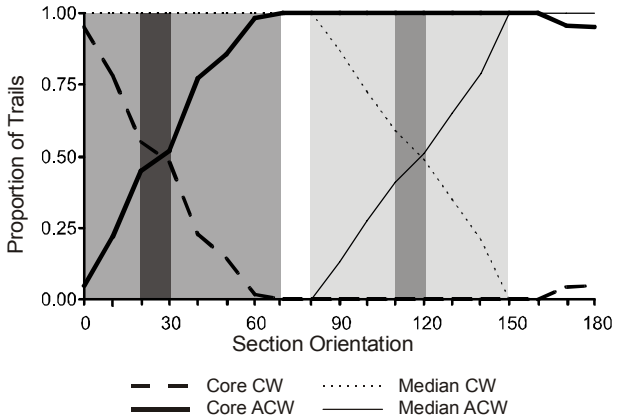


**Figure 7.** Probability plot for asymmetry data collected from thin-sections. Lighter grey areas show region over which both asymmetries are observed, dark grey bars indicate the interval over which the dominance of one asymmetry gives way to the other. See appendix 1 for the raw data.

## *3.3 HRXCT Data*

### 3.3.1 FIA Data

FIA orientations for the core part of the garnet, which were determined to a 5° interval for both plunge and plunge direction from a total of 58 garnets, are shown in Fig. 8 a and b and listed in appendix 2. The stereonets shows that these data have a clustered distribution that may be slightly skewed. The mean FIA orientation for these data plunges at 10.6° towards 200.5° (see table 2). Eigenvalue methods (Woodcock 1977, Woodcock & Naylor 1983) confirm that the data are clustered with moderate strength (table 2 and Fig. 9). The data can be shown to be symmetrical using the tests described by Fisher et al. (1987) and have a 95% confidence cone with a semi-angle of 4.1°. Colatitude and longitude q-q plots performed as goodness of fit tests for the Watson distribution, (Fig. 10) indicate that the data are well represented by a Watson distribution. The colatitude q-q plot (Fig. 10b) appears to curve up slightly at higher values, but it does not deviate markedly from a straight line. This is confirmed by a formal test based on the modified Kolmogorov-Smirnov statistic, $M_B(D_N)$, with a value of 0.614 which is well below the critical value at 95% confidence of 1.09 (Table 2b.).

| | | eigenvalues (normalized) | | | eigenvectors | | | | | |
|---|---|---|---|---|---|---|---|---|---|---|
| **Core FIAs** | **n** | **t1** | **t2** | **t3** | **t1** | **t2** | **t3*** | **K (shape)** | **C (strength)** | **95% Conf. Cone** |
| **All Data** | 58 | 0.033 | 0.058 | 0.909 | 0.2 → 110.4 | 79.4 → 19.3 | 10.6 → 200.5 | 4.92 | 3.31 | 4.15 |
| **Drill Core 1** | 24 | 0.022 | 0.062 | 0.916 | 5.7 → 110.1 | 76.0 → 356.6 | 12.8 → 201.4 | 2.60 | 3.74 | 6.14 |
| **Drill Core 2** | 10 | 0.008 | 0.046 | 0.946 | 8.1 → 294.3 | 72.0 → 50.2 | 16.0 → 202.0 | 1.71 | 4.79 | i.d. |
| **Drill Core 3** | 8 | 0.013 | 0.068 | 0.920 | 44.9 → 312.8 | 41.8 → 106.1 | 13.7 →208.7 | 1.55 | 4.29 | i.d. |
| **Drill Core 4** | 15 | 0.028 | 0.054 | 0.918 | 38.2 →284.1 | 51.8 → 101.5 | 1.3 → 193.1 | 4.41 | 3.48 | i.d. |
| | | | | | | | | | | |
| **Foliations** | | | | | | | | | | |
| **All Data** | 55 | 0.045 | 0.082 | 0.873 | 22.8 → 194.9 | 60.3 → 57.5 | 18.0 → 292.8 | 3.94 | 2.97 | 5.31 |
| **Drill Core 1** | 22 | 0.024 | 0.051 | 0.925 | 4.2 → 21.4 | 81.5 → 141.2 | 7.3 → 290.9 | 3.77 | 3.66 | i.d. |
| **Drill Core 2** | 10 | 0.018 | 0.034 | 0.949 | 40.8 → 179.1 | 32.3 → 56.0 | 32.4 → 302.3 | 5.29 | 3.97 | i.d. |
| **Drill Core 3** | 8 | 0.010 | 0.054 | 0.936 | 7.4 → 216.1 | 59.8 → 113.2 | 29.1 → 310.2 | 1.68 | 4.56 | i.d. |
| **Drill Core 4** | 15 | 0.043 | 0.061 | 0.896 | 39.2 → 25.8 | 45.6 → 172.4 | 17.4 → 281.0 | 7.66 | 3.03 | i.d. |

**Parametric Analysis (3-D)**

| | n | mean | 95% Cone | k | k upper | k lower | Pn | Mb(Dn) |
|---|---|---|---|---|---|---|---|---|
| **Core FIAs** | 58 | 10.6 → 200.5 | 4.15 | 11.621 | 13.774 | 8.1773 | 4.05 | 0.61358 |
| **Foliations** | 55 | 18.0 → 292.8 | 5.31 | 8.6024 | 9.947 | 5.8206 | 5.32 | 1.1821 |
| **Critical Values (95% confidence)** | | | | | | | < 5.99 | < 1.09 |

* mean orientation of FIAs and poles to foliation data.

**Table 2.** Statistical analysis of spherical data. "K" and "C" are shape parameters after Woodcock (1977). Parametric analysis is done for a Watson bipolar model. Pn is a symmetry and longitude goodness-of-fit test; Mb(Dn) is a colatitude goodness-of-fit test for this distribution. i.d. stands for insufficient data for the test to be meaningful. See text for further discussion.

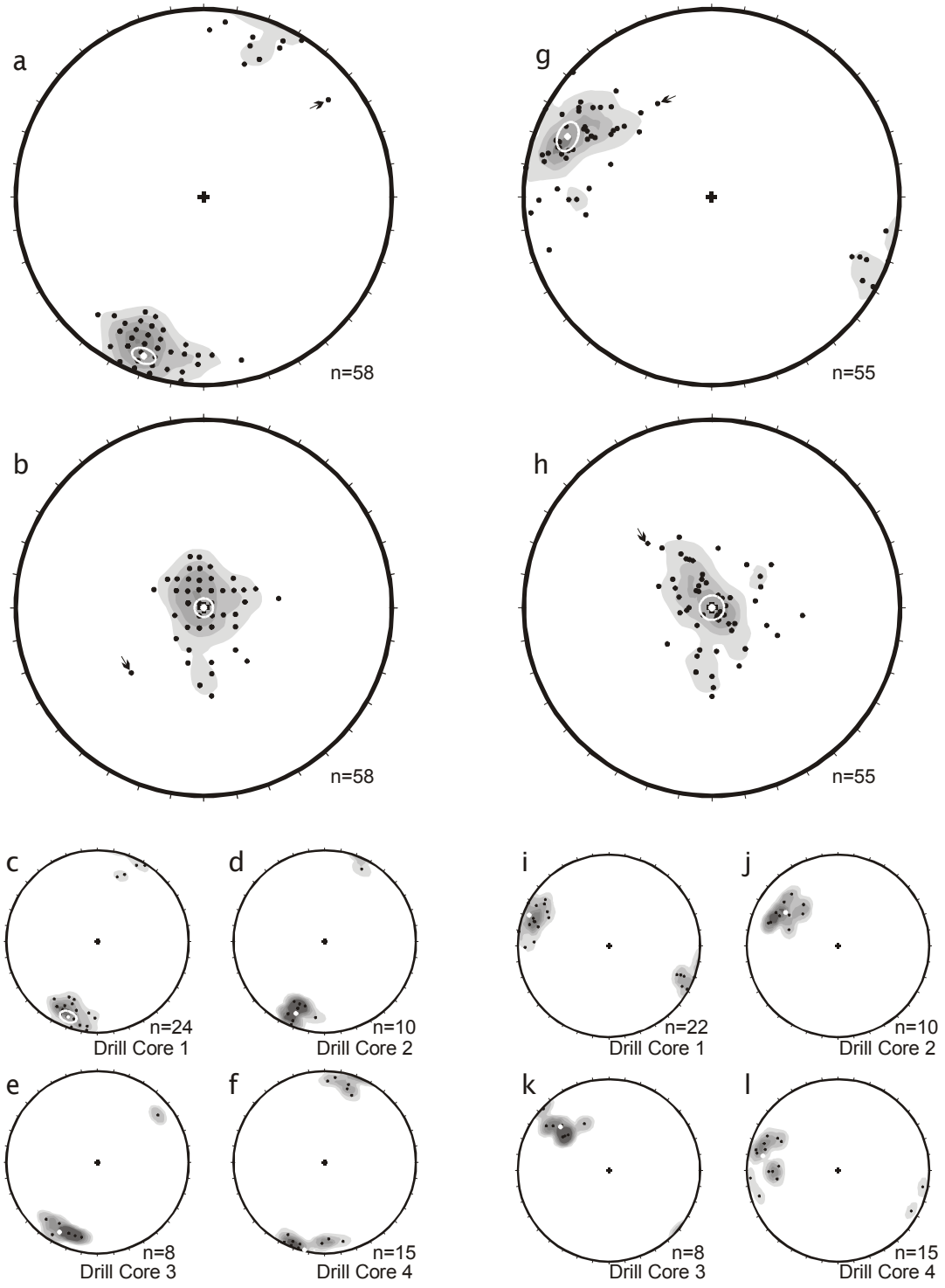


**Figure 8.** Equal-area stereonets of FIAs (a-f) and poles to foliation (g-j) in the cores of the prophyroblasts. (a-b) and (g-h) are the whole datasets with the data rotated so that the mean orientation is 90° → 000° in (b) and (h). This allows the shapes of the distributions to be seen more clearly. The FIA data shows a moderately clustered distribution while the foliations are more dispersed with a slight girdle character. The smaller stereonets show the data recorded for the individual drill cores, as labelled. See text for further discussion. Contouring done using Dips version 5.0 (www.rocscience.com) with 5% contour intervals using the Schmidt distribution method. The white crosses show the mean orientations in each projection and white circles the 95% confidence cone where calculated. Small arrows point to garnet 3 in drill core 3. See text for discussion.

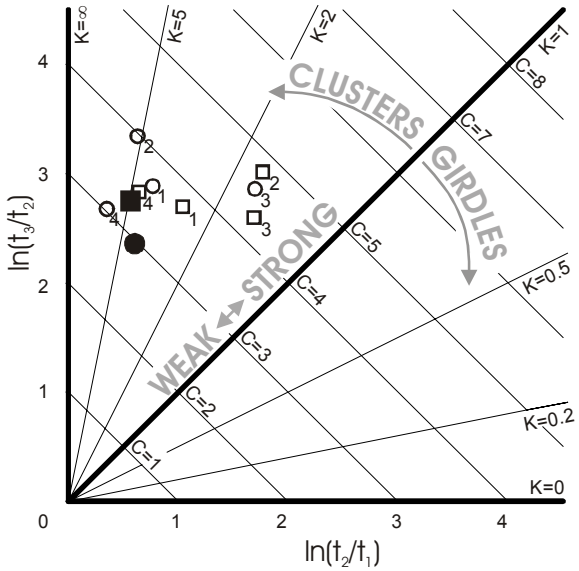


**Figure 9.** Eigenvalue ratio graph of Woodcock (1977) for core FIA (squares) and foliation (circles) data for the whole dataset (solid) and individual drill cores (open, numbered). This plot shows Woocock's shape (K) and strength parameters (C). Note that all datasets have similar values, with the exception of drill cores two and three.

The colatitude q-q (Fig. 10 b) plot also shows that the data from the four drill cores form part of the same distribution (in that the data all lie on the same trend), even though their mean orientations differ slightly. This was confirmed by a formal test with an $N_r$ statistic value of 3.30, which is well below the critical value at 95% confidence of 12.58. Stereonets for each drill core are shown in Fig. 8c-f and results of eigenvalue analysis are given in table 2 and Fig. 9. Data from the four drill cores have similar shape and strength parameters to the whole dataset. Drill cores two and three, while still clustered, approach girdle distributions. Drill core three varies more in dip than dip direction and drill core four varies more in dip direction than dip. However, both have relatively low sample counts. Drill core four has a much gentler plunge than the others do.

The trend data for the core FIA was also analysed for direct comparison with the traditional methods of FIA measurement and the results are presented in table 3. There is good agreement between the asymmetry method, the MLE approach and the mean value from the HRXCT data.

The trend of the median FIA could be measured in only seventeen porphyroblasts (appendix 2, Fig. 11) as it occurs over such a short interval of the garnet radius; the resolution of the HRXCT data is not high enough to resolve such fine features. It was not possible to determine plunges, as the region in which the flip in asymmetry occurred was difficult to intersect with horizontal to sub-horizontal sections. The mean trend of the data is 116.9° with a 95% confidence interval of 114.2° to 119.6° (table 3). The absolute range of data is only 20°. This agrees well with the results of the asymmetry method and MLE approach (table 3). The

median for the four drill cores was not analysed individually because there was insufficient data to do so.

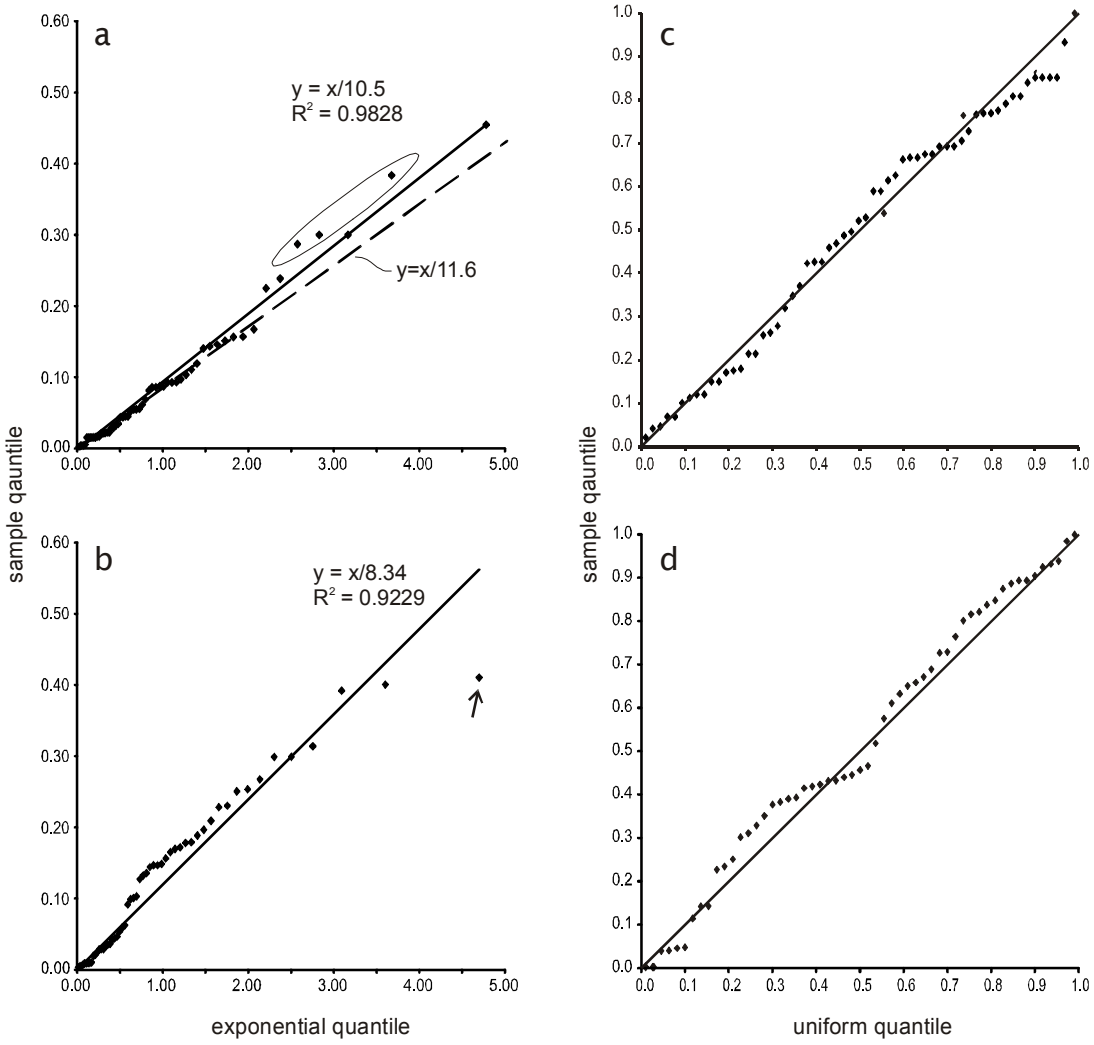


**Figure 10.** Colatitude (a and b) and longitude (c and d) probability plots for core FIA (a and c) and foliation (b and d) data to check the goodness of fit of the Watson bipolar distribution to these data. These plots indicate that the assumption that the Watson bipolar distribution fits these data is reasonable. The three points circled in the FIA colatitude plot, and the point marked with an arrow in the foliation colatitude plot may be discordant as they lie some distance from the line of best fit. See test for discussion of formal tests. The dashed line in (a) shows the trend using y=x/k where k is the maximum likelihood estimate for this dataset. The longitude plot also gives an indication as to whether the data from the four drill cores are all from the same distribution. These plots show no departure from a 1:1 line indicating that these data are all from the same distribution.

| Core FIAs | n | R | R/n | mean | 95% upper | 95% lower | interval |
|---|---|---|---|---|---|---|---|
| **All Data** | 58 | 53.86 | 0.93 | 20.60 | 23.40 | 17.81 | 5.59 |
| **Core 1** | 24 | 22.84 | 0.95 | 21.52 | 25.17 | 17.86 | 7.31 |
| **Core 2** | 10 | 9.81 | 0.98 | 22.05 | 25.12 | 17.89 | 7.22 |
| **Core 3** | 8 | 7.27 | 0.91 | 29.17 | 40.26 | 19.84 | 20.41 |
| **Core 4** | 15 | 13.81 | 0.92 | 13.03 | 19.48 | 5.87 | 13.60 |
| **Asymmetry Method** | | | | 25 | 0* | 70* | |
| **Max. Likelihood Technique** | | | | 24.68 | 27.88 | 21.47 | 6.41 |
| | | | | | | | |
| **Median** | | | | | | | |
| **FIA** | 17 | 16.70 | 0.98 | 116.91 | 119.64 | 114.17 | 5.47 |
| **Asymmetry Method** | | | | 115 | 80* | 150* | |
| **Max. Likelihood Technique** | | | | 116.3 | 119.83 | 112.75 | 7.08 |
| | | | | | | | |
| **Foliations** | | | | | | | |
| **All Data** | 55 | 47.50 | 0.87 | 23.37 | 27.34 | 19.40 | 7.94 |
| **Core 1** | 22 | 20.88 | 0.95 | 21.01 | 25.13 | 16.68 | 8.45 |
| **Core 2** | 10 | 9.22 | 0.92 | 32.60 | 41.06 | 24.64 | 16.42 |
| **Core 3** | 8 | 7.71 | 0.96 | 40.52 | 47.12 | 36.08 | 11.04 |
| **Core 4** | 15 | 13.24 | 0.88 | 10.99 | 20.27 | 2.45 | 17.82 |

*Asymmetry method confidence interval is the range over which both asymmetries are observed rather than 95% confidence interval.

**Table 3.** Statistical analysis of circular data (i.e trends/strikes). Where n <25, 95% confidence interval is calculated using bootstrapping techniques with 20,000 resamples.

### 3.3.2 Foliation Data

The orientations of the foliation in the centre of the garnet porphyroblasts are shown in Fig. 8c and d and listed in appendix 2. They could be measured in all but three of the porphyroblasts for which FIAs were measured; the trails in those three were too smoothly curving or disjointed to measure. These data show a similar distribution pattern to the FIA data although they are less strongly clustered. The mean orientation of the pole to the foliation plunges at 18° towards 292.8° with a 95% confidence cone semi-angle of 5.3°. Eigenvalue methods confirm the observation of a more weakly clustered distribution (table 2 and Fig. 9) than for the FIA data. The data can be shown to be symmetrical using the tests described by Fisher et al. (1987) and has a 95% confidence cone with a semi-angle of 5.3°. While colatitude and longitude q-q plots (Fig. 10) suggest that the Watson bipolar model may be an acceptable description of the data, the formal colatitude test does not hold at the 5% confidence level with an $M_B(D_N)$ value of 1.18 (table 2b). The last point on the colatitude plot (core 3, garnet 3; marked with arrow in Figs. 8b,g,h and 10b) lies some way off the best fit line suggesting it may be discordant. As the data cannot be confidently approximated by a parametric distribution it is not possible to do a formal discordance test. However looking at the stereonets (Fig. 8c and d) this point does not lie at a significant distance from the rest of the population and may be assumed to be part of it.

As for the FIA data, a colatitude q-q plot (Fig. 10 d) shows that the data from the four drill cores all form part of the same distribution. In this case the $N_r$ statistic value is 8.543, which is below the critical value mentioned in 3.3.1. Stereonets for each drill core are shown in Fig 8i-l and results of eigenvalue analysis in table 2 and Fig. 9. The four drill cores have similar shape and strength parameters to the whole dataset. Drill core three shows data approaching a girdle distribution varying more in dip than dip direction.

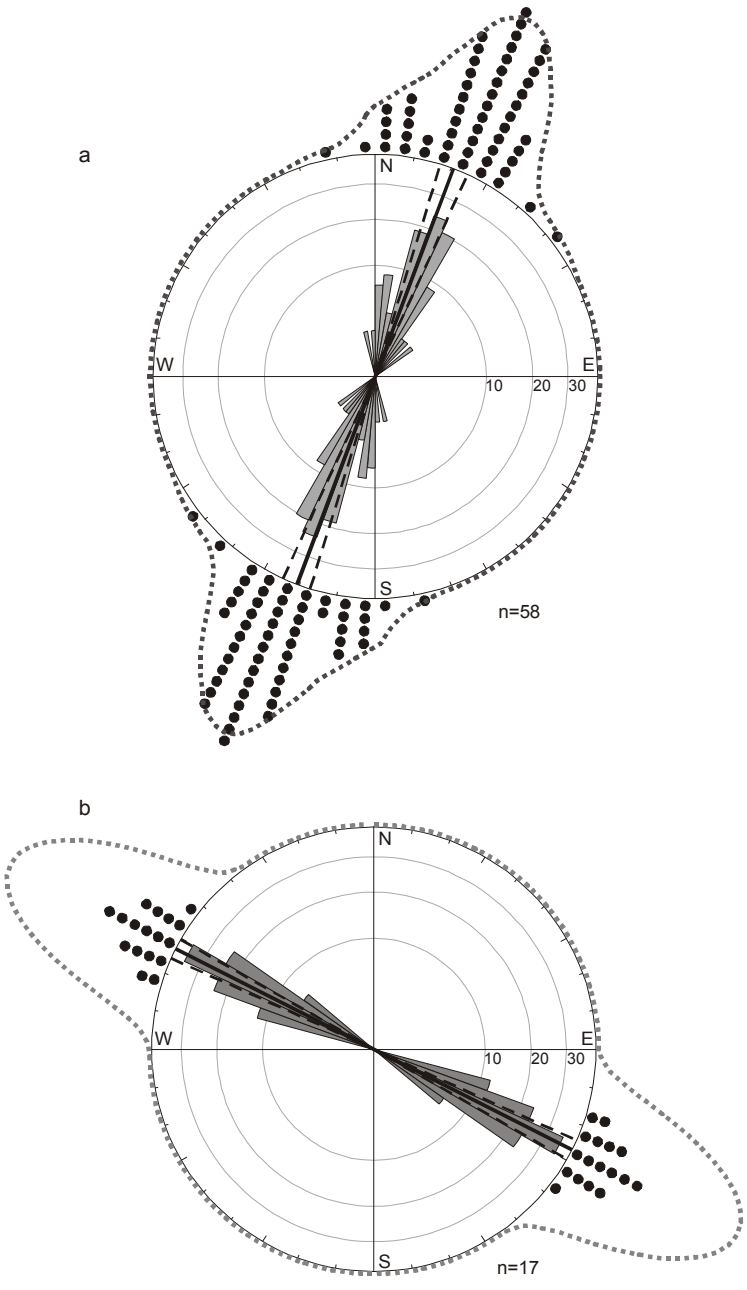


**Figure 11.** Raw data plot, rose diagram and non-parametric density estimates of core (a) and median (b) data. The rose diagram has 5° bins with a scale proportional to the square root of the relative frequency; the dotted lines are non-parametric density estimates (Fisher, 1993) with a smoothing parameter of 0.467 for the core data and 0.627 for the median data. The mean FIA orientations are shown with the solid black line and the 95% confidence interval with the dashed lines.

| Correlation Analysis<br>Spherical Data | Test Value | Critical Value | Significance Prob. | Correl. Coef. |
|---|---|---|---|---|
| **FIA vs Size** | 2.12 | 7.82 | 0.549 | na |
| **FIA vs Foliation Orientation** | 16.18 | 16.92 | 0.063 | na |
| **Circular Data** | **Test Value** | **Critical Value** | **Significance Prob.** | **Correl. Coef.** |
| **FIA trend vs size** | 0.34 | 1.96 | 0.37 | na |
| **FIA vs Fol'n trends** | 2.97 | 1.96 | 0.0015 | 0.68 |

**Table 4.** Results of correlation analyses. Only FIA trend versus foliation trend show a statistically significant correlation. See text for a discussion of correlation tests used.

### 3.3.3 Correlations

There is no correlation between garnet size and FIA orientation or between the FIA orientations and the poles to the foliations, with the hypothesis that there is no correlation holding at the 95% confidence level in both cases (see table 4). However there is a good correlation between the *trends* of the FIA and the foliations, with the probability significance that there is no correlation being less than 1%.

# 4 Discussion

## *4.1 FIAs from HRXCT*

Chapter 1 demonstrated that HRXCT is capable of imaging inclusion trails in garnet porphyroblasts and here the technique has been applied to analysing the FIA orientations within different portions of a sample. The method used to measure the orientations did not use a 3-D version of the data (Fig. 7, Chapter 1), but rather used multiple 2-D slices. This approach was taken because measuring the orientation of a FIA is difficult in a 3-D dataset. Unless there was a continuous inclusion trail running through the centre of each of the porphyroblasts it would be difficult to determine where the axis went, particularly if the axes are not truly linear, due to parallax error or difficulty in aligning individual inclusions. An immersive 3-D visualization environment would help to address this issue but at this these are not readily available. By taking numerous 2-D slices these issues are alleviated. The HRXCT data can be sliced at any orientation and through any part of the porphyroblast. This allows the asymmetry method to be used. Multiple sections can be taken at each orientation, spaced fractions of a millimetre apart, so that the asymmetry can be determined in that orientation with a high degree of confidence. Cut effects can be avoided by taking sections at or near the centre of the porphyroblasts. In some instances the FIA appear to have a curvilinear nature (see below for a discussion of the significance of this). The 2-D technique used here allows the orientation for the centre part of the FIA to be measured, and helps to average out any variation within a porphyroblast.

The range over which the asymmetry flip could be determined varied from porphyroblast to porphyroblast, but was less than 5° in all cases. This lack of certainty is the result of poor inclusion trail density, the curvilinear nature of the axes and limitations in the resolution of the HRXCT technique. For these reason, all asymmetries were recorded at 5° intervals. A potential problem with this is the case where the FIA lies exactly on a multiple of 5°. In this case the inclusion trails would form a coaxial pattern and no asymmetry would be apparent. To deal with this situation a FIA that lies at a multiple of 5° would be included in the lower 5° interval. For example, if a clockwise asymmetry was observed in the 25° section and the 30° orientations displayed a coaxial pattern, the FIA would be assigned to the 25° to 30° interval. However, this did not occur with this dataset.

## *4.2 Formation of Curved Inclusion Trails*

As discussed earlier, there are two competing hypotheses for how curved inclusion trails form; the first states that the porphyroblasts have rotated relative to a fixed geographic reference frame during shearing (referred to as the rotation hypothesis from here on); the second states that the porphyroblasts have not-rotated relative to a fixed geographic reference frame and that the curvature is a result of the porphyroblasts overgrowing crenulated foliations early during the formation of one, or a succession of, crenulation cleavages (the non-rotation hypothesis). The following discussion will examine the data presented in this paper to see if either one of these models is favoured. A fixed geographic reference frame is assumed in the following discussion.

### 4.2.1 Geometry of Inclusion Trails

Detailed examination of the 3-D geometry of the inclusion trails in this sample was not an aim of this study. However, the inclusion trails in the cores of most of the porphyroblasts have a doubly curving non-cylindrical geometry. This indicates the garnet porphyroblasts were rotating relative to the foliation that was included as they grew. If the non-rotation hypothesis holds, this curvature must be the result of deformation with a non-coaxial shearing component. In the PBIS strain model coaxial deformation early in an event will not have partitioned at the scale of a porphyroblast (compare Fig. 2b with Fig. 2c). A growing porphyroblast will include the curvature of the foliation being crenulated, partitioning the more intense deformation around its rim as shearing intensifies. The strain does not appear to intensify towards the edges of the core part of the garnet. This observation is consistent with the suggestion by Bell and Hayward (1991) and Bell et al. (2004) that porphyroblasts only grow early in deformation. They argue that growth only occurs syn-deformation and stops once the crenulation cleavage has begun to differentiate (stage 3 of Bell & Rubenach 1983).

Under the non-rotational hypothesis the relative rotation of porphyroblast and foliation is implied. However, as Stallard et al. (2002) argue, the geometry of curved inclusion trails does not provide conclusive evidence as to the processes that form them. Both hypotheses can be used to explain the observed geometries; taken individually, the 3-D inclusion trail geometry of the cores of the porphyroblasts studied here cannot be used to argue for or against either model.

### 4.2.2 Core Foliation Data

The orientations of the poles to the core foliations show a moderately clustered distribution with a shallow westerly plunge. The centred stereonet in Fig. 9h shows that these data have a slight girdle component to its distribution with an axis plunging at 22.8° towards 194.9°, similar to the orientation of the core FIA. This suggests that there may be some rotation of the foliation about that FIA.

It is important to note the eigenvalue analysis shows that the data has a predominantly clustered distribution. If the porphyroblasts have not rotated, then the distribution observed must be attributed to a primary variation in the orientation of the foliation before porphyroblast growth. There is little literature on the amount of variation in the orientation of a single foliation. Many factors will influence this such as cleavage refraction, reactivation, intensity of the foliation and the anastomosing nature of foliations. Treagus (1983, 1988) demonstrated that cleavage orientation can vary markedly as the result of relatively small variations in the competency of rock. Variations in the mineralogy of the matrix are observed in sample V209 (Fig. 3); therefore, it is possible that cleavage refraction may be the cause of some the variation in the orientation of the foliation. Bell (1978`; Fig. 22) measured the preferred orientation of micas in a slaty cleavage and found distributions similar to those observed here for the core foliation. He attributed this to the anastomosing nature of foliations. It can be concluded that the distribution observed in the orientations of the foliation measured in the cores of the porphyroblasts is consistent with the variation being a primary feature of the rock that has not been modified by subsequent foliation forming events. The slight girdle distribution of these data about the FIA observed in Fig. 9h is consistent with the interpretation that the growth of the garnet cores occurred early in the same deformation that resulted in strong partitioning and development of a new foliation. The amount of rotation is small and the variation is dependent on the amount the foliation had rotated before individual porphyroblasts nucleated. This may also explain why these data do not fit a Watson bipolar distribution to an acceptable level of confidence.

If the rotational hypothesis was correct, a shape parameter (Woodcock 1977) no greater than two would be expected but the foliation data has a shape parameter of 3.9. Drill Core 3 has a shape parameter of only 1.68 with a $t_1$ axis that is approximately the same as the core FIA. This is most likely a result of the small sample size as the variation in FIA dip in the drill core is

only 40º, which is less than that for the total sample population. For the rotation hypothesis to hold, all porphyroblasts must have rotated by similar amounts to each other. The volume of garnet in this sample is such that it is highly unlikely that there would be no interaction between them. Garnets "colliding" should either act as one and rotate together or act like interconnecting cogs driving one another in opposite directions. It is difficult to imagine a clustered distribution if rotation had been the case, because of the range of possible rotation rates, as pointed out by Beirmier and Stüwe (2003), who showed that interaction between porphyroblasts could result in rotation rates between 25% and 75% of the shear strain rate using numerical models. The radius of garnet porphyroblasts varies from 1mm to over 3mm yet they have a consistent foliation orientation. This is problematic if the garnet sizes are related to either the relative timing of nucleation or termination of growth. If all the porphyroblasts nucleate at the same point in time, continue to grow for the same time period, are all subject to the same shear strain rate, and all display the same relationship between shear strain rate and rotation rate, then the total amount of rotation will be the same for each of them and the preserved foliation would maintain a consistent orientation. This requires a set of circumstances that are considered highly improbable. For example, there have been several papers written that demonstrate that the size of garnet porphyroblasts correlate with timing of nucleation (e.g. Chernoff & Carlson 1997, Spear & Daniel 2003), while others give an example of a complicated growth history (Beirmeier & Stuwe 2003).

### 4.2.3 Core FIA Data

The core FIA data has a moderately clustered distribution, similar to that of the core foliation data. Comparing the centred steronet (8b) with that of the foliation data (8h) the tighter cluster is readily observed. A slightly skewed distribution is observed (see also Fig.11a). However, this does not appear significant and these data are well represented by a Watson bipolar model, suggesting that the slightly skewed nature is the result of sampling error. There is no suggestion of a girdle component to the distribution. The 95% confidence cone has a semiangle of only 4.15º.

According to Bell et al. (1995), FIAs are equivalent to the intersection axis between two foliations. If the non-rotation model is correct some conclusions about these foliations can be drawn. It was not possible to directly measure the second, crenulating foliation in any of the porphyroblasts because only the curvature into it is preserved. There are also complications that result from the influence of the porphyroblast shape. It is impossible to derive the orientation of the crenulating foliation from the FIA and core foliation data alone because there are many solutions to this problem (Fig. 12a). However, the most likely orientation for the crenulating foliation in this is a sub-horizontal foliation with a southerly dip, as demonstrated in Fig. 12.

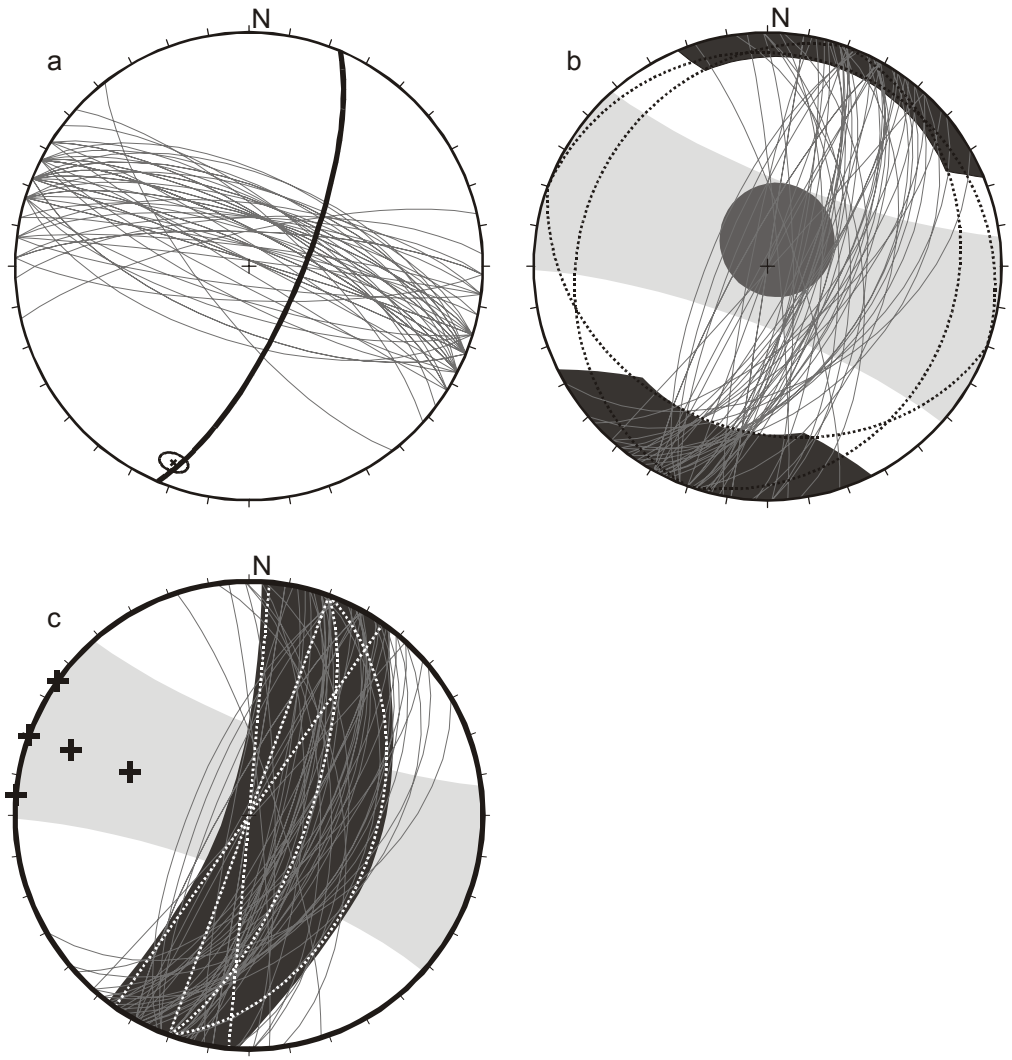


**Figure 12.** A series of equal area stereonets demonstrating that the core FIA is most likely the result of the crenulation of a steep foliation by a sub-horizontal one. (a) shows the mean FIA and 95% confidence interval (cross and circle), the mean core foliation (heavy black line) and the great circles perpendicular to the 58 FIA measurements (light grey lines). The pole to the foliation intersecting with the steep core foliation to form the FIAs must lie on this great circle for each FIA, so the mean orientation must lie in the light grey areas of (b) and (c). In (b) the crenulating foliation is taken to be sub-horizontal with a mean dip and dip-direction of 10° → 200° with a 20° spread (poles would plot in mid-grey circle). The possible intersections between this (dotted lines) and the steep core foliation (light grey lines) are shown in dark grey. Note that this distribution closely matches that for the actual FIA measurements. In (c), the crenulating foliation (dotted lines with + marking the poles) has a moderate to steep dip as in. The range of possible intersections has a much greater spread so is considered an unlikely scenario.

The alignment of zones of maximum curvature of the inclusion trails in the core part of porphyroblasts supports this conclusion.

When introducing the concept of FIAs, Hayward (1990) argued that they would generally have a shallow plunge. This was based on the observation of alternating near-vertical and near horizontal foliations by Bell and Johnson (1989) who proposed a orogenic model involving cycles of horizontal compression and gravitational collapse. The data presented here is in agreement with this idea, and other published data (see Bell et al. 1992c and references

therein). An important implication of this model is that the FIA orientation represents the strike of the sub-vertical foliation. When looking for correlations between the FIAs and sub-vertical core foliation preserved in the porphyroblasts, the only correlation found is between their 2-D trends. There was no statistically significant correlation between the spherical datasets. This means that the dip of the foliation has little to do with the orientation of the FIAs and that they do indeed reflect the strike of the steep foliation.

If a rotational model applies, the FIA is the rotation axis about which the porphyroblasts rotate as they include a single foliation. It is not possible to draw any conclusions about the orientation of this foliation if it is not preserved in the matrix. The effects of subsequent deformation events also need to be considered.

As mentioned above the FIAs appear to be curvilinear, a result of the progressive nature of deformation. A process by which this would occur in the non-rotational model is shown in Fig. 34 of Bell et al. (1986). As deformation progresses the crenulation hinge is rotated towards the orientation of the stretching lineation of the deformation event that the porphyroblast has grown in, resulting in asymmetrical curvature of the FIA in the plane of the later foliation. This is the same as the concept as that for doubly plunging folds that form as a result of heterogeneous strain. In a rotational model, a shift in the stretching direction would be required, or a rotation of the foliation relative to the porphyroblast.

The orientation of the core FIA, as measured here, differs by 24º from that reported by Bell et al. (1998). They used the asymmetry method to determine the FIAs and did not have sections cut at 010º and 020º. The discrepancy results from sampling error in the selection of porphyroblasts within a section. The garnet density in this sample is unusually high and it would not be a common approach to examine every porphyroblast when up to 130 are present in each section. Bell et al. (1998) started with sections cut at 30º increments. They incorrectly determined that the FIA lay between the 030º and 060º, although this overlaps the distribution of FIAs measured by HRXCT. Appendix 1 lists the asymmetry observations for all garnets in all sections cut for this sample. The 030º section contains roughly the same number of garnets with each asymmetry. If the garnets sampled had predominantly clockwise trails one could easily come to an erroneous conclusion about the location of the FIA. A similar error could have been made with the 040º section. This suggests that care must be taken to record the asymmetry in all porphyroblasts in a thin section when applying the asymmetry method, particularly in sections containing trails with both asymmetries. The median FIA value reported by Bell et al. (1998) correlates well with that reported here.

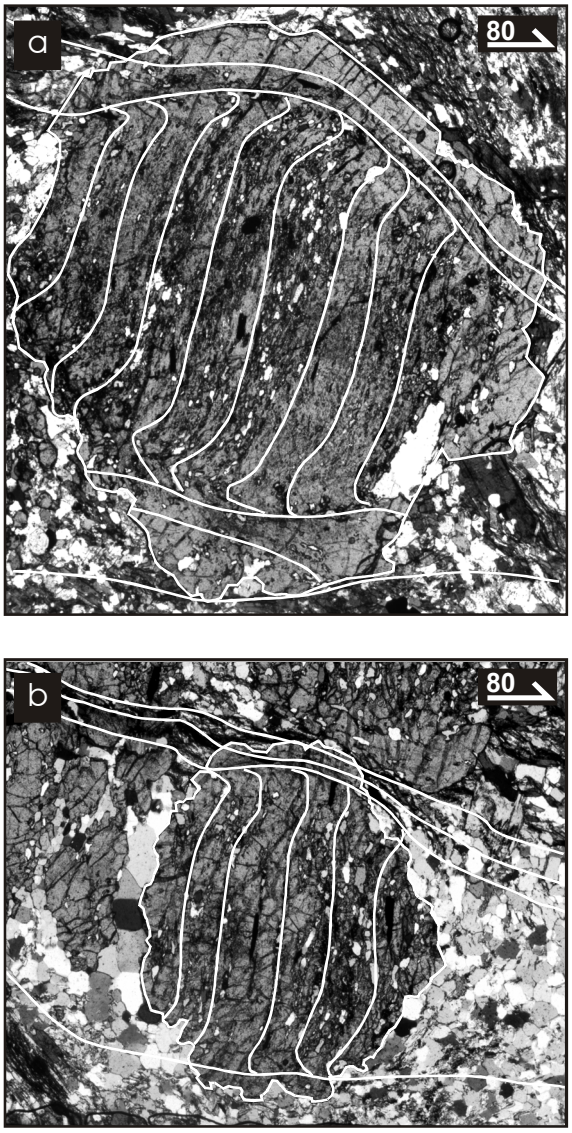


**Figure 13.** Photomicrographs from a vertical thin section of sample V209 showing the history preserved in the inclusion trails. Both show the steep trails in the core of the garnet that curves in a top to the east sense. This is interpreted as S1 being crenulated by a sub-horizontal S2. S2 then curves into S3 which is only preserved in a small part radial increment of garnet. S3 is interpreted as being sub-vertical, and is more pronounced in the upper part of the garnet in (b). S3 then curves into S4, a sub-horizontal foliation that is preserved in the rim of the garnets. Bottom edge of both images is approximately 4.5mm.

### 4.2.4 Variation Between Drill Cores

Statistical tests show that all four drill cores sample the same population for both the FIAs and core foliations. The variations seen in the mean orientations are simply a reflection of the low number of observations from each drill core. There is no evidence of a pre-existing folding of the core foliation. It is possible that if more measurements were made at the locations of each of the drill cores the variation in mean orientations would prove significant. This would be due to the anastomosing nature of foliations and would be the case in either the rotation or the non-rotation models.

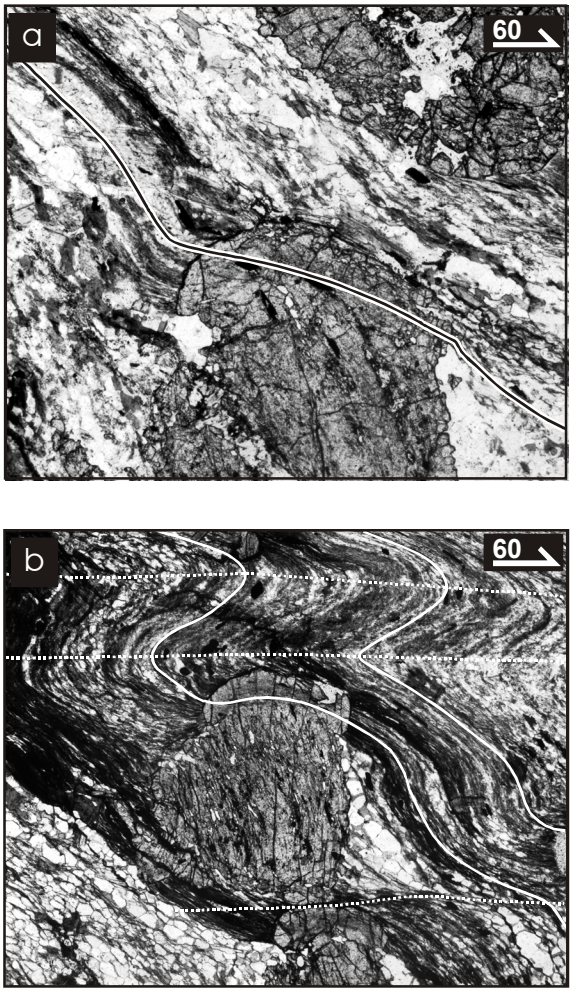


**Figure 14.** Photomicrographs from a vertical thin section of sample V209 showing the S4 to S5 transition in (a) and the S4 to S5 (solid lines) to S6 (dotted lines) transitions in (b). The garnets in both images have been cut close to their rim so the trails do not show the full history. Bottom edge of (a) is approximately 4.5mm and of (b) is 6mm.

### 4.2.5 Median FIA Data

Although the number of observations is low (n=17) the median FIA appear to be sampling an even tighter distribution. Bell and Johnson (1989) argued that as strain is concentrated against rigid bodies such as porphyroblasts it will more closely reflect the direction of bulk shortening. This would result in a more tightly clustered distribution of FIAs that form in growth increments on pre-existing porphyroblasts in the non-rotation model. The plunge of the median FIA could not be measured. It is most likely horizontal as curvature attributed to this event is restricted to the top and bottoms of the porphyroblasts. In the rotational model, the tighter distribution of a later FIA event would be expected as earlier FIA would have been subjected to more deformation events.

## *4.3 Evidence for Non-rotation and a Prolonged History*

Does the evidence support a rotation or non-rotation hypothesis? The clustering of the FIA and foliation data for the core provides compelling evidence that the porphyroblasts in this

sample have not rotated. The clustering of the core foliation data is difficult to reconcile with the rotation hypothesis because a more girdle like distribution about the roatation axis would be expected from rotation in a single foliation forming event. The Woodcock shape parameter (K) for the foliation data is 3.9; it would be expected to be less than two if the porphyroblasts had rotated. Subsequent foliation forming events would create a dispersed distribution. The median FIA is roughly orthogonal to the core FIA. In the rotation hypothesis, this would indicate a second rotation about an axis perpendicular to the first, yet there is no evidence that the core FIAs have been redistributed in such a way. A girdle distribution about the median FIA would be expected. As well as the foliation forming events that formed the core and median foliations, there is evidence for at least three more foliations in the sample (Fig. 14). Again, there is no evidence that the deformation events forming these foliations have affected the distribution of the earlier structures preserved in the porphyroblasts. As mentioned above, the distribution of data observed here is best explained by the variation of the primary fabrics without any rotation with respect to a fixed geographic reference frame.

If rotation had occurred, all the porphyroblasts would have to have rotated by approximately the same amount as each other in each deformation event. This is considered implausible given the garnet density and the interference that would result (Beirmeier & Stuwe 2003). Another hypothesis is that the porphyroblasts did rotate as the garnet cores grew but not in latter deformation events. This would require that all the porphyroblasts rotated in a remarkably consistent manner in the foliation-forming event preserved in the garnet cores and for the deformation mechanism to change between deformation events. Both of these conditions are highly improbable. It is important to note that the rotation and non-rotation hypotheses for the formation of curved inclusion trails are mutually exclusive in the one foliation-forming event because they require opposite shear senses (see Fig.1); curvature cannot form by a combination of the two. If there were a switch from a rotation to a non-rotation process a reversal in the asymmetry of the inclusion trails would be expected.

As the porphyroblasts have not rotated the structures preserved within them can be used to determine the early deformation history preserved in this sample (Figs. 13 and 14). Garnet nucleated and grew during the early stages of the development of a sub-horizontal foliation ($S_2$) that was crenulating a steeply east dipping foliation ($S_1$). The porphyroblasts preserved the curvature of $S_1$ towards $S_2$ as they grew early in $D_2$ before significant differentiation had occurred (Fig. 13). The core FIA preserves the orientation of the intersection between these two foliations ($L_2^1$). The shear sense on $S_2$ was top to the east. A sub-vertical 110º striking crenulation cleavage with a south side down shear sense then developed ($S_3$). The curvature of $S_2$ into $S_3$ was captured in a small radial increment of garnet growth and is preserved as the median FIA (equivalent to $L_3^2$, Fig 13). This growth could have occurred early in $D_3$, $D_4$ or

both. Another sub-horizontal foliation then formed ($S_4$) which is preserved in some of the porphyroblasts as a truncational surface. $L_4^3$ would have approximately the same orientation as $L_3^2$ and the median FIA. $S_3$ curves into $S_4$ with a top to the south shear sense on $S_4$. The dominant matrix foliation formed next ($S_5$) with a sub-vertical north-northeast strike and a west side up shear sense (Fig 14a). The curvature of $S_4$ into $S_5$ is preserved in the rims of some of the porphyroblasts and the rim FIA is equivalent to $L_5^4$. The final deformation event formed a sub-horizontal foliation, $S_6$, that crenulates and folds $S_5$ in the matrix with a top to the west asymmetry (Figs 3 and 14b). Only $S_5$ and $S_6$ are preserved in the matrix and the earlier events can only be determined by studying the inclusion trail geometry. This demonstrates the value of curved inclusion trails of which Rosenfeld imagined.

# References


Aerden, D. 2004. Correlating deformation in Variscan NW-Iberia using porphyroblasts; implications for the Ibero-Armorican Arc. *Journal of Structural Geology* **26**(1), 177-196.

Aerden, D. 2005. Comment on Reference frame, angular momentum, and porphyroblast rotation by Dazhi Jiang and Paul F. Williams. *Journal of Structural Geology*, In Press.

Aerden, D. G. A. M. 1995. Porphyroblast non-rotation during crustal extension in the Variscan Lys-Caillaouas Massif, Pyrenees. *Journal of Structural Geology* **17**, 709-725.

Bauer, R. L., Ketcham, R. A., Dennison, C. & Carlson, W. D. 1998. X-ray computed tomography (CT) imaging of spiral inclusion trails and the external morphology of garnet porphyroblasts. *EOS* **79**(17), 357.

Beirmeier, C. & Stuwe, K. 2003. Strain rates from snowball garnet. *Journal of Metamorphic Geology* **21**, 253-268.

Bell, T. H. 1978. The development of slaty cleavage across the Nackara Arc of the Adelaide Geosyncline. *Tectonophysics* **51**(3-4), 171-174.

Bell, T. H. 1981. Foliation development -- The contribution, geometry and significance of progressive, bulk, inhomogeneous shortening. *Tectonophysics* **75**(3-4), 273-296.

Bell, T. H. 1985. Deformation partitioning and porphyroblast rotation in metamorphic rocks: a radical reinterpretation. *Journal of Metamorphic Geology* **3**, 109-118.

Bell, T. H. & Chen, A. 2002. The development of spiral-shaped inclusion trails during multiple metamorphism and folding. *Journal of Metamorphic Geology* **20**(4), 397 -412.

Bell, T. H., Duncan, A. C. & Simmons, J. V. 1989. Deformation partitioning, shear zone development and the role of undeformable objects. *Tectonophysics* **158**(1-4), 163-171.

Bell, T. H., Forde, A. & Hayward, N. 1992a. Do smoothly-curving spiral shaped inclusion trails signify porphyroblast rotation? *Geology* **20**, 59-62.

Bell, T. H., Forde, A. & Hayward, N. 1992b. Do smoothly curved, spiral-shaped inclusion trails signify porphyroblast rotation?: Reply. *Geology* **20**(11), 1055-1056.

Bell, T. H., Forde, A. & Wang, J. 1995. A new indicator of movement direction during orogenesis: measurement technique and application to the Alps. *Terra Nova* **V. 7**, 500-508.

Bell, T. H., Ham, A. P. & Hickey, K. A. 2003. Early formed regional antiforms and synforms that fold younger matrix schistosities: their effect on sites of mineral growth. *Tectonophysics* **367**(3-4), 253 -278.

Bell, T. H., Ham, A. P. & Kim, H. S. 2004. Partitioning of deformation along an orogen and its effects on porphyroblast growth during orogenesis. *Journal of Structural Geology* **26**(5), 825 -845.

Bell, T. H. & Hayward, N. 1991. Episodic metamorphic reactions during orogenesis; the control of deformation partitioning on reaction sites and reaction duration. *Journal of Metamorphic Geology* **9**(5), 619-640.

Bell, T. H. & Hickey, K. A. 1997. Distribution of pre-folding linear indicators of movement direction around the Spring Hill Synform, Vermont; significance for mechanism of folding in this portion of the Appalachians. *Tectonophysics* **274**(4), 275-294.

Bell, T. H. & Hickey, K. A. 1999. Complex microstructures preserved in rocks with a simple matrix; significance for deformation and metamorphic processes. *Journal of Metamorphic Geology* **17**(5), 521-535.

Bell, T. H., Hickey, K. A. & Upton, G. J. G. 1998. Distinguishing and correlating multiple phases of metamorphism across a multiply deformed region using the axes of spiral, staircase and sigmoidal inclusion trails in garnet. *Journal of Metamorphic Geology* **16**(6), 767-794.

Bell, T. H., Hickey, K. A. & Wang, J. 1997. Spiral and staircase inclusion trail axes within garnet and staurolite porphyroblasts from schists of the Bolton Syncline, Connecticut; timing of porphyroblast growth and the effects of fold development. *Journal of Metamorphic Geology* **15**(4), 467-478.

Bell, T. H. & Johnson, S. E. 1989. Porphyroblast inclusion trails: the key to orogenesis. *Journal of Metamorphic Geology* **7**, 279-310.

Bell, T. H. & Johnson, S. E. 1990. Rotation of relatively large rigid objects during ductile deformation: Well established fact or intuitive prejudice. *Australian Journal of Earth Sciences* **37**, 441-446.

Bell, T. H., Johnson, S. E., Davis, B., Forde, A., Hayward, N. & Witkins, C. 1992c. Porphyroblast inclusion-trail orientation data; eppure non son girate! *Journal of Metamorphic Geology* **10**(3), 295-307.

Bell, T. H. & Mares, V. M. 1999. Correlating deformation and metamorphism around orogenic arcs. *American Mineralogist* **84**(11-12), 1727 -1740.

Bell, T. H. & Rubenach, M. J. 1983. Sequential porphyroblast growth and crenulation cleavage development during progressive deformation. *Tectonophysics* **92**(1-3), 171-194.

Bell, T. H., Rubenach, M. J. & Fleming, P. D. 1986. Porphyroblast nucleation, growth and dissolution in regional metamorphic rocks as a function of deformation partitioning during foliation development. *Journal of Metamorphic Geology* **4**, 37-67.

Bell, T. H. & Welch, P. W. 2002. Prolonged Acadian orogenesis: Revelations from foliation intersection axis (FIA) controlled monazite dating of foliations in porphyroblasts and matrix. *American Journal of Science* **302**(7), 549 -581.

Berger, M. J., Hubbell, J. H., Seltzer, S. M., Coursey, J. S. & Zucker, D. S. 1999. XCOM: Photon Cross Section Database (version 1.2), [Online]. **2002**. National Institute of Standards and Technology, Gaithersburg, MD.

Bonse, U. & Beckmann, F. 2001. Multiple-beam X-ray interferometry for phase-contrast microtomography. *Journal of Synchrotron Radiation* **8**(Part 1), 1-5.

Bonse, U. & Busch, F. 1996. X-ray computed microtomography (μCT) using synchrotron radiation (SR). *Progress in biophysics and molecular biology* **65**, 133-169.

Bronnikov, A. V. 2002. Theory of quantitative phase-contrast computed tomography. *Journal of the Optical Society of America A-Optics & Image Science* **19**(3), 472-480.

Carlson, W. D. & Denison, C. 1992. Mechanisms of porphyroblast crystallization; results from high-resolution computed X-ray tomography. *Science* **257**(5074), 1236-1239.

Ceriani, S., Mancktelow, N. S. & Pennacchioni, G. 2003. Analogue modelling of the influence of shape and particle/matrix interface lubrication on the rotational behaviour of rigid particles in simple shear. *Journal of Structural Geology* **25**(12), 2005-2021.

Chernoff, C. B. & Carlson, W. 1997. Disequilibrium for Ca during growth of pelitic garnet. *Journal of Metamorphic Geology* **15**(4), 421-438.

Chernoff, C. B. & Carlson, W. 1999. Trace element zoning as a record of chemical disequilibrium during garnet growth. *Geology* **27**(6), 555-558.

Cifelli, R. L., Rowe, T. B., Luckett, W. P., Banta, J., Reyes, R. & Howes, H. I. 1996. Fossil evidence for the origin of the marsupial pattern of tooth replacement. *Nature* **379**, 715-718.

Cihan, M. 2004. The drawbacks of sectioning rocks relative to fabric orientations in the matrix: A case study from the Robertson River Metamorphics (Northern Queensland, Australia). *Journal of Structural Geology* **26**, 2157 -2174.

Cihan, M. & Parsons, A. 2005. The use of porphyroblasts to resolve the history of macro-scale structures: an example from the Robertson River Metamorphics, North-Eastern Australia. *Journal of Structural Geology* **27**(6), 1027-1045.

Daniel, C. G. & Spear, F. S. 1998. Three-dimensional patterns of garnet nucleation and growth. *Geology* **v.26**, 503-506.

Daniel, C. G. & Spear, F. S. 1999. The clustered nucleation and growth processes of garnet in regional metamorphic rocks from north-west Connecticut, USA. *Journal of Metamorphic Geology* **17**(5), 503.

Davis, B. K. 1993. Mechanism of emplacement of the Cannibal Creek Granite with special reference to timing and deformation history of the aureole. *Tectonophysics* **224**, 337-362.

De Man, B., Nuyts, J., Dupont, P., Marchal, G. & Suetens, P. 2001. An iterative maximum-likelihood polychromatic algorithm for CT. *IEEE Transactions on Medical Imaging* **20**(10), 999-1008.

Denison, C., Carlson, W. D. & Ketcham, R. A. 1997. Three-dimensional quantitaitve textural analysis of metamorphic rocks using high-resolution computed X-ray tomography: Part I. Methods and techniques. *Journal of Metamorphic Geology* **15**(1), 29-44.

Dilmanian, F. A. 1992. Computed tomography with monochromatic X-rays. *American Journal of Physiological Imaging* **7**, 175-193.

Elbakri, I. A. & Fessler, J. A. 2003. Segmentation-free statistical image reconstruction for polyenergetic x-ray computed tomography with experimental validation. *Physics in Medicine & Biology* **48**(15), 2453-2477.

Evins, P. M. 2005. A 3D study of aligned porphyroblast inclusion trails across shear zones and folds. *Journal of Structural Geology* **27**(7), 1300-1314.

Fisher, N. I. 1993. *Statistical analysis of circular data*. Cambridge University Press, Cambridge, [England].

Fisher, N. I. & Lee, A. J. 1983. A correlation coefficient for circular data. *Biometrika* **70**(2), 327-332.

Fisher, N. I., Lewis, T. & Embleton, B. J. J. 1987. *Statistical analysis of spherical data*. Cambridge University Press, Cambridge [England] ; Melbourne.

Ham, A. P. & Bell, T. H. 2004. Recycling of foliations during folding. *Journal of Structural Geology* **26**(11), 1989-2009.

Hayward, N. 1990. Determination of early fold axis orientations in multiply deformed rocks using porphyroblast inclusion trails. *Tectonophysics* **V. 179**, 353-369.

Hayward, N. 1992. Microstructural analysis of the classical spiral garnet porphyroblasts of South-east Vermont; evidence for non-rotation. *Journal of Metamorphic Geology* **10**(4), 567-587.

Hickey, K. A. & Bell, T. H. 1999. Behaviour of rigid objects during deformation and metamorphism; a test using schists from the Bolton Syncline, Connecticut, USA. *Journal of Metamorphic Geology* **17**(2), 211-228.

Hobbs, B. E., Means, W. D. & Williams, P. F. 1976. *An Outline of Structural Geology*. John Wiley and Sons, New York.

Huddlestone-Holmes, C. R. & Ketcham, R. A. 2005. Getting the inside story: using computed X-ray tomography to study inclusion trails in garnet porphyroblasts. *American Mineralogist* **90**, ea1-ea17.

Ikeda, T., Shimobayashi, N., Wallis, S. R. & Tsuchiyama, A. 2002. Crystallographic orientation, chemical composition and three dimensional geometry pf sigmoidal garnet: evidence for rotation. *Journal of Structural Geology* **24**, 1633-1646.

Ilg, B. R. & Karlstrom, K. E. 2000. Porphyroblast inclusion trail geometries in the Grand Canyon: evidence for non-rotation and rotation? *Journal of Structural Geology* **22**, 231-243.

Johnson, S. E. 1990. Lack of porphyroblast rotation in the Otago schists, New Zealand: implications for crenulation cleavage development, folding and deformation partitioning. *Journal of Metamorphic Geology* **8**, 13-30.

Johnson, S. E. 1993a. Testing models for the development of spiral-shaped inclusion trails in garnet porphyroblasts: to rotate or not to rotate, that is the question. *Journal of Metamorphic Geology* **11**, 635-659.

Johnson, S. E. 1993b. Unravelling the spirals: a serial thin-section study and three dimensional computer-aided reconstruction of spiral-shaped inclusion trails in garnet porphyroblasts. *Journal of Metamorphic Geology* **11**, 621-634.

Johnson, S. E. 1999. Porphyroblast microstructures: A review of current and future trends. *American Mineralogist* **V.84**, 1711-1726.

Johnson, S. E. & Moore, R. R. 1996. De-bugging the 'millipede' porphyroblast microstructure: a serial thin-section study and 3-D computer animation. *Journal of Metamorphic Geology* **14**, 3-14.

Jones, K. W., Feng, H., Lindquist, W. B., Adler, P. M., Thovert, J. F., Vekemans, B., Vincze, L., Szaloki, I., Van Grieken, R., Adams, F. & Riekel, C. 2003. Study of the microgeometry of porous materials using synchrotron computed microtomography. In: *Applications of X-Ray Computed Tomography in the Geosciences* (edited by Mees, F., Swennen, R., Van Geet, M. & Jacobs, P.). *Geological Society Special Publication (215)* **215**. Geological Society of London, London, 39-49.

Jung, W. S., Ree, J. H. & Park, Y. 1999. Non-rotation of garnet porphyroblasts and 3-D inclusion trail data: an example from the Imjingang belt, South Korea. *Tectonophysics* **307**(3-4), 381-395.

Kak, A. C. & Slaney, M. 1988. *Principles of Computerized Tomographic Imaging*. The Institute of Electrical and Electronics Engineers, Inc., New York.

Kalukin, A. R., Van Geet, M. & Swennen, R. 2000. Principal components analysis of multienergy X-ray computed tomography of mineral samples. *IEEE Transactions on Nuclear Science* **47**(5), 1729-1736.

Ketcham, R. A. 2004. Efficient and flexible three-dimensional measurement of features in CT data volumes: implications for quantitative analysis of metamorphic textures. In: *32nd International Geological Congress* **Abstract Volume, Part 1**, Florence, Italy, Abstract 93-4, 445.

Ketcham, R. A. & Carlson, W. D. 2001. Acquisition, optimization and interpretation of X-ray computed tomographic imagery: applications to the geosciences. *Computers and Geosciences* **27**, 381-400.

Ketcham, R. A. & Ryan, T. 2004. Quantification and visualization of anisotropy in trabecular bone. *Journal of Microscopy* **213**, 158-171.

Koeberl, C., Denison, C., Ketcham, R. A. & Reimold, W. U. 2002. High resolution X-ray computed tomography of impactites. *Journal of Geophysical Research - Planets* **107(E10)**, 5089.

Krukowski, S. T. 1988. Sodium metatungstate: a new heavy-mineral separation medium for the extraction of conodonts from insoluble residues. *Journal of Paleontology* **62**(2), 314-316.

Kyle, J. R. & Ketcham, R. A. 2003. In-situ distribution of gold in ores using high-resolution X-ray computed tomography. *Economic Geology* **98**, 1697-1701.

Lee, H., Lee, B.-J. & Otoh, S. 2000. Significance of systematic changes in crenulation asymmetries within meta-sediments across the Ogcheon Supergroup in the Goesan area, southern Korea. Hanrimwon Publishing Company for the Geological Society of Korea, Seoul, South Korea, 115-134.

Lister, G. S. & Williams, P. F. 1983. The partitioning of deformation in flowing rock masses. *Tectonophysics* **92**, 1-33.

Mancktelow, N. S., Arbaret, L. & Pennacchioni, G. 2002. Experimental observations on the effect of interface slip on rotation and stabilisation of rigid particles in simple shear and a comparison with natural mylonites. *Journal of Structural Geology* **24**(3), 567-585.

Marschallinger, R. 1998. Three-dimensional reconstruction and modelling of microstructures and microchemistry in geological materials. *Scanning* **20**, 65-73.

Masuda, T. & Mochizuki, S. 1989. Development of snowball structure: numerical simulation of inclusion trails during synkinematic porphyroblast growth in metamorphic rocks. *Tectonophysics* **170**, 141-150.

Mees, F., Swennen, R., van Geet, M. & Jacobs, P. 2003. *Applications of X-ray computed tomography in the geosciences*. Geological Society of London, London.

Natterer, F. & Ritman, E. L. 2002. Past and Future Directions in X-Ray Computed Tomography (CT). *International Journal of Imaging Systems and Technology* **12**, 175-187.

Passchier, C. W. & Trouw, R. A. J. 1996. *Microtectonics*. Springer-Verlag, Berlin.

Passchier, C. W., Trouw, R. A. J., Zwart, H. J. & Vissers, R. L. M. 1992. Porphyroblast rotation: eppur si muove? *Journal of Metamorphic Geology* **10**, 283-294.

Powell, D. & Treagus, J. E. 1967. On the geometry of S-shaped inclusion trails in garnet porphyroblasts. *Mineralogical Magazine* **36**, 453-456.

Powell, D. & Treagus, J. E. 1970. Rotational fabrics in metamorphic minerals. *Mineralogical Magazine* **37**(No. 291), 801-813.

Proussevitch, A., Ketcham, R. A., Carlson, W. & Sahagian, D. 1998. Preliminary results of X-ray CT analysis of Hawaiian vesicular basalts. In: *American Geophysical Union 1998 spring meeting* (edited by Anonymous) **79**. American Geophysical Union, 360.

Ramsay, J. G. 1962. The geometry and mechanics of formation of 'similar' type folds. *Journal of Geology* **70**, 309-327.

Rosenfeld, J. 1968. Garnet rotations due to the major paleozoic deformations in southeast Vermont. In: *Studies of Appalachian Geology: Northern and Maritime* (edited by Zen, E., White, W. S., Hadley, J. B. & Thompson, J., J.B.). Wiley-Interscience Publishers, New York, 185 - 202.

Rosenfeld, J. L. 1970. *Rotated Garnets in Metamorphic Rocks. Geological Society of America Special Paper, 129*. Geological Society of America, Boulder, Colarado.

Rowe, T. 1996. Coevolution of the mammalian middle ear and neocortex. *Science* **273**, 651-654.

Samanta, S. K., Mandal, N. & Chakraborty, C. 2002a. Development of structures under the influence of heterogeneous flow field around rigid inclusions: insights from theoretical and numerical models. *Earth-Science Reviews* **58**(1-2), 85-119.

Samanta, S. K., Mandal, N., Chakraboty, C. & Majumder, K. 2002b. Simulation of inclusion trail patterns within rotating synkinematic porphyroblasts. *Computers and Geosciences* **28**, 297-308.

Sayab, M. 2005. Microstructural evidence for N-S shortening in the Mount Isa Inlier (NW Queensland, Australia): the preservation of early W-E-trending foliations in porphyroblasts revealed by independent 3D measurement techniques. *Journal of Structural Geology* **27**(8), 1445-1468.

Schoneveld, C. 1977. A study of some typical inclusion patterns in strongly paracrystalline-rotated garnets. *Tectonophysics* **39**, 453-471.

Spear, F. & Yao, K. 2001. The three dimensional geometry of garnet growth, Harpswell Neck, Maine, USA. In: *Eleventh Annual V.M. Goldschmidt Conference, Hot Springs, VA, USA. Abstract number, 3693.* (edited by Bodnar, R. J. & Hochella, M. F.). Lunar and Planetary Institute, Houston, Texas.

Spear, F. S. & Daniel, C. G. 1998. Three-dimensional imaging of garnet porphyroblast sizes and chemical zoning: Nucleation and growth history in the garnet zone. *Geological Materials Research* **1**(1), 1-43.

Spear, F. S. & Daniel, C. G. 2001. Diffusion control of garnet growth, Harpswell Neck, Maine, USA. *Journal of Metamorphic Geology* **19**(2), 179.

Spear, F. S. & Daniel, C. G. 2003. Three-dimensional imaging of garnet porphyroblast sizes and chemical zoning; nucleation and growth history in the garnet zone. *American Mineralogist* **88**(1), 245.

Stallard, A. & Hickey, K. A. 2001. Shear zone vs folding for spiral inclusion trails in the Canton Schist. *Journal of Structural Geology* **23**, 1845-1864.

Stallard, A., Ikei, H. & Masuda, T. 2002. Numerical simulations of spiral-shaped inclusion trails: can 3D geometry distinguish between end-member models of spiral formation? *Journal of Metamorphic Geology* **20**, 801-812.

Steinhardt, C. 1989. Lack of porphyroblast rotation in noncoaxially deformed schists from Petrel Cove, South Australia, and its implications. *Tectonophysics* **158**, 127-140.

Stewart, L. K. 1997. Experimental investigation of the effects of fluid heterogeneity upon the motion of rigid ellipsoidal inclusions during bulk inhomogeneous shortening. *Journal of Structural Geology* **19**(9), 1231-1243.

Takeda, T., Momose, A., Yu, Q. W., Yuasa, T., Dilmanian, F. A., Akatsuka, T. & Itai, Y. 2000. New types of X-ray computed tomography (CT) with synchrotron radiation: Fluorescent X-ray CT and phase-contrast X-ray CT using interferometer. *Cellular & Molecular Biology* **46**(6), 1077-1088.

ten Grotenhuis, S. M., Passchier, C. W. & Bons, P. D. 2002. The influence of strain localisation on the rotation behaviour of rigid objects in experimental shear zones. *Journal of Structural Geology* **24**(3), 485-499.

Timms, N. E. 2003. Garnet porphyroblast timing and behaviour during fold evolution: implications from a 3-D geometric analysis of a hand-sample scale fold in a schist. *Journal of Metamorphic Geology* **21**(9), 853-873.

Torikoshi, M., Tsunoo, T., Endo, M., Noda, K., Kumada, M., Yamada, S., Soga, F. & Hyodo, K. 2001. Design of synchrotron light source and its beamline dedicated to dual-energy x-ray computed tomography. *Journal of Biomedical Optics* **6**(3), 371-377.

Torikoshi, M., Tsunoo, T., Sasaki, M., Endo, M., Noda, Y., Ohno, Y., Kohno, T., Hyodo, K., Uesugi, K. & Yagi, N. 2003. Electron density measurement with dual-energy x-ray CT using synchrotron radiation. *Physics in Medicine & Biology* **48**(5), 673-685.

Treagus, S. H. 1983. A new theory of finite strain variation through contrasting layers, and its bearing on cleavage refraction. *Journal of Structural Geology* **5**, 351-358.

Treagus, S. H. 1988. Strain refraction in layered systems. *Journal of Structural Geology* **10**(5), 517-527.

Tsuchiyama, A., Nakamura, T., Nakano, T. & Nakamura, N. 2002. Three-dimensional description of the Kobe meteorite by micro X-ray CT method: Possibility of three-dimensional curation of meteorite samples. *Geochemical Journal* **36**, 369-390.

Upton, G. J. G. & Fingleton, B. 1989. *Spatial Data Anlysis by Example, Volume 2: Categorical and Directional Data*. John Wiley & Sons, Chichester.

Upton, G. J. G., Hickey, K. A. & Stallard, A. 2003. Regression models for cyclic data. *Royal Statistical Society* **Journal. Series C: Applied Statistics. 52**(Part 2), 227-235.

Wellington, S. L. & Vinegar, H. J. 1987. X-ray computerized tomography. *Journal of Petroleum Technology*(August 1987), 885-898.

Williams, P. F. & Jiang, D. 1999. Rotating garnets. *Journal of Metamorphic Geology* **17**, 367-378.

Woodcock, N. H. 1977. Specification of fabric shapes using an eigenvalue method. *Geological Society of America Bulletin* **88**, 1231-1236.

Woodcock, N. H. & Naylor, M. A. 1983. Randomness testing in three-dimensional orientation data. *Journal of Structural Geology* **5**(5), 539-548.

Yamaya, T., Obi, T., Yamaguchi, M. & Ohyama, N. 2000. An acceleration algorithm for image reconstruction based on continuous-discrete mapping model. *Optical Review* **7**(2), 132-137.

Yeh, M.-W. & Bell, T. H. 2004. Significance of dextral reactivation of an E-W transfer fault in the formation of the Pennsylvania orocline, central Appalachians. *Tectonics* **23**, TC5009, doi:10.1029/2003TC001593.

# Appendix 1. V209 Asymmestry Data.

**Asymmetry observations from thin sections, sample V209.**

| | | *Core* | | | | *Median* | | | | |
|---|---|---|---|---|---|---|---|---|---|---|
| Orientaion* | Rim Cut | cw | acw | millipede | amb.# | cw | acw | millipede | amb.# | Total |
| 000 | 24 | 41 | 2 | 0 | 3 | 43 | 0 | 0 | 3 | 70 |
| 010 | 33 | 46 | 13 | 0 | 39 | 54 | 0 | 0 | 44 | 131 |
| 020 | 35 | 34 | 28 | 4 | 4 | 51 | 0 | 0 | 19 | 105 |
| 030 | 31 | 11 | 12 | 1 | 7 | 23 | 0 | 0 | 8 | 62 |
| 040 | 27 | 5 | 17 | 2 | 11 | 20 | 0 | 0 | 15 | 62 |
| 050 | 50 | 4 | 24 | 1 | 21 | 26 | 0 | 0 | 24 | 100 |
| 060 | 39 | 1 | 52 | 0 | 15 | 47 | 0 | 0 | 21 | 107 |
| 070 | 16 | 0 | 25 | 0 | 1 | 23 | 0 | 0 | 3 | 42 |
| 080 | 34 | 0 | 42 | 0 | 6 | 39 | 0 | 0 | 9 | 82 |
| 090 | 38 | 0 | 49 | 0 | 5 | 40 | 6 | 1 | 7 | 92 |
| 100 | 28 | 0 | 55 | 0 | 1 | 34 | 13 | 3 | 6 | 84 |
| 110 | 25 | 0 | 43 | 0 | 5 | 23 | 16 | 3 | 6 | 73 |
| 120 | 25 | 0 | 50 | 0 | 1 | 20 | 21 | 4 | 6 | 76 |
| 130 | 41 | 0 | 41 | 1 | 5 | 8 | 15 | 8 | 16 | 88 |
| 140 | 17 | 0 | 31 | 0 | 2 | 5 | 19 | 2 | 7 | 50 |
| 150 | 26 | 0 | 41 | 1 | 10 | 0 | 32 | 2 | 18 | 78 |
| 160 | 28 | 0 | 30 | 0 | 9 | 0 | 24 | 0 | 15 | 67 |
| 170 | 26 | 2 | 42 | 0 | 8 | 0 | 38 | 0 | 14 | 78 |

* all orientations are to the left i.e. ←
# amb. = ambiguous

# Appendix 2. FIAs from HRXCT.

**FIA Measurements from HRXCT data, Sample V209.**

| | | | Core FIA* | | Core Foliation (Pole) | | Median FIA* |
|---|---|---|---|---|---|---|---|
| Core | Garnet | Diameter | Plunge | Direction | Plunge | Direction | Trend |
| 1 | 3 | 2.0 | 32.5 | 202.5 | 16.2 | 289.0 | - |
| 1 | 4 | 1.6 | 22.5 | 207.5 | 0.0 | 279.0 | - |
| 1 | 5 | 1.8 | 32.5 | 207.5 | 13.5 | 290.9 | - |
| 1 | 6 | 1.8 | 2.5 | 32.5 | 2.7 | 119.0 | 122.5 |
| 1 | 8 | 1.5 | 27.5 | 202.5 | 16.1 | 112.7 | - |
| 1 | 11 | 1.8 | 22.5 | 217.5 | 15.6 | 306.6 | - |
| 1 | 13 | 1.8 | 12.5 | 202.5 | 10.5 | 299.3 | - |
| 1 | 16 | 1.7 | 22.5 | 187.5 | 21.7 | 285.1 | 107.5 |
| 1 | 17 | 1.7 | 17.5 | 207.5 | 17.8 | 303.0 | 117.5 |
| 1 | 18 | 1.6 | 7.5 | 27.5 | - | - | - |
| 1 | 19 | 1.7 | 17.5 | 182.5 | 9.1 | 269.4 | - |
| 1 | 20 | 2.0 | 27.5 | 17.5 | 11.0 | 285.7 | - |
| 1 | 21 | 1.7 | 12.5 | 197.5 | 28.6 | 295.4 | 117.5 |
| 1 | 23 | 1.6 | 2.5 | 187.5 | 19.7 | 273.3 | 107.5 |
| 1 | 24 | 1.7 | 22.5 | 197.5 | 13.1 | 290.2 | - |
| 1 | 25 | 1.5 | 17.5 | 207.5 | 0.0 | 298.0 | - |
| 1 | 26 | 2.1 | 7.5 | 187.5 | 0.0 | 279.0 | 122.5 |
| 1 | 27 | 1.7 | 22.5 | 22.5 | 12.0 | 113.0 | - |
| 1 | 28 | 1.6 | 17.5 | 197.5 | 0.3 | 111.0 | - |
| 1 | 29 | 1.7 | 2.5 | 197.5 | 15.2 | 288.0 | - |
| 1 | 30 | 2.0 | 17.5 | 212.5 | 20.7 | 113.3 | - |
| 1 | 31 | 1.6 | 17.5 | 212.5 | 9.7 | 119.7 | - |
| 1 | 35 | 1.5 | 7.5 | 192.5 | 24.6 | 299.5 | - |
| 1 | 38 | 1 | 12.5 | 207.5 | - | - | - |
| 2 | 2 | 2.0 | 12.5 | 27.5 | 23.2 | 289.9 | 122.5 |
| 2 | 3 | 1.7 | 17.5 | 187.5 | 43.5 | 288.8 | - |
| 2 | 5 | 1.9 | 27.5 | 202.5 | 41.3 | 320.4 | 112.5 |
| 2 | 6 | 2.1 | 27.5 | 207.5 | 37.6 | 302.5 | - |
| 2 | 8 | 1.8 | 22.5 | 202.5 | 21.7 | 288.3 | - |
| 2 | 9 | 2.0 | 12.5 | 207.5 | 29.7 | 297.5 | - |
| 2 | 10 | 1.6 | 27.5 | 197.5 | 47.0 | 312.3 | - |
| 2 | 11 | 1.7 | 22.5 | 202.5 | 25.6 | 309.9 | 112.5 |
| 2 | 12 | 1.4 | 7.5 | 202.5 | 25.5 | 318.4 | |
| 2 | 14 | 1.7 | 2.5 | 202.5 | 24.5 | 298.5 | 112.5 |
| 2 | 16 | 1.5 | 12.5 | 207.5 | - | - | - |
| 3 | 1 | 1.7 | 7.5 | 212.5 | 37.9 | 304.3 | 127.5 |
| 3 | 3 | 2.0 | 17.5 | 52.5 | 42.3 | 330.0 | 122.5 |
| 3 | 6 | 1.5 | 17.5 | 197.5 | 38.1 | 306.2 | - |
| 3 | 7 | 2.6 | 17.5 | 192.5 | 40.1 | 309.3 | 117.5 |
| 3 | 8 | 2.0 | 17.5 | 202.5 | 29.3 | 312.0 | - |
| 3 | 9 | 2.1 | 17.5 | 202.5 | 22.0 | 307.6 | 117.5 |
| 3 | 11 | 1.7 | 22.5 | 212.5 | 16.6 | 304.2 | - |
| 3 | 12 | 1.7 | 17.5 | 222.5 | 1.6 | 312.0 | - |
| 4 | 1 | 1.7 | 12.5 | 167.5 | 10.7 | 252.9 | - |
| 4 | 2 | 1.7 | 2.5 | 202.5 | 15.1 | 290.7 | 117.5 |
| 4 | 4 | 1.9 | 17.5 | 177.5 | 33.6 | 262.6 | - |
| 4 | 5 | 2.1 | 22.5 | 22.5 | 15.4 | 296.1 | 112.5 |
| 4 | 7 | 1.0 | 12.5 | 17.5 | 4.3 | 265.2 | - |
| 4 | 8 | 1.6 | 17.5 | 17.5 | 9.8 | 119.7 | - |
| 4 | 9 | 1.7 | 7.5 | 7.5 | 35.4 | 274.1 | - |
| 4 | 11 | 1.7 | 2.5 | 207.5 | 6.9 | 101.7 | - |
| 4 | 12 | 1.9 | 7.5 | 202.5 | 31.5 | 297.2 | - |
| 4 | 13 | 1.0 | 12.5 | 182.5 | 10.9 | 282.9 | - |
| 4 | 15 | 2.1 | 12.5 | 207.5 | 26.8 | 298.7 | - |
| 4 | 16 | 1.8 | 7.5 | 197.5 | 8.7 | 284.8 | - |
| 4 | 18 | 1.7 | 12.5 | 2.5 | 29.7 | 269.1 | 117.5 |
| 4 | 24 | 1.9 | 2.5 | 197.5 | 18.7 | 286.9 | - |
| 4 | 25 | 1.6 | 12.5 | 182.5 | 25.0 | 269.5 | - |

*Middle value of 5° interval for which the data was measured.

# Chapter 3. Model validation for MLE logistic regression on cyclic data using bootstrapping.

# Abstract

Motivated by common chi-squared assumptions made for the modelling of logistic regressions, we investigate the distribution of logistic regression parameters and model goodness-of-fit for binary data with cyclic sampling properties using the bootstrap. Two re-sampling methods for the bootstrap are demonstrated, illustrating and compensating for the effects which sparse sampling can have on the distributions of the model fit and logistic parameters. For non-sparse data, we demonstrate the inadequacy of the chi-squared assumption for the logistic model fit, whilst providing more realistic and robust bootstrapped confidence intervals for the logistic model parameters.


# 1 Introduction

In this paper, methods for estimating binomial variables with cyclic properties are investigated using the parametric bootstrap. The motivation for developing this method was provided by Upton et al. (2003) who developed a method of cyclic logistic regression using maximum likelihood estimation (MLE) for modelling this type of data. They based confidence intervals for the model parameters on the model deviance using a chi-squared distribution with one degree of freedom, and based a goodness-of-fit test on a chi-squared distribution with degrees of freedom equal to the number of sampling orientations minus the number of model parameters. However, a $\chi^2$ distribution for a model is only exact for normal (Gaussian) models and, in general, does not provide a very good approximation for the sampling distribution (Dobson 1990). To better approximate the distribution of the model fit, we utilise the parametric bootstrap.

The bootstrap approach can have several complications arising from sampling inadequacy (Efron & Tibshirani 1993); however, once this issue is overcome, more robust and realistic estimates can be derived for model parameters and overall model fit. Here we illustrate a method of employing bootstrapping for the MLE of the cyclic logistic regression to obtain robust estimates of the variability of the model parameters and the goodness-of-fit of the model. Examples from geological settings are used.

# 2 Geological Background

The geological problem of measuring the trend of a linear fabric in rocks, the foliation intersection or inflection axis (*FIA*) preserved within porphyroblasts, was examined by Upton et al. (2003) and is revisited here. FIA are the axes of curvature of surfaces (*inclusion trails*) overgrown by and preserved inside of mineral grains (*porphyroblasts*) that are large compared to the smaller sizes of grains in the surrounding matrix (Fig. 1). It has been proposed that FIA record the orientation of fold axes that existed when the porphyroblasts grew (Hayward 1990).

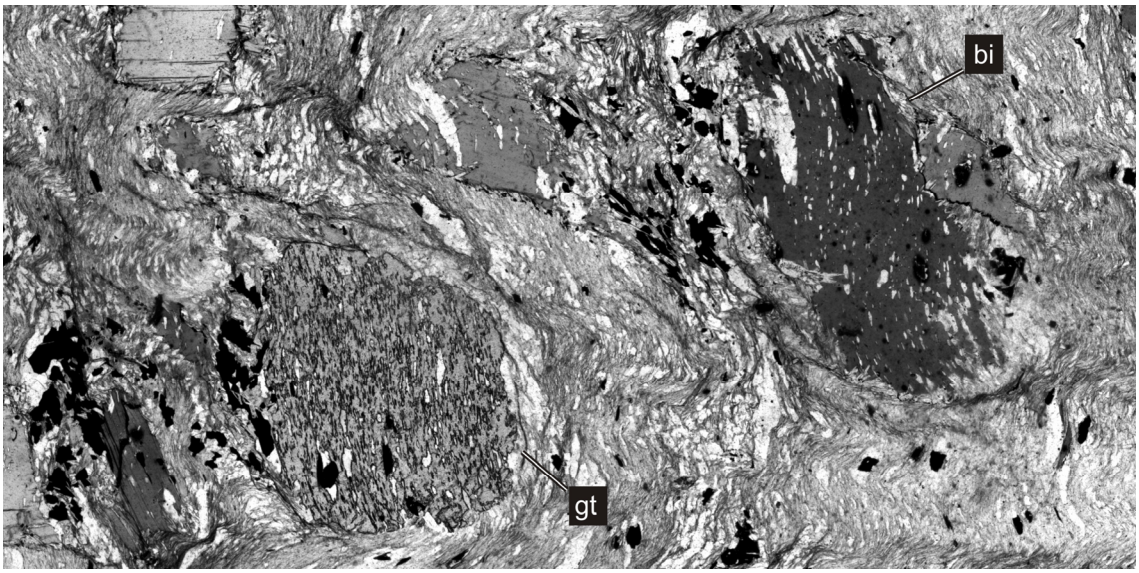


**Figure 1.** This is a photomicrograph of a vertical thin section of schistose rock containing garnet (gt) and biotite (bi) porphyroblasts. Both the garnet and biotite contain inclusion trails, made up of elongate quartz grains, which have an anticlockwise or "Z" shaped asymmetry. The foliation in the matrix is defined by the alignment of quartz and mica and is approximately vertical. The bottom edge of the image is approximately 8mm long.

Furthermore, the orientation of these axes may reflect the relative motion of the tectonic plates that form the Earth's crust (Bell et al. 1995). These axes are of considerable interest to geologists and methods for their statistical analysis are important.

The FIA orientation in a single porphyroblast reflects that of the foliations (sub-planar alignment of matrix grains) in the rock that the inclusion trails preserve. Their orientations vary between porphyroblasts within a rock sample. FIA are three-dimensional data with a spherical distribution; however, geologists are most interested in their trend in a horizontal plane reducing the problem to two dimensions. It is generally not possible to measure the FIA in individual porphyroblasts, so the method used provides an estimate of the mean trend of the FIA in a given rock sample. The asymmetry method relies on the fact that a simple asymmetrically folded surface with a sub-horizontal axis will appear to have opposite asymmetries when cut by two vertical planes that strike either side of the fold axis (Bell et al. 1998). The fold asymmetry appears anticlockwise in one ("Z", left side of Fig. 2a) and clockwise in the other ("S", right side of Fig. 2a). Note that both these planes are being viewed in the same direction – clockwise about a vertical axis. Curved inclusion trails preserved in porphyroblasts are analogous to such a fold. Figure 2b-h shows how this concept is applied to measuring FIAs. Geologists prepare thin slices of rock (*thin sections*) that can be examined with an optical microscope. The asymmetries of inclusion trails in porphyroblasts intersected by the thin section are recorded. The FIA trend is recorded as being the midway point between the two vertical thin-sections with a close

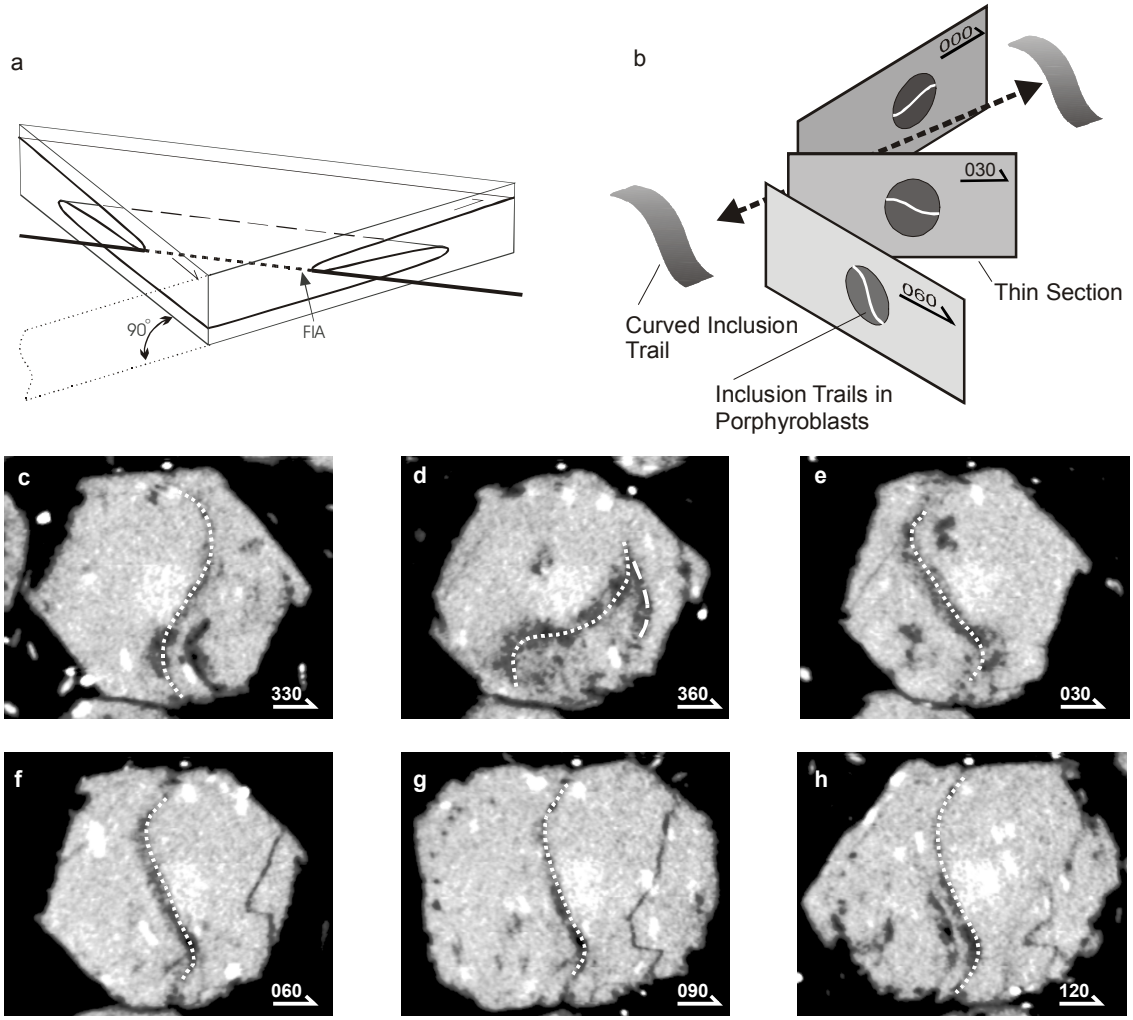


**Figure 2.** An illustration of what FIA are and the asymmetry method used to determine them. A slab of "rock" with an asymmetrically folded surface is shown in (a), cut by two vertical sections 90º apart. The fold asymmetry appears anticlockwise in the section one on the left ("Z" shaped) and clockwise in the section on the right hand side ("S" shaped). The FIA must lie between these sections (modified from Bell et al. 1998). (b) shows how the asymmetry method is applied in thin sections. Three sections are shown spaced at 30º, with the FIA axis between the 0º and 30º sections. The dark grey circle represents a porphyroblast with the inclusion trail asymmetry shown in white, flipping from clockwise in the 0º to anticlockwise in the 30º and 60º sections. An example from the V209 sample is shown in (c) to (h). These are sections at 30º radial increments through X-ray CT data for a single porphyroblast (light grey). The dotted white lines highlight the inclusion trails; they switch asymmetry from anticlockwise to clockwise between the 360º and 30º sections.

angular spacing where the observed dominant asymmetry switches. Sections are typically cut at a 10˚ angular spacing in the vicinity of the FIA.

High Resolution X-ray Computed Tomography (HRXCT) has been used to measure the FIA in 58 porphyroblasts from a single sample in chapter 1. A set of asymmetry observations was derived from this dataset in order to test the MLE cyclic logistic regression. The asymmetry was determined in each individual porphyroblast sectioned at 10 ° increments from 0° to 170°

| Orientation | Clockwise | Anticlockwise | Total |
|---|---|---|---|
| 0 | 2 | 56 | 58 |
| 10 | 11 | 47 | 58 |
| 20 | 24 | 34 | 58 |
| 30 | 50 | 8 | 58 |
| 40 | 56 | 2 | 58 |
| 50 | 57 | 1 | 58 |
| 60 | 58 | 0 | 58 |
| 70 | 58 | 0 | 58 |
| 80 | 58 | 0 | 58 |
| 90 | 58 | 0 | 58 |
| 100 | 58 | 0 | 58 |
| 110 | 58 | 0 | 58 |
| 120 | 58 | 0 | 58 |
| 130 | 58 | 0 | 58 |
| 140 | 58 | 0 | 58 |
| 150 | 58 | 0 | 58 |
| 160 | 58 | 0 | 58 |
| 170 | 57 | 1 | 58 |

**Table 1** Asymmetry data based on 58 FIA measurements from HRXCT data from sample V209.

and the results are shown in table 1. Deriving the asymmetry data in this manner simulates the way that it is normally collected using the asymmetry method. In addition, the data used by Upton et al. (2003) is also re-examined.

# 3 Cyclic Logistic Regression

Measurements of FIA orientations are characterised by asymmetry counts on an angular region of periodicy of π. Further symmetry of the counts occurs through a reflection about the axis of the FIA. If we define μ as the direction of the FIA and $\theta_i$ as the $i^{th}$ orientation from north, then the following properties apply regarding the probability, $P(\theta_i) = \varpi_i$, of observing a clockwise inclusion trail geommetry as opposed to an anti-clockwise one:

$$P(\theta_i - \mu) = P(\theta_i - \mu + \pi) = 1 - P(\mu - \theta_i) \tag{1}$$

with $0 \le \mu < \pi, 0 \le \theta_i < \pi$ and $P(\theta_i - \mu)$ monotonically decreases (or increases) from $P(\pm\pi/2) = 1$ to $P(\mp\pi/2) = 0$ with $P(0) = 1/2$. Thus, the probability of observing a positive asymmetry (clockwise) at an angle $\theta_i$ is symmetric and cyclic about $\mu$. Following Upton et al. (2003), the logistic regression with a sinusoidal transform to model $P(\theta_i - \mu)$ is used to model π cyclic effects.

$$x_i = \sin(\theta_i - \mu) \tag{2}$$

The logistic function is then used to model the probability of observing a particular asymmetry.

$$P(x_i) = \frac{1}{1 + e^{\beta x_i}} \tag{3}$$

# 4 Maximum Likelihood Estimation

Given a specified model, $P(\boldsymbol{\theta} \mid \boldsymbol{\phi})$ with parameters $\boldsymbol{\phi}$, observed data, $\boldsymbol{\theta}$ and joint probability density function $L(\boldsymbol{\phi} \mid \boldsymbol{\theta})$, the maximum likelihood estimator, $\hat{\boldsymbol{\phi}}$, is defined as

$$L\left(\hat{\boldsymbol{\phi}} \mid \boldsymbol{\theta}\right) \geq L(\boldsymbol{\phi} \mid \boldsymbol{\theta}); \forall \boldsymbol{\phi} \in \Theta, \tag{4}$$

where $\Theta$ represents all possible values of $\boldsymbol{\phi}$. Given $L(\boldsymbol{\phi} \mid \boldsymbol{\theta})$ the data is treated as fixed and $\boldsymbol{\phi}$ as a variable parameter(s). The value for $\hat{\boldsymbol{\phi}}$ that maximises the joint probability of the data is sought.

For count type data the model can generally be defined as $P(\boldsymbol{\theta}_i \mid \boldsymbol{\phi}) = \varpi_i$, where $\varpi_i$ is the probability of a success (e.g. clockwise observation) on the $i^{\text{th}}$ orientation. If there are $r_i$ successes out of a total number observations at the $i^{th}$ position, $n_i$, then the joint probability function is (Dobson 1990)

$$L(\boldsymbol{\phi} \mid \boldsymbol{\theta}) = \prod_{i=1}^{m} \varpi_i^{r_i} \left(1 - \varpi_i\right)^{n_i - r_i}; \quad i = 1 \ldots m \tag{5}$$

Equally, the value $\hat{\boldsymbol{\phi}}$ that maximises Eqn. 5 is also the value that maximises the log-likelihood function so that $\ell(\boldsymbol{\phi} \mid \boldsymbol{\theta}) = \log\left(L(\boldsymbol{\phi} \mid \boldsymbol{\theta})\right)$ since the logarithmic function is monotonic. Thus

$$\ell\left(\hat{\boldsymbol{\phi}} \mid \boldsymbol{\theta}\right) \geq \ell(\boldsymbol{\phi} \mid \boldsymbol{\theta}); \forall \boldsymbol{\phi} \in \Theta \tag{6}$$

and the equivalent expression for Eqn (5) is

$$\ell(\boldsymbol{\phi} \mid \boldsymbol{\theta}) = \sum_{i=1}^{m} \left\{ r_i \log(\varpi_i) + (n_i - r_i) \log\left(1 - \varpi_i\right) \right\} \qquad i = 1 \ldots m \tag{7}$$

Commonly, it is easier to work (optimise) the log-likelihood function than the likelihood function itself. For the above cyclic logistic regression model in Eqn. (3), the log likelihood function is

$$\ell(\beta, \mu \mid \theta) = \sum_{i=0}^{m} r_i \sin(\theta_i - \mu)\beta - n_i \left( \sin(\theta_i - \mu)\beta + \ln\left(1 + e^{\beta \sin(\theta_i - \mu)}\right) \right) \tag{8}$$

where $r_i$ is the number of clockwise orientations out of a total number of observations, $n_i$, at orientation $\theta_i$. The maximum of Eqn. (4) corresponds to the most likely values $\left(\hat{\beta},\hat{\mu}\right)$ given the data $\boldsymbol{\theta}$.

Using MLE, an estimate of both the distribution of the model parameters and the goodness-of-fit can be determined based on a measure called deviance. Deviance is calculated as the relative change in the log-likelihood value with reference to a null hypothesis, which is usually the maximised model for parameter distributions or the saturated model for goodness-of-fit estimation. Typically, the deviance, D, is *assumed* to asymptotically follow a $\chi_p^2$ distribution with *p* degrees of freedom. Here *p* is the difference between the number of orientations and the number of model parameters.

For the goodness-of-fit,

$$^{G}D = 2\left(\ell^*\left(\boldsymbol{\theta}\right) - \ell\left(\hat{\boldsymbol{\phi}}\,|\,\boldsymbol{\theta}\right)\right) \tag{9}$$

where $\ell^*\left(\boldsymbol{\theta}\right)$ is the saturated model. In the case of the cyclic logistic regression the model is given by

$$\ell^*\left(\boldsymbol{\theta}\right) = \sum_{i=1}^{m}\left\{r_i\log\left(r_i\right) + \left(n_i - r_i\right)\log\left(n_i - r_i\right) - n_i\log\left(n_i\right)\right\}. \tag{10}$$

$^{G}D$ is assumed to follow a $\chi_p^2$ distribution with $p = m - 2$ degrees of freedom. This assumes that under the null hypothesis the *m* orientations are independent with a standard deviation equal to 1 (Dobson, 1990).

The distribution of the model parameters, $^{M}D$, is given by

$$^{M}D = 2\left(\ell\left(\hat{\boldsymbol{\phi}}\,|\,\boldsymbol{\theta}\right) - \ell\left(\boldsymbol{\phi}\,|\,\boldsymbol{\theta}\right)\right). \tag{11}$$

$^{M}D$ is assumed to follow a $\chi_p^2$ distribution with $p = 1 or 2$ degrees of freedom, depending on whether either $\beta or \mu$ are fixed $\left(p = 1\right)$ or allowed to vary simultaneously $\left(p = 2\right)$.

The maximization of $\ell\left(\boldsymbol{\phi}\,|\,\boldsymbol{\theta}\right)$ is the equilivant of the minimization of $-\ell\left(\boldsymbol{\phi}\,|\,\boldsymbol{\theta}\right)$. We employed the quasi-Newton optimizer in Matlab to perform this operation.

# 5 Bootstrap

The fundamental principle of the bootstrap is that a resample *with replacement* of a random sample from a certain population is considered to be a random sample of that population (Efron & Tibshirani 1993). Thus, the collected data can be re-sampled multiple

times and empirical distributions of population parameters (such as the mean) can be obtained, rather than relying on asymptotic assumptions about the data.

In the classical non-parametric bootstrap by Efron and Tibshirani (1993), re-sampling of the original sample, $\boldsymbol{\theta}^0$, is done with replacement such that the bootstrapped sample, $\boldsymbol{\theta}^j$, is the same size as the original data. That is, if there are *k* observations in $\boldsymbol{\theta}^0$, then $\boldsymbol{\theta}^0$ is sampled *k* times with replacement to form $\boldsymbol{\theta}^j$. In total, *B* bootstrapped samples are formed from which empirical distributions of the population parameters can be derived. In the case of MLE cyclic logistic regression, the distributions $\hat{F}_\beta(\theta), \hat{F}_\mu(\theta) and\ \hat{F}_{G_D}$ for the cyclic logistic regression parameters $\beta, \mu$ and ${}^G D$ respectively are important.

For each of the *B* bootstrapped samples $\boldsymbol{\theta}^j, j = 1 \ldots B$, MLE is used to calculate $\beta^j, \mu^j$ and ${}^G D^j$ using Eqns. (8-10), where $r_i$ and $n_i$ are from $\boldsymbol{\theta}^j$. Using these *B* estimates, the empirical distributions, $\hat{F}_\beta(\theta_i), \hat{F}_\mu(\theta_i) and\ \hat{F}_{G_D}$, are formed and from them the respective confidence intervals for $\beta, \mu$ can be found.

There are three primary methods that can be used to calculate confidence intervals (CI) using bootstrap methods: (1) CI based on *t*-tables; (2) the percentile method; and (3) the percentile method adjusted for bias and acceleration ($BC_a$). In this paper we provide CI based on the percentile and $BC_a$ methods as they tend to be more robust CI estimates (Efron & Tibshirani 1993).

To summarize, the percentile method sorts the bootstrapped values in ascending order and selects the $100 \cdot \alpha^{th}, \alpha \in (0,1)$, interval, $\left[\phi_L^{\alpha/2}, \phi_H^{\alpha/2}\right]$, such that $1-\alpha/2$ percent of the values are above and below the CI. Let $\hat{C}$ be the cumulative distribution function of $\hat{\phi}^j$. Thus

$$\hat{C}(\phi) = \int_{-\infty}^{\phi} \hat{F}(t)\, dt \tag{12}$$

and the $1-\alpha/2$ percentile interval is

$$\left[\phi_L^{\alpha/2}, \phi_H^{\alpha/2}\right] = \left[\hat{C}^{-1}(\alpha/2), \hat{C}^{-1}(1-\alpha/2)\right] \tag{13}$$

The BCa method is similar to the percentile method; however, a correction to the upper and lower $\alpha$ values, $\alpha^1, \alpha^2$, is made to allow for bias and acceleration in $\hat{F}_i(t_i)$ from a normal distribution. The values for $\alpha^1, \alpha^2$ are given by

$$\alpha^1 = \Phi\left(\hat{z}_0 + \frac{\hat{z}_0 + z^{(\alpha)}}{1-\hat{a}\left(\hat{z}_0 + z^{(\alpha)}\right)}\right)$$
$$\alpha^2 = \Phi\left(\hat{z}_0 + \frac{\hat{z}_0 + z^{(1-\alpha)}}{1-\hat{a}\left(\hat{z}_0 + z^{(1-\alpha)}\right)}\right) \quad (14)$$

where $\Phi(\cdot)$ is the standard normal cumulative distribution function and $z^{(\alpha)}$ is the $100\cdot\alpha^{th}$ percentile point of a standard normal distribution. The value $\hat{z}_0$ is a bias correction term approximated by the bootstraped samples:

$$\hat{z}_0 = \Phi^{-1}\left(\frac{\#\left\{\hat{\phi}^j < \hat{\phi}^0\right\}}{B}\right) \quad (15)$$

where $\hat{\phi}^0$ is the MLE from the original data. In addition, in Eqn (14), the term $\hat{a}$ corresponds to the acceleration, which for one parameter estimate, can be approximated by $\hat{z}_0$ to the second order.

Both of the above CI methods, and bootstrapping in general, are the result of the central limit theorem where $\hat{F}_\beta(\theta_i)$ and $\hat{F}_\mu(\theta_i)$ are approximately normal as *n,* the total sample size of the original data, gets large. This also raises the question of adequate sampling since if *n* is too small, the bootstrap method will produce biased estimates for $\hat{F}_\beta(\theta_i)$ and $\hat{F}_\mu(\theta_i)$ (Efron & Tibshirani 1993).

In this investigation, two methods for re-sampling are considered. The first resampling method (method A) consists of resampling on all observations irrespective of the orientation, while the second method (method B) resamples within each orientation. For example, if our data consisted of two orientations with 10 and 20 observations in each orientation $n_1$ and $n_2$ respectively, then for method A, each bootstrap sample will have 30 observations, however $n_1$ may or may not equal 10. For method B, $n_1$ will equal 10 since for the bootstrap sample the resampling is performed on each orientation individually.

The two bootstrap methods were investigated to determine the effect that sparse data would have. Method (A) treats all observations equally and can result in bootstrap samples that have no data in some orientations. In some cases, as in those provided by Upton et al. (2003) where for most orientations there is only one observation per orientation, the data is sparse. In these situations, the variability in the bootstrap samples using method A is largely due to the variation in the probability that the orientation(s) are sampled and not the variation of binomial probability at each orientation. Thus the distributions of $\beta$ and $\mu$ are more reflective of how

the model parameters vary as the sampling distributions of the orientations vary near the FIA. Method (B) eliminates this effect by ensuring each orientation is represented in the bootstrap samples. However, for very sparse data, it may not be possible to employ method B since redrawing one observation from a sample size of one (per orientation) will result in the exact same sample and thus no variation in the cyclic logistic regression parameters.

For data rich samples, where the binomial variability can be estimated through resampling, the variation in the cyclic logistic regression parameters resulting from method A or B will be largely influenced by the binomial variation, rather than the distribution of sampling orientations.

# 6 Results and Discussion

Table 2 shows the results of the analysis of the data presented in Upton et al. (2003) using the chi-squared method and the two bootstrap methods. The confidence intervals for all methods exhibit broad similarities for $\beta$ and $\mu$, with the exception of the CA1 Rim and CA1 Core data. In the CA1 Rim, the CI from the method A bootstrap is substantially wider than that from the other methods. Due to the lack of sampling within orientations for the CA1 Core data, method B only generates one unique bootstrap sample, and hence results in a nil variation in $\beta$ and $\mu$.

| | | | | CA1 | Rim | Middle | Core | Rim* |
|---|---|---|---|---|---|---|---|---|
| | | | *n* | | 16 | 27 | 21 | 16 |
| | | | *m* | | 10 | 14 | 12 | 10 |
| | | | *μ* | | 49 | 19 | 74 | 50 |
| | | | *ß* | | 92.13 | 3.48 | 3.54 | ~168 |
| | | | $^{G}D$** | | 0 | 8.5 | 17.72 | 0 |
| *99% Confidence intervals* | | *Upton* | *μ* | | (47,51) | (351,57) | (37,112) | (28,67) |
| | | | *ß* | | - | (1.13,8.41) | (0.67,9.24) | (2.53,>800) |
| | *Bootstrap Method A* | *BCa* | *μ* | | - | (5.4,84.0) | (33.6,89.6) | (34.8,84.4) |
| | | | *ß* | | - | (0.92,111) | (-0.41,451) | (115,781) |
| | | *Percentiles* | *μ* | | - | (355,63.5) | (40.2,97.7) | (26.1,70.8) |
| | | | *ß* | | - | (1.51,760) | (1.55,685) | (88.2,634) |
| | *Bootstrap Method B* | *BCa* | *μ* | | - | (10.5,52.2) | NA | (45.1,49.7) |
| | | | *ß* | | - | (1.72,118) | NA | (133,132) |
| | | *Percentiles* | *μ* | | - | (0,44.8) | NA | (45.1,56.2) |
| | | | *ß* | | - | (1.77,776) | NA | (132,577) |

* Results for MLE and CI for Rim data reprocessed using more accurate maximization techniques than those used in Upton et al. (2003).
** $^{G}D$ is equivalent to Upton's "C".

**Table 2.** Results for the CA1 Core, Middle and Rim data for the data presented in Upton et al. (2003). Confidence intervals for model parameters could not be calculated for the core data using bootstrap method B as only one permutation of the data is possible. In all cases 5000 bootstrap resamples were made.

The Core, Mid and Rim data are all sparsely sampled. This has produced three unique results with bootstrapping and the Chi-Squared approximation. To assess the model validity, we examine the empirical distributions of $\beta$ and $\mu$ and the model deviance in Figures 3 and 4, which, theoretically, should be approximately normal for $\beta$ and $\mu$ and $\chi^2$ for the model deviance. Excessive deviation from the normal distribution is evident and is a result of inadequate sampling. For method A, the bootstrap on this sparse data is not adequately modelling the variability in the binomial probability at each orientation; it is modeling the probability that the orientation(s) are sampled instead. Thus the distributions of $\beta$ and $\mu$ are more reflective of how the model parameters vary as the sampling distributions of the orientations vary. Method B will not be affected in this way, as the probability of an orientation being sampled is invariant. However, it is affected by the sparse nature of the data in that a small number of unique data permutations are generated from the 5000 bootstrap samples (4, 60 and 1 for the CA1 Rim, Mid and Core data respectively).

In the case of the CA1 Mid data, the relative frequencies of the 60 permutations tend towards a normal distribution for $\mu$; the distribution for $\beta$ is also approaching a more central distribution (see inset in Fig. 4b) although it has outliers that distort it. The deviance shows a limiting $\chi^2$ distribution. The CA1 Core data shows the opposite extreme with the paucity of the data resulting in only one possible permutation, therefore acting as a point estimator for $\beta$ and $\mu$. Only the method B bootstrap of the CA1 Mid data demonstrates an adequate model fit.

Table 3 shows the results for the combined data (Upton et al. 2003) and the v209 data. There is good agreement between all three methods and the model parameters clearly exhibit asymptotic normality (Figure 5); this demonstrates both adequate data sampling and model fit (see also figure 6a-b). However, there is one main discrepancy in assessing the model fits between the bootstrapping procedures and the $\chi^2$ approach; this is the determination of the appropriate degrees of freedom of the model deviance. The degrees of freedom of the model deviance for the v209 and combined data are estimated to be approximately 5 and 12 respectively (Fig. 5). According to the classical $\chi^2$ approach, the degrees of freedom would be 16 and 15 ($m$-2) respectively.

The discrepancy in the degrees of freedom for the model fit can be attributed to dependence of the log-likelihood deviance on variation at each orientation. In Upton (2003), the assumption of unit independence of the sampling orientations in the logistic model gives rise to the approximation of a $\chi^2$ fit with m-2 degrees of freedom. This assumption of independence is not the case here, as the correlations of deviance between orientations are substantially different from zero (Table 4). If there were independence between orientations,

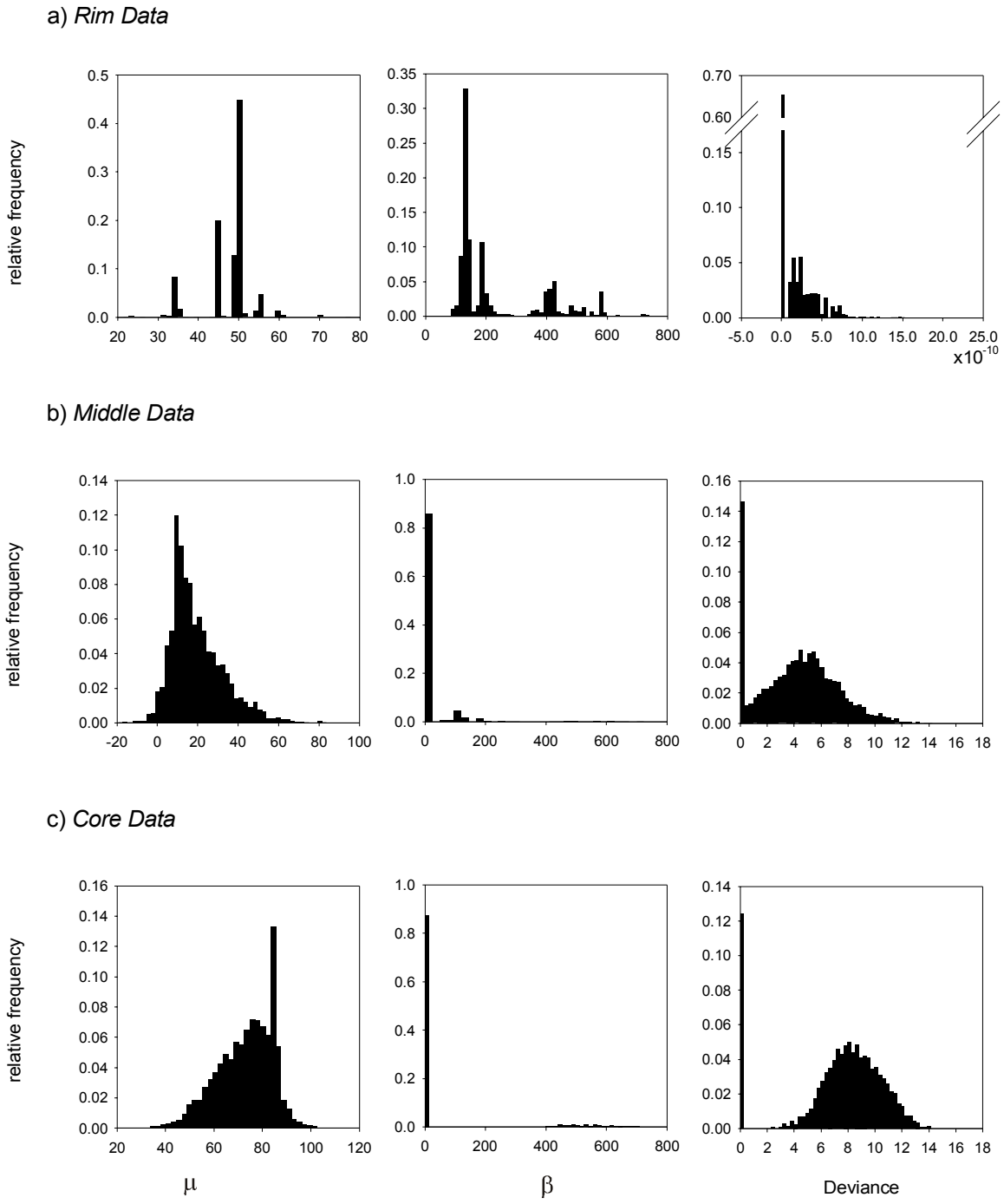


**Figure 3.** Bootstrapped empirical distributions of $\beta$, $\mu$ and deviance for (a) the CA1 Rim, (b) CA1 Middle and (c) CA1 Core data from Upton et al. (2003) using Bootstrap method A with 5000 bootstraps. $\beta$ and $\mu$ do not show normal distributions for any of the data.

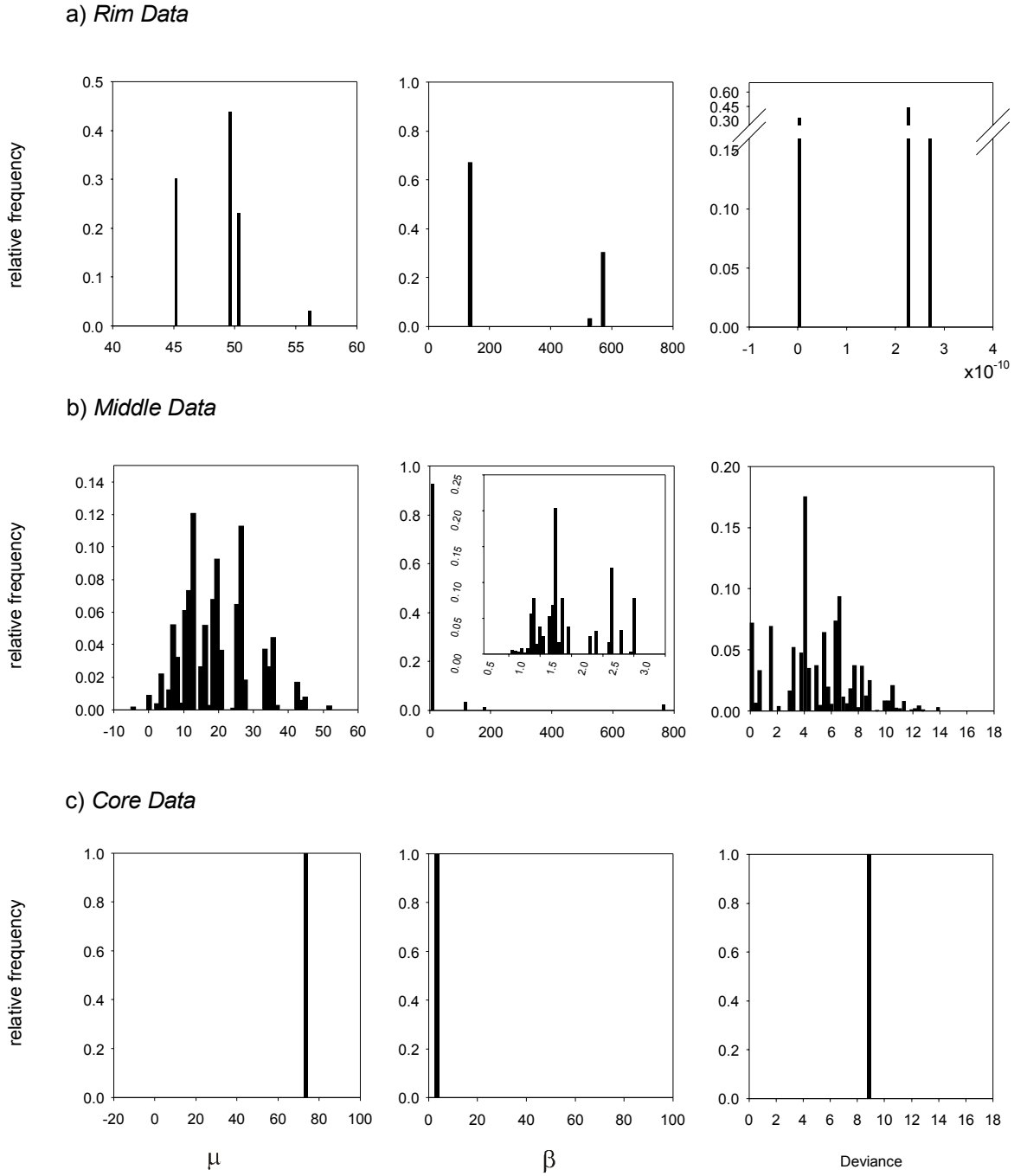


**Figure 4.** Bootstrapped empirical distributions of $\beta$, $\mu$ and deviance for (a) the CA1 Rim, (b) CA1 Middle and (c) CA1 Core data from Upton et al. (2003) using Bootstrap method B with 5000 bootstraps. Note the limited number of permutations, particularly for the Rim and Core data.

| | | | | CA1 All | V209 |
|---|---|---|---|---|---|
| | | | *n* | 64 | 986 |
| | | | *m* | 17 | 18 |
| | | | *μ* | 50 | 20.4 |
| | | | ß | 2.85 | 9.39 |
| | | | $^{G}D$** | 14.53 | 3.79 |
| *99% Confidence intervals* | | *Upton* | *μ* | (28,71) | (17.5,23.3) |
| | | | ß | (1.46,4.74) | (7.38,12.02) |
| | *Bootstrap Method A* | *BCa* | *μ* | (27.6,72.5) | (17.6,23.0) |
| | | | ß | (1.12,3.98) | (7.25,11.51) |
| | | *Percentiles* | *μ* | (27.5,72.3) | (17.7,23.0) |
| | | | ß | (1.71,5.54) | (7.73,12.36) |
| | *Bootstrap Method B* | *BCa* | *μ* | (28.7,67.3) | (17.6,23) |
| | | | ß | (1.38,3.92) | (7.16,11.5) |
| | | *Percentiles* | *μ* | (29.2,67.8) | (17.6,23.0) |
| | | | ß | (1.91,4.87) | (7.72,12.3) |

** $^{G}D$ is equivalent to Upton's "C".

**Table 3.** Results for the combined CA1 data in Upton et al. (2003) and for sample V209. 25000 bootstrap resamples were made in each case.

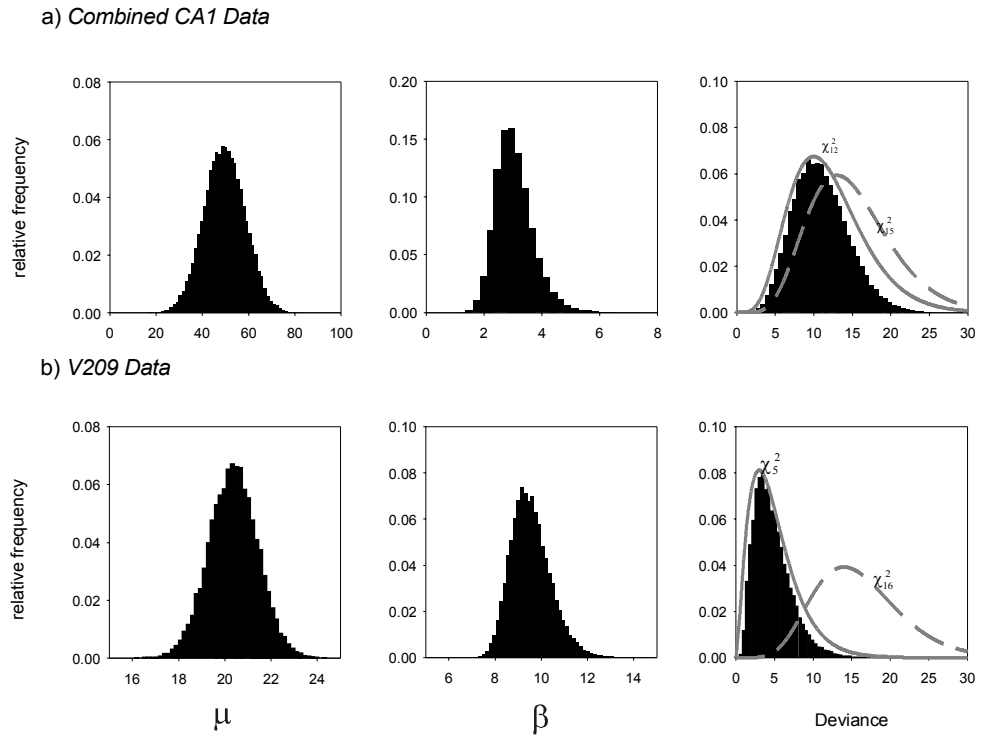


**Figure 5.** Bootstrapped empirical distributions of $\beta$, $\mu$ and deviance for (a) the combined CA1 data from Upton et al. (2003), and (b) sample V209 using Bootstrap method A with 25000 bootstraps. The distributions of $\beta$ and $\mu$ show normal and log-normal distributions respectively. For the deviance plots, the best fitting $\chi^2$ distributions are shown with solid lines and the $\chi^2$ distributions with *m*-2 degrees of freedom are shown with dashed lines.

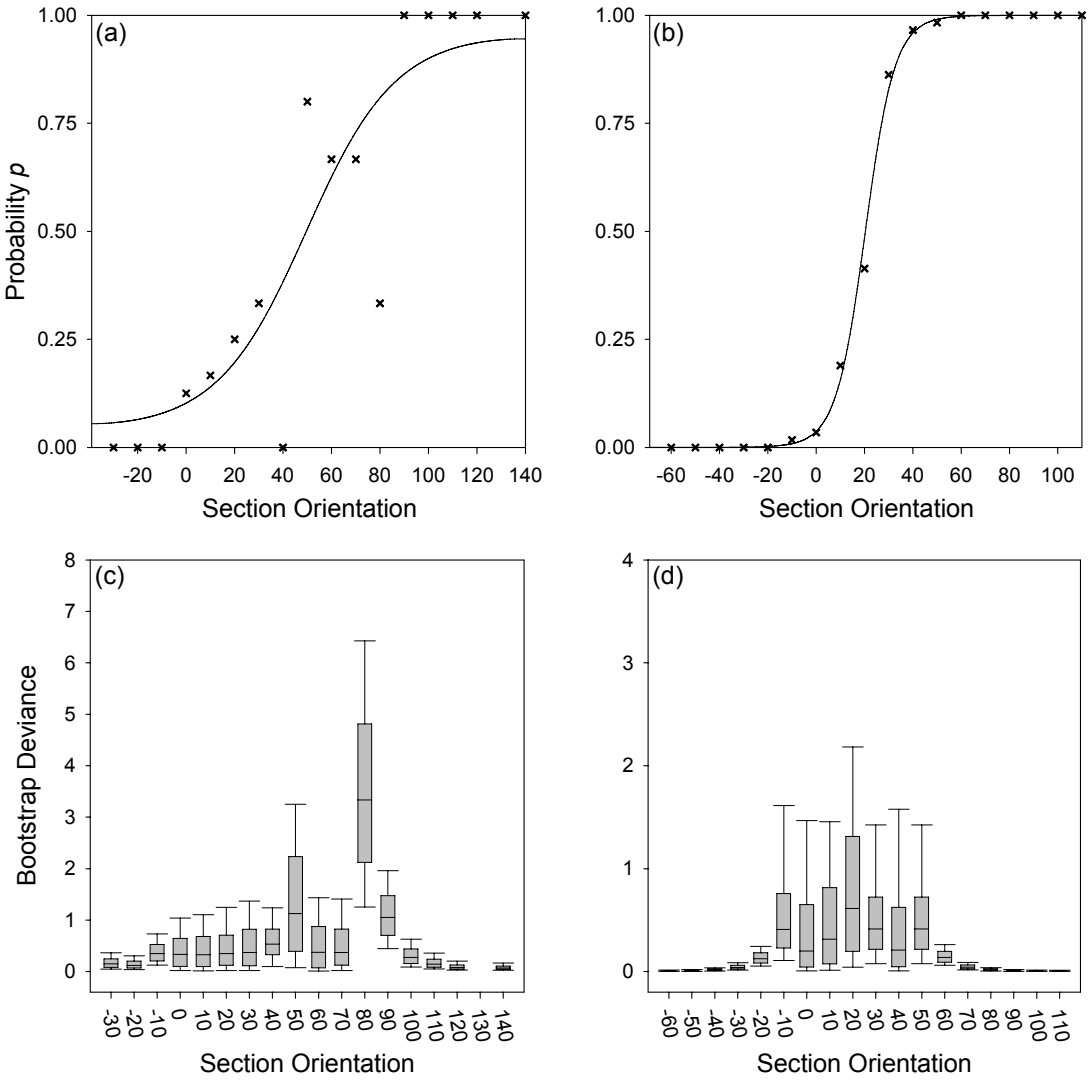


**Figure 6.** Probability plots showing the fit of the models to the observed probabilities (crosses) for (a) the combined CA1 data from Upton et al. (2003), and (b) V209 data. Box plots of bootstrap deviance are shown in (c) and (d). The V209 has fewer section orientations with significant deviance.

the correlations would be approximately zero. Furthermore, the variability for each orientation is non-uniform as orientations further away from the FIA will have very little or no variability as compared to those closest to the FIA, as shown in Figure 6e-f. These results suggest that the goodness-of-fit test of Upton et al. (2003) is flawed. They assume that there are two fixed parameters ( $\beta$ and $\mu$ ) and that the probability of success can vary in each of *m* orientations; this is clearly not the case.

# 7 Conclusions

We examined methods for assessing the validity of logistic models for cyclic data, using bootstrapping methods. We have demonstrated that the goodness-of-fit test prescribed by Upton et al. (2003) is inappropriate because it does not adjust the degrees of freedom to take into account the dependencies within the model that contribute towards the model deviance.

In assessing the validity of the bootstrapped model estimates, we recommend examining the distributions of $\beta$ and $\mu$ as well as the deviance. Primarily, the distributions of $\beta$ and $\mu$ should be approximately normal, and, secondly the deviance distribution should approximate a $\chi^2$ type distribution. Further work to determining the null distribution of partially dependant deviance is still required to ascertain a formal test for the model goodness-of-fit. When determining the confidence intervals for $\beta$ and $\mu$, we recommend using the percentile method unless the distributions of $\beta$ and $\mu$ show departure from normality; in this case the $BC_a$ method should be used.

In employing bootstrapping techniques we encountered challenges using the sparse data used by Upton et al. (2003). In some circumstances the data was too sparse to assess model validity using the bootstrap. In others the resampling method for the bootstrap had a substantial influence in determining model validity. For our data we found that:

- For sparse data with $n_i = 1$, bootstrap on all observations (Method A);
- For sparse data with some 5~> $n_i > 1$ near the FIA, bootstrap within the observations (Method B);
- For rich data with $n_i$ ~> 4 for most orientations, bootstrap on all observations (Method A).

Caution must be applied where $n_i <$ ~5 and an indication of whether there is sufficient data can be gained by comparing the bootstrap distributions of $\beta$ and $\mu$, which should approximate a normal distribution.

| Deg | 0 | 10 | 20 | 30 | 40 | 50 | 60 | 70 | 80 | 90 | 100 | 110 | 120 | 130 | 140 | 150 | 160 | 170 |
|---|---|---|---|---|---|---|---|---|---|---|---|---|---|---|---|---|---|---|
| **0** | 1.00 | 0.17 | -0.03 | 0.05 | 0.00 | 0.05 | -0.04 | -0.04 | -0.05 | -0.05 | -0.05 | -0.05 | -0.05 | -0.06 | -0.06 | -0.06 | -0.06 | 0.09 |
| **10** | 0.17 | 1.00 | 0.47 | -0.08 | 0.02 | -0.08 | 0.03 | 0.03 | 0.03 | 0.03 | 0.03 | 0.03 | 0.03 | 0.04 | 0.04 | 0.04 | 0.04 | -0.16 |
| **20** | -0.03 | 0.47 | 1.00 | -0.07 | 0.06 | -0.07 | 0.10 | 0.10 | 0.10 | 0.10 | 0.10 | 0.10 | 0.10 | 0.11 | 0.11 | 0.11 | 0.11 | 0.11 |
| **30** | 0.05 | -0.08 | -0.07 | 1.00 | 0.16 | 1.00 | 0.10 | 0.10 | 0.09 | 0.09 | 0.09 | 0.09 | 0.09 | 0.08 | 0.08 | 0.08 | 0.08 | -0.05 |
| **40** | 0.00 | 0.02 | 0.06 | 0.16 | 1.00 | 0.16 | -0.04 | -0.04 | -0.03 | -0.03 | -0.03 | -0.03 | -0.03 | -0.03 | -0.03 | -0.03 | -0.02 | 0.08 |
| **50** | 0.05 | -0.08 | -0.07 | 1.00 | 0.16 | 1.00 | 0.10 | 0.10 | 0.09 | 0.09 | 0.09 | 0.09 | 0.09 | 0.08 | 0.08 | 0.08 | 0.08 | -0.05 |
| **60** | -0.04 | 0.03 | 0.10 | 0.10 | -0.04 | 0.10 | 1.00 | 1.00 | 0.99 | 0.97 | 0.96 | 0.95 | 0.94 | 0.93 | 0.91 | 0.89 | 0.86 | 0.09 |
| **70** | -0.04 | 0.03 | 0.10 | 0.10 | -0.04 | 0.10 | 1.00 | 1.00 | 1.00 | 0.99 | 0.98 | 0.97 | 0.97 | 0.96 | 0.94 | 0.92 | 0.89 | 0.09 |
| **80** | -0.05 | 0.03 | 0.10 | 0.09 | -0.03 | 0.09 | 0.99 | 1.00 | 1.00 | 1.00 | 0.99 | 0.99 | 0.98 | 0.97 | 0.96 | 0.94 | 0.91 | 0.09 |
| **90** | -0.05 | 0.03 | 0.10 | 0.09 | -0.03 | 0.09 | 0.97 | 0.99 | 1.00 | 1.00 | 1.00 | 1.00 | 0.99 | 0.98 | 0.97 | 0.96 | 0.93 | 0.09 |
| **100** | -0.05 | 0.03 | 0.10 | 0.09 | -0.03 | 0.09 | 0.96 | 0.98 | 0.99 | 1.00 | 1.00 | 1.00 | 1.00 | 0.99 | 0.98 | 0.97 | 0.94 | 0.09 |
| **110** | -0.05 | 0.03 | 0.10 | 0.09 | -0.03 | 0.09 | 0.95 | 0.97 | 0.99 | 1.00 | 1.00 | 1.00 | 1.00 | 1.00 | 0.99 | 0.97 | 0.95 | 0.09 |
| **120** | -0.05 | 0.03 | 0.10 | 0.09 | -0.03 | 0.09 | 0.94 | 0.97 | 0.98 | 0.99 | 1.00 | 1.00 | 1.00 | 1.00 | 0.99 | 0.98 | 0.96 | 0.09 |
| **130** | -0.06 | 0.04 | 0.11 | 0.08 | -0.03 | 0.08 | 0.93 | 0.96 | 0.97 | 0.98 | 0.99 | 1.00 | 1.00 | 1.00 | 1.00 | 0.99 | 0.97 | 0.09 |
| **140** | -0.06 | 0.04 | 0.11 | 0.08 | -0.03 | 0.08 | 0.91 | 0.94 | 0.96 | 0.97 | 0.98 | 0.99 | 0.99 | 1.00 | 1.00 | 1.00 | 0.99 | 0.10 |
| **150** | -0.06 | 0.04 | 0.11 | 0.08 | -0.03 | 0.08 | 0.89 | 0.92 | 0.94 | 0.96 | 0.97 | 0.97 | 0.98 | 0.99 | 1.00 | 1.00 | 1.00 | 0.10 |
| **160** | -0.06 | 0.04 | 0.11 | 0.08 | -0.02 | 0.08 | 0.86 | 0.89 | 0.91 | 0.93 | 0.94 | 0.95 | 0.96 | 0.97 | 0.99 | 1.00 | 1.00 | 0.10 |
| **170** | 0.09 | -0.16 | 0.11 | -0.05 | 0.08 | -0.05 | 0.09 | 0.09 | 0.09 | 0.09 | 0.09 | 0.09 | 0.09 | 0.09 | 0.10 | 0.10 | 0.10 | 1.00 |

**Table 4.** Deviance correlations between sampled orientations for the V209 data.

# References


Bell, T. H., Forde, A. & Wang, J. 1995. A new indicator of movement direction during orogenesis: measurement technique and application to the Alps. *Terra Nova* **V. 7**, 500-508.

Bell, T. H., Hickey, K. A. & Upton, G. J. G. 1998. Distinguishing and correlating multiple phases of metamorphism across a multiply deformed region using the axes of spiral, staircase and sigmoidal inclusion trails in garnet. *Journal of Metamorphic Geology* **16**(6), 767-794.

Dobson, A. 1990. *An Introduction to Generalized Linear Models*. Chapman & Hall, London.

Efron, B. & Tibshirani, R. 1993. *An Introduction to the Bootstrap*. Chapman & Hall, New York.

Hayward, N. 1990. Determination of early fold axis orientations in multiply deformed rocks using porphyroblast inclusion trails. *Tectonophysics* **V. 179**, 353-369.

Upton, G. J. G., Hickey, K. A. & Stallard, A. 2003. Regression models for cyclic data. *Royal Statistical Society Journal. Series C: Applied Statistics.* **52**(Part 2), 227-235.

# Chapter 4. Foliation Intersection Axes in porphyroblasts: Understanding your FIA

# Abstract

A technique that allows the confidence intervals to be assigned to the orientations of foliation intersection/inflection axes in porphyroblasts (FIA) measured by the asymmetry method is presented. Parameters, μ (FIA orientation) and β (shape parameter) for a cyclic logistic regression are calculated using maximum likelihood estimation (MLE). The bootstrapping of MLE of parameters provides confidence intervals and allow the model fit to be assessed, and this is demonstrated using several examples.

Analysis of the sensitivity of the bootstrapped MLE approach to the number of observations per thin section orientation shows that a minimum of 10 are required to produce accurate results. Detailed studies, which compare the orientation of FIA quantitatively, should use this technique so that the inferences can be made with confidence. For regional studies, if the number of samples is sufficient, the distribution of FIA sets (a temporally related grouping of FIA) can be determined without using the bootstrapped MLE approach as the precision of individual measurements is less important. This is because the large sample size reduces the effect of measurement errors. Relative timing criteria and FIA orientations are the best criteria for grouping data into sets. Using microstructural textures as a criterion is totally unreliable because deformation partitioning can result in highly variable distributions of strain from grain to orogen scale.

The distribution of FIAs is similar at both intra-sample and inter-sample scales and is unimodal, symmetrical and have a peak at their mean with probabilities decaying monotonically to either side of it, similar to a normal distribution. The maximum range of FIA orientations in a single set will generally be in the order of 40° to 80°. Consistently grouped FIA distributions suggest that any rotation of porphyroblasts relative to a fixed geographic reference frame is unlikely. The distribution of FIAs actually represents the distribution of the foliations that form them.


# 1 Introduction

FIA (foliation intersection/inflection axes *in porphyroblasts*) are the axes of curvature (or intersection) of foliations preserved as inclusion trails in porphyroblasts; they are interpreted as being equivalent to the intersection lineation between the foliations produced by two deformation events. This paper examines the significance of FIA data and how it can be applied to solving geological problems.

FIAs provide a potentially powerful tool for investigating the deformation history of orogenic belts. Such studies are difficult because the effects of the youngest deformation events obliterate or reorient structures formed earlier during orogenesis. A window into these older events is provided by inclusion trails in porphyroblastic minerals. These trails preserve the

fabrics that were in the rock at their time of formation. Hayward (1990) and Bell et al. (1995) introduced a method for measuring FIA as a means of quantifying these microstructures.

The quantitative application of FIAs requires consideration of their statistical significance to ensure that the data are properly understood and that they are not being over interpreted. Johnson (1999b) suggested that several aspects regarding the measurement and significance of individual FIA needed clarification. Once individual FIA measurements have been obtained, their correlation and grouping in a geological region needs to be determined; this has typically been done by examining the relative timing and orientation of FIAs (e.g. Bell et al. 1998, Yeh & Bell 2004). Stallard et al. (2003) raised concerns about this approach and about the significance that could be given to a FIA orientation.

This chapter reviews the current literature, defines FIAs, examines the sources of variation in their orientations on the hand sample and regional scale, describes how to measure FIAs, and outlines the statistical methods that have been applied to FIA analysis to date. A technique for quantifying the error in FIA measurements is introduced, and the reliability of individual FIA measurements is examined. The significance of FIA data at the regional scale is also considered. Several case studies of the application of FIA data are presented.

## 1.1 What is a FIA?

The generic description of FIAs states that they are the axis of curvature of curved inclusion trails within porphyroblasts. While the method for determining the orientation of a FIA is independent of the processes that formed the curved inclusion trails, their interpretation is not. According to Hayward (1990) and Bell et al. (1995), a foliation inflection or intersection axis in a porphyroblast (FIA) is the intersection of successive foliations, or the curvature of one into the next, which has been overgrown by a porphyroblast (Fig. 1). FIA can be equated with the intersection lineation between these two foliations or the fold axis of the second event. Alternatively, they represent the axis of rotation of the porphyroblast while it was growing (e.g. Rosenfeld 1970). However, there is a growing weight of evidence that firmly suggests porphyroblast generally do not rotate relative to a fixed geographic reference frame during ductile deformation (e.g. Aerden 2004, Aerden 1995, Bell & Chen 2002, Bell & Hickey 1999, Evins 2005, Fyson 1980, Hayward 1992, Johnson 1990, Jung et al. 1999, Steinhardt 1989). This is an important observation because it means that FIAs preserve the orientations of a range of fabrics through subsequent deformation events, even though they may be obliterated in the matrix.

The majority of published FIA data involves trends only. Where plunges have been measured they are generally sub-horizontal (e.g. Chapter 2`; Bell et al. 1998, Bell & Wang 1999, Hayward 1990, Stallard et al. 2003, Timms 2003). Hayward (1990) argued that this

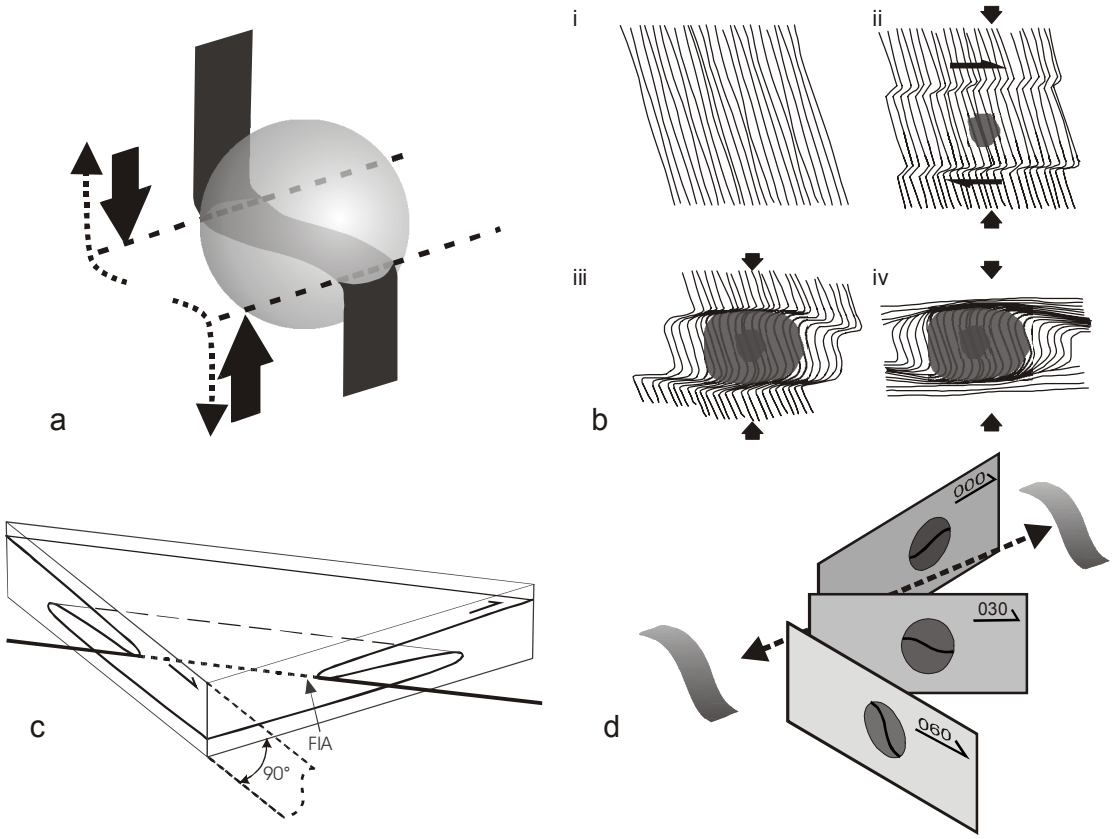


**Figure 1.** A series of sketches demonstrating what FIA are and how the asymmetry method is used to find them. The two models for the formation of curved inclusion trails are shown (a). A spherical porphyroblast is shown along with a curved foliation plane that it includes. The dashed lines show the axes of rotation of this foliation plane. The large solid arrows show the shear sense that would have been necessary to form this geometry via porphyroblast rotation; the dotted arrows show the shear sense that would have rotated a flat foliation to the vertical in an irrotational model. The progressive development of curved trails in the deformation partitioning model is shown in (b). A porphyroblast (grey oval) grows in the crenulation hinge (ii), eventually overgrowing the curvature of the sub vertical foliation into the flat foliation (iii). The deformation intensifies against the edge of the porphyroblast that has stopped growing (iv). The asymmetry method used for finding FIA is shown in (c) and (d). The block of rock containing an asymmetric fold shown in (c) has been cut by two sections at 90˚ to each other; each section shows the opposite asymmetry so the fold axis must lie between these sections. The application of this technique in thin section is shown in (d); in this case the FIA is oriented at approximately 015°. Vertical thinsections striking at 000°, 030° and 060° are shown and the flip in asymmetry of the inclusion trails in the "porphyroblasts" from clockwise to anticlockwise occurs between the 000° and 030° sections. Extra sections between these two would allow the FIA to be constrained further. A similar process can be used to define the plunge of the FIA.

observation supports the hypothesis that a cyclic pattern of overprinting sub-horizontal and sub-vertical foliation occurs during orogenesis (Bell & Chen 2002, Bell & Johnson 1989). Therefore, FIA trends will reflect the strike of sub-vertical foliations during orogenesis. Bell et al. (1995) demonstrated that this gives a history of the direction of bulk shortening that the rock had been subjected to and the direction of plate motion, with an example from the Alps. Johnson (1999a) discussed the importance of repeated steep and flat foliations and suggested that they are the result of fundamental processes in the formation of orogens.

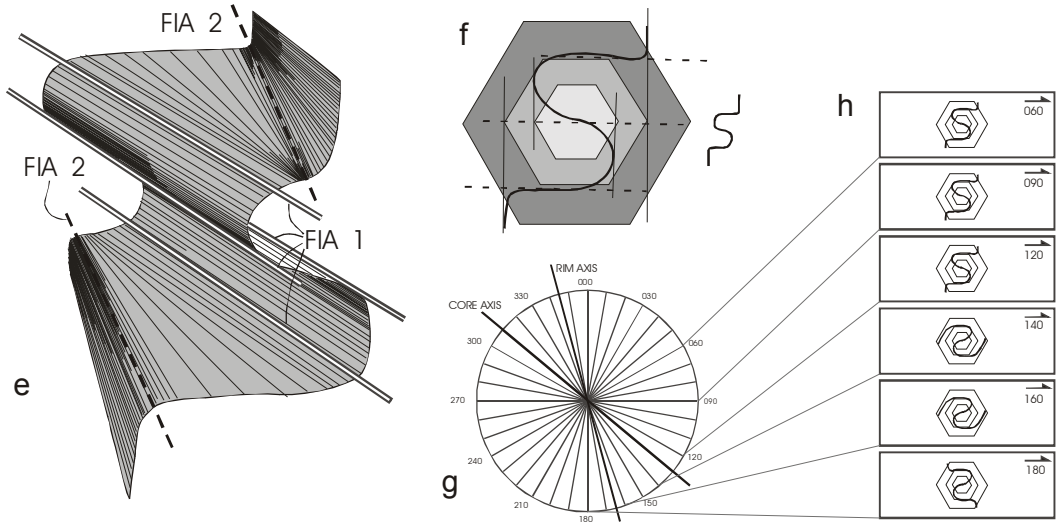


**Figure 2.** (a) shows a 3-D sketch of an inclusion trail from a porphyroblast that has three stages of growth; the core and median have the same FIA orientation while the rim has a different FIA. A section through the core of the porphyroblast showing the core, median and rim is shown in (b). The compass in (c) shows the different orientations of the core and median versus the rim FIA. (d) shows what would be seen in vertical thin sections through such a porphyroblast; the change in asymmetry of the core/median trails from clockwise to anticlockwise occurs between the 120° and 140° sections. In the rim the change is from anticlockwise to clockwise between the 160° and 180° sections. After Bell et al. (2003).

FIA *set* is the term given to a group of FIA orientations from different samples that are interpreted to have formed at the same time (e.g. Bell et al. 1998). Porphyroblasts with complex inclusion trails can have a succession of FIAs with different orientations from core to rim (Figs.2 & 3.). Bell et al. (1998) described how this occurs with episodic porphyroblast growth over multiple deformation events. Individual porphyroblasts that have multiple FIA orientations allow the relative timing of different FIA sets to be determined.

## *1.2 Causes of Variation in FIA orientations*

If FIAs develop as Hayward (1990) and Bell et al. (1995) suggest, then individual FIA orientations will vary in the same way that the fabrics forming them vary; this will be the case from hand sample to orogen scale. Many factors will influence the orientation of a single foliation including cleavage refraction, cleavage reactivation, cleavage intensity, and their anastomosing character. Local variations in regional stress caused by contrasting rheologies (e.g. igneous intrusions, basement highs) will cause regional variation in orientation in the same way that foliations wrap around porphyroblasts at hand sample scale. Treagus (1983, 1988) demonstrated that cleavage orientation can vary markedly as the result of relatively small variations in the competency of rock. Bell (1978`; Fig. 22 therein) measured the preferred orientation of micas in a slaty cleavage and found distributions of ± 35º that he attributed to the anastomosing nature of foliations. No literature quantifies the variation in orientation of a single foliation. However, there is a great deal of foliation orientation data published in regional

studies. In general, where the effects of later deformations can be ruled out, the data have clustered distributions,.

FIA may be curved or offset because the foliations that form them wrap around pre-existing porphyroblasts. Hayward (1990`; fig 6.) suggested that this may result in as much as 45º of angular deviation of the foliation. This variation would happen on the scale of a porphyroblast with the orientation of the foliation affected by the different crystal faces. All of these sources of variation in FIA orientations are most likely normally distributed. An exception is where a crenulation cleavage preserves a relict foliation in its hinges. In this case the FIA may have a bimodal distribution or be skewed.

If FIAs form by rotation of porphyroblasts as they grow then the distribution of FIAs formed in a single foliation-forming event would also show a normal distribution, assuming the porphyroblasts were not rotated by subsequent events. If the porphyroblasts are affected by subsequent deformation events it is highly probable that the amount an individual porphyroblast rotates will vary because of the heterogeneity of strain and the interference of other grains (Beirmeier & Stuwe 2003). This variation in rotation would lead to a girdle like distribution after a single overprinting event and subsequent events would lead to a random distribution (Ham & Bell 2004). The growing body of FIA data with non-random data distributions (e.g. Bell et al. 2004, Bell et al. 1998, Stallard et al. 2003, Yeh & Bell 2004) strongly suggests that rotation is an unlikely mechanism for their formation.

If FIAs do form as a result of overprinting foliations then deformation partitioning may complicate matters further. Bell and Hayward (1991) describe how deformation partitioning can be used to explain how simple and complex inclusion trails can coexist in the same outcrop. They argue that porphyroblast growth only occurs in zones actively undergoing deformation; that simple inclusion trails form in zones microfolded by one episode of foliation development and porphyroblast growth and complex trails form where these episodes are repeated. It is therefore conceivable that a rock that has undergone multiple foliation forming events will have FIAs equivalent to $L_2^1, L_3^1, L_3^2, L_4^1, L_4^2, L_4^3 .....$ and so on (terminology from Bell & Duncan 1978). Accepting that a cyclic pattern of overprinting sub-horizontal and sub-vertical foliations can develop, this deformation partitioning argument should be able to generate FIAs with a sub-vertical plunge. FIA at this orientation would only occur if two vertical foliations form it that are at a high angle to each other. This case would be readily identified because vertical thin sections would contain coaxial geometries regardless of their orientation while horizontal sections would contain asymmetrical geometries. When the two overprinting foliations are at a low angle to each other, the second is likely to reactivate the first and porphyroblast growth is unlikely (Bell 1986, Bell et al. 2004).

## 1.3 Statistics of FIAs – Exisiting Work

Despite the growing body of literature using FIA data, there is little written on the statistical significance of FIA. Bell and Hickey (1997) briefly discussed the accuracy of FIA determinations due to measurement errors. They determined that the total accumulated analytical error in collecting an oriented sample, reorienting it and preparing the thin sections was ± 8º. This error is expected to have a normal distribution. Bell et al. (1998) discussed some of the aspects of analysis of regional FIA datasets. They employ Watson's $U^2$ test modified for grouped data to confirm whether the FIA data come from a random population and a chi-squared test to confirming whether FIA sets differ significantly from each other. Yeh (2003) and Yeh and Bell (2004) applied these tests and also implemented a moving average method to discern peaks in FIA data from a region. None of these tests address the distribution of FIAs within a sample, or on a regional scale, except to show that they do not represent a random distribution and that FIA sets can be differentiated from each other. Yeh and Bell (2004) also commented that the variation of FIA orientations in a FIA set ranges from 30º to 50º based on a review of published data. They argue that this distribution is a result of the anastomosing nature of foliations.

The asymmetry method for measuring FIAs determines them for a sample rather than for individual porphyroblasts. Consequently, meaningful estimates of the distribution of FIAs in a sample have not been possible using that approach. Typically FIA measurements have been reported as the mid-point of the range over which the dominant asymmetry flips with no indication of the spread within a sample. Stallard et al. (2003) demonstrated a technique for quantifying the reliability of FIA measurements using data for samples collected from Georgia, USA. They used a method developed by Upton et al. (2003) for the analysis of cyclic logistic data using a maximum likelihood technique to fit a regression model to the asymmetry data. They argued that the range over which FIAs occur in a single sample is in the order of 50º. Chapter 3 demonstrates several flaws in the assumptions in Upton et al.'s (2003) approach and presents a more robust technique using bootstrapping. This technique is summarised in the methods section. Upton et al. (2003) express some concern on the reliability of the technique for samples in which only a small number of observations have been made and this issue is examined in more detail below.

# 2 Methods

## 2.1 How are FIAs Determined?

The asymmetry method most commonly used for determining FIA orientations was first described Hayward (1990) and then expanded to include plunges by Bell et al. (1995). The method relies on the fact that a simple asymmetrically folded surface with a sub-horizontal axis

will appear to have opposite asymmetries when cut by two vertical planes that strike either side of the fold axis (Fig. 1c`; Bell et al. 1998). The fold asymmetry appears anticlockwise in one ("Z", left side of Fig. 1c) and clockwise in the other ("S", right side of Fig. 1c). Note that both these planes are viewed in the same direction – for example clockwise about a vertical axis. Curved inclusion trails preserved in porphyroblasts are analogous to such a fold. Figure 1d shows how this concept is applied in thin-sections. The trend of the FIA is constrained to lie between two vertical thin sections with a close angular spacing which have the opposite observed dominant asymmetries. Sections are typically cut at a 10˚ angular spacing and the FIA trend is recorded as being midway point of this interval. In some cases a thin section may have both asymmetries in equal proportions, with sections either side having opposite asymmetries dominating. When this occurs, the FIA is interpreted to be parallel to the thin section. Once the trend of a FIA in a sample has been determined, the plunge can be found using a similar approach. A series of sections perpendicular to the vertical plane containing the FIA trend with different dips are cut; the FIA plunge is determined as being between the two sections across which the inclusion trail asymmetry changes.

Powell and Treagus (1967) were the first to publish a method of determining what are now called FIAs in garnet using thick sections and a universal stage. Busa and Graham (1992) used a similar technique looking at staurolite grains. These techniques are inaccurate as they only measure a short segment of the axis and make assumptions about the relationship between the elongation of included grains and the orientation of the FIA. Rosenfeld (1970) described several techniques for finding FIAs. These methods were in part based on the assumption that curved trails are the result of porphyroblast rotation. His techniques included one for finding the FIA in a single large porphyroblast (tens of millimetres in diameter) that is not practical for the majority of rocks that have smaller porphyroblast sizes, or those with multiple FIAs. For these rocks he used a method based on the same asymmetry principle as used later by Hayward (1990). However, he used the main schistosity in the rock as the reference plane (i.e. all sections cut perpendicular to the main schistosity in the rock) instead of the horizontal. This was based on the flawed assumption that the matrix foliation was the one that formed the curved inclusion trails. If the actual FIA orientation lies at a high angle to this schistosity it would be difficult to constrain it with this approach. There is no way of determining whether this schistosity was the dominant one at the time of porphyroblast growth. The asymmetry method allows the trend of a FIA to be determined in all cases except those rare cases with a vertical or near-vertical plunge.

Determining a FIA orientation is complicated when more than one FIA are preserved in a sample. Figure 2a shows an inclusion trail that has two distinct FIAs lying at an angle to each other. Depending on the orientation of the thin section, either a staircase or spiral geometry will be observed (Fig. 2d). Such samples provide valuable relative timing criteria for FIAs as those in the core of the garnets must form before those in their outer parts. See Fig.3 for an example.

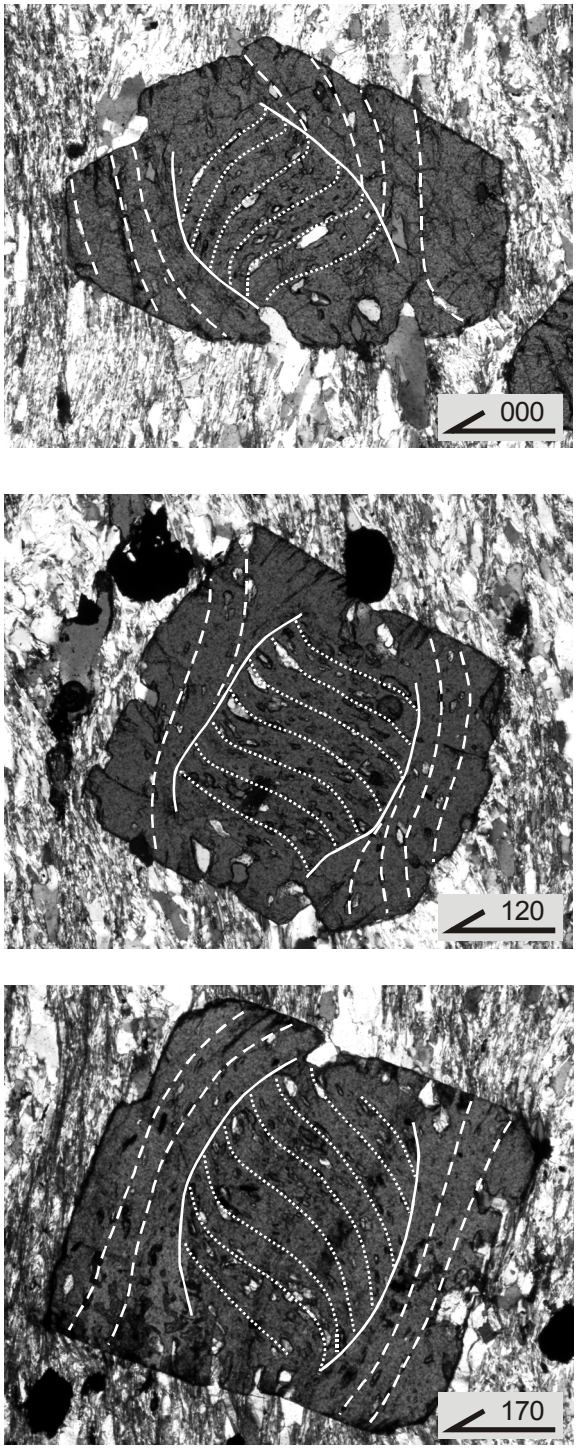


**Figure 3.** An example of a multi-FIA sample. Three photomicrographs are all from the same sample (CH57) and show the geometries that occur when FIAs of different orientations are preserved in the same porphyroblast. These porphyroblasts have a core and rim (solid lines mark the transition). The core inclusion trails (dotted lines) are anticlockwise in the 000° section and switch to clockwise for the 120° and 170° sections. The rim inclusion trails (dashed lines) switch from anticlockwise in the 000° and 120° sections to clockwise at 170°. Where the core and rim asymmetries are the same the inclusion trails have a spiral geometry; where they differ they have a staircase geometry. Partially crossed polars, bottom edge of photomicrographs is approximately 3mm.

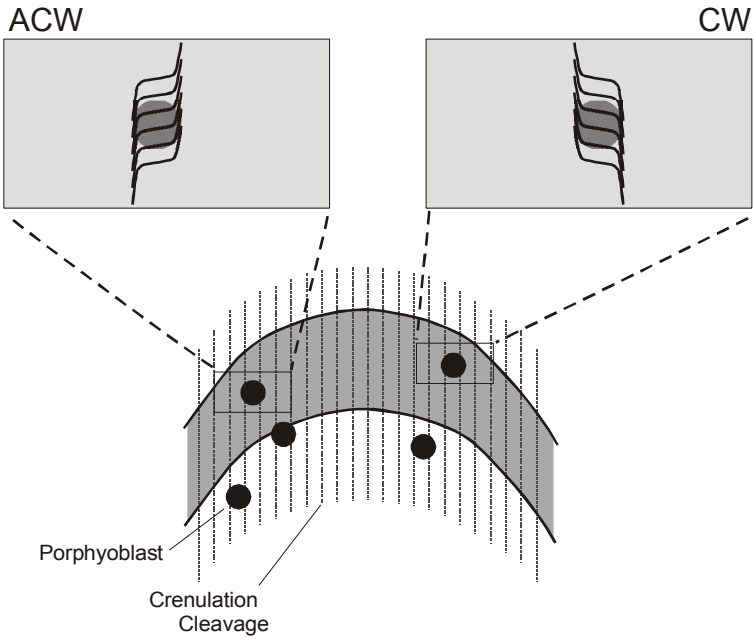


**Figure 4.** Reversals in crenulation asymmetry across a small-scale fold. A thin-section scale fold is shown (grey). The two thin sections show opposite asymmetries even though they have the same orientation. Attempts to define the FIA using the asymmetry method would not work in this case.

Care must be taken when recording these asymmetries, as it may be difficult to distinguish inclusion trails in different parts of a porphyroblast within and between sections, particularly where the thin sections intersect porphyroblasts off centre.

Another complication in this method for measuring FIA orientations is that it relies on the assumption that the asymmetry was the same throughout the rock sample when the porphyroblasts grew. This will not be the case if there are reversals in asymmetry related to features such as small-scale folds (Fig. 4). In this situation the asymmetry method may fail. However, the asymmetry does not change across many small scale folds (e.g. Bell et al. 2003) so this generally is not a problem.

Aerden presented an alternative technique for determining FIAs called *FitPitch* (Aerden 2003). In this technique the pitches of planar fabrics in porphyroblasts are measured and planes of best fit are determined and their intersections are recorded as the FIA. The *FitPitch* technique is similar to that of Hayward (1990) and Bell et al. (1995) in that multiple vertical thin sections are required and the resultant measurements are average values for the sample from which they come. It is well suited to samples where the inclusion trails are planar and characterized by an earlier foliation that is truncated by a later one. While goodness-of-fit parameters are provided to aid in the evaluation of the results of the technique, no confidence intervals are generated for the FIA orientations calculated nor is there a description of the distribution of the FIAs in the sample.

## 2.2 Maximum Likelihood Estimation of FIA Parameters

In order to provide a test of the statistical significance of a FIA measurement determined using the asymmetry method, a parametric model is fitted to the data. The parametric model used is the logistic model that was suggested by Upton et al. (2003). It relates the probability *p* of observing a particular asymmetry (clockwise or anticlockwise) in a thin section with orientation θ to the trend of the FIA (μ) and a shape parameter (β). The probability density function for the logistic model is

$$p(\theta,\beta,\mu)=\frac{e^{\beta\sin(\theta-\mu)}}{1+e^{\beta\sin(\theta-\mu)}}. \qquad (1)$$

β describes the rate at which the switch in asymmetry occurs. The higher the magnitude of β, the smaller the interval over which this switch occurs. A value of ∞ or -∞ would indicate an instant flip. Values that approach zero represent a more gradual change with zero indicating a random distribution. Figure 5 shows the distributions for a range of β values for a data population with a mean orientation (μ) of 90º.

To find the values of μ and β a Maximum Likelihood Estimate (MLE) is made. The MLE finds the values (a hypothesis) of the parameters which have the highest likelihood given the data. This differs from the traditional probabilistic approach that asks what is the probability that our data matches a chosen hypothesis? In this case we are interested in the values of μ and β that maximize the log-likelihood equation

$$\log L=\sum_{i=1}^{m}2\left(r_i\log\{p(\theta_i)\}+(n_i-r_i)\log\{1-p(\theta_i)\}\right) \qquad (2)$$

where $r_i$ is the number of, say, clockwise observations and $n_i$ is the total number of observations at each of *m* orientations for which we have data. We used the quasi-Newton optimizer in Matlab R14 (www.mathworks.com) to find the minima of –log *L* for the examples presented here.

When fitting a parametric model to the data, we must concern ourselves with two questions: does the parametric model provide a good fit to the data; and how much confidence can we have in our model parameters? Upton et al. (2003) based confidence intervals for these parameters on the model deviance using a chi-squared distribution with one degree of freedom. They also had a goodness-of-fit test based on a chi-squared distribution with degrees of freedom equal to the number of sampling orientations minus the number of model parameters. Chapter 3 demonstrates how this approach is flawed as it overestimates the degrees of freedom in the data. Here, we apply the bootstrap techniques described in chapter 3 to determine the confidence intervals for μ and β and to examine the goodness-of-fit of the model.

The bootstrapping procedure allows the empirical distributions of the model parameters to be determined by simulating repeated sampling of the original population. The goodness-of-fit of the model can be determined from these parameters, along with confidence intervals for μ

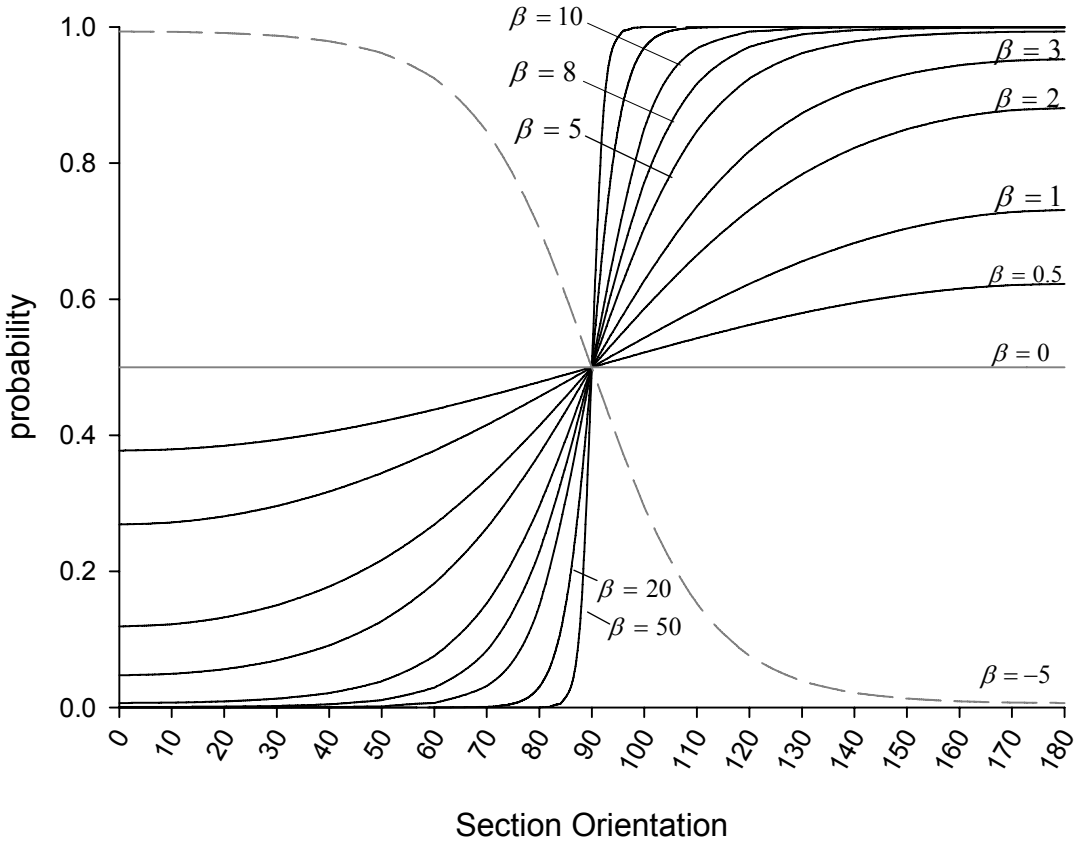


**Figure 5.** Graph showing the probability of a success at a given section orientation for different values of β according to the cyclic logistic model; a success is arbitrarily defined as observing a particular asymmetry (e.g. clockwise). Higher values of β show a more rapid change in asymmetry. μ = 90º in all cases. The dashed line shows that the sign of β determines whether the switch is from "successes" to "failures" or vice versa.

and β. Goodness-of-fit is determined informally by inspecting the distributions of μ and β, which should be normal or log normal, plus the deviance which should have some form of chi-squared distribution whose degrees of freedom will be less than or equal to *m*-2. Confidence intervals for the model parameters μ and β are determined from the bootstrapped data by the percentile method adjusted for bias and acceleration ($BC_a$) as discussed in Chapter 3. Two bootstrapping methods can be applied. One resamples within section orientations (method A) and the other across section orientations (method B; see chapter 3). Which of these methods produces a better model fit will depend on the nature of the sample population. Method B is preferred, except where the total number of observations is small.

### 2.2.1 Implementation of MLE

The MLE technique described above and in chapter 3 attempts to find the parameters μ and β of a cyclic logistic model that fits the data. Before we can interpret the geological meaning of these values, we have to be sure that the cyclic logistic model is a good fit. If it is not, these parameters may be meaningless. Graphical procedures are used to assess the goodness-of-fit of the model to the data. To demonstrate the MLE technique, asymmetry data was generated for sample V209, based on the measurements obtained using HRXCT in chapter 2 (Appendix 1.1). This was done by determining what asymmetries would be observed if all 58 garnets measured were intersected by thin sections cut at 10º increments from 0º to 170º. The resulting asymmetry data is a perfect representation of the sampled data, free from observation errors or sampling bias. There is a large number of observations (N = 58) and the sample is unimodal and symmetrical about its mean.

Figure 6 shows the results of the bootstrap MLE analysis of this data. The distributions of μ and β are normal and lognormal respectively indicating that they are well represented by the logistic model. The deviance plot shows a chi-squared distribution with approximately five degrees of freedom. While this distribution, combined with those for μ and β, may be enough to satisfy us that the model is a good fit for the data, we can gain further confidence by examining a boxplot of the deviance (Fig. 6e). The boxplot shows that for a number of section orientations (60º through 160º) there is very little variation in probability of a given observation. This lack of variance means that only seven orientations contribute to the freedom of the data to vary. The number of degrees of freedom for the deviance should be five because the values of two parameters (μ and β) are fixed. A chi-squared distribution with five degrees of freedom matches the distribution observed, so we can be very confident that the data is well represented by the logistic model with the values for μ and β calculated.

Given that the proposed model has a good fit for the data, we can now determine the confidence intervals for the parameters μ and β. Because the data is so well behaved the percentile method can be used. For a 95% confidence interval the parameter values at 2.5% and 97.5% of the bootstrap distributions are taken. Unlike a normal distribution for linear data these values cannot be directly related to the shape of the distribution; they simply represent the confidence that can be placed in the mean values calculated for μ and β. The parameter β describes the spread of the data and is analogous to the concentration parameter *kappa* of a von Mises distribution.

For comparison, Figure 7 shows the results of using the bootstrap MLE approach for the sample CA10 Core from Stallard et al. (2003, see also Appendix 1.2). In this case, the cyclic logistic model is a poor fit for the data. This is demonstrated by the departure from normal of the μ and β distributions and the multiple peaks in the deviance distribution. The hypothesis that the cyclic logistic model can be used to describe this data must be rejected and confidence

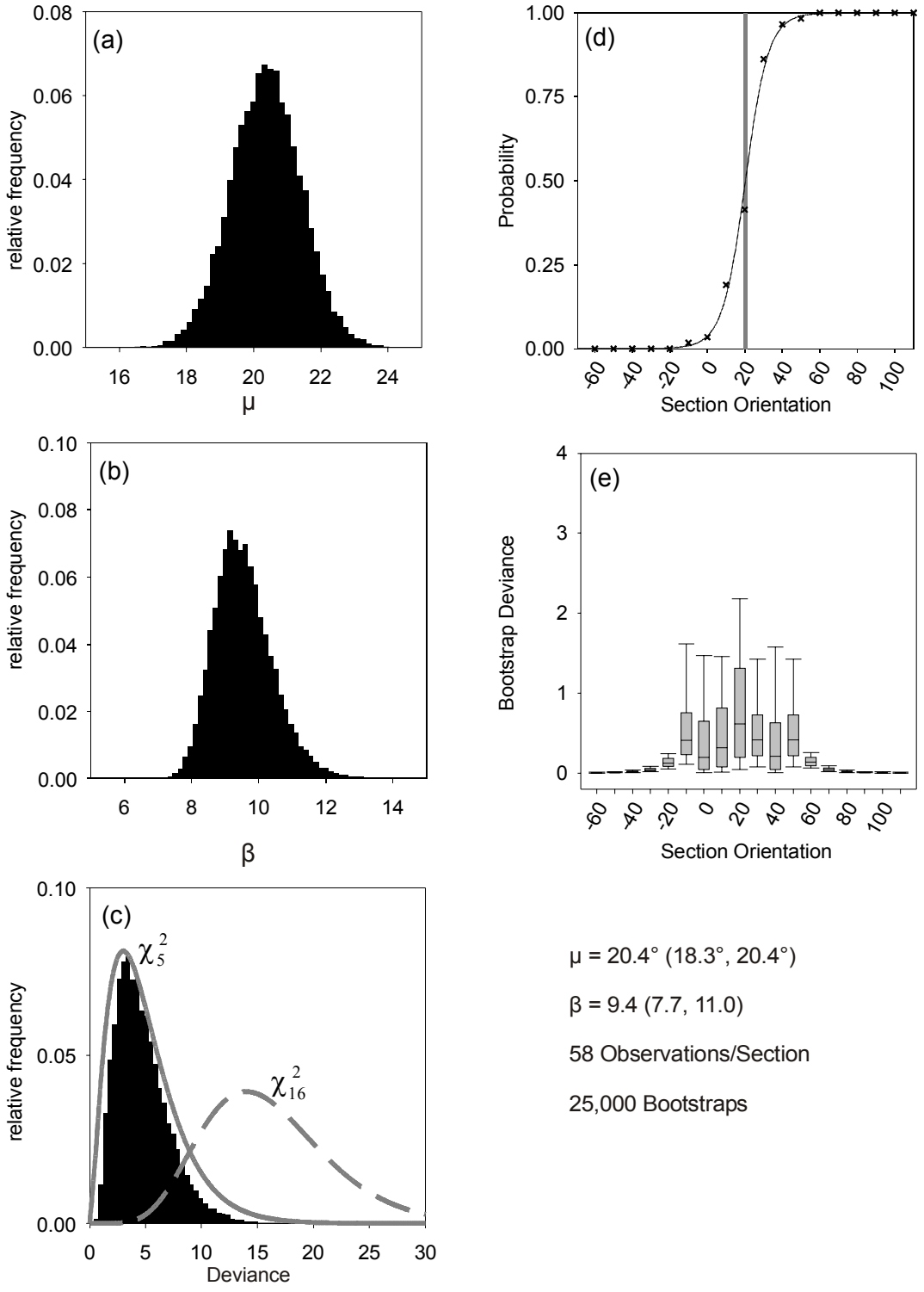


**Figure 6.** Plots of the results of bootstrap MLE analysis for the HRXCT data from sample V209. (a), (b) and (c) are probability plots of the bootstrapped μ, β and deviance data respectively. The distributions of μ and β are normal and log-normal respectively. The deviance has a distribution that is approximated by a chi-squared distribution with 5 degrees of freedom. These distributions indicate that the cyclic logistic model is a good fit for the data. In (d) the model (solid line) is shown with the raw data (crosses) and the mean μ (grey line). The boxplot in (e) demonstrates that only some of the sections contribute to the variability of the data. 95% confidence intervals for μ and β in brackets.

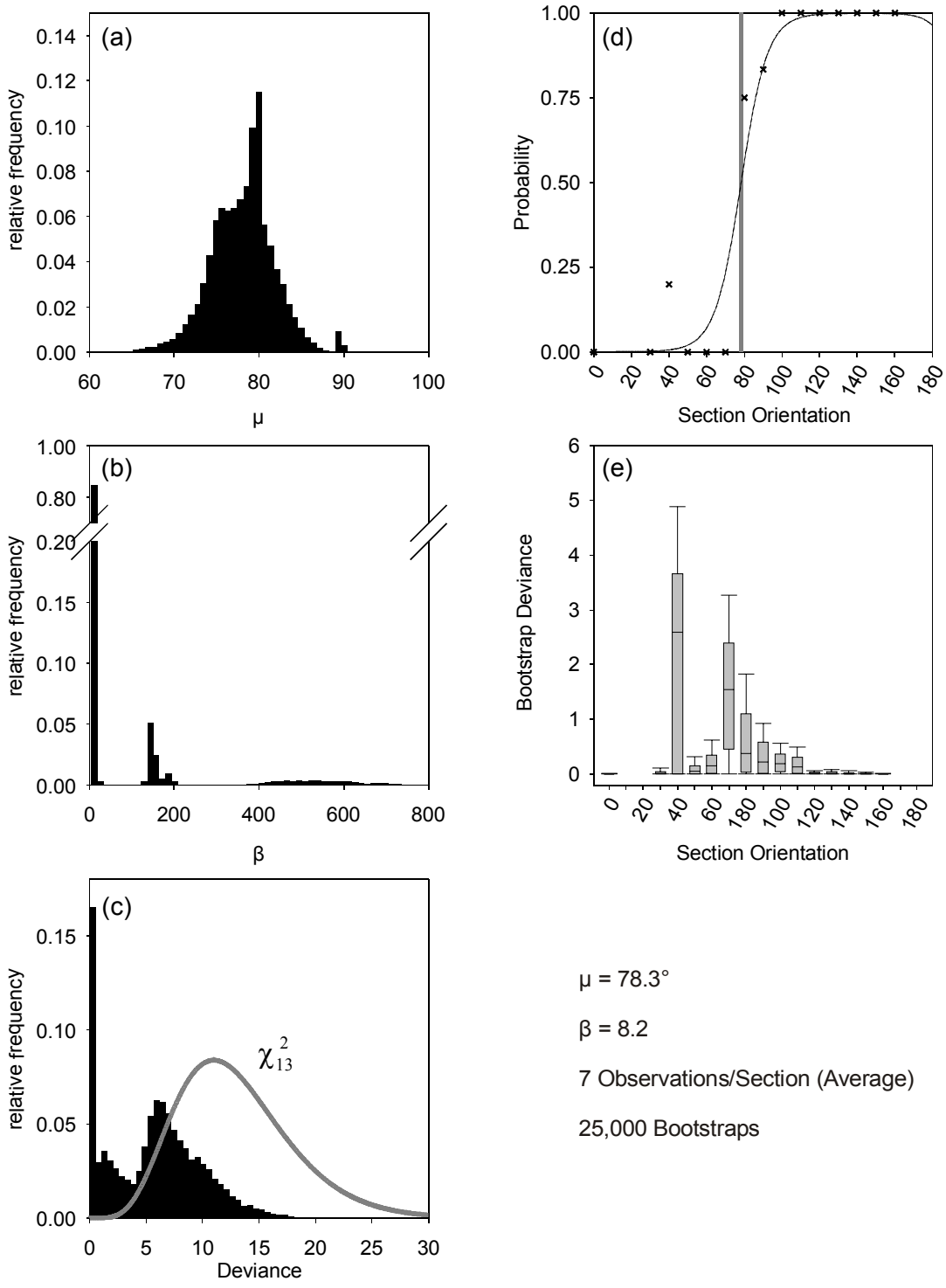


**Figure 7.** Plots of the results of bootstrap MLE analysis for sample CA10 Core from Stallard et al. (2003). The probability plots in (a), (b) and (c) of the bootstrapped μ, β and deviance data respectively show significant departure from their expected distributions. This indicates that the cyclic logistic model is a poor fit for the data. In (d) the model (solid line) is shown with the raw data (crosses) and the mean μ (grey line). The raw data at 40˚ stands out as being anomalous. The boxplot in (e) demonstrates this also. See text for discussion.

intervals for μ and β cannot be determined using the bootstrap technique. There are several explanations for the poor fit of the model. First is sampling error, whereby asymmetry observations have been misinterpreted. Examples of this are confusing trails in the median with those in the core of a garnet, or simply getting the asymmetry wrong. Second, the underlying FIA population may not have a distribution that can be described using the cyclic logistic model. This could result from mixed populations being sampled, or the underlying population has a girdle rather than clustered distribution. Third is that the sample is not representative of the true population. If the number of observations is small, particular in the region of the FIA, random chance may result in a biased sample. This may be the case for the CA10 Core data. For example, in the 40º section there are only five observations. The true probability of a clockwise observation may be lower than 0.2 but there are insufficient observations to demonstrate this. The locations of the thin sections may also introduce bias into the sample if the population distribution varies through the specimen.

Even though our chosen model cannot describe the CA10 core data, it would be possible to conclude that the true orientation of μ must be between 60º and 90º from studying the bootstraped μ distribution; therefore, the calculated mean of 78.3 is reasonable. Caution must be exercised here in case the cause of the poor fit of the model is a result of some geological process rather than sampling irregularities.

### 2.2.2 Sensitivity to Sample Size

As for all statistical tests, the MLE cyclic logistic regression technique described above is sensitive to the number of observations that make up the sample. Applying bootstrap methods addresses this issue by creating many samples of the original data population based on the original sample; however, bootstrapping cannot improve on a sample that was unrepresentative of the sampled population in the first place. There will be some minimum amount of data that will be required to adequately describe the underlying distribution. This issue has been examined to attempt to provide guidance on the minimum number of observations that should be obtained to provide a representative sample for measuring FIAs.

A modified bootstrapping technique was used to test the sensitivity of the MLE of the model parameters to the number of observations. Strictly speaking, the bootstrap method involves resampling of the original sample, $\theta^0$, with each resample $\theta^j$ containing the same number of observations as the original data. In this case, we are interested to see what the effect of the number of observations has on the values we obtain for μ, β and their confidence intervals. To do this we take a sub-sample, $\theta_{Ni}$, with $N$ observations of the original data and then perform the bootstrap technique described in chapter 3, substituting $\theta_{Ni}$ for $\theta^0$; the bootstrap is performed $B$ times and for each bootstrapped sample, $\theta_{Ni}^j, j = 1...B$, we calculate

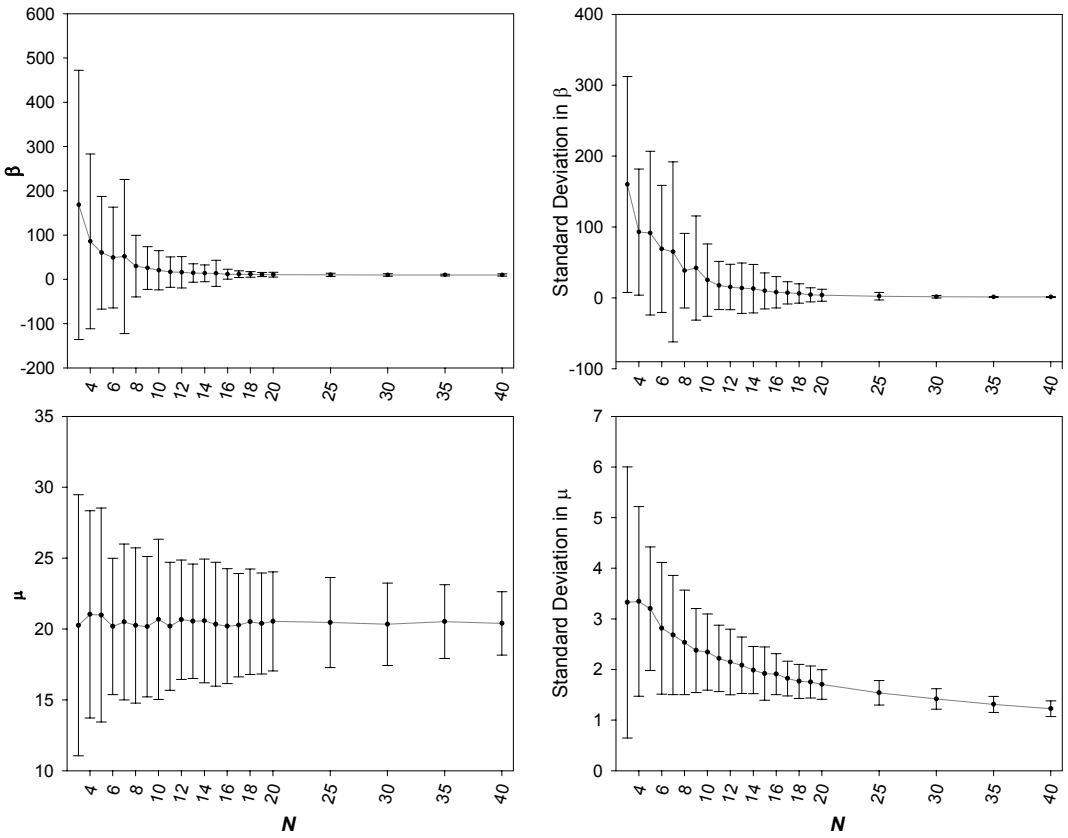


**Figure 8.** Plots of sample size sensitivity analysis for the HRXCT data from sample V209. Mean values for μ and β are shown in (a) and (b) and standard deviations in (c) and (d). Error bars show 95% confidence intervals. See text for further discussion.

MLE for $\beta_{Ni}^{j}$ and $\mu_{Ni}^{j}$. This process is repeated *i* times for each *N* allowing the distributions of $\beta_{N}^{j}$ and $\mu_{N}^{j}$ to be determined. For these tests $B = 2000$, $i = 100$ and $N$ varies from 3 to 40.

The results of these tests are plotted in Figure 8 for the data from the HRXCT study of sample V209. This data was has 58 observations in each section orientation and is well described by a cyclic logistic regression. The plots of the mean values of μ and β (Fig.8a and b) display asymptotically decreasing confidence intervals with increasing *N* as expected. The point at which the amount of variability decreases to some limit is at around $N = 15$ in this sample. The standard deviation plots (Fig.8c and d) show a similar trend; this indicates that the data is approaching a point that represents the natural variability in the sample. As *N* increases the standard deviation for β stabilizes while that for μ continues to decrease.

This technique has been applied to twelve other datasets from eight different samples. These datasets were selected because the number of observations was high and the bootstrap MLE analysis showed that the cyclic logistic model fits the data well. The results are shown in Appendix 2. In general, these data demonstrate that the minimum number of observations

required to represent the sampled population is between eight and fifteen. They all show the same pattern of the standard deviation for β stabilizing while that for μ continues to decrease. The increase in confidence in the mean of μ, by increasing the number of observations much above ten, is less than a few degrees.

In some cases, *N* was allowed to exceed the number of observations in the original sample. This resulted in an over sampling of the data causing spurious results with variability increasing at higher *N* (e.g. CH2, CH22, CH49). While these results are included in Appendix 2, the over sampled parts on the plots were not considered for this interpretation.

# 3 Examples

The bootstrap MLE approach gives a method in which the distribution of FIAs in a single sample can be measured. It allows confidence intervals to be assigned to these measurements. None of the published literature containing FIA data include such statistical analysis, with the exception of Stallard et al. (2003). Some examples of the application of the technique are explored to investigate the importance of such an analysis where FIA data are used are given in the following section.

## *3.1 Stallard et al. Data*

Stallard et al. (2003) presented the first application of a MLE technique to the analysis of FIA data collected by the asymmetry method. They examine data collected from 25 samples from the Canton Schist in the Southern Blue Ridge, Georgia. 61 FIAs were determined with 14 samples containing core, media and rim FIAs that allowed the relative timing to be determined. The MLE technique used was that detailed by Upton et al. (2003). As discussed above and in chapter 3 this technique is flawed, particularly in regard to the goodness-of-fit test. Stallard et al. (2003) state that in all cases the goodness-of-fit was acceptable; however, using the bootstrap techniques outlined in chapter 3, very few if any of their data can be modelled using the cyclic logistic model (Fig. 7; Figs. 3 and 4 of Chapter 3). This poor fit appears to be due to the small sample sizes used in their study in which there are only two or three observations per section orientation. Stallard et al. (2003) note they have samples with wide 95% confidence limits. This is most likely the result of sparse sampling where chance results in an apparently anomalous observation whose influence would be reduced if the number of observations were increased. As a result the 95% confidence intervals they present are unreliable. However, they observe that the true intra sample FIA spread is likely to be in the range of 30˚-50˚; this is not unreasonable compared to the results of the HRXCT study in Chapter 2.

In the second part of their paper, Stallard et al. (2003) investigate approaches to correlating FIAs between samples. They suggest three possible approaches; using relative timing and textural criteria; using orientation, relative timing and patterns of changing FIA

orientation; and using relative timing and orientation alone. The third is the technique that has been used in all other literature to date (e.g. Bell et al. 1998, Yeh & Bell 2004). Stallard et al. (2003) conclude that the first approach is preferred. In their interpretation of the Canton Schist data via this approach, they make the assumption that the truncation plane preserved at the core-rim boundary of garnet porphyroblasts formed at the same time throughout the study area. Based on this, a second assumption is made that all the FIAs measured in the core of garnets belong to one set, and similarly for median and rim data giving a total of three FIA sets. Supposing the first assumption holds, it is not necessary that the second will follow. Assuming that metamorphic reactions producing porphyroblastic phases will coincide in all rocks, regardless of compositional variations and P-T gradients is precarious, even where samples are from a locality with a relatively small spatial extent. If the assumption that the core-rim transition can be correlated from sample to sample is valid, no justification was given for separating the core and median data into separate FIA sets based on textural grounds.

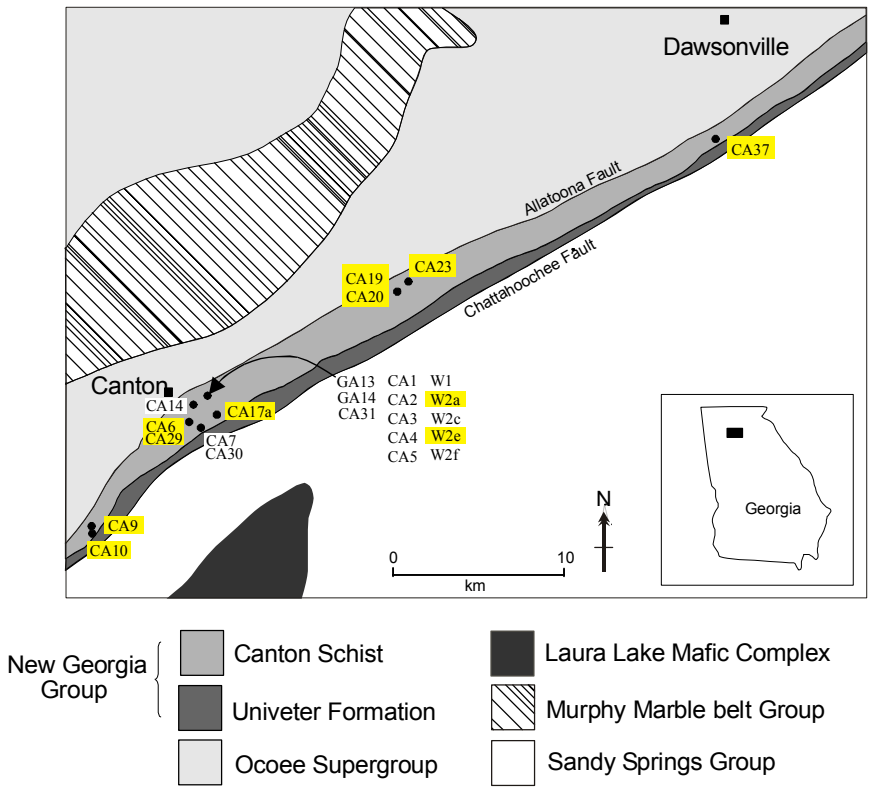


**Figure 9.** Locality map showing sample locations from Stallard et al. (2003). Rim FIAs could only de determined in samples from three closely spaced localities. Samples for which no rim FIA was measured are highlighted in yellow.

Looking at the data of Stallard et al. (2003) in more detail, only 14 of the 25 samples analysed had sufficient rim growth to be analysed, as the other 11 did not preserve what was interpreted as being a pervasive deformation event. The distribution of sample localities consists of a cluster of 19 samples in the immediate vicinity of Canton (Fig. 9), with two samples (CA9 and CA10) well to the south west, three (CA19, CA20 and CA23) over 10km to the north east, and one sample (CA37) over 20km to the north east. It is interesting to note that none of the samples located outside the cluster near Canton have data reported for rim FIAs given that the core-rim transition is used as a temporal marker for all samples (Fig. 9). This demonstrates the problems of trying to use inclusion trail textures as temporal markers between samples. Deformation partitioning can result in highly variable distributions of strain from grain to orogen scale (e.g. Bell et al. 2004) making features such as the intensity of a foliation preserved in porphyroblasts totally unreliable for such correlations.

A significant consequence of Stallard et al. (2003) using textural criteria for the interpretation of FIA data was that supposedly temporally related FIAs have a spread of orientations of greater than 140˚. This then raises the question of what FIAs are. If they do represent the intersection/inflection axis between foliations then Stallard et al. (2003) are suggesting that a foliation may vary by up to 140˚ as it forms. They list the possible sources of variation in foliation orientation as: heterogeneous rheology (i.e., refraction); rotation of the kinematic reference frame; anastomosing of foliations around inhomogeneities such as granites; and rotation of porphyroblasts relative to each other. No literature documents the range of orientations a single foliation can have; however, a 140˚ spread appears as implausible as suggesting that the cores of all garnets in a field area grew at the same time. A rotation argument is difficult to reconcile with the clustered nature of the data in Stallard et al. (2003) and the consistently shallow plunges they have reported. Bell et al. (2004) give an example of how deformation partitioning provides a mechanism for variation in FIA orientations preserved in the cores of porphyroblasts and throughout their growth. Another important issue is that a FIA set represents FIAs with similar orientations and need not represent a single foliation-forming event. Studies demonstrating that spiral inclusion trails form as the result of porphyroblasts overgrowing many foliation events with similar strikes are an example of this (Bell et al. 1992, Johnson 1993). Such sequences of foliations result from the direction of bulk shortening remaining constant for a period. FIAs that form over such a long period may show some variation in orientation due to slight variations in the bulk shortening direction that are too small to distinguish.

Using the orientations of FIAs along with relative timing removes the subjectivity involved in attempting to correlate textures. Figure 10 shows a reinterpretation of the FIA data in Stallard et al. (2003) using this method; this is the same approach as their method 3. In this case four distinct FIA sets have been differentiated based on analysis of the non-parametric

data is from a random distribution can be rejected.. A north-south FIA set is attributed to CA19a and CA20 and the relative timing of this set cannot be determined as this orientation was only reported for single FIA samples. Relative timing criteria for the other three sets suggest a progression from, NE-SW to SE-NW to E-W sets. Each set has a spread of less than 70˚. These spreads are comparable to those in the other studies cited above. This is despite the fact that the FIA measurements in Stallard et al. (2003) are based on a small number of observations in each sample that would be prone to sampling error.

## *3.2 Correlating Deformation Along Orogens*

It has been suggested that FIAs can be used to correlate deformation events along orogenic belts (Bell et al. 1998, Bell & Mares 1999). In this section the use of FIAs for such correlations is demonstrated by comparing new data from the Murphy Syncline in the Western Blue Ridge of North Carolina with data published on the Baltimore-Washington anticlinorium in Maryland (Yeh & Bell 2004).

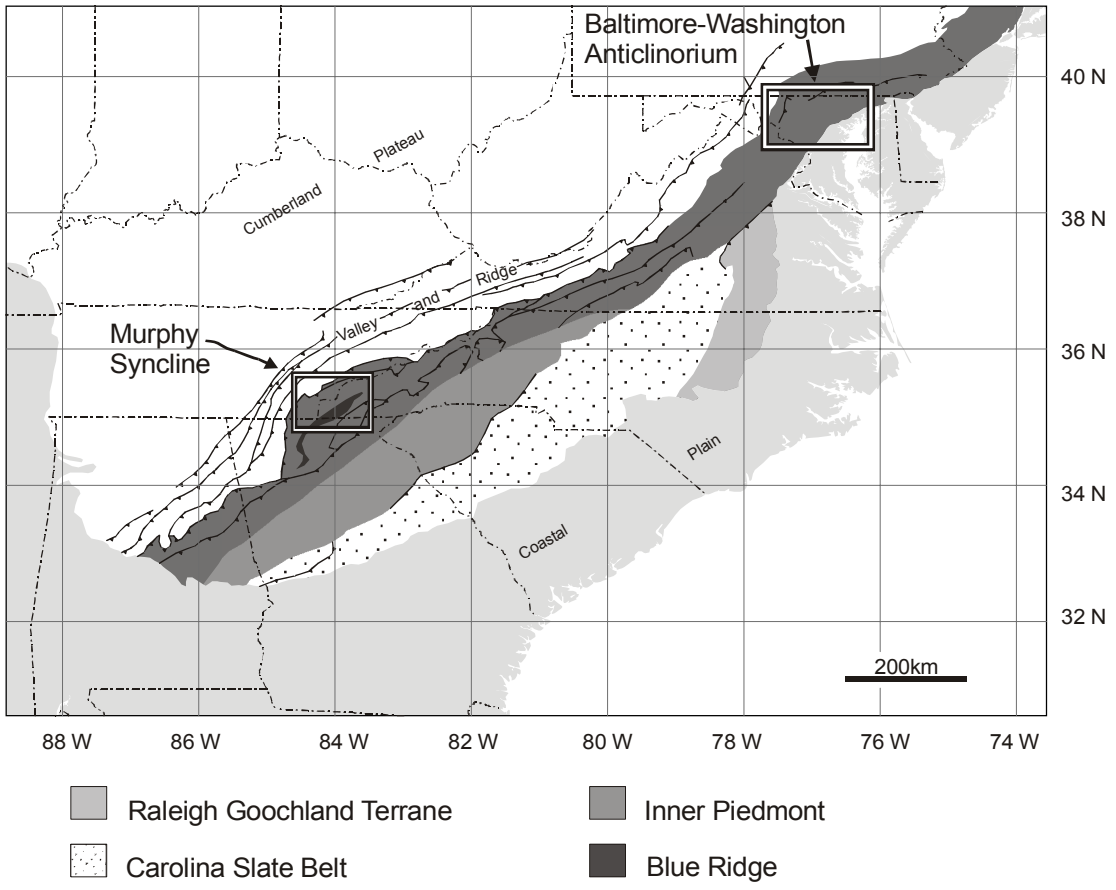


**Figure 11.** Simplified regional geology map of the central and southern Appalachians. The relative positions of the Murphy Syncline and Baltimore-Washington anticlinorium are shown.

### 3.2.1 Geological Setting – Murphy Syncline

The Murphy Syncline extends from south-west North Carolina into northern Georgia and nearby Tennessee (Fig. 11). It forms part of the western Blue Ridge of the Appalachian Orogeny (Hatcher 1987) and is bounded to the east by the Hayesville Fault and to the west by the Great Smoky and Greenbrier Faults. The rocks in the study area are meta-sediments from the late Pre-Cambrian to early Cambrian Murphy Belt and Great Smoky Groups (Hatcher 1987, Mohr 1973, Wiener & Merschat 1992). The Murphy Syncline is isoclinal with a moderately southeast dipping axial plane. Mohr (1973) suggests that the Murphy Syncline is a D1 structure, which formed either prior to or during the peak of regional metamorphism. Metamorphic grade ranges from green schist to amphibolite facies, with the lowest grades in the core of the syncline. The metamorphic peak in the western Blue Ridge was thought to have been reached during the Taconic orogeny at approximately 450 Ma, with little if any effect from either the Acadian or Alleghanian orogenies (e.g. Glover et al. 1983, Hatcher 1987, Rodgers 1987). However, Unrug and Unrug (1990) and Tull et al. (1993) have argued that the peak of metamorphism was in a single Acadian event based on fossil assemblages, as do recent electron probe micro-analyser (EPMA) age dates obtained from monazite (Kohn & Malloy 2004). Connelly and Dallmeyer (1993) argue for a polymetamorphic history involving both Taconic and Acadian events.

### 3.2.2 FIA Data – Murphy Syncline

63 FIA measurements have been made from 38 samples collected from the Murphy Syncline. The bootstrap MLE approach was applied to 20 FIAs from 14 samples (see Appendix 1.3). A $U^2$ test, as described by Bell et al. (1998), confirms that the data is non-random with a value of 0.321; this is significantly higher than the critical value at the 95% confidence level of 0.187, which means the hypothesis that the data is from a random distribution can be rejected. The data are plotted on a rose diagram in Figure 12, along with a non-parametric density estimate. There are four distinct peaks in the data at 60˚, 100˚, 140˚ and at 170˚. The 100˚ peak is the most pronounced. Figure 13 shows the data from all samples with estimated error. The FIAs and errors determined using the bootstrap MLE approach are plotted in Figure 13a. It was not possible to use this approach in all cases primarily due to insufficient sample sizes. The other 43 FIAs were measured using the asymmetry method and are plotted in Figure 13b. The errors in this plot are based on the sensitivity to sample size analysis in section 2.2.2. When the number of observations was small ($N$ = 3), the 95% confidence interval for the FIA orientation was never greater than ± 20˚ (appendix 2). This range seems to be a reasonable guide to the confidence that can be placed on an individual FIA measurement determined by the asymmetry method.

FIAs were assigned to different FIA sets using their orientations and relative timing criteria. Figure 13 shows 14 samples containing multiple FIA orientations that could be used to distinguish the sequence in which the FIAs formed. As a result, 6 possible FIA sets have been identified; N-S; NE-SW; E-W; SE-NW; N-S; and E-W. These will be referred to as FIA sets 1 to 6 respectively. Two FIA sets are repeated – sets 1 and 5 are both N-S and sets 3 and 6 are both E-W. Where samples have only a single FIA that is in either of these orientations it is impossible to declare which of the two possible FIA sets they belong to. Such single FIA samples could not be used to draw conclusions about the P-T conditions, or be dated to provide an age, for a particular FIA forming event. However, this does not change the FIA pattern in a region. There is only a single FIA measured as part of set 6. This measurement was made in kyanite from sample CH35. The relative timing of kyanite and staurolite in this sample is ambiguous; there are no clear overprinting criteria and the matrix foliation truncates inclusion trails from both types of porphyroblasts. If the kyanite predates the staurolite, this FIA would belong to set 3 and there would be no evidence for a 6$^{th}$ set.

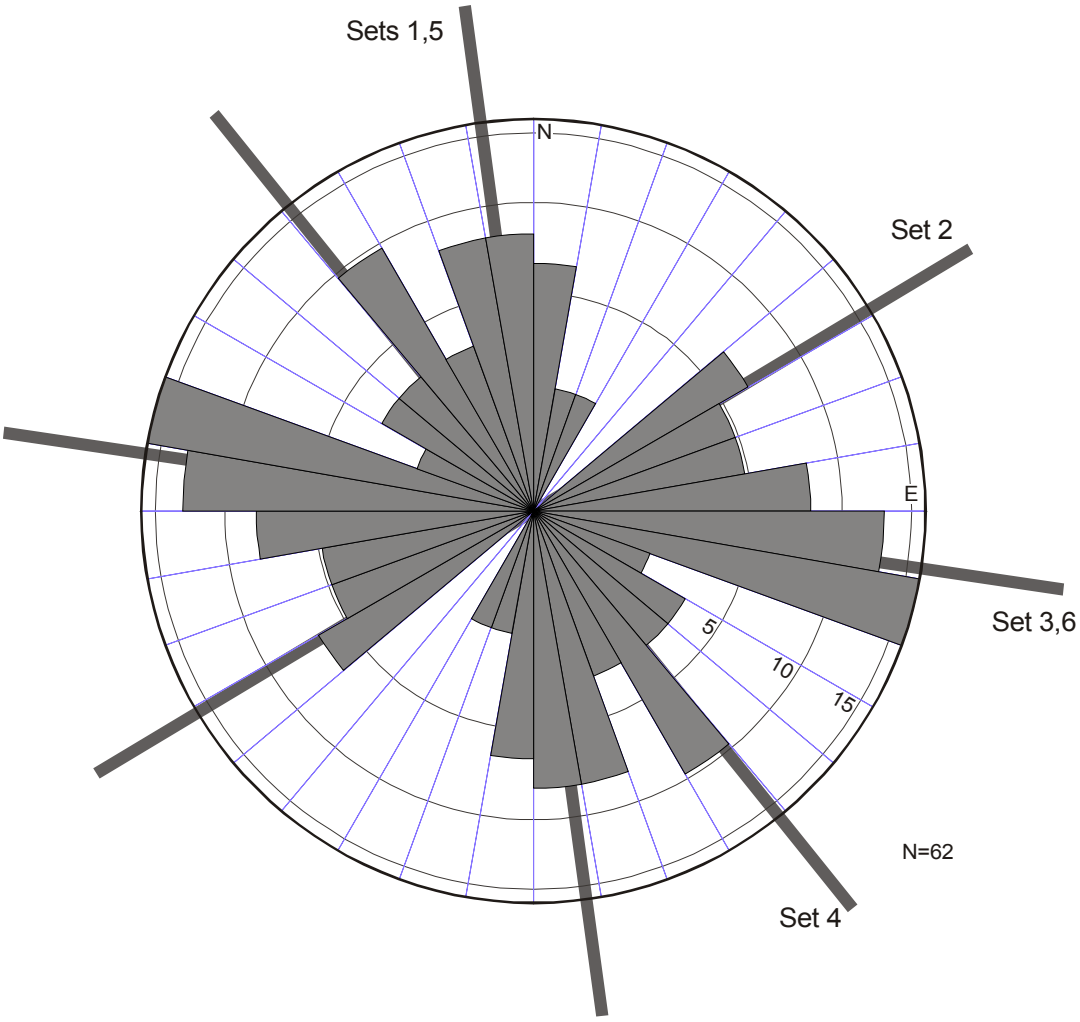


**Figure 12.** Murphy Syncline FIA data. Rose diagram with non-parametric density estimate (dashed line). Rose diagram bin radii proportional to square root of frequency, non-parametric smoothing factor 0.4 $H_0$. The data has peaks at approximately 60˚, 100˚, 140˚ and 170˚.

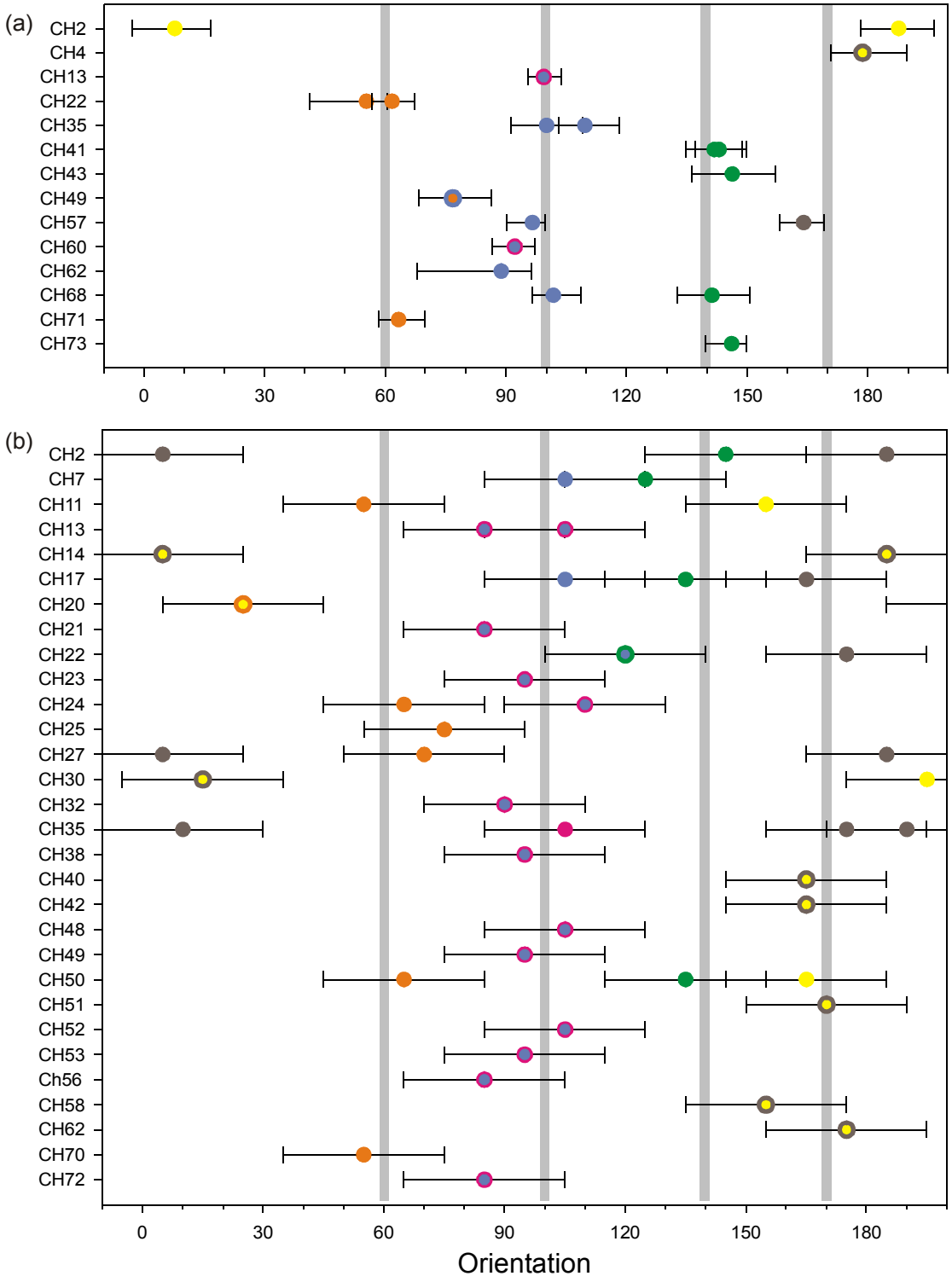


**Figure 13.** Distribution of FIAs with errors. Data analysed using the bootstrap MLE approach shown in (a). The error bars show the 95% confidence intervals. The data in (b) are for FIAs determined by the asymmetry method with error bars set at 20˚. Where FIA orientations are near 0˚ or 180˚ they have also been plotted twice, once at the original reading, $\mu_0$, and again at $\mu_0 \pm 180$˚ (so 175˚ becomes -5˚ and 5˚ becomes 185˚). FIA sets 1 through 6 in yellow, orange, blue, green, brown and pink. Colours are combined where no relative timing criteria are present to determine which FIA set an observation belongs to.

### 3.2.3 Comparison with Maryland Data

Yeh and Bell (2004) measured 221 FIAs in 140 oriented samples collected from the Baltimore-Washington anticlinorium within the Baltimore terrane of the eastern Maryland piedmont. They derived a sequence of 8 FIA sets using a similar approach to that applied to the Murphy Syncline data above. Deformation and metamorphism in the Baltimore terrane extended from the late Taconic (510 to 460 Ma) through to the early Acadian (408 to 360 Ma`; Yeh & Bell 2004 and references therein). This is a similar time period to that suggested by Connelly and Dallmeyer (1993) for metamorphism in the Murphy Syncline. If the assumption that FIAs represent the direction of bulk shortening within an orogenic belt at a given point in time is correct, then if the Baltimore and Murphy regions were undergoing deformation and metamorphism contemporaneously, their FIA progressions should be the same.

The progression of FIA sets derived from the Murphy region data is strikingly similar to that from the Baltimore region. The exception is that FIA set 1 from the Baltimore region is not represented in the Murphy data. Set 1 from the Murphy region correlates with sets 2 and 3 from the Baltimore region although they are recorded in too few samples to be separated. Sets 2, 3, 4 and 5 from the Murphy region correlate with sets 4,5, 6 and 7 from the Baltimore region respectively. These FIA sets are the most strongly represented in the Murphy region data and the correlation between the two regions is remarkable. As mentioned above, there may or may not be a 6$^{th}$ FIA set in the Murphy region data. If this FIA set does exist, it correlates with set 8 from the Baltimore region.

The correlation of FIA sets between the Murphy Syncline and the Baltimore-Washington anticlinorium provides strong evidence that these two regions underwent similar deformation histories. Recent EPMA age dating of monazite from the Murphy Syncline yield ages at both 450 Ma and 400 Ma (pers comm. Lisowiec 2005`; Kohn & Malloy 2004). This also supports the hypothesis that FIAs represent the direction of relative motion of tectonic plates; these regions are over 750 km apart and it is hard to imagine circumstances where identical FIA progressions could be developed by anything other than plate scale processes.

## *3.3 Detailed Studies – FIAs Across a Fold*

Another possible application of FIA data is in detailed studies where their orientations are compared to constrain age dates or deformation processes such as folding, or the rotational behaviour of porphyroblasts. An example of this was presented by Timms (2003) who did a study of matrix foliations and inclusion trails in garnet porphyroblasts preserved in a hand-sample-scale fold. The study included a comparison of the FIAs in each limb of the fold to make some inferences about fold forming processes and the porphyroblast rotation problem. The only measure of confidence he gives for the FIA measurements is the range over which both asymmetries are observed. The bootstrap MLE approach was applied to some of the data in

Timms (2003) to demonstrate how such a study can benefit from a technique that allows confidence intervals to be given to FIA measurements.

The fold is a tight, upright anticline and has a WSW trending fold axis. Timms (2003) uses the asymmetry method to determine the trend and plunge for a FIA preserved in the core of garnet porphyroblasts as well as the trend of a FIA in their rims on both limbs of the fold. He also used a technique similar to *FitPitch* (Aerden 2003) called the plane intersection method to determine the core FIA. This technique calculates the intersection of plains estimated from inclusion trail pitch measurements; no error estimates are provided.

The bootstrap MLE approach was applied to data collected by the asymmetry method for both the trend and plunge of the core FIA on the north and south limbs of the fold. The model fit for the trend data is poor on both limbs of the fold. This is most likely due to the lack of asymmetry observations particularly near the FIA (see appendix 1.4). The MLE of cyclic logistic model parameters uses observations of inclusion trail asymmetry. If the FIA in a porphyroblast has the same orientation as the thin section that intersects it, then it will show a millipede-like texture, that is, a symmetrical pattern. The data from Timms (2003) presented in appendix 1.4 includes observations of virtual millipedes with highest counts in the vicinity of the asymmetry switch. To make use of these data in the MLE approach, two observations of millipede-like inclusion trails were counted as one clockwise and one anticlockwise observation. If the total number of millipede-like observations was odd, the remaining one was ignored to keep the number of observations as an integer. The use of millipede-like observations is discussed further in 4.2.2. Bootstrap MLE results for data including the millipede-like observations produces good model fits for data from both the north and south limbs of the fold (Figs. 14 and 15 respectively). The results are presented in Table 1.

| | **μ** | | | **β** | |
|---|---|---|---|---|---|
| | **mean** | **95% Conf.** | **90% Conf.** | **mean** | **95% Conf.** |
| **North Limb** | | | | | |
| FIA Trend | 33.7° | 27.9° to 40.7° | 28.8° to 39.6° | 5.9 | 3.9 to 7.6 |
| FIA Plunge | 2.5° SSW | -9.1° to 12.3° | | 4.3 | 2.7 to 5.3 |
| **South Limb** | | | | | |
| FIA Trend | 18.8° | 11.6° to 28.1° | 12.6° to 26.6° | 4.0 | 3.1 to 4.6 |
| FIA Plunge | 20.4° SSW | 12.6° to 26.8° | | 6.2 | 4.4 to 9.1 |
| **Homogeneity Analysis** | | **Critical Values** | | | |
| **Yr Trend** | 9971 | **95%** | 3.84 | | |
| **Yr Plunge** | 9645 | **99%** | 6.63 | | |

**Table 1.** Analysis of core FIA data from Timms (2003). The Yr parameter is from a test similar to a t-test (p. 115-117 Fisher, 1993). It shows that the hypothesis that the data from the two limbs have different means at a very high level of confidence.

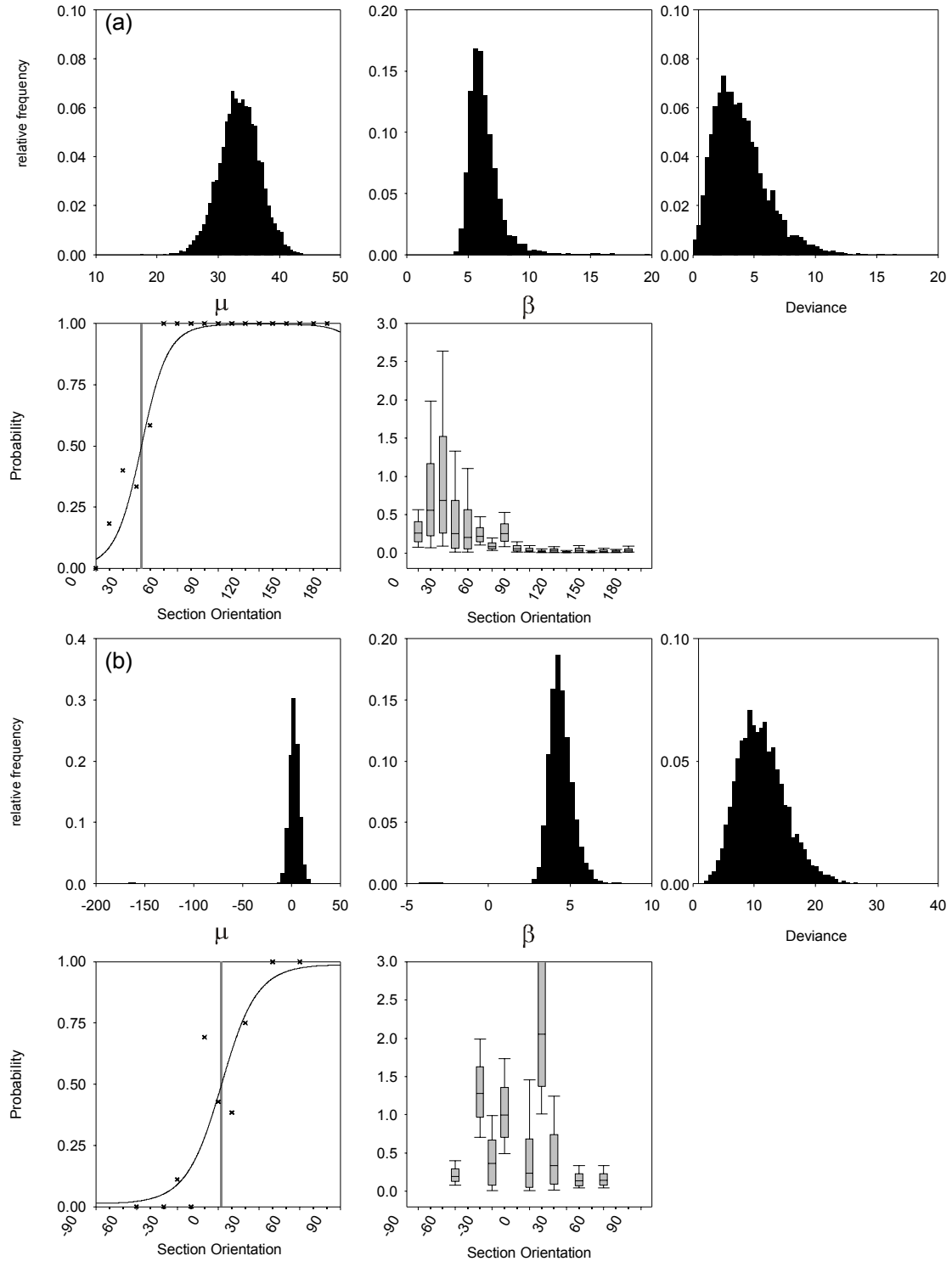


**Figure 14.** Bootstrap MLE applied to North limb FIA from Timms (2003). The trend is in (a) and the plunge is in (b). Plunges are to the SSW (negative plunges are to the NNE). Millipede-like data included.

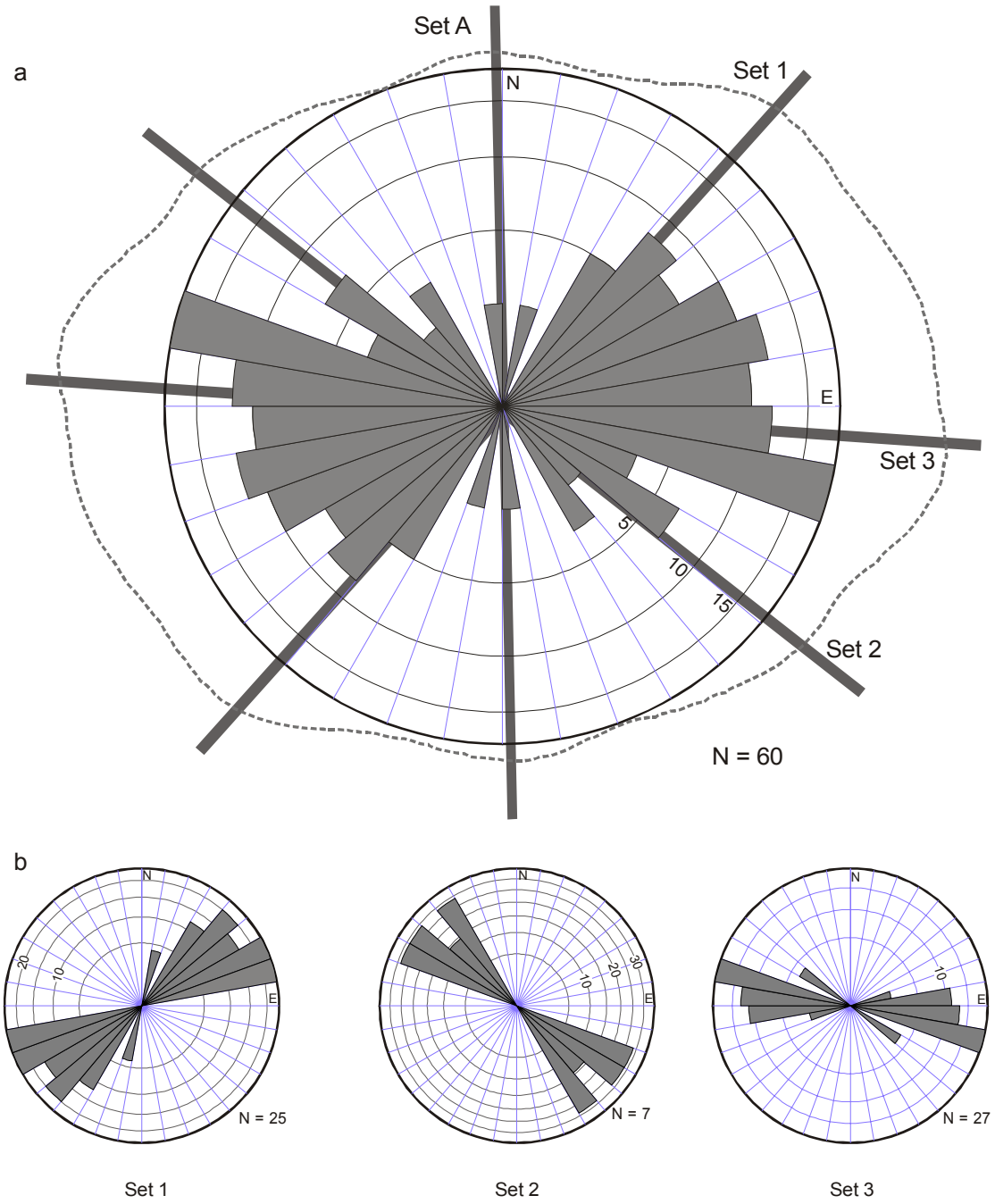


**Figure 10.** Reinterpreted FIA data from Stallard et al. (2003). A rose diagram with non-parametric density estimate (dashed line) for the whole dataset is shown in (a). The non-parametric density estimate is a similar approach to the moving averages used by Yeh and Bell (2004). Rose diagram bin radii proportional to square root of frequency. Non-parametric smoothing factor 0.6 $H_0$.The NE -SW, SE-NW and E-W FIA sets are shown in (b).

density estimate (Fisher 1993) in Figure. 10. This is similar to the weighted average approach used by Yeh (2003) and Yeh and Bell (2004) and is preferred to rose diagrams which can be distorted by the selection of cell boundaries (Fisher 1993). A $U^2$ test, as described by Bell et al. (1998), confirms that the data is non-random with a value of 0.857; this is significantly higher than the critical value at the 95% confidence level of 0.187, which mean the hypothesis that the

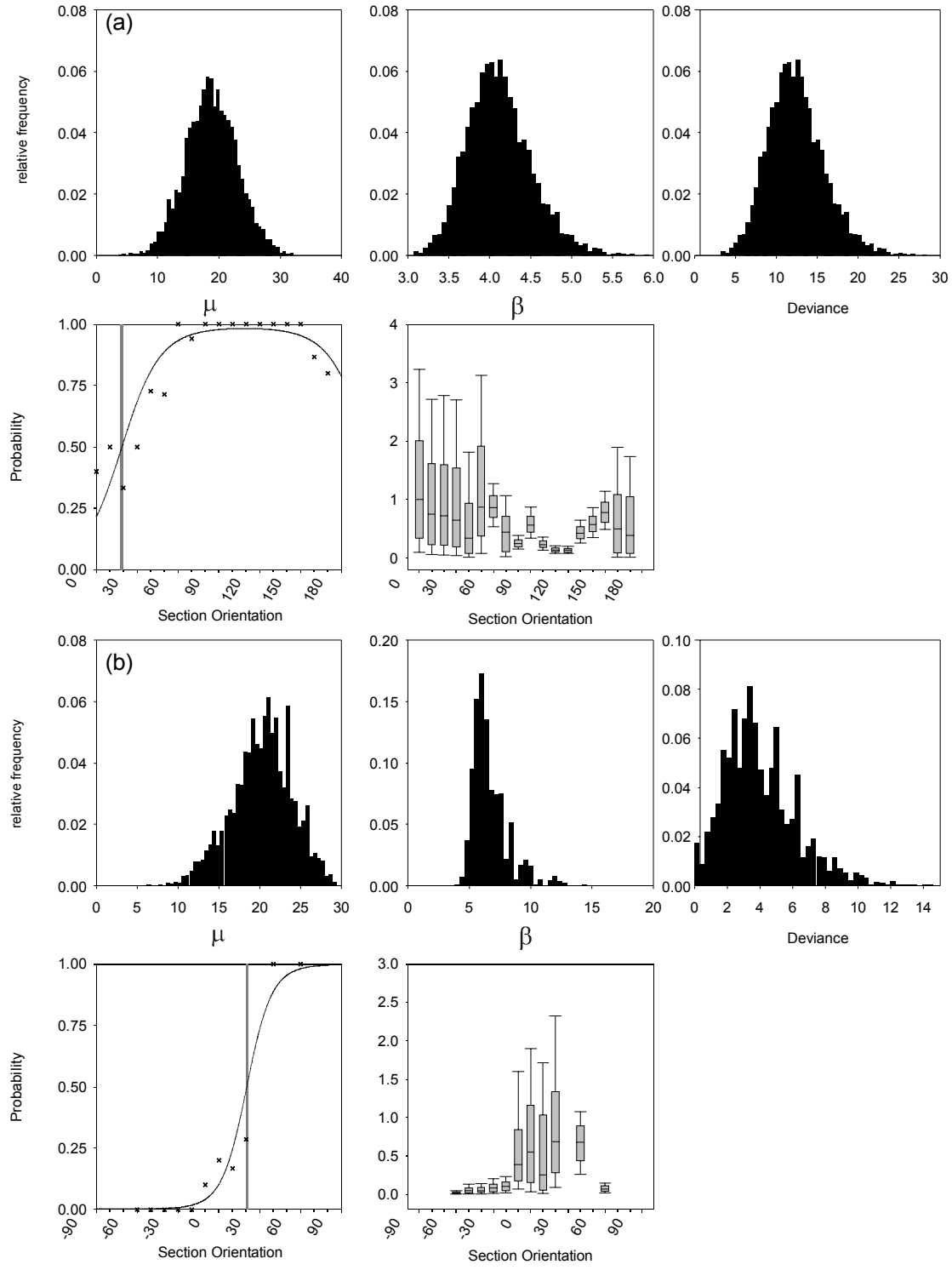


**Figure 15.** Bootstrap MLE applied to South limb FIA from Timms (2003). The trend is in (a) and the plunge is in (b). The model fit to the plunge data is only just acceptable. Plunges are to the SSW (negative plunges are to the NNE). Millipede-like data included.

The confidence intervals derived for the trends of the FIAs on the two limbs of the fold overlap slightly at the 95% confidence level. The plunges do not overlap at this confidence level. A test for homogeneity, called the $Y_r$ test (Fisher 1993), which is similar to a t-test used for linear data, shows that the mean orientations of both the trends and plunges on each side of the fold differ from each other at even the 99% confidence level (Table. 1). These results confirm that the FIA orientations differ across the limbs of the fold to a high level of certainty.

Timms (2003) does not provide error estimates for the FIAs calculated using the *plane intersection method*. Considering that the standard deviations given for the best fit poles to the estimated planes are in the order of 15°, the 95% confidence interval in the intersection of the planes (i.e. the FIA) will be correspondingly large. It is important in drawing conclusions from such data that the level of confidence that can be placed in the conclusions is considered. The MLE approach described here makes it possible to test hypotheses about the relationship between FIA orientations with some statistical certainty.

# 4 Discussion and Conclusions

## *4.1 The Variability of FIAs*

FIA orientations will vary at both the hand sample and regional scales. The study presented in chapter 2 demonstrates this variability in a single sample and shows that FIAs in a FIA set can vary by 70°. The shape parameter, β, in the cyclic logistic model provides a measure of this spread. Analysis of the data presented here shows that β values range from 3.5 to 9.4 with an average of 5.6. Figure 16 shows probability plots based on β values from 20 samples normalized to $\mu = 90°$ and demonstrates the consistency of the modelled FIA distributions. They show that the range of FIAs in sample will generally be between 40° to 80°. These distributions are unimodal, symmetrical, have a peak at their mean and the probabilities decay monotonically away from it, as occurs in a normal distribution. In plain English, FIAs will be clustered in a narrow interval about the mean and will have progressively fewer observations towards the extremes of the range.

The trends of FIAs show a similar distribution on the regional scale. Bell and Mares (Bell & Mares 1999) describe FIA distributions from the Kimberley orogenic arc in Western Australia. They identified two FIA sets that are at right angles to each other, allowing them to be easily distinguished. The first FIA set has 58 measurements with a spread of 50°; the second has a spread of 30° but is represented by only 8 measurements. Similar FIA distributions were found in the three main FIA sets in the reinterpreted Canton Schist data (section 3.1); these sets had ranges of 70°, 40° and 60° respectively. The Murphy Syncline data (section 3.2) shows spreads of 60°, 40°, 30° and 50° for FIA sets 2 to 5. This spread in FIA data on regional scales

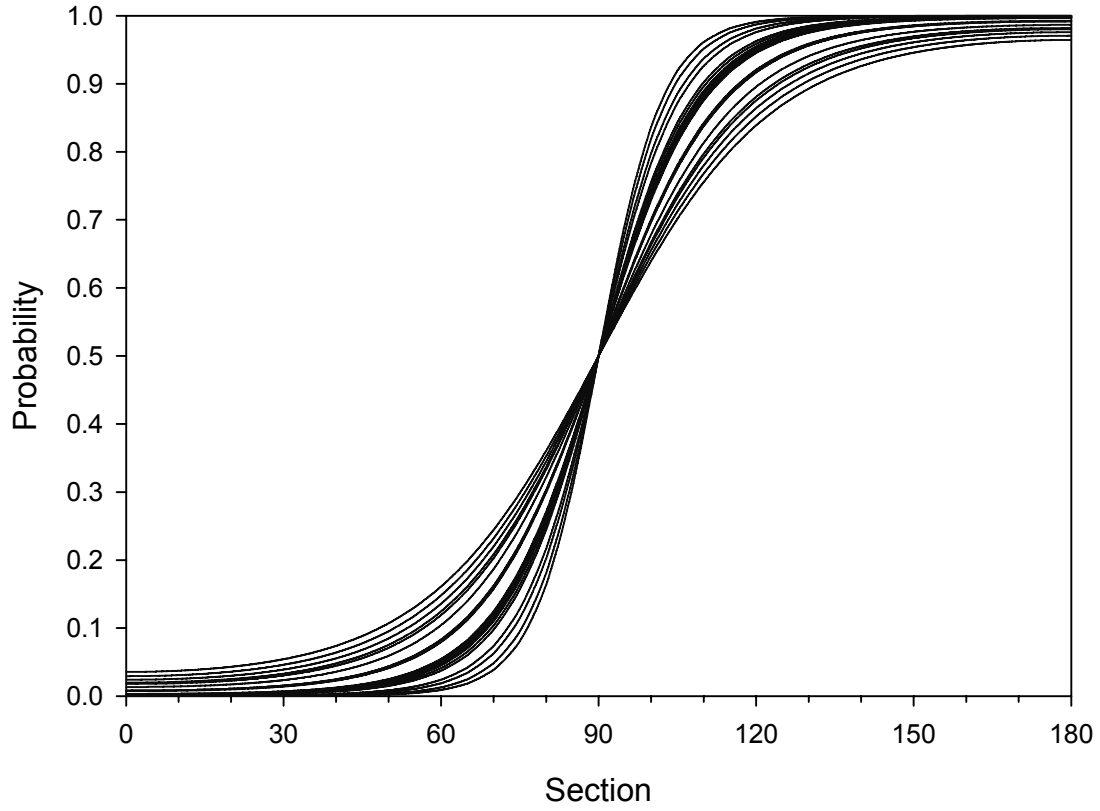


**Figure 16.** FIA distributions from real samples. This plot shows the FIA distributions from 20 samples analysed from Vermont, New Hampshire and North Carolina, normalized to a FIA orientation of 90˚.

is typical of all results in the literature published to date (e.g. Bell et al. 1998, Cihan & Parsons 2005, Sayab 2005, Yeh & Bell 2004). It could be argued that these distributions are an artefact because most studies of FIA data use orientation to group the data. However, distributions of this size are also found where FIA sets lie at high angles to each other (e.g. Bell & Mares 1999, Sayab 2005) and when relative timing criteria allow them to be clearly differentiated (e.g. Bell et al. 1998, Yeh & Bell 2004). The shapes of regional FIA distributions are generally the same as those within a sample, approximating a normal distribution.

The distribution of FIAs at hand sample scale is very similar to that observed at regional scales. If porphyroblast rotation were a common process, it would be difficult to imagine the circumstances where such consistent FIA groupings would form, especially in multi-FIA samples. These distributions suggest that the variation in FIA orientations is related to variations in the foliations that form them and is consistent with a non-rotational model. The literature does not provide an adequate discussion of the variability of foliations at any scale. While the processes that may cause the orientation of a foliation to vary (described in section 1.2) have been addressed in the literature, no study has linked these processes to hand sample and regional

scale variations. This gap in knowledge is begging to be filled. The distribution of FIAs may actually provide us with a hypothesis to test – that is, that foliations formed in a single event vary in orientation by up to 70° on all scales.

The conclusions of Stallard et al. (2003) that FIA orientations can vary by up to 140° was based on the flawed approach of correlating FIAs between samples using microstructural textures. Unfortunately their conclusions have been used by at least one author to question the significance of FIA measurements (Vernon 2004). The consistent results obtained here and in other FIA studies demonstrate that large variations in FIA orientations within a set do not occur.

## 4.2 The Collection and Use of FIA Data

FIA studies to date contain no indication of any kind of minimum standard for the measurement and presentation of data. This lack of standards is the case for most structural data; for example, there is no standard for presenting fold axes measured in an area. This raises the following questions: should a shape analysis based on eigenvalues be used (Woodcock 1977); or is a stereonet enough, and, if so, should equal angle or equal area be used? It seems that the geological community is not critical of how such data is presented. FIAs, on the other hand, are not measured directly and the concept that they remain consistently oriented in spite of the overprinting effects of younger deformations is difficult for many to accept. The following section explores the best practice for determining and reporting FIA data.

### 4.2.1 Comparison of FIA Measurement Techniques

The two basic techniques for measuring FIAs are the asymmetry and the *FitPitch* methods. The most commonly used asymmetry method uses the asymmetry of curved inclusion trails to define the trend of a FIA. The *FitPitch* method measures FIAs by first finding the orientations of planar foliations that result in straight inclusion trails in thin section and by then calculating their intersection. The plane intersection method used by Timms (2003) is similar to the *FitPitch* except that it relies on the user determining which pitches should be grouped together to define a particular foliation. *FitPitch* determines fits of one, two or three model planes to the pitch data and provides parameters that help to assess which model planes best fit the data. Comparison studies of the *FitPitch* and asymmetry methods produce comparable results (Timms 2003`; unpublished data, Bruce, 2005).

To use the asymmetry method, inclusion trails must exhibit some curvature. If the inclusion trails are straight, the *FitPitch* and plane intersection methods can be used. The advantage of the asymmetry method is that a confidence interval can be assigned to FIA measurements using the bootstrapped MLE approach. *FitPitch* does not provide a measure of error for its FIA estimates and neither does the plane intersection method as applied by Timms (2003). Because the plane intersection method is based on the intersection of two planes fitted

to pitch data, error estimates for the orientation of these planes could be propagated to determine the error of a FIA measured this way.

Both of these approaches for finding FIAs require a minimum amount of data to get meaningful results. For the asymmetry method, samples where the number of observations in each thin section is less than ten should be treated with caution, particularly within a 60° interval centred on the point at which the asymmetries flip. It is likely that a similar number of observations would be required for the *FitPitch* approach.

### 4.2.2 Using "Millipedes" with the Bootstrapped MLE Appraoch

The asymmetry method relies on the fact that the intersection of a curved inclusion trail in thin section will either be clockwise or anticlockwise. The FIA lies at the point at which the probability of observing a particular geometry (e.g. clockwise), is half. A third possible geometry that may be observed in thin sections that are parallel to the FIA are millipede-like inclusion trail geometries. The term millipede was first used by Rubenach and Bell (1980) to describe inclusion trails that form as the result of coaxial deformation. True millipede trails display no asymmetry regardless of the orientation they are intersected at. Millipede-like refers to the case when inclusion trails that appear to be millipedes are observed as the result of a cut effect (Bell and Bruce, pers. comm., 2005). These features will be observed when curved inclusion trails are intersected by a thin section cut parallel to their axis of curvature (e.g fig 4.d,f in Stallard et al. 2002).

The occurrence of millipede-like geometries is used in the asymmetry method as an indication that the thin section containing them lies close to the orientation of the FIA. These observations can be important in examples where the number of porphyroblasts with clear asymmetries is low in sections oriented near the FIA. The data from Timms (2003) examined in section 3.3 is a good example of this (appendix 1.4). The bootstrapped MLE approach is based on a logistic model which looks at the probability of a success (clockwise observation) or a failure (anticlockwise observation). To include millipede-like observations they need to be reclassified as one of these two options. The recommended approach is to count each two millipede-like observations as one clockwise and one anticlockwise observation. If there were an odd number of observations the last is ignored to keep the number of observations as an integer. Millipede-like data push the observed probability of a success towards 0.5 when used in this way. The effect of counting a millipede-like observation as both one clockwise and one anticlockwise observation is to weight them as two observations, which would bias the results.

Before using millipede-like inclusion trails in the asymmetry method, it is imperative that the user is certain that they are not true millipedes. If millipede textures are observed in all section orientations in a sample then they most likely are true millipedes and should not be used. Collecting sufficient asymmetry observations so that millipede-like observations do not have to

be used would avoid this issue altogether. Other types of inclusion trail geometries, such as straight or shotgun patterns cannot be interpreted as having a geometry related to the FIA orientation and are of no value in determining FIAs using the asymmetry method.

### 4.2.3 Detailed Studies

FIAs provide a potential marker that can be used as a reference frame both within and between samples. When used in this way, it is important that potential errors in the orientation of FIA measurements are given. The analysis of the core FIA data from Timms (2003) in section 3.3 demonstrates how inferences made based on FIA data can be strengthened when the confidence in a FIA measurement is provided. The bootstrapped MLE approach provides a technique whereby confidence intervals of a FIA measurement can be readily determined. It also helps the recognition of samples where FIAs may be from a mixed or randomly distributed population, and where the number of observations is insufficient to have confidence in a FIA measurement.

Another example of where the bootstrapped MLE approach would have been of benefit appears in a paper on dating of FIAs by Bell and Welch (2002). They used EPMA age dating of monazite to constrain the timing of FIA formation in several samples from Vermont. This involved correlating FIAs between sample and within a regional data set. The strength of such correlations may be called into question unless the confidence intervals for the orientations of the FIAs in each sample are given, as they are for the age dates.

As well as reporting the orientations for FIAs, shape parameters ($\beta$) and their confidence intervals, the raw asymmetry counts, the number of bootstraps, the bootstrap technique used, and plots of the distributions of $\mu$, $\beta$ and the sample deviance should also be included when reporting the results of detailed studies. Any relative timing criteria should also be described. Providing the information allows the reader to confirm the goodness-of-fit of the proposed model parameters and to re-evaluate the data as they see fit. Techniques such as *FitPitch* or the plane intersection method should only be used for detailed studies if errors for the determined FIA orientations are calculated.

### 4.2.4 Regional Studies

Regional FIA studies are concerned with the distribution and relative timing of FIA sets for the region as a whole rather than within individual samples. Any error in individual measurements will be accommodated within the distribution of FIAs in a set if a sufficiently large number of measurements have been made. The number of FIA measurements required would depend on the number and distribution of FIA sets in the region, so the minimum sample size will vary. Descriptive statistical techniques for circular data, such as those outlined in Fisher (1993) or Mardia and Jupp (2000), can be applied. These methods would allow the inferences based on the distributions of FIA sets to be made with proper statistical rigour.

A key component of the analysis of regional datasets is the determination of FIA sets. There are three components to this: defining the trends of FIA sets; deciding which measurements belong in each set; and determining the relative timing of FIA sets. Graphical techniques such as the weighted average approach used by Yeh and Bell (2004) or the non-parametric density estimate used here provide a means of identifying peaks in the whole data set. The non-parametric density estimate, which was recommended by Fisher (1993), provides a way of exploratory analysis of circular data. It is comparable to a weighted average and allows data to be examined without the bias that may be present in a rose diagram due to the location of bin boundaries. A parametric density estimate is similar to the moving average used by Yeh and Bell (2004) and has the advantage of avoiding the issues that arise in presenting circular data on a linear plot. Once these peaks are identified the individual FIA measurements can be assigned to FIA sets based on their orientation. It is important to emphasize the point that using inclusion trail textures is a totally unreliable approach due to the effects of deformation partitioning.

The order in which the FIA sets formed can be determined using relative timing criteria once the orientations of FIA sets have are identified. Relative timing criteria can only be applied within samples. Applying these criteria between samples makes too great an assumption on the pervasiveness of deformation and metamorphism. The are only two reliable relative timing criteria; where two or more FIAs with different orientations are found in individual porphyroblasts; and where different FIAs are preserved in different porphyroblastic phases with clear overprinting relationships. Absolute timing using *in situ* age dating could also be used, although this would be impractical for large datasets. In some cases relative timing criteria may reveal FIA sets that overlap or are repeated, such as in the Murphy Syncline data described in section 3.2.2. It is not possible to assign a FIA measurement to one of these sets for single FIA samples when overlap or repitition occurs.

The bootstrapped MLE approach would provide little additional information for large regional datasets. There may be some value in analysing a group of representative samples from the region to characterize the typical intra sample FIA distributions. This scrutiny may prove critical when trying to assign a FIA measurement to a given FIA set. It is also recommended that the bootstrap MLE approach be applied when a sample is being used to determine a FIA set's age or the P-T conditions it formed under. This approach provides some certainty that the data from that sample does have an orientation that matches the FIA set in question.

## 4.3 The Significance of FIAs

FIAs preserve the fabrics formed by the deformation events that were active at the time the porphyroblasts grew. Importantly, they preserve the orientation of these fabrics through subsequent deformation events that reorient or destroy the equivalent fabrics in the matrix. FIAs are analogous to the intersection lineation between subsequent foliations. Their significance is

similar to that of intersection lineations with the distinction that they will not have been reoriented by subsequent deformation events. The consistent distribution of FIAs within samples together with the fact that they can easily be grouped as FIA sets suggest that any reorientation of FIAs by rotation of porphyroblasts relative to each other is insignificant.

Because foliations typically form in sub-horizontal and sub-vertical orientations (Bell & Johnson 1989, Bell & Newman 2006), FIA trends will reflect the orientation of the sub-vertical foliations that formed them. If foliations form perpendicular to the direction of bulk shortening, so will FIAs. A FIA set can represent a number of foliation forming events, so it is representative of a time period when the direction of horizontal bulk shortening was relatively constant. FIA sets can be correlated between samples or between regions providing a more detailed history of the deformation than is possible by using macro-scale structures or matrix microstructures. This history provides a reference frame in which age dates and P-T paths can be placed.

FIA data have been applied to many geological problems: investigating tectono-metamorphic histories and correlating multiple phases of metamorphism on local and orogenic scales (e.g. Bell et al. 2005, Bell et al. 1998, Bell & Mares 1999, Cihan & Parsons 2005, Lee et al. 2000, Sayab 2005, Yeh & Bell 2004); investigating foliation development and folding mechanisms (Bell & Hickey 1997, Timms 2003); arguing for the lack of porphyroblast rotation (Bell et al. 1997, Ham & Bell 2004, Hickey & Bell 1999); studying porphyroblast nucleation and growth relative to deformation (Bell et al. 2003, Bell et al. 2004); reconstructing plate motions (Bell et al. 1995); constraining age dates (Bell & Welch 2002); defining complex deformation partitioning patterns (Bell et al. 2004); and investigating pluton emplacement mechanisms and timing (Davis 1993). The analytical techniques recommended here will enhance future applications of FIA data by ensuring that the interpretations are statistically valid.

# References

Aerden, D. 2003. Preferred orientation of planar microstructures determined via statistical best-fit of measured intersection-lines: the 'FitPitch' computer program. *Journal of Structural Geology* **25**(6), 923-934.

Aerden, D. 2004. Correlating deformation in Variscan NW-Iberia using porphyroblasts; implications for the Ibero-Armorican Arc. *Journal of Structural Geology* **26**(1), 177-196.

Aerden, D. G. A. M. 1995. Porphyroblast non-rotation during crustal extension in the Variscan Lys-Caillaouas Massif, Pyrenees. *Journal of Structural Geology* **17**, 709-725.

Beirmeier, C. & Stuwe, K. 2003. Strain rates from snowball garnet. *Journal of Metamorphic Geology* **21**, 253-268.

Bell, T. H. 1978. The development of slaty cleavage across the Nackara Arc of the Adelaide Geosyncline. *Tectonophysics* **51**(3-4), 171-174.

Bell, T. H. 1986. Foliation development and reactivation in metamorphic rocks: the reactivation of earlier foliations and decrenulation due to shifting patterns of deformation partitioning. *Journal of Metamorphic Geology* **4**, 421-444.

Bell, T. H. & Chen, A. 2002. The development of spiral-shaped inclusion trails during multiple metamorphism and folding. *Journal of Metamorphic Geology* **20**(4), 397 -412.

Bell, T. H. & Duncan, A. C. 1978. A rationalized and unified shorthand terminology for lineations and fold axes in tectonites. *Tectonophysics* **47**(1-2), T1-T5.

Bell, T. H., Forde, A. & Hayward, N. 1992. Do smoothly-curving spiral shaped inclusion trails signify porphyroblast rotation? *Geology* **20**, 59-62.

Bell, T. H., Forde, A. & Wang, J. 1995. A new indicator of movement direction during orogenesis: measurement technique and application to the Alps. *Terra Nova* **V. 7**, 500-508.

Bell, T. H., Ham, A. P., Hayward, N. & Hickey, K. A. 2005. On the development of gneiss domes. *Australian Journal of Earth Sciences* **42**(2), in press.

Bell, T. H., Ham, A. P. & Hickey, K. A. 2003. Early formed regional antiforms and synforms that fold younger matrix schistosities: their effect on sites of mineral growth. *Tectonophysics* **367**(3-4), 253 -278.

Bell, T. H., Ham, A. P. & Kim, H. S. 2004. Partitioning of deformation along an orogen and its effects on porphyroblast growth during orogenesis. *Journal of Structural Geology* **26**(5), 825 -845.

Bell, T. H. & Hayward, N. 1991. Episodic metamorphic reactions during orogenesis; the control of deformation partitioning on reaction sites and reaction duration. *Journal of Metamorphic Geology* **9**(5), 619-640.

Bell, T. H. & Hickey, K. A. 1997. Distribution of pre-folding linear indicators of movement direction around the Spring Hill Synform, Vermont; significance for mechanism of folding in this portion of the Appalachians. *Tectonophysics* **274**(4), 275-294.

Bell, T. H. & Hickey, K. A. 1999. Complex microstructures preserved in rocks with a simple matrix; significance for deformation and metamorphic processes. *Journal of Metamorphic Geology* **17**(5), 521-535.

Bell, T. H., Hickey, K. A. & Upton, G. J. G. 1998. Distinguishing and correlating multiple phases of metamorphism across a multiply deformed region using the axes of spiral, staircase and sigmoidal inclusion trails in garnet. *Journal of Metamorphic Geology* **16**(6), 767-794.

Bell, T. H., Hickey, K. A. & Wang, J. 1997. Spiral and staircase inclusion trail axes within garnet and staurolite porphyroblasts from schists of the Bolton Syncline, Connecticut; timing of porphyroblast growth and the effects of fold development. *Journal of Metamorphic Geology* **15**(4), 467-478.

Bell, T. H. & Johnson, S. E. 1989. Porphyroblast inclusion trails: the key to orogenesis. *Journal of Metamorphic Geology* **7**, 279-310.

Bell, T. H. & Mares, V. M. 1999. Correlating deformation and metamorphism around orogenic arcs. *American Mineralogist* **84**(11-12), 1727 -1740.

Bell, T. H. & Newman, R. 2006. Appalachian orogenesis: the role of repeated gravitational collapse. In: *Styles of Continental Compression. Geological Society of America Speacial Paper xxx.* (edited by Mazzoli, S. & Butler, R.) **In Press**. Geological Society of America, Bolder, Colarado.

Bell, T. H. & Rubenach, M. J. 1980. Crenulation cleavage development--evidence for progressive bulk inhomogeneous shortening from "millipede" microstructures in the robertson river metamorphics. *Tectonophysics* **68**(1-2), T9-T15.

Bell, T. H. & Wang, J. 1999. Linear indicators of movement direction (mineral elongation lineations, stretching lineations and slickensides) versus Foliation Intersection Axes in porphyroblasts (FIAs) and their relationships to directions of relative plate motion. *Earth Science Frontiers* **6**, 31-47.

Bell, T. H. & Welch, P. W. 2002. Prolonged Acadian orogenesis: Revelations from foliation intersection axis (FIA) controlled monazite dating of foliations in porphyroblasts and matrix. *American Journal of Science* **302**(7), 549 -581.

Cihan, M. & Parsons, A. 2005. The use of porphyroblasts to resolve the history of macro-scale structures: an example from the Robertson River Metamorphics, North-Eastern Australia. *Journal of Structural Geology* **27**(6), 1027-1045.

Connelly, J. B. & Dallmeyer, R. D. 1993. Polymetamorphic Evolution of the Western Blue Ridge - Evidence from Ar-40/Ar-39 Whole-Rock Slate/Phyllite and Muscovite Ages. *American Journal of Science* **293**(4), 322-359.

Davis, B. K. 1993. Mechanism of emplacement of the Cannibal Creek Granite with special reference to timing and deformation history of the aureole. *Tectonophysics* **224**, 337-362.

Evins, P. M. 2005. A 3D study of aligned porphyroblast inclusion trails across shear zones and folds. *Journal of Structural Geology* **In Press, Corrected Proof**, 1300-1314.

Fisher, N. I. 1993. *Statistical analysis of circular data*. Cambridge University Press, Cambridge, [England].

Fyson, W. K. 1980. Fold fabrics and emplacement of an Archean granitoid pluton, Cleft Lake, Northwest Territories. *Canadian Journal of Earth Science* **V.17**, 325 - 332.

Glover, L., Speer, J. A., Russell, G. S. & Farrar, S. S. 1983. Ages of Regional Metamorphism and Ductile Deformation in the Central and Southern Appalachians. *Lithos* **16**(3), 223-245.

Ham, A. P. & Bell, T. H. 2004. Recycling of foliations during folding. *Journal of Structural Geology* **26**(11), 1989-2009.

Hatcher, R. D. 1987. Tectonics of the Southern and Central Appalachian Internides. *Annual Review of Earth and Planetary Sciences* **15**, 337-362.

Hayward, N. 1990. Determination of early fold axis orientations in multiply deformed rocks using porphyroblast inclusion trails. *Tectonophysics* **V. 179**, 353-369.

Hayward, N. 1992. Microstructural analysis of the classical spiral garnet porphyroblasts of South-east Vermont; evidence for non-rotation. *Journal of Metamorphic Geology* **10**(4), 567-587.

Hickey, K. A. & Bell, T. H. 1999. Behaviour of rigid objects during deformation and metamorphism; a test using schists from the Bolton Syncline, Connecticut, USA. *Journal of Metamorphic Geology* **17**(2), 211-228.

Johnson, S. E. 1990. Lack of porphyroblast rotation in the Otago schists, New Zealand: implications for crenulation cleavage development, folding and deformation partitioning. *Journal of Metamorphic Geology* **8**, 13-30.

Johnson, S. E. 1993. Unravelling the spirals: a serial thin-section study and three dimensional computer-aided reconstruction of spiral-shaped inclusion trails in garnet porphyroblasts. *Journal of Metamorphic Geology* **11**, 621-634.

Johnson, S. E. 1999a. Near-orthogonal foliation development in orogens: meaningless complexity, or reflection of fundamental dynamic processes. *Journal of Structural Geology* **21**, 1183-1187.

Johnson, S. E. 1999b. Porphyroblast microstructures: A review of current and future trends. *American Mineralogist* **V.84**, 1711-1726.

Jung, W. S., Ree, J. H. & Park, Y. 1999. Non-rotation of garnet porphyroblasts and 3-D inclusion trail data: an example from the Imjingang belt, South Korea. *Tectonophysics* **307**(3-4), 381-395.

Kohn, M. J. & Malloy, M. A. 2004. Formation of monazite via prograde metamorphic reactions among common silicates: implications for age determinations. *Geochimica et Cosmochimica Acta* **68**(1), 101-113.

Lee, H., Lee, B.-J. & Otoh, S. 2000. Significance of systematic changes in crenulation asymmetries within meta-sediments across the Ogcheon Supergroup in the Goesan area, southern Korea. Hanrimwon Publishing Company for the Geological Society of Korea, Seoul, South Korea, 115-134.

Mardia, K. V. & Jupp, P. E. 2000. *Directional Statistics*. J. Wiley, Chichester, England.

Mohr, D. W. 1973. Stratigraphy and Structure of Part of Great Smoky and Murphy Belt Groups, Western North-Carolina. *American Journal of Science* **A273**, 41-71.

Powell, D. & Treagus, J. E. 1967. On the geometry of S-shaped inclusion trails in garnet porphyroblasts. *Mineralogical Magazine* **36**, 453-456.

Rodgers, J. 1987. The Appalachian-Ouachita Orogenic Belt. *Episodes* **10**(4), 259-266.

Rosenfeld, J. L. 1970. *Rotated Garnets in Metamorphic Rocks. Geological Society of America Special Paper, 129*. Geological Society of America, Boulder, Colarado.

Sayab, M. 2005. Microstructural evidence for N-S shortening in the Mount Isa Inlier (NW Queensland, Australia): the preservation of early W-E-trending foliations in porphyroblasts revealed by independent 3D measurement techniques. *Journal of Structural Geology* **27**(8), 1445-1468.

Stallard, A., Hickey, K. A. & Upton, G. J. G. 2003. Measurement and correlation of microstructures: the case of foliation intersection axes. *Journal of Metamorphic Geology* **21**, 241-252.

Stallard, A., Ikei, H. & Masuda, T. 2002. Numerical simulations of spiral-shaped inclusion trails: can 3D geometry distinguish between end-member models of spiral formation? *Journal of Metamorphic Geology* **20**, 801-812.

Steinhardt, C. 1989. Lack of porphyroblast rotation in noncoaxially deformed schists from Petrel Cove, South Australia, and its implications. *Tectonophysics* **158**, 127-140.

Timms, N. E. 2003. Garnet porphyroblast timing and behaviour during fold evolution: implications from a 3-D geometric analysis of a hand-sample scale fold in a schist. *Journal of Metamorphic Geology* **21**(9), 853-873.

Treagus, S. H. 1983. A new theory of finite strain variation through contrasting layers, and its bearing on cleavage refraction. *Journal of Structural Geology* **5**, 351-358.

Treagus, S. H. 1988. Strain refraction in layered systems. *Journal of Structural Geology* **10**(5), 517-527.

Tull, J. F., Ausich, W. I., Groszos, M. S. & Thompson, T. W. 1993. Appalachian Blue Ridge Cover Sequence Ranges at Least into the Ordovician. *Geology* **21**(3), 215-218.

Unrug, R. & Unrug, S. 1990. Paleontological Evidence of Paleozoic Age for the Walden-Creek Group, Ocoee Supergroup, Tennessee. *Geology* **18**(11), 1041-1045.

Upton, G. J. G., Hickey, K. A. & Stallard, A. 2003. Regression models for cyclic data. *Royal Statistical Society* **Journal. Series C: Applied Statistics. 52**(Part 2), 227-235.

Vernon, R. H. 2004. *A practical guide to rock microstructure*. Cambridge, Cambridge University Press, United Kingdom.

Wiener, L. S. & Merschat, C. E. 1992. Geological map of south-western North Carolina including adjoining south-eastern Tennesseeand Northern Georgia. Division of Land Resources, North Carolina Department of Environment, Health, and Natural Resources.

Woodcock, N. H. 1977. Specification of fabric shapes using an eigenvalue method. *Geological Society of America Bulletin* **88**, 1231-1236.

Yeh, M.-W. 2003. The significance and application of foliation intersection/inflection axes (FIA) within porphyroblasts; a review. *Diqiu Kexue Jikan = TAO, Terrestrial, Atmospheric and Oceanic Sciences* **14**(4), 401-419.

Yeh, M.-W. & Bell, T. H. 2004. Significance of dextral reactivation of an E-W transfer fault in the formation of the Pennsylvania orocline, central Appalachians. *Tectonics* **23**, TC5009, doi:10.1029/2003TC001593.

# Appendix 1. Raw Data

## Appendix 1.1 V209 X-ray CT data

| Orientation | Clockwise | Anticlockwise | Total |
|---|---|---|---|
| 0 | 2 | 56 | 58 |
| 10 | 11 | 47 | 58 |
| 20 | 24 | 34 | 58 |
| 30 | 50 | 8 | 58 |
| 40 | 56 | 2 | 58 |
| 50 | 57 | 1 | 58 |
| 60 | 58 | 0 | 58 |
| 70 | 58 | 0 | 58 |
| 80 | 58 | 0 | 58 |
| 90 | 58 | 0 | 58 |
| 100 | 58 | 0 | 58 |
| 110 | 58 | 0 | 58 |
| 120 | 58 | 0 | 58 |
| 130 | 58 | 0 | 58 |
| 140 | 58 | 0 | 58 |
| 150 | 58 | 0 | 58 |
| 160 | 58 | 0 | 58 |
| 170 | 57 | 1 | 58 |

Asymmetry data based on 58 FIA measurements from HRXCT data from sample V209 (Chapter 2).

## Appendix 1.2 CA10 Core data

| Orientation | Clockwise | Anticlockwise | Total |
|---|---|---|---|
| 0 | 0 | 6 | 6 |
| 30 | 0 | 8 | 8 |
| 40 | 1 | 4 | 5 |
| 50 | 0 | 4 | 4 |
| 60 | 0 | 3 | 3 |
| 70 | 0 | 7 | 7 |
| 80 | 3 | 1 | 4 |
| 90 | 5 | 1 | 6 |
| 100 | 6 | 0 | 6 |
| 110 | 14 | 0 | 14 |
| 120 | 4 | 0 | 4 |
| 130 | 10 | 0 | 10 |
| 140 | 14 | 0 | 14 |
| 150 | 10 | 0 | 10 |
| 160 | 6 | 0 | 6 |

From Stallard et al. (2003).

## *Appendix 1.3 Murphy Syncline Data*

| Orientation | | 0 | 10 | 20 | 30 | 40 | 50 | 60 | 70 | 80 | 90 | 100 | 110 | 120 | 130 | 140 | 150 | 160 | 170 |
|---|---|---|---|---|---|---|---|---|---|---|---|---|---|---|---|---|---|---|---|
| Sample | | | | | | | | | | | | | | | | | | | |
| CH2r | CW | 4 | 4 | 4 | 3 | 1 | ns | 1 | ns | ns | 0 | ns | ns | 0 | ns | ns | 0 | 1 | 3 |
| | Total | 7 | 11 | 9 | 8 | 18 | ns | 8 | ns | ns | 14 | ns | ns | 10 | ns | ns | 8 | 7 | 7 |
| CH4r | CW | 2 | 2 | 1 | ns | ns | ns | 0 | ns | ns | 0 | ns | ns | 0 | ns | ns | ns | 2 | 2 |
| | Total | 5 | 7 | 6 | ns | ns | ns | 3 | ns | ns | 4 | ns | ns | 5 | ns | ns | ns | 9 | 8 |
| CH13l | CW | 18 | 29 | 22 | 21 | 26 | 23 | 22 | 25 | 26 | 14 | 15 | 5 | 3 | 2 | 0 | 0 | 0 | 0 |
| | Total | 18 | 29 | 22 | 21 | 27 | 23 | 22 | 25 | 29 | 25 | 27 | 20 | 25 | 24 | 24 | 24 | 26 | 23 |
| CH22r | CW | 25 | 20 | 18 | 12 | 15 | 18 | 7 | 5 | 2 | 2 | 0 | 0 | 0 | ns | 0 | ns | 0 | ns |
| rim | Total | 25 | 21 | 18 | 12 | 16 | 23 | 20 | 13 | 9 | 12 | 14 | 13 | 17 | ns | 14 | ns | 22 | ns |
| CH22r | CW | 1 | 1 | 0 | 0 | 2 | 5 | 11 | 9 | 8 | 13 | 13 | 13 | 17 | ns | 14 | ns | 21 | ns |
| core | Total | 25 | 20 | 18 | 12 | 16 | 19 | 15 | 10 | 9 | 13 | 13 | 13 | 17 | ns | 14 | ns | 22 | ns |
| CH35l | CW | 0 | ns | 1 | ns | 1 | ns | 0 | ns | 1 | 8 | 6 | 7 | 5 | 6 | 8 | ns | 9 | ns |
| Plag. | Total | 11 | ns | 19 | ns | 12 | ns | 7 | ns | 9 | 16 | 14 | 10 | 7 | 8 | 8 | ns | 10 | ns |
| CH35l | CW | 15 | ns | 22 | ns | 21 | ns | 17 | ns | 20 | 12 | 10 | 3 | 4 | 1 | 2 | ns | 0 | ns |
| Plag. | Total | 15 | ns | 22 | ns | 21 | ns | 17 | ns | 21 | 17 | 15 | 6 | 11 | 9 | 9 | ns | 7 | ns |
| CH41r | CW | 0 | 0 | ns | 0 | ns | ns | 0 | ns | ns | 0 | 0 | 0 | 1 | 1 | 3 | 6 | 7 | 18 |
| Biotite | Total | 11 | 14 | ns | 21 | ns | ns | 11 | ns | ns | 11 | 8 | 10 | 6 | 7 | 6 | 8 | 9 | 18 |
| CH41r | CW | 0 | 0 | ns | 0 | ns | ns | 0 | ns | ns | 0 | 0 | 0 | 1 | 1 | 3 | 4 | 6 | 10 |
| | Total | 11 | 11 | ns | 6 | ns | ns | 11 | ns | ns | 6 | 4 | 7 | 6 | 13 | 6 | 6 | 7 | 10 |
| CH43l | CW | 10 | ns | 4 | ns | 9 | ns | 5 | ns | 7 | ns | 8 | ns | 6 | ns | 6 | 6 | 2 | 2 |
| | Total | 10 | ns | 5 | ns | 10 | ns | 5 | ns | 8 | ns | 9 | ns | 6 | ns | 7 | 8 | 7 | 10 |
| CH49r | CW | 13 | ns | 5 | ns | 10 | ns | 8 | 4 | 3 | 3 | 2 | 1 | 2 | ns | 0 | ns | 0 | ns |
| | Total | 13 | ns | 5 | ns | 10 | ns | 11 | 8 | 9 | 11 | 8 | 9 | 8 | ns | 10 | ns | 9 | ns |
| CH57l | CW | 0 | ns | ns | 0 | ns | ns | 0 | ns | 0 | 1 | 6 | 6 | 11 | ns | ns | 7 | 13 | 12 |
| core | Total | 15 | ns | ns | 9 | ns | ns | 6 | ns | 6 | 8 | 7 | 7 | 11 | ns | ns | 7 | 13 | 12 |
| CH57l | CW | 2 | ns | ns | 1 | ns | ns | 0 | ns | 0 | 0 | 0 | 0 | 0 | ns | ns | 0 | 5 | 10 |
| rim | Total | 14 | ns | ns | 8 | ns | ns | 6 | ns | 6 | 8 | 7 | 7 | 11 | ns | ns | 7 | 13 | 12 |
| CH60l | CW | 0 | ns | ns | 0 | ns | ns | 0 | ns | 1 | 3 | 6 | 5 | 4 | ns | ns | 4 | ns | ns |
| | Total | 7 | ns | ns | 5 | ns | ns | 5 | ns | 5 | 10 | 7 | 5 | 4 | ns | ns | 4 | ns | ns |
| CH62l | CW | 9 | ns | ns | 7 | ns | ns | 6 | ns | ns | 4 | 1 | 1 | 0 | ns | ns | 0 | ns | ns |
| | Total | 9 | ns | ns | 7 | ns | ns | 7 | ns | ns | 4 | 12 | 8 | 10 | ns | ns | 8 | ns | ns |
| CH68r | CW | 0 | ns | ns | 0 | ns | ns | 0 | ns | 0 | 2 | 3 | 6 | 11 | 9 | 10 | 8 | 5 | ns |
| | Total | 14 | ns | ns | 20 | ns | ns | 9 | ns | 7 | 10 | 7 | 8 | 12 | 9 | 10 | 8 | 5 | ns |
| CH68r | CW | 2 | ns | ns | 0 | ns | ns | 0 | ns | 0 | 0 | 0 | 0 | 0 | 2 | 4 | 7 | 5 | ns |
| Plag. | Total | 10 | ns | ns | 7 | ns | ns | 5 | ns | 2 | 4 | 4 | 4 | 5 | 5 | 7 | 10 | 5 | ns |
| CH71l | CW | 0 | ns | ns | ns | 0 | ns | 2 | 4 | 4 | ns | ns | ns | 5 | ns | ns | 6 | ns | ns |
| | Total | 5 | ns | ns | ns | 5 | ns | 6 | 5 | 4 | ns | ns | ns | 5 | ns | ns | 6 | ns | ns |
| CH73r | CW | 0 | ns | 0 | ns | ns | ns | ns | 0 | ns | 0 | ns | ns | 0 | 0 | 2 | 8 | 6 | 9 |
| | Total | 4 | ns | 4 | ns | ns | ns | ns | 7 | ns | 4 | ns | ns | 5 | 5 | 8 | 12 | 6 | 9 |

Asymmetry Observations for Murphy Syncline FIA. Only clockwise or anticlockwise observations were recorded. All FIA are in garnet unless otherwise noted. l and r indicate whether the section orientation is to the left or right respectively. ns = no section

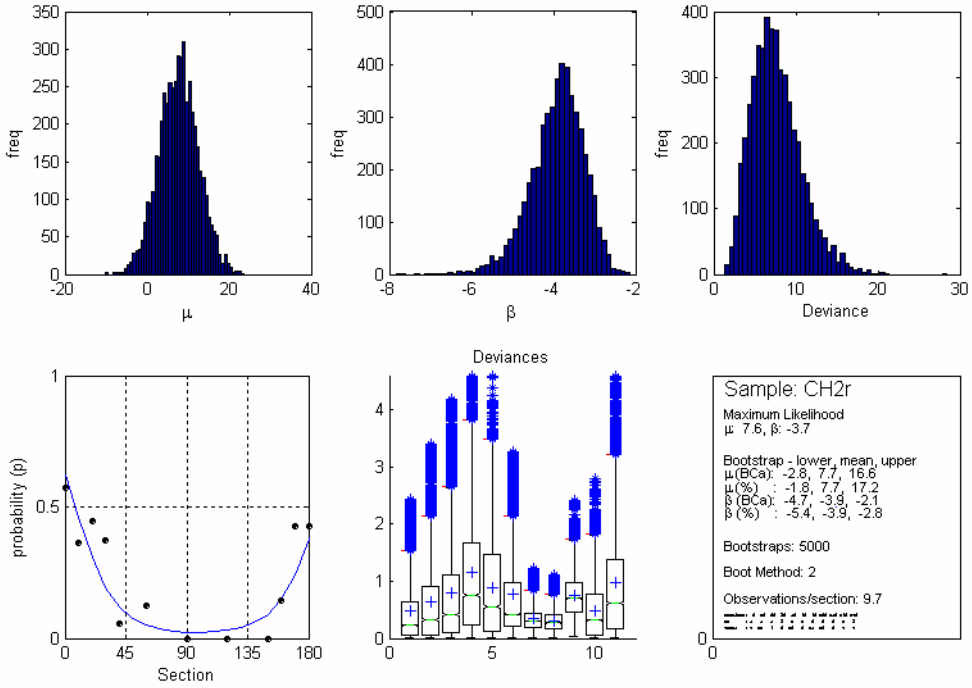
freq
μ
β
Deviance
probability (p)
Section
Deviances
Sample: CH2r
Maximum Likelihood
μ 7.6, β: -3.7
Bootstrap - lower, mean, upper
μ(BCa): -2.8, 7.7, 16.6
μ(%) : -1.8, 7.7, 17.2
β(BCa): -4.7, -3.9, -2.1
β(%) : -5.4, -3.9, -2.8
Bootstraps: 5000
Boot Method: 2
Observations/section: 9.7

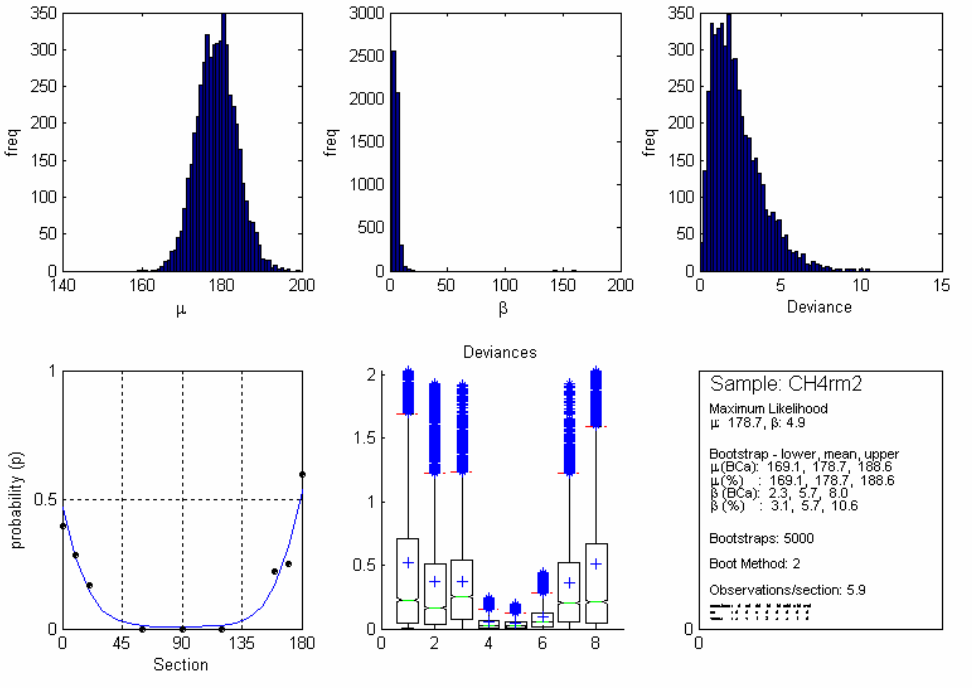
freq
μ
β
Deviance
probability (p)
Section
Deviances
Sample: CH4rm2
Maximum Likelihood
μ 178.7, β: 4.9
Bootstrap - lower, mean, upper
μ(BCa): 169.1, 178.7, 188.6
μ(%) : 169.1, 178.7, 188.6
β(BCa): 2.3, 5.7, 8.0
β(%) : 3.1, 5.7, 10.6
Bootstraps: 5000
Boot Method: 2
Observations/section: 5.9

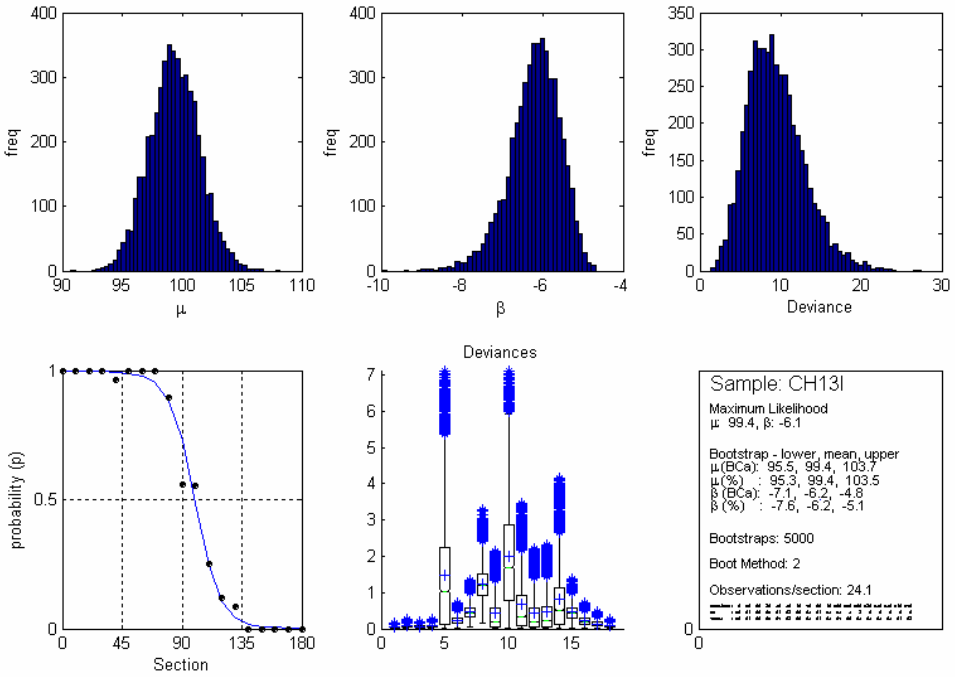
freq
μ
β
Deviance
probability (p)
Section
Deviances
Sample: CH13I
Maximum Likelihood
μ 99.4, β: -6.1
Bootstrap - lower, mean, upper
μ(BCa): 95.5, 99.4, 103.7
μ(%) : 95.3, 99.4, 103.5
β (BCa): -7.1, -6.2, -4.8
β (%) : -7.6, -6.2, -5.1
Bootstraps: 5000
Boot Method: 2
Observations/section: 24.1

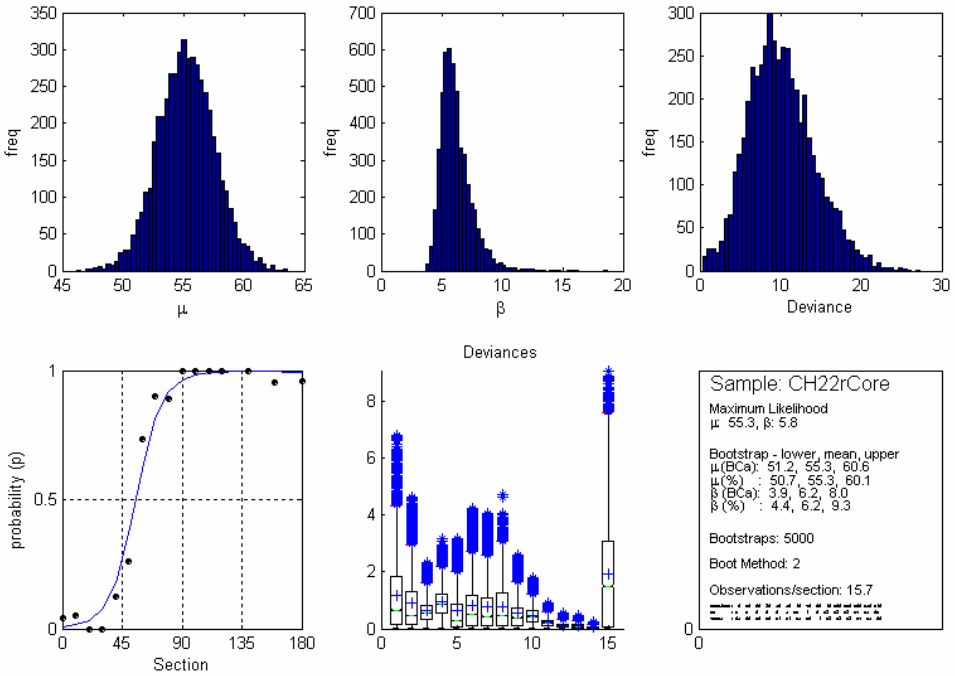
freq
μ
β
Deviance
probability (p)
Section
Deviances
Sample: CH22rCore
Maximum Likelihood
μ 55.3, β: 5.8
Bootstrap - lower, mean, upper
μ(BCa): 51.2, 55.3, 60.6
μ(%) : 50.7, 55.3, 60.1
β (BCa): 3.9, 6.2, 8.0
β (%) : 4.4, 6.2, 9.3
Bootstraps: 5000
Boot Method: 2
Observations/section: 15.7

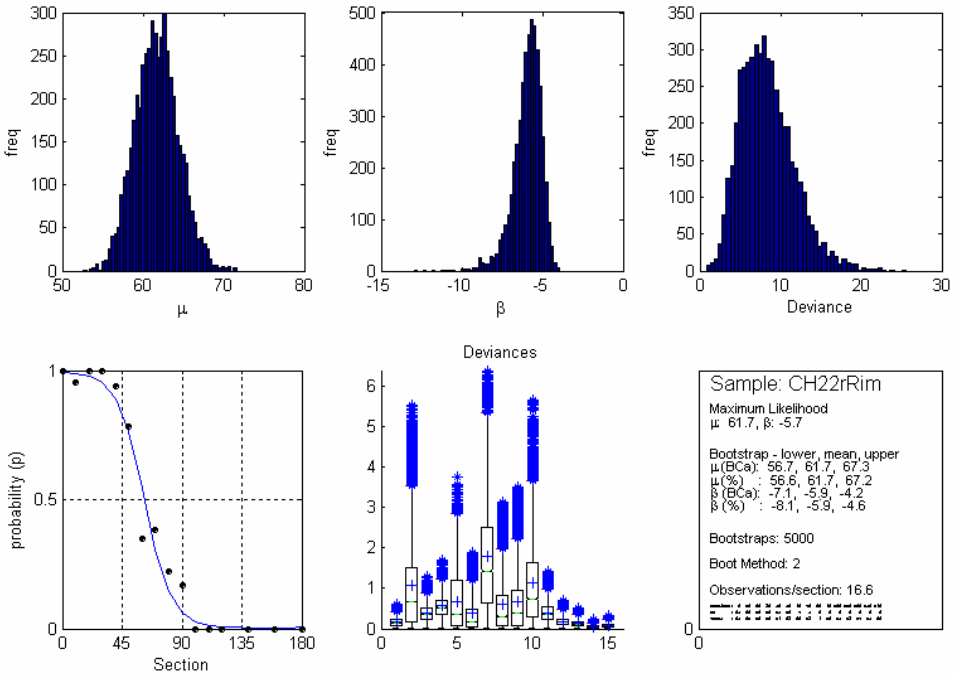
freq
μ
β
Deviance
probability (p)
Section
Deviances
Sample: CH22rRim
Maximum Likelihood
μ 61.7, β: -5.7
Bootstrap - lower, mean, upper
μ (BCa): 56.7, 61.7, 67.3
μ (%) : 56.6, 61.7, 67.2
β (BCa): -7.1, -5.9, -4.2
β (%) : -8.1, -5.9, -4.6
Bootstraps: 5000
Boot Method: 2
Observations/section: 16.6

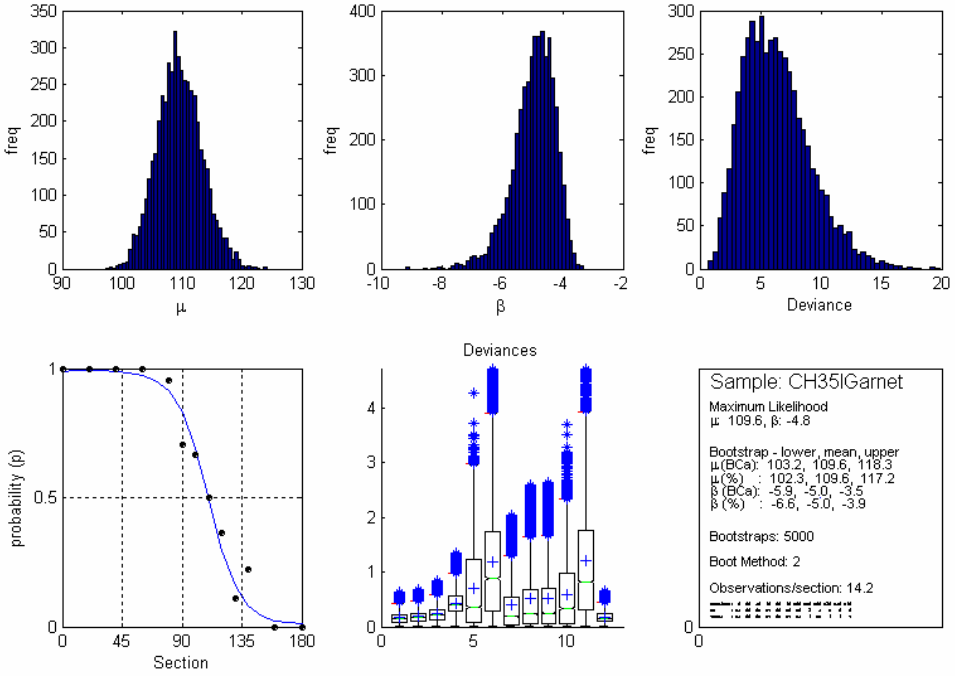
freq
μ
β
Deviance
probability (p)
Section
Deviances
Sample: CH35lGarnet
Maximum Likelihood
μ 109.6, β: -4.8
Bootstrap - lower, mean, upper
μ (BCa): 103.2, 109.6, 118.3
μ (%) : 102.3, 109.6, 117.2
β (BCa): -5.9, -5.0, -3.5
β (%) : -6.6, -5.0, -3.9
Bootstraps: 5000
Boot Method: 2
Observations/section: 14.2

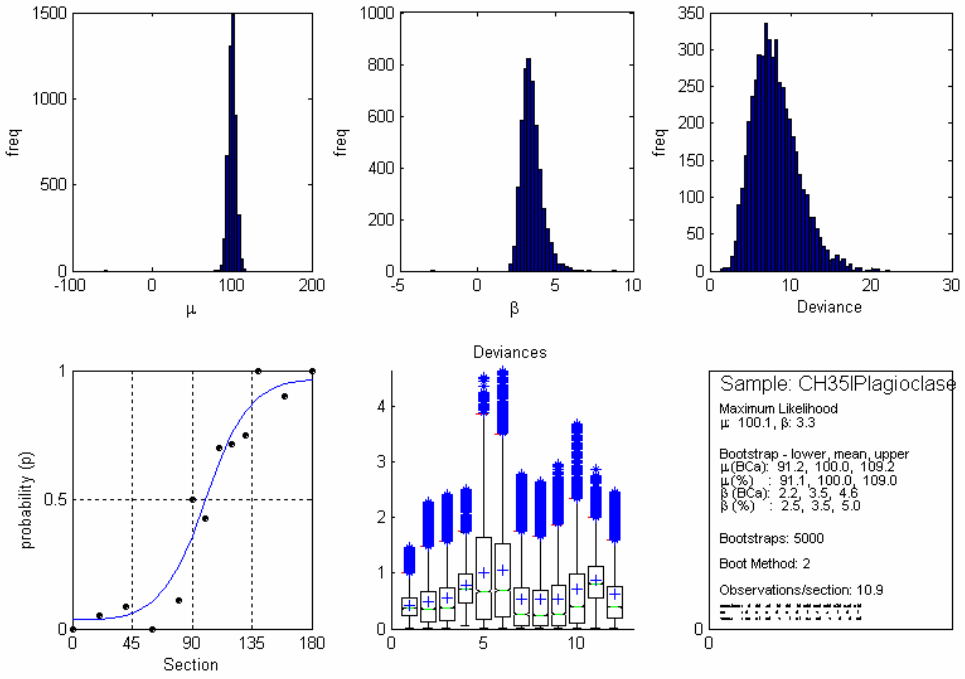
freq
μ
β
Deviance
probability (p)
Section
Deviances
Sample: CH35lPlagioclase
Maximum Likelihood
μ: 100.1, β: 3.3
Bootstrap - lower, mean, upper
μ(BCa): 91.2, 100.0, 109.2
μ(%) : 91.1, 100.0, 109.0
β(BCa): 2.2, 3.5, 4.6
β(%) : 2.5, 3.5, 5.0
Bootstraps: 5000
Boot Method: 2
Observations/section: 10.9

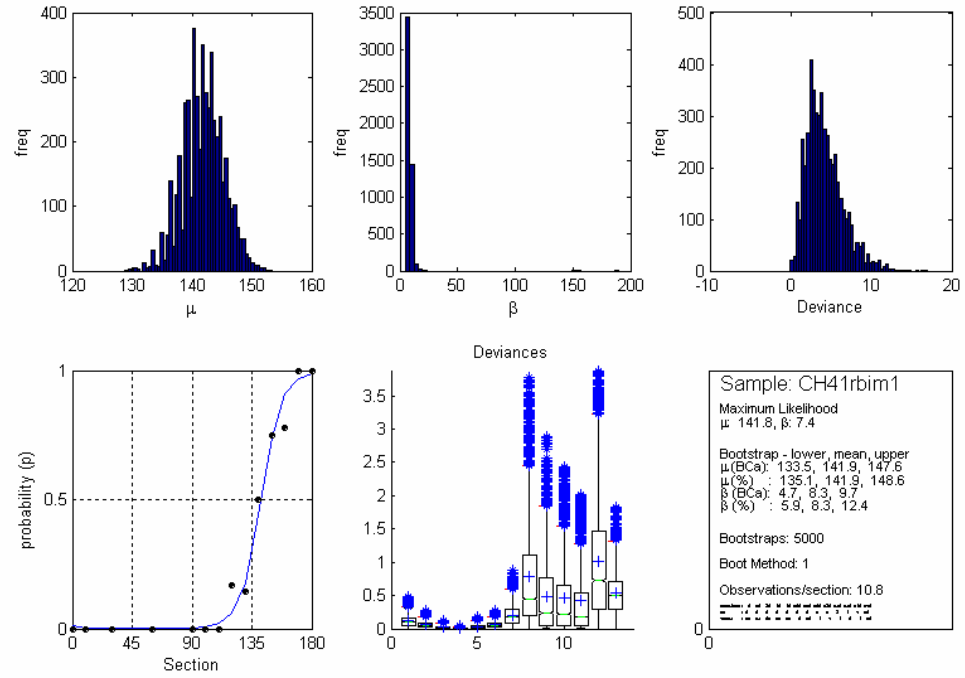
freq
μ
β
Deviance
probability (p)
Section
Deviances
Sample: CH41rbim1
Maximum Likelihood
μ: 141.8, β: 7.4
Bootstrap - lower, mean, upper
μ(BCa): 133.5, 141.9, 147.6
μ(%) : 135.1, 141.9, 148.6
β(BCa): 4.7, 8.3, 9.7
β(%) : 5.9, 8.3, 12.4
Bootstraps: 5000
Boot Method: 1
Observations/section: 10.8

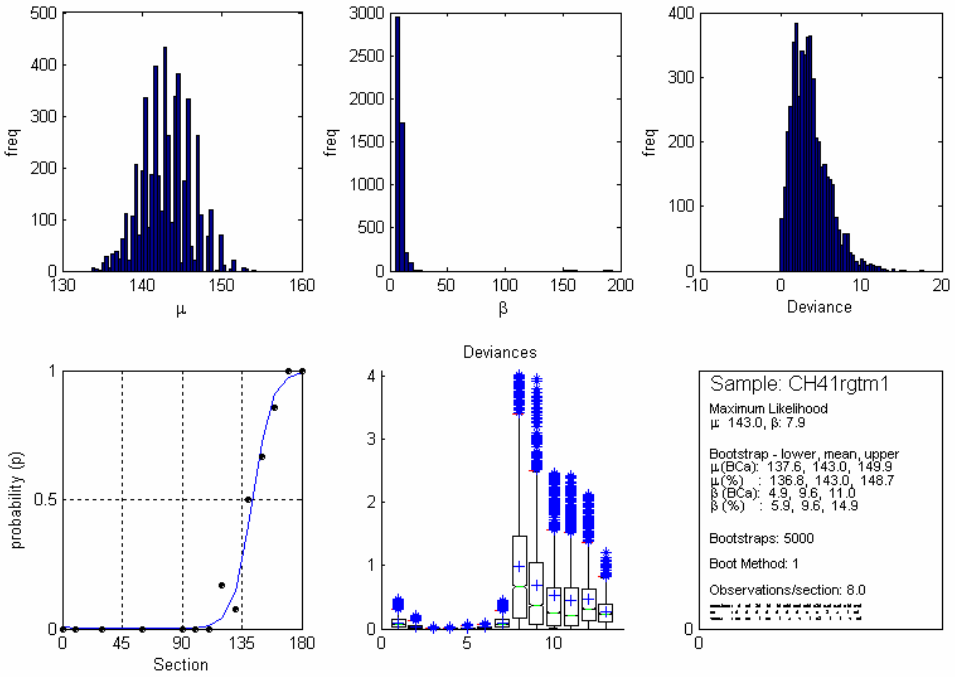
freq
μ
β
Deviance
probability (p)
Section
Deviances
Sample: CH41rgtm1
Maximum Likelihood
μ: 143.0, β: 7.9
Bootstrap - lower, mean, upper
μ (BCa): 137.6, 143.0, 149.9
μ (%) : 136.8, 143.0, 148.7
β (BCa): 4.9, 9.6, 11.0
β (%) : 5.9, 9.6, 14.9
Bootstraps: 5000
Boot Method: 1
Observations/section: 8.0

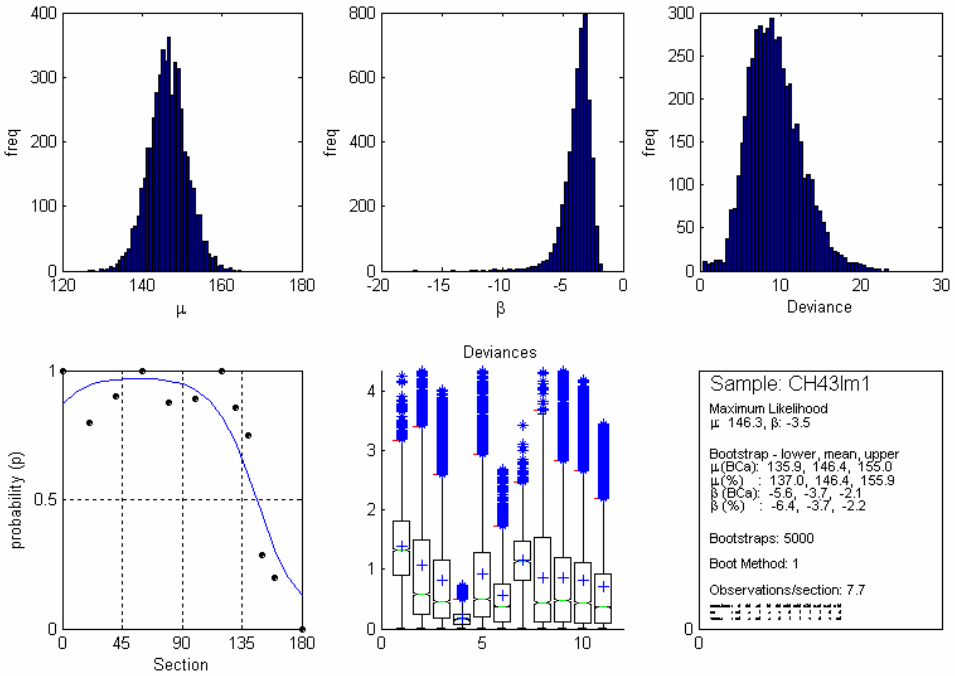
freq
μ
β
Deviance
probability (p)
Section
Deviances
Sample: CH43lm1
Maximum Likelihood
μ: 146.3, β: -3.5
Bootstrap - lower, mean, upper
μ (BCa): 135.9, 146.4, 155.0
μ (%) : 137.0, 146.4, 155.9
β (BCa): -5.6, -3.7, -2.1
β (%) : -6.4, -3.7, -2.2
Bootstraps: 5000
Boot Method: 1
Observations/section: 7.7

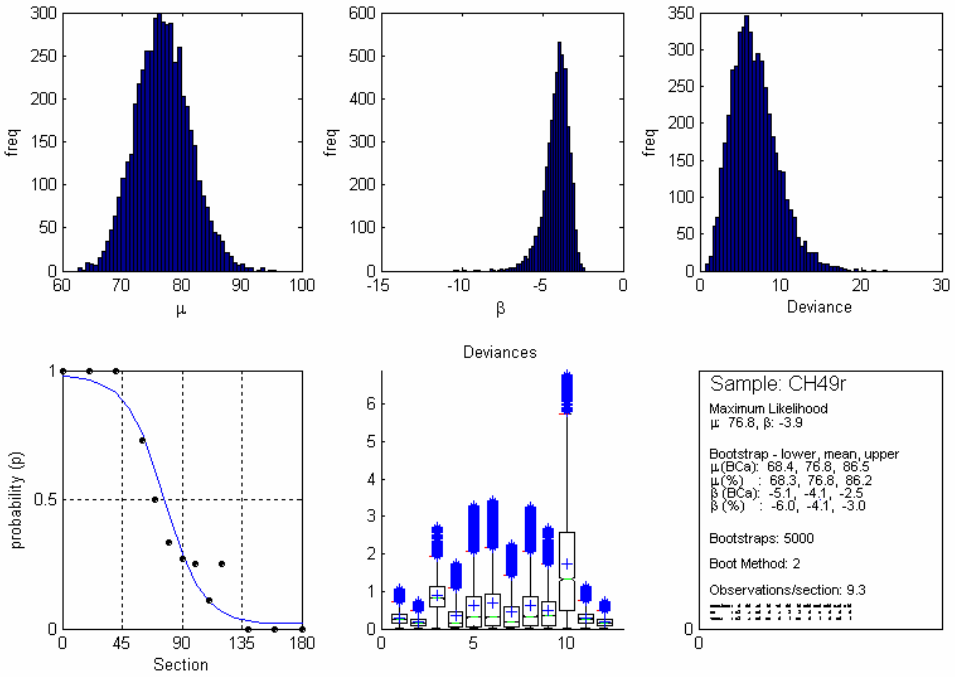
freq
μ
β
Deviance
probability (p)
Section
Deviances
Sample: CH49r
Maximum Likelihood
μ 76.8, β: -3.9
Bootstrap - lower, mean, upper
μ(BCa): 68.4, 76.8, 86.5
μ(%) : 68.3, 76.8, 86.2
β (BCa): -5.1, -4.1, -2.5
β (%) : -6.0, -4.1, -3.0
Bootstraps: 5000
Boot Method: 2
Observations/section: 9.3

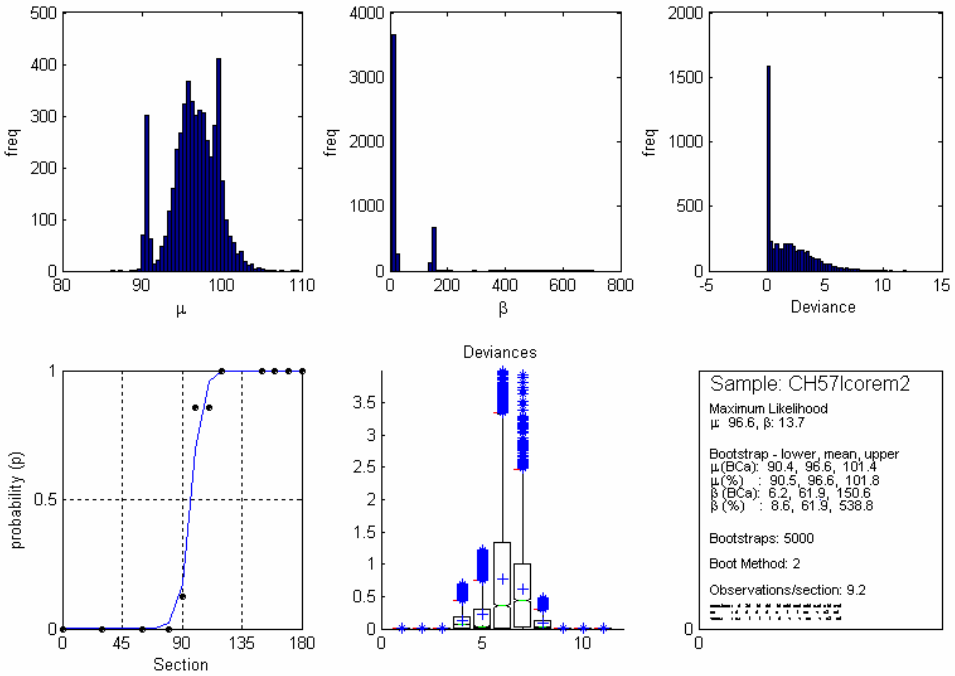
freq
μ
β
Deviance
probability (p)
Section
Deviances
Sample: CH57Icorem2
Maximum Likelihood
μ 96.6, β: 13.7
Bootstrap - lower, mean, upper
μ(BCa): 90.4, 96.6, 101.4
μ(%) : 90.5, 96.6, 101.8
β (BCa): 6.2, 61.9, 150.6
β (%) : 8.6, 61.9, 538.8
Bootstraps: 5000
Boot Method: 2
Observations/section: 9.2

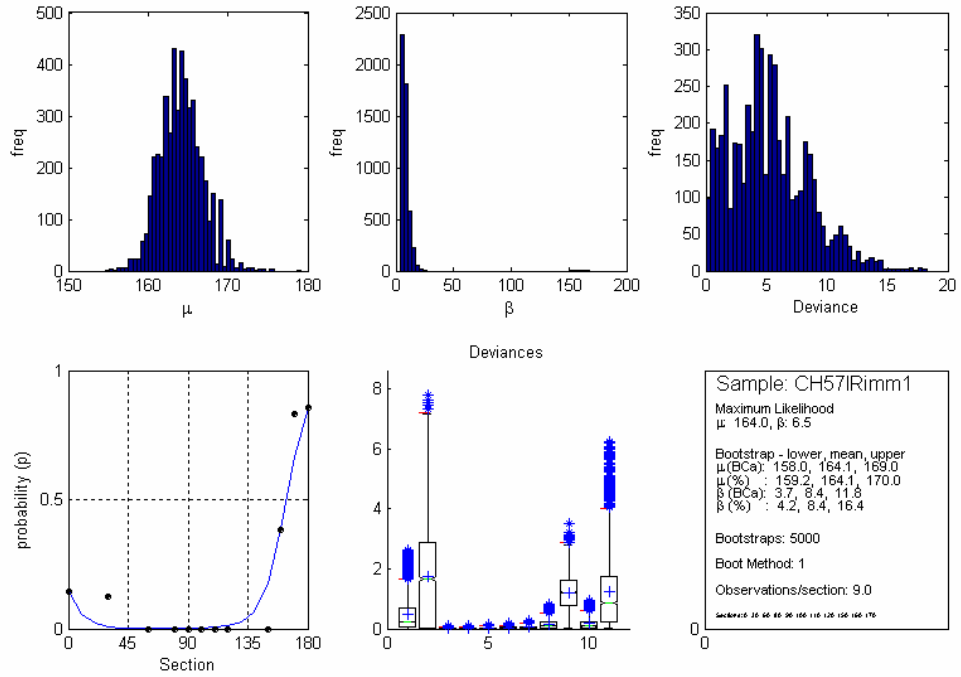
freq
μ
β
Deviance
probability (p)
Section
Deviances
Sample: CH57IRimm1
Maximum Likelihood
μ: 164.0, β: 6.5
Bootstrap - lower, mean, upper
μ(BCa): 158.0, 164.1, 169.0
μ(%) : 159.2, 164.1, 170.0
β(BCa): 3.7, 8.4, 11.8
β(%) : 4.2, 8.4, 16.4
Bootstraps: 5000
Boot Method: 1
Observations/section: 9.0

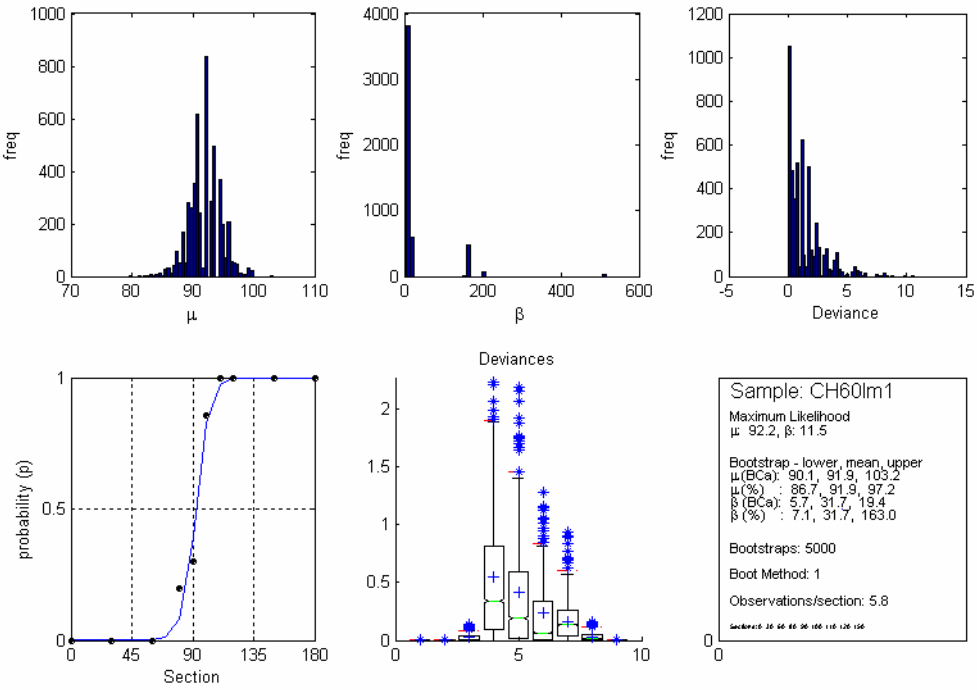
freq
μ
β
Deviance
probability (p)
Section
Deviances
Sample: CH60Im1
Maximum Likelihood
μ: 92.2, β: 11.5
Bootstrap - lower, mean, upper
μ(BCa): 90.1, 91.9, 103.2
μ(%) : 86.7, 91.9, 97.2
β(BCa): 5.7, 31.7, 19.4
β(%) : 7.1, 31.7, 163.0
Bootstraps: 5000
Boot Method: 1
Observations/section: 5.8

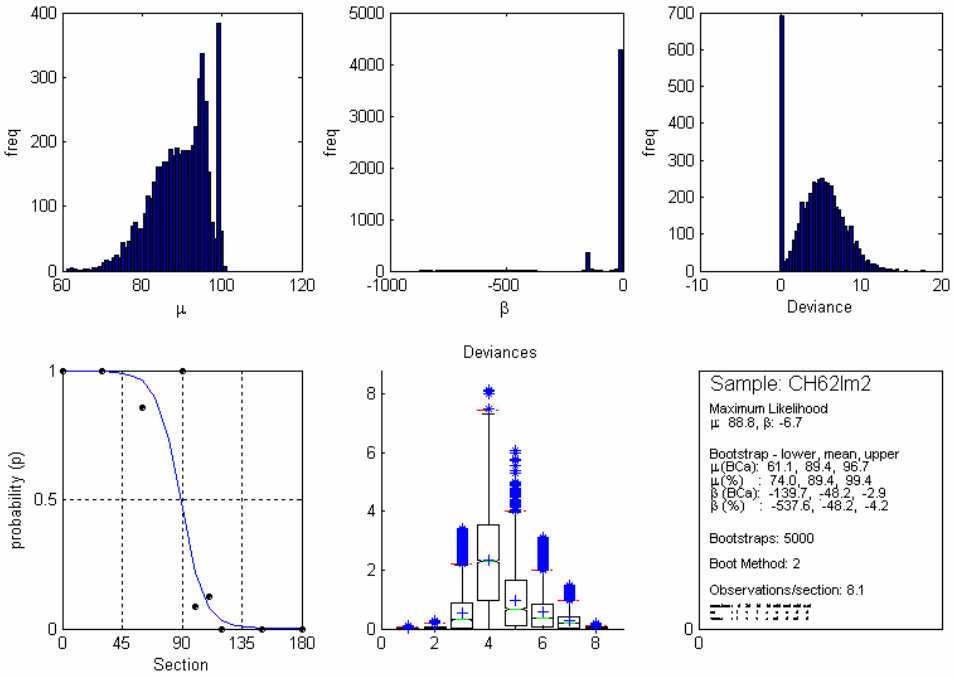
freq
μ
β
Deviance
Deviances
probability (p)
Section
Sample: CH62lm2
Maximum Likelihood
μ: 88.8, β: -6.7
Bootstrap - lower, mean, upper
μ(BCa): 61.1, 89.4, 96.7
μ(%) : 74.0, 89.4, 99.4
β(BCa): -139.7, -48.2, -2.9
β(%) : -537.6, -48.2, -4.2
Bootstraps: 5000
Boot Method: 2
Observations/section: 8.1

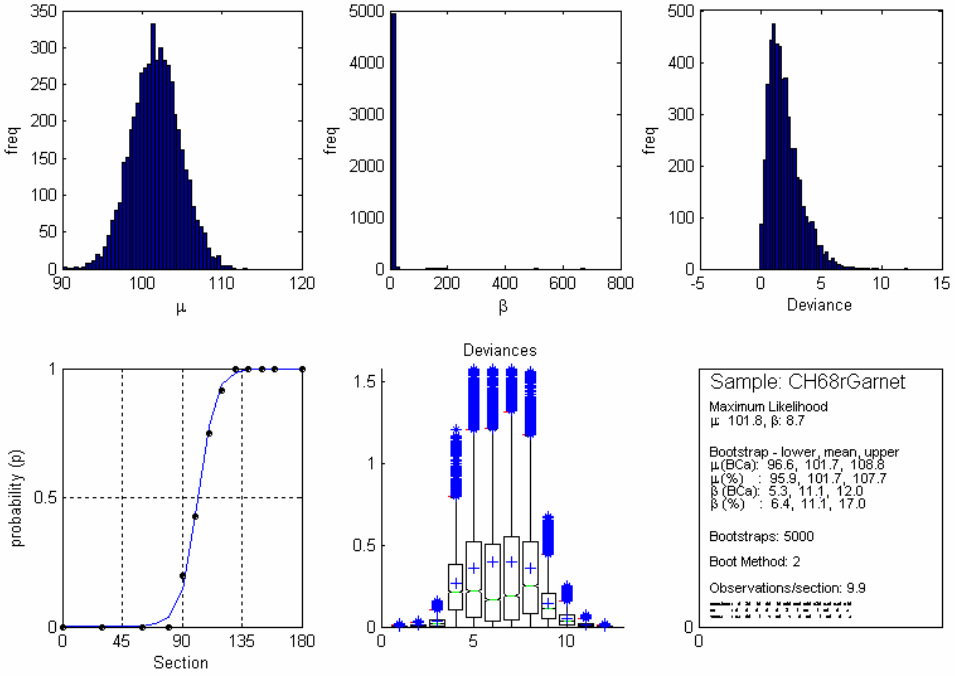
freq
μ
β
Deviance
Deviances
probability (p)
Section
Sample: CH68rGarnet
Maximum Likelihood
μ: 101.8, β: 8.7
Bootstrap - lower, mean, upper
μ(BCa): 96.6, 101.7, 108.8
μ(%) : 95.9, 101.7, 107.7
β(BCa): 5.3, 11.1, 12.0
β(%) : 6.4, 11.1, 17.0
Bootstraps: 5000
Boot Method: 2
Observations/section: 9.9

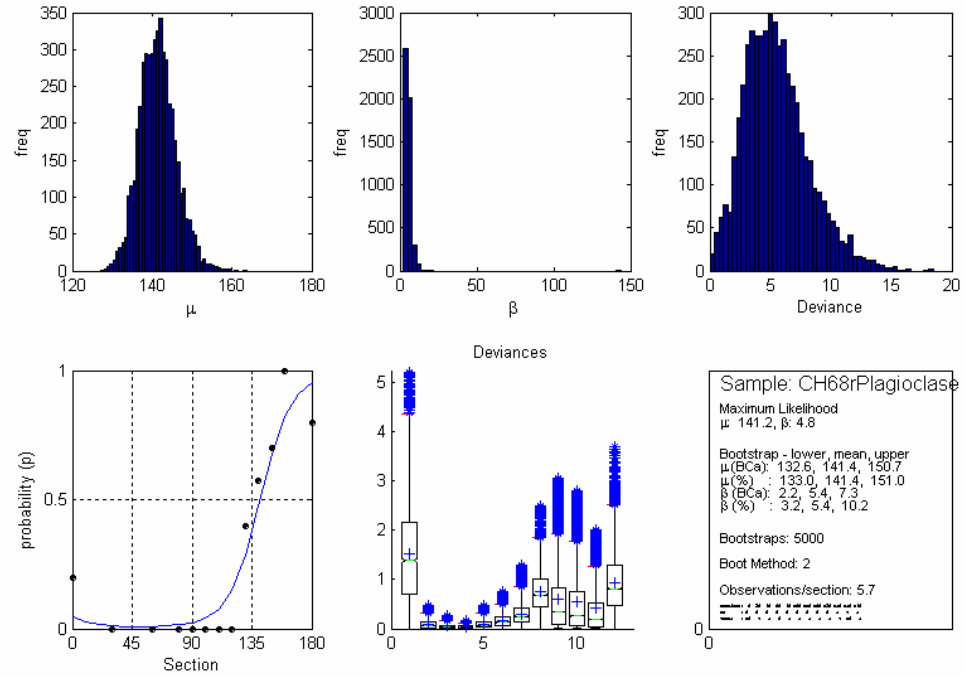
freq
μ
β
Deviance
Deviances
probability (p)
Section
Sample: CH68rPlagioclase
Maximum Likelihood
μ: 141.2, β: 4.8
Bootstrap - lower, mean, upper
μ(BCa): 132.8, 141.4, 150.7
μ(%) : 133.0, 141.4, 151.0
β(BCa): 2.2, 5.4, 7.3
β(%) : 3.2, 5.4, 10.2
Bootstraps: 5000
Boot Method: 2
Observations/section: 5.7

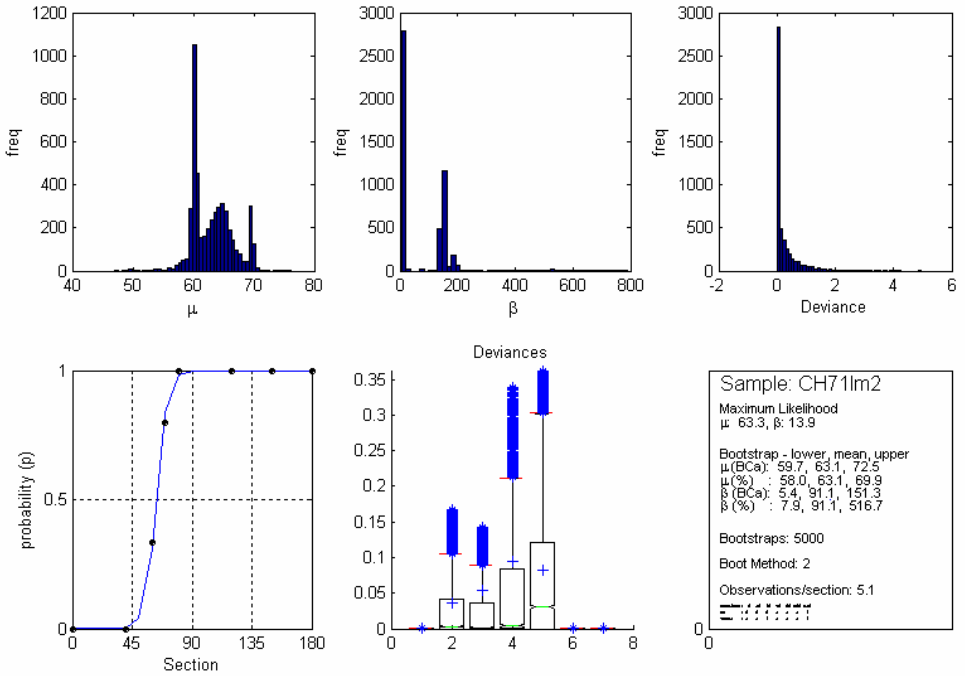
freq
μ
β
Deviance
Deviances
probability (p)
Section
Sample: CH71lm2
Maximum Likelihood
μ: 63.3, β: 13.9
Bootstrap - lower, mean, upper
μ(BCa): 59.7, 63.1, 72.5
μ(%) : 58.0, 63.1, 69.9
β(BCa): 5.4, 91.1, 151.3
β(%) : 7.9, 91.1, 516.7
Bootstraps: 5000
Boot Method: 2
Observations/section: 5.1

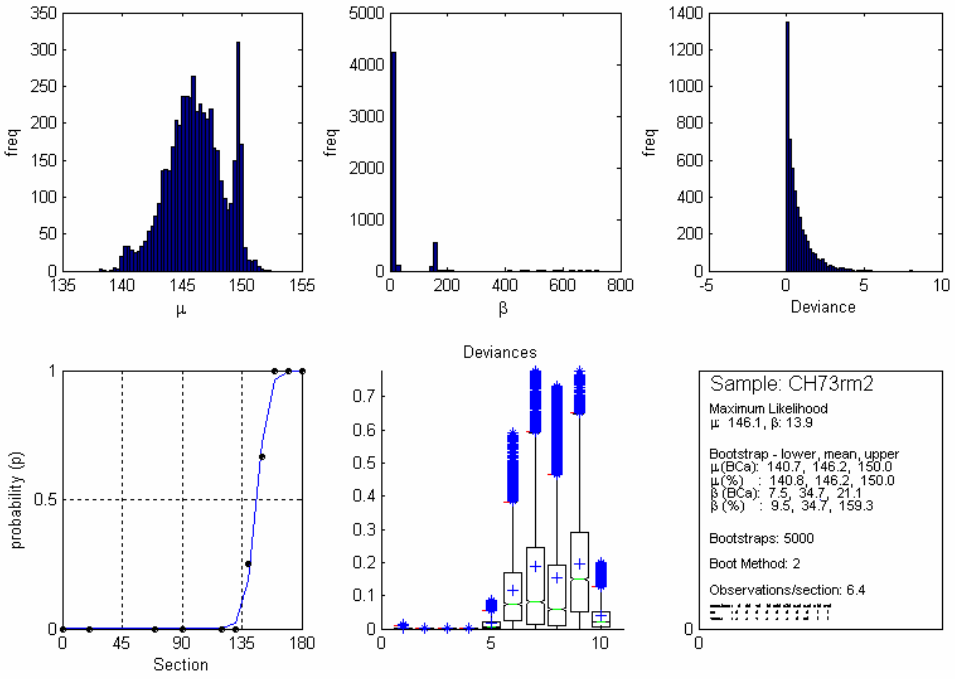
freq
μ
β
Deviance
probability (p)
Section
Deviances
Sample: CH73rm2
Maximum Likelihood
μ: 146.1, β: 13.9
Bootstrap - lower, mean, upper
μ(BCa): 140.7, 146.2, 150.0
μ(%) : 140.8, 146.2, 150.0
β(BCa): 7.5, 34.7, 21.1
β(%) : 9.5, 34.7, 159.3
Bootstraps: 5000
Boot Method: 2
Observations/section: 6.4

# *Appendix 1.4 NT191 Data*

Asymmetry observations derived from fig. 15 of Timms (2003).
orient = section orientation, cw = clockwise, acw = anticlockwise, st = straight,
milli = virtual millipede, sg = shotgun
* these values, modified to include millipede data
[#] positive plunge is to the SSW
[&] plunge values normalized so that 90° dip to the NNW is 0°, 0° dip is 90° and 90° to the SSW is 180° for the bootstrap MLE approach
data in shaded columns were used for the bootstrap MLE approach

**North Limb Trend**

| orient | cw | acw | st | milli | sg | total | cw* | total* |
|---|---|---|---|---|---|---|---|---|
| 0 | 0 | 8 | 3 | 0 | 0 | 11 | 0 | 8 |
| 10 | 1 | 8 | 1 | 2 | 0 | 12 | 2 | 11 |
| 20 | 0 | 1 | 4 | 4 | 0 | 9 | 2 | 5 |
| 30 | 1 | 7 | 5 | 10 | 0 | 23 | 6 | 18 |
| 40 | 2 | 0 | 2 | 10 | 0 | 14 | 7 | 12 |
| 50 | 1 | 0 | 4 | 0 | 0 | 5 | 1 | 1 |
| 60 | 1 | 0 | 9 | 0 | 0 | 10 | 1 | 1 |
| 70 | 10 | 0 | 11 | 0 | 0 | 21 | 10 | 10 |
| 80 | 5 | 0 | 10 | 0 | 0 | 15 | 5 | 5 |
| 90 | 6 | 0 | 0 | 0 | 0 | 6 | 6 | 6 |
| 100 | 5 | 0 | 10 | 0 | 0 | 15 | 5 | 5 |
| 110 | 11 | 0 | 9 | 0 | 0 | 20 | 11 | 11 |
| 120 | 4 | 0 | 8 | 0 | 0 | 12 | 4 | 4 |
| 130 | 14 | 0 | 2 | 0 | 0 | 16 | 14 | 14 |
| 140 | 4 | 0 | 0 | 0 | 0 | 4 | 4 | 4 |
| 150 | 5 | 0 | 4 | 0 | 0 | 9 | 5 | 5 |
| 160 | 2 | 0 | 8 | 0 | 0 | 10 | 2 | 2 |
| 170 | 2 | 0 | 3 | 0 | 0 | 5 | 2 | 2 |

**South Limb Trend**

| cw | acw | st | milli | sg | total | cw* | total* |
|---|---|---|---|---|---|---|---|
| 1 | 3 | 3 | 6 | 0 | 13 | 4 | 10 |
| 0 | 0 | 2 | 14 | 0 | 16 | 7 | 14 |
| 0 | 3 | 0 | 7 | 0 | 10 | 3 | 9 |
| 0 | 0 | 6 | 8 | 0 | 14 | 4 | 8 |
| 5 | 0 | 4 | 7 | 0 | 16 | 8 | 11 |
| 4 | 1 | 11 | 2 | 0 | 18 | 5 | 7 |
| 13 | 0 | 6 | 0 | 0 | 19 | 13 | 13 |
| 16 | 1 | 2 | 0 | 0 | 19 | 16 | 17 |
| 9 | 0 | 11 | 0 | 0 | 20 | 9 | 9 |
| 27 | 0 | 11 | 0 | 0 | 38 | 27 | 27 |
| 13 | 0 | 3 | 0 | 0 | 16 | 13 | 13 |
| 8 | 0 | 3 | 0 | 0 | 11 | 8 | 8 |
| 7 | 0 | 3 | 0 | 0 | 10 | 7 | 7 |
| 19 | 0 | 4 | 0 | 0 | 23 | 19 | 19 |
| 19 | 0 | 11 | 0 | 0 | 30 | 19 | 19 |
| 17 | 0 | 7 | 0 | 0 | 24 | 17 | 17 |
| 11 | 0 | 7 | 4 | 0 | 22 | 13 | 15 |
| 6 | 0 | 8 | 4 | 0 | 18 | 8 | 10 |

**North Limb Plunge**

| orient[#] | norm[&] | cw | acw | st | milli | sg | total | cw* | total* |
|---|---|---|---|---|---|---|---|---|---|
| -60 | 30 | 0 | 10 | 5 | 0 | 0 | 15 | 0 | 10 |
| -50 | | ns | ns | ns | ns | ns | ns | | |
| -40 | 50 | 0 | 25 | 15 | 0 | 0 | 40 | 0 | 25 |
| -30 | 60 | 1 | 8 | 3 | 0 | 1 | 13 | 1 | 9 |
| -20 | 70 | 0 | 6 | 3 | 0 | 4 | 13 | 0 | 6 |
| -10 | 80 | 6 | 1 | 7 | 6 | 0 | 20 | 9 | 13 |
| 0 | 90 | 3 | 4 | 4 | 1 | 0 | 12 | 3 | 7 |
| 10 | 100 | 3 | 6 | 3 | 4 | 0 | 16 | 5 | 13 |
| 20 | 110 | 3 | 1 | 6 | 0 | 7 | 17 | 3 | 4 |
| 30 | | ns | ns | ns | ns | ns | ns | | |
| 40 | 130 | 2 | 0 | 4 | 0 | 0 | 6 | 2 | 2 |
| 50 | | ns | ns | ns | ns | ns | ns | | |
| 60 | 150 | 6 | 0 | 1 | 0 | 4 | 11 | 6 | 6 |

**South Limb Plunge**

| cw | acw | ST | milli | SG | Total |
|---|---|---|---|---|---|
| 0 | 8 | 3 | 0 | 0 | 11 |
| 0 | 17 | 4 | 0 | 0 | 21 |
| 0 | 12 | 0 | 0 | 0 | 12 |
| 0 | 10 | 0 | 0 | 0 | 10 |
| 0 | 6 | 3 | 0 | 4 | 13 |
| 1 | 9 | 2 | 0 | 0 | 12 |
| 2 | 8 | 9 | 0 | 0 | 19 |
| 1 | 5 | 6 | 1 | 0 | 13 |
| 2 | 5 | 8 | 0 | 0 | 15 |
| ns | ns | ns | ns | ns | ns |
| 6 | 0 | 1 | 0 | 0 | 7 |
| ns | ns | ns | ns | ns | ns |
| 4 | 0 | 2 | 0 | 0 | 6 |

ns = no section

# Appendix 2. Sensitivity Analysis

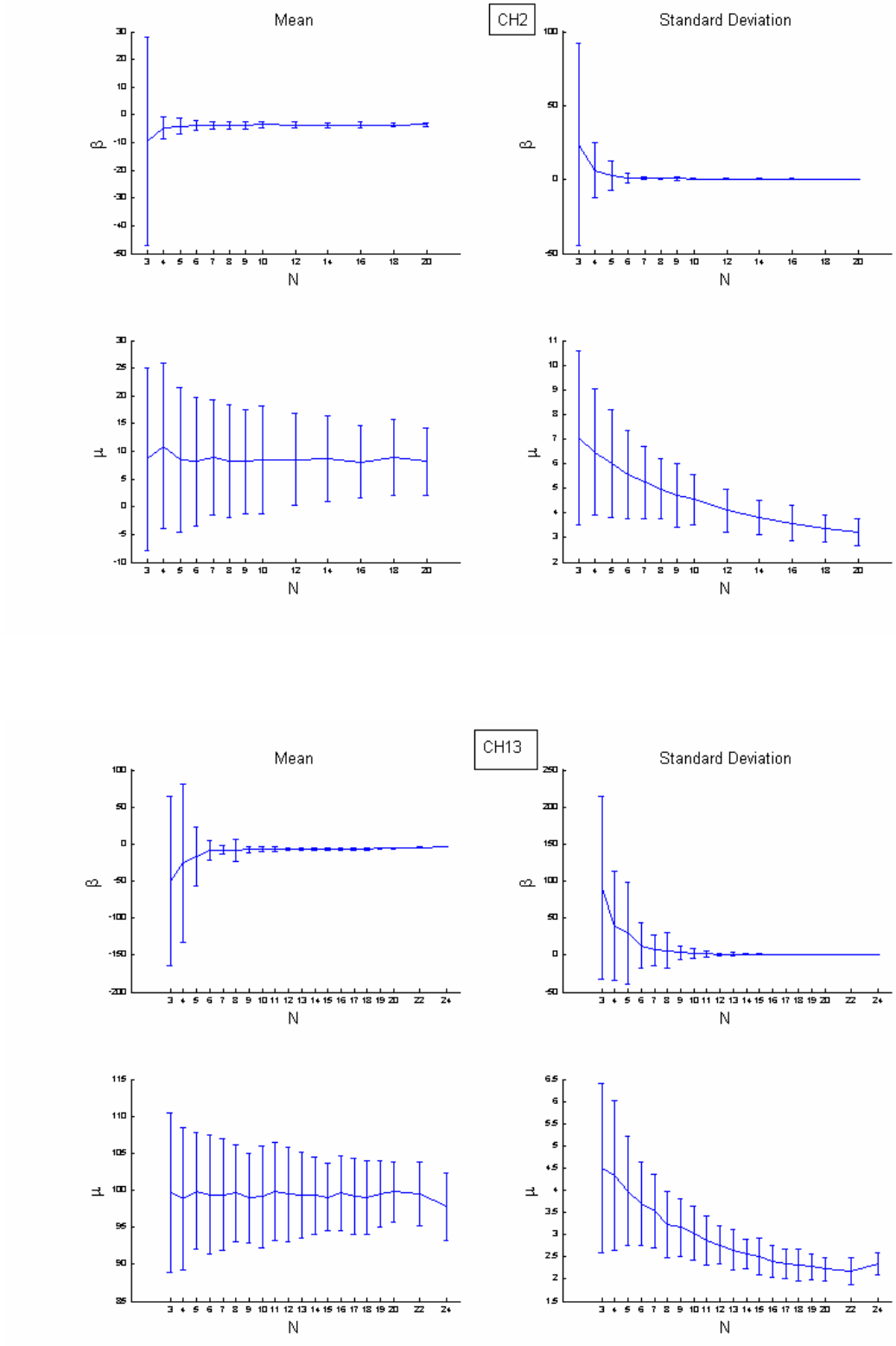

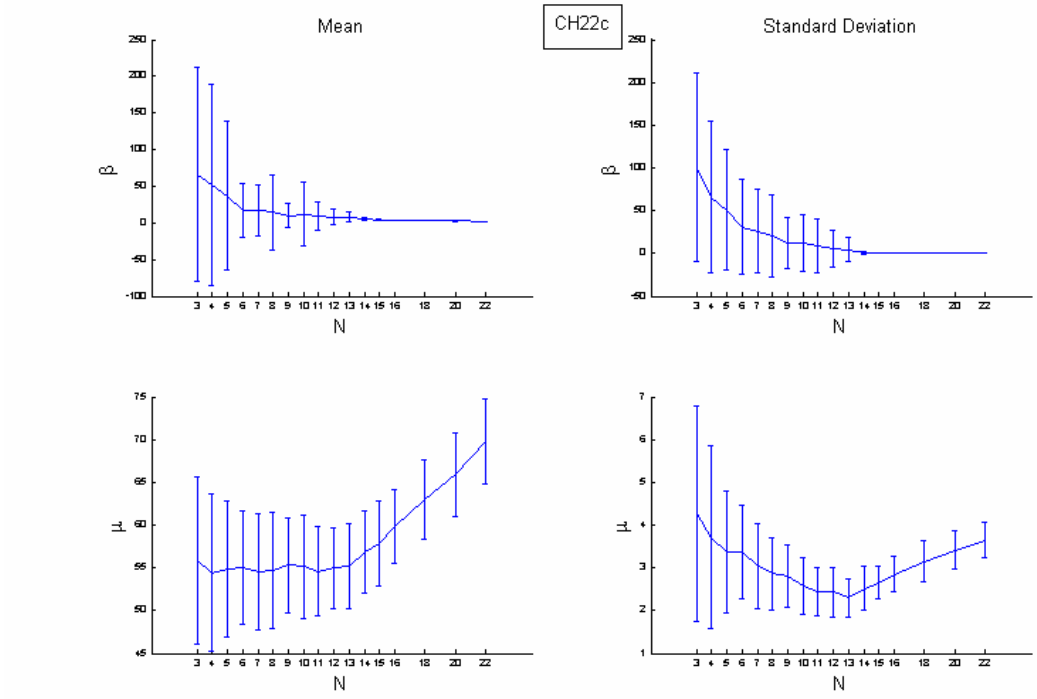
CH22c
Mean
Standard Deviation
β
μ
N

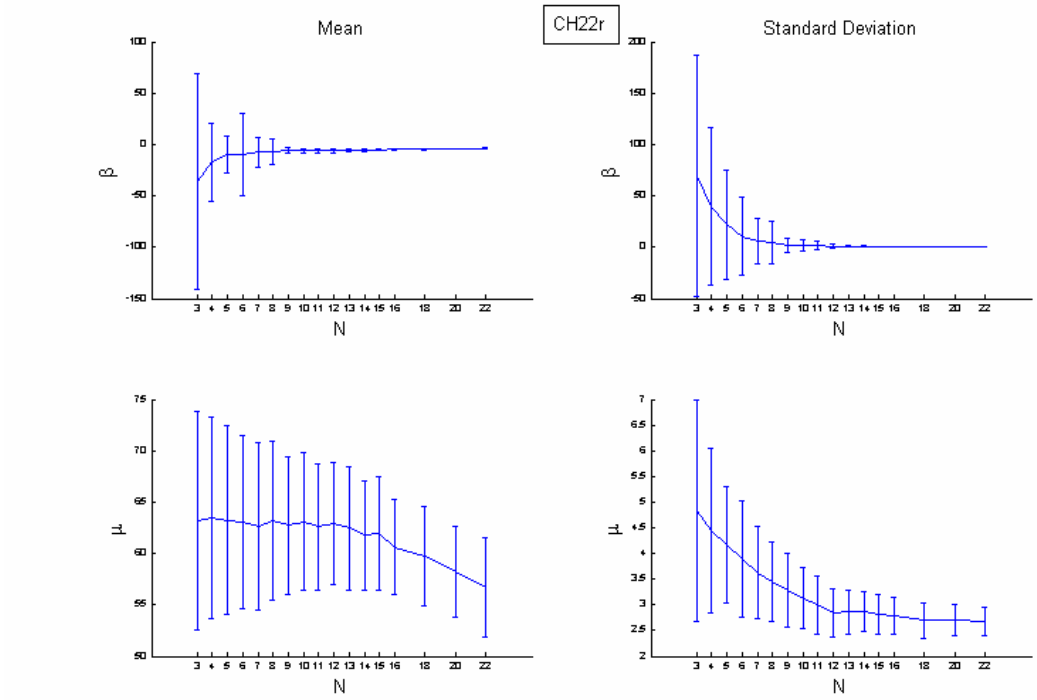
CH22r
Mean
Standard Deviation
β
μ
N

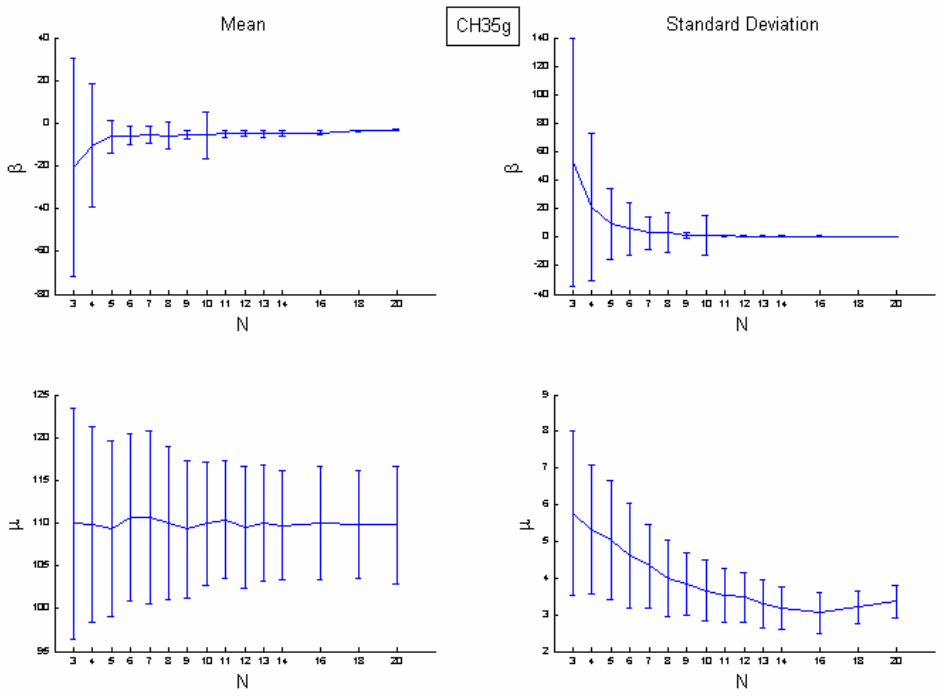
Mean
CH35g
Standard Deviation
β
N
μ
N
β
N
μ
N

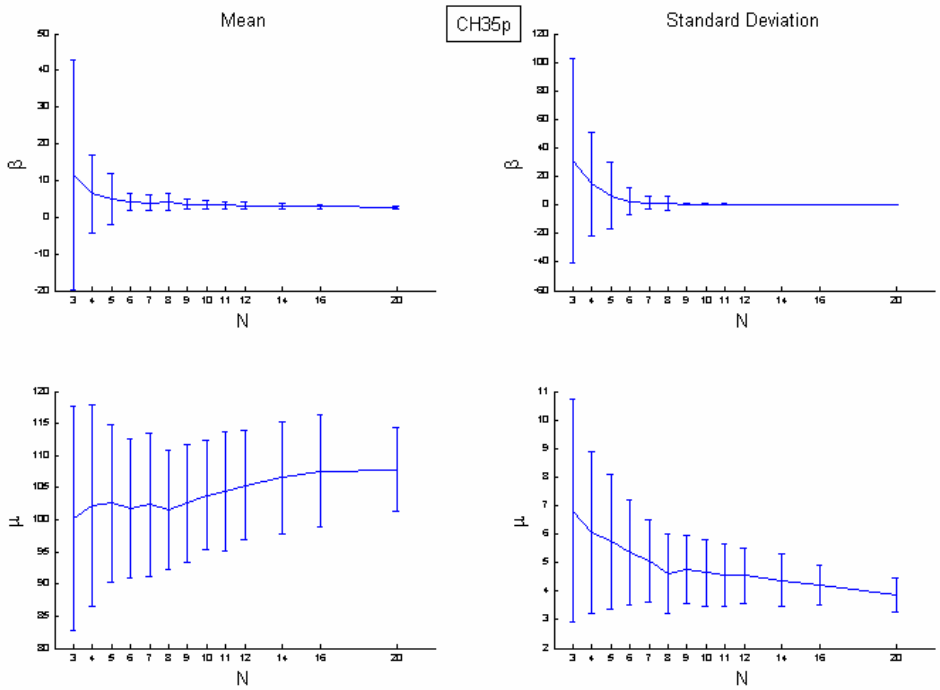
Mean
CH35p
Standard Deviation
β
N
μ
N
β
N
μ
N

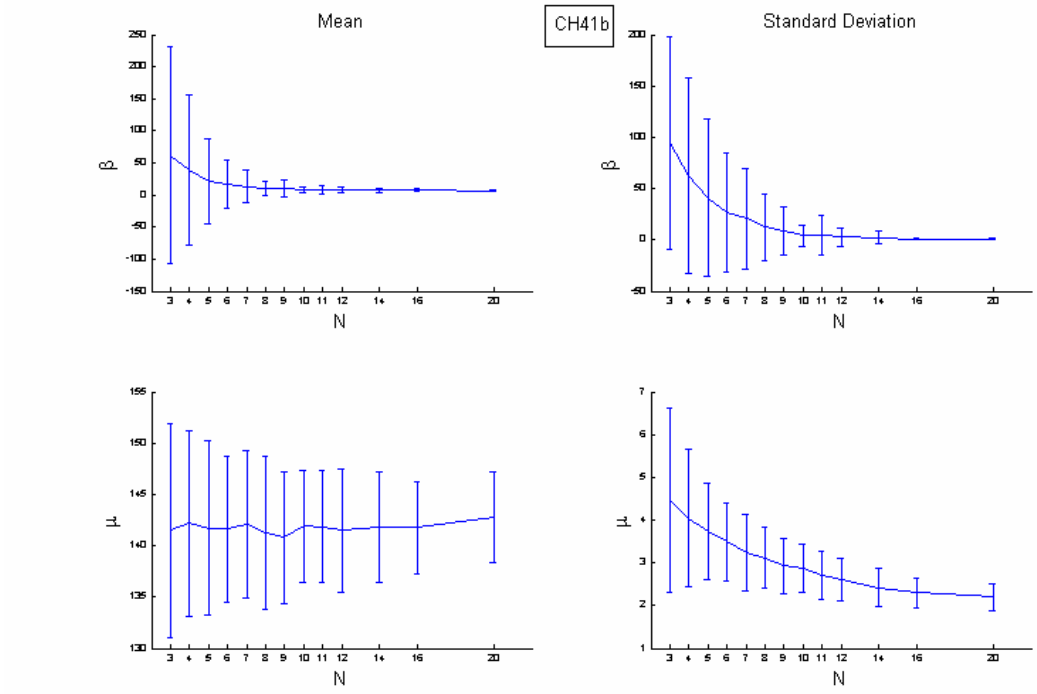
CH41b
Mean
Standard Deviation
β
μ
N

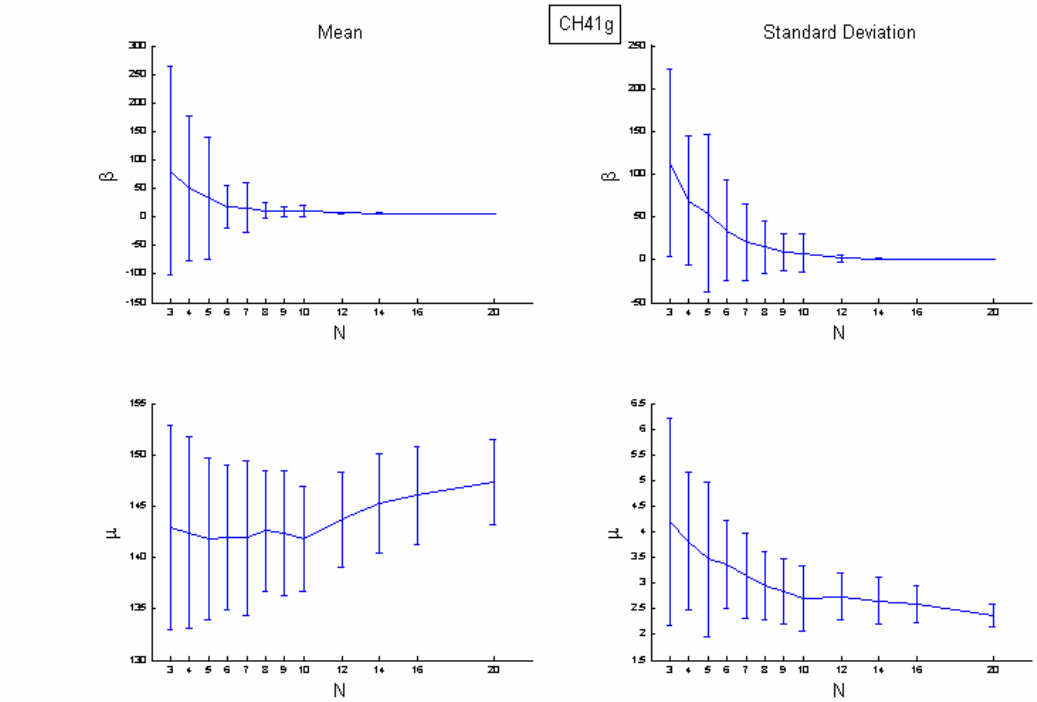
CH41g
Mean
Standard Deviation
β
μ
N

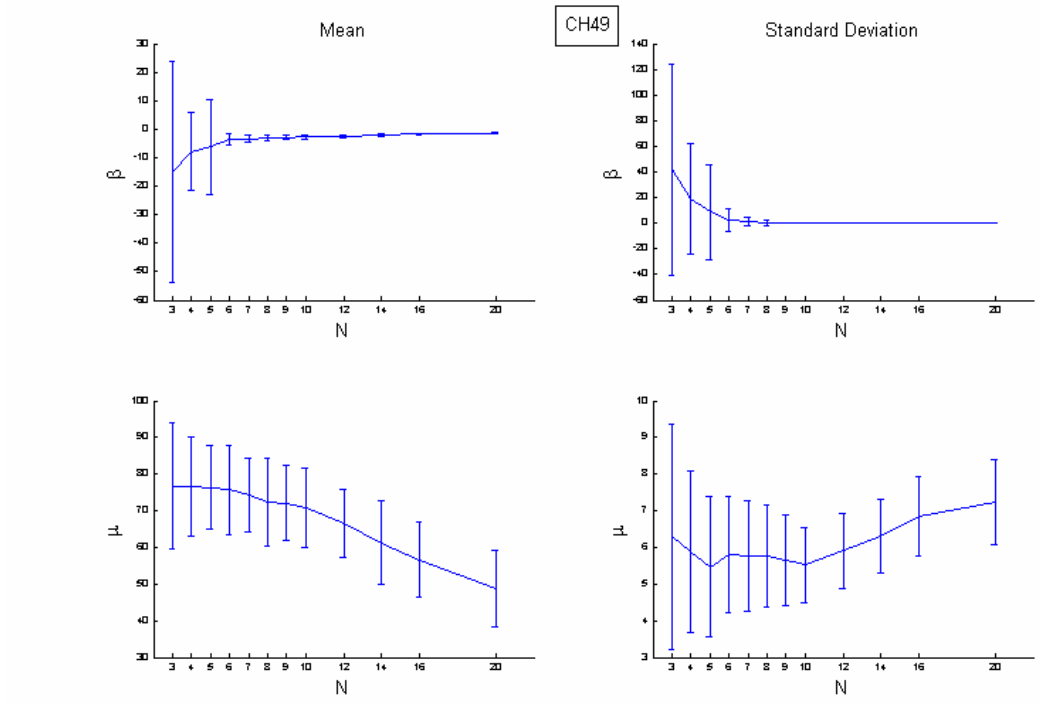
CH49
Mean
Standard Deviation
β
μ
N

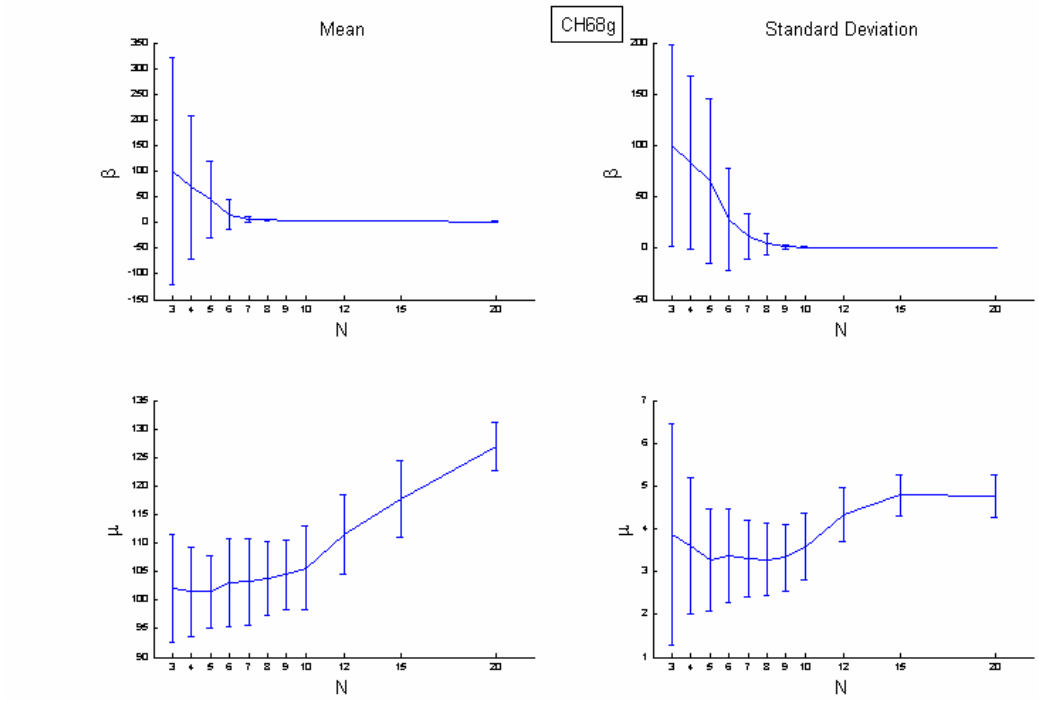
CH68g
Mean
Standard Deviation
β
μ
N

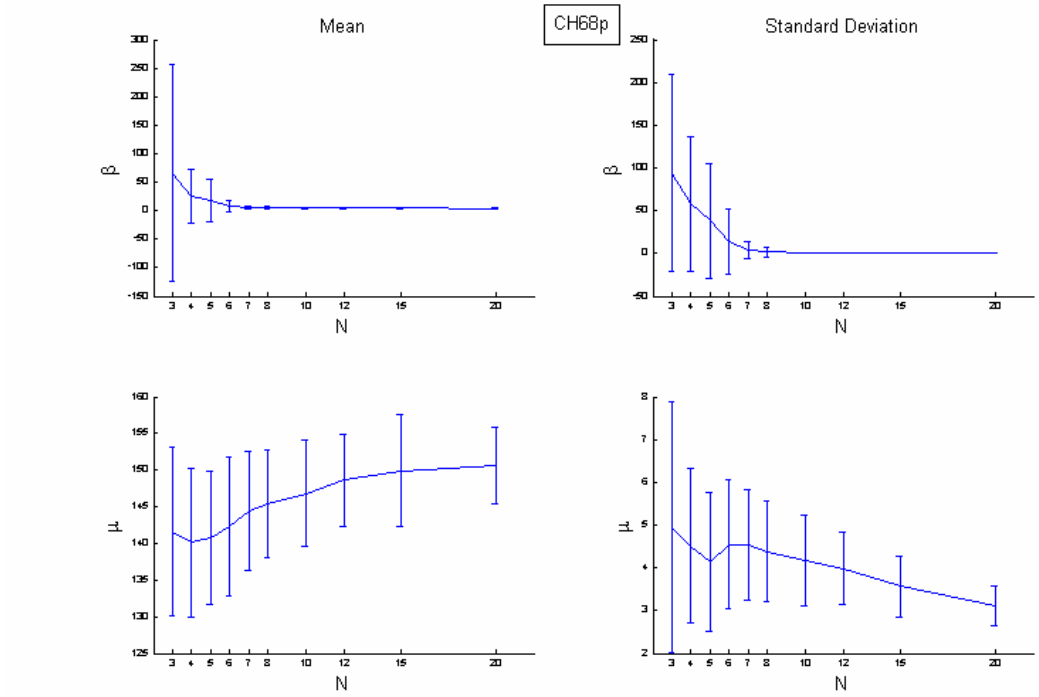
CH68p
Mean
Standard Deviation
β
μ
N

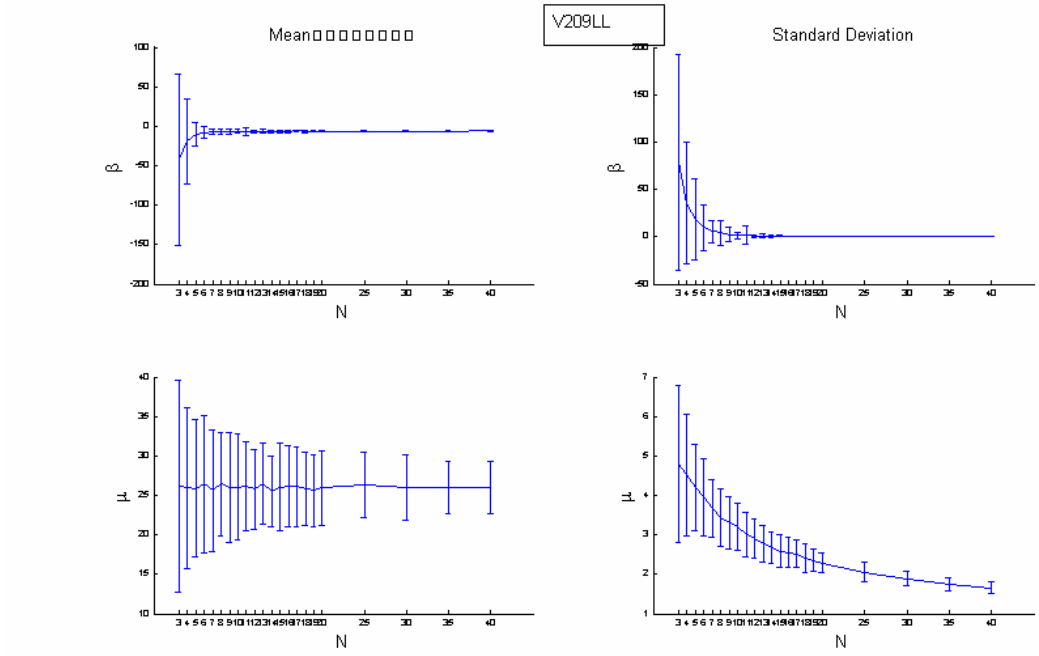
V209LL
Mean
Standard Deviation
β
μ
N

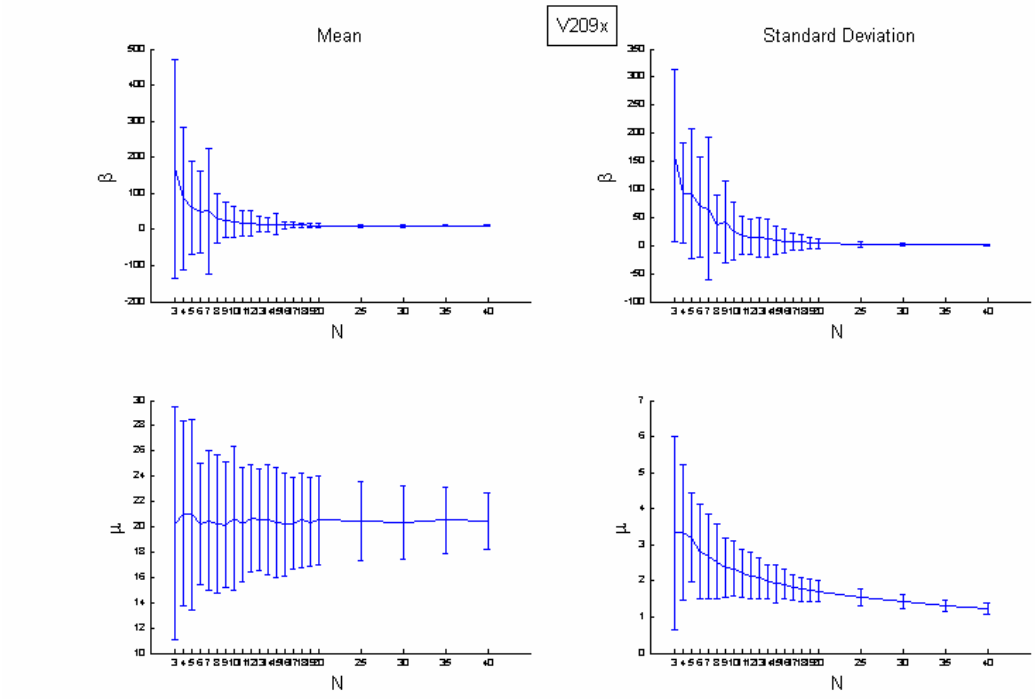
V209x
Mean
Standard Deviation
β
N
μ

# Conclusions

This thesis has addressed several of the key concerns regarding FIA data, as well as developing new techniques for studying FIAs. Chapter 1 demonstrated how HRXCT could be used to analyse the three-dimension geometries of inclusion trails in garnet porphyroblasts. Guidelines for sample selection for such studies are as follows. Firstly, 5 to 10 mm diameter garnets that could be scanned individually, or in cores drilled from a sample, provide a voxel size of 5 to 10 microns, which is the optimal resolution. Scanning a larger sample at low resolution would allow the garnets within it to be located so that they can be extracted. Inclusion trails composed of minerals with significantly different attenuation coefficients to garnet are necessary to provide high contrast. Quartz and iron/titanium oxides, which are common inclusions in garnet, are ideal. Given the voxel size described above, an inclusion size ranging from fifty microns to 0.2 mm in maximum dimension is ideal. This size allows the shape of individual inclusions to be clearly imaged. An appropriate range for the inclusion density is from ten to thirty percent. If the density is too high, images are confusing; if it is too low, the trails are not adequately defined.

The second chapter uses data generated by the HRXCT technique described in chapter 1 to determine the range of FIA orientations in single sample. A FIA was measured in the core of 58 porphyroblasts. The FIAs have a moderate to tightly clustered distribution that is difficult to reconcile with a rotational hypothesis for the formation of curved inclusion trail, particular in light of the subsequent deformation events that affected this sample. One of the latter events formed a FIA in the median of the porphyroblasts that has a trend at approximately 90° to that in the core. The most likely source of variation in FIA orientations, which formed during a particular stage of porphyroblast growth in a single sample, is in the variation of the foliations that form them.

The third chapter presents the background for a technique that can be used to quantify the accuracy of FIAs measured using the asymmetry method. It also provides a measure of the distribution of FIAs in a sample. The technique uses maximum likelihood estimation (MLE) to fit a cyclic logistic regression to asymmetry data. By applying bootstrapping to this approach, flaws in the assumptions regarding the goodness-of-fit test for the original technique were highlighted. As a result, graphical procedures for determining the fit of the model to the data were suggested, based on examining the distributions of the bootstrapped parameters and the model deviance. The fact that the technique is sensitive to sample size was also highlighted.

As part of a demonstration of the application of the bootstrapped MLE approach (chapter 4), an analysis of its sensitivity to the number of observations in each section orientation was made. The results of this suggest that a minimum of 10 observations per section orientation are needed in the vicinity of the FIA to produce repeatable results. The FIA distributions described in chapter 4 agree with the results of chapter 2, and show that their range in a sample will generally be in the order of 40° to 80°. These distributions are unimodal,

symmetrical and have a peak at their mean, and the probabilities decay monotonically away from it, as occurs in a normal distribution.

A FIA *set* is the term given to a group of FIA orientations from different samples that are interpreted to have formed at the same time. The correlation of FIAs between samples should be done based on orientation and relative timing criteria. Using inclusion trail textures assumes that metamorphic and strain conditions were similar in the samples being compared. This is precarious because deformation partitioning can result in highly variable distributions of strain. Therefore, the intensity of a foliation preserved in porphyroblasts is totally unreliable for such correlations. With large datasets, determining the error in individual FIA measurements is not important, because the errors will tend to average out. Placing a particular FIA measurement in one FIA set or the other that have similar orientations requires appropriate relative timing criteria. The distribution of FIAs in a FIA set is similar to that for a FIA in a sample.

Providing estimates of the error in the measured FIA orientation are essential if FIA orientations are used as timing markers for P-T calculations and age determinations, or for detailed analysis of structural processes at outcrop scale,. Inferences made based on FIA data are strengthened when this is done.

FIAs have been demonstrated to have consistent regional patterns that can be correlated along orogens. It is difficult to conceive how such distributions can develop if rotation of porphyroblasts relative to each other is a common phenomenon. This suggests that they do reflect plate scale processes and that their orientations relate to the relative direction of plate motion.

This thesis has addressed many of the questions regarding the distribution of FIAs and their significance. It has examined their distribution in a single sample, provided a method for determining the error in FIA measurements made using the asymmetry method, and discussed the application and significance of FIA data in detailed and regional studies. This framework will enhance future applications of FIA data by ensuring that their interpretations are statistically valid.

# Directions for Future Research

The following are avenues for future research that follow on from the work described herein.

The application of the HRXCT technique in this thesis was focussed on the specific problem of the distribution of FIA in a single sample. This technique could also be applied to detailed studies of the three-dimensional geometry of curved inclusion trails in garnet. This may help address the ongoing controversy of the mode of formation of these features. It could also be conducted in conjunction with electron microprobe analysis to investigate the relationships between compositional zoning and microstructures. This would provide insight into the links between metamorphic and microstructural processes.

The FIA distribution was measured for a single sample in chapter 2. It would be useful to apply this technique to a number of samples to determine if the intra sample distribution of FIAs varies between samples. Samples with a range of inclusion trail geometries could be studied, including those with true spirals.

The goodness-of-fit test for the cyclic logistic model described in chapter 3 uses a graphical approach. A formal approach that can be used in conjunction with this is highly desirable. Such a test requires the issue of dependant chi-squared distributions with fractional degrees of freedom to be addressed. This is a problem that has received very little attention in the literature.

A result of the growing body of FIA data are questions regarding the processes that form foliations. The variation in FIA orientations appears to represent the variation in the orientation of the foliations that form them. It is typically accepted that foliations form perpendicular to the direction of bulk shortening. A difficulty with this interpretation is that shear should not occur on surfaces that are perpendicular to the axis of principal stress. The fact that porphyroblast rotation is highly unlikely also suggests that strain models that include pervasive spin and vorticity are also problematic. The progressive, bulk inhomogeneous shortening (PBIS) model addresses these issues by partitioning deformation into zones of shortening and anastomosing zones of shearing. Clearly more work needs to be done to investigate how foliations form in order to address the issues of lack of porphyroblast rotation, and the relationship between stress and strain as cleavages form.

# Appendix A: Adobe Acrobat Version of Chapter 1.

This chapter has been accepted for publication by The American Mineralogist as an electronic article. It is best viewed as an interactive Adobe Acrobat document, which can be found on the CD in this appendix.

The CD contains a pdf file \\chapter1\InsideStory.pdf and the vrml files for appendix 1 of the chapter in \\chapter1\vrml\.

# Appendix B: JCU Sample Collection, Murphy Syncline Samples, Sample V209

**Murphy Syncline Samples**

| JCU Collection Number | Sample Number | Latitude | Longitude | Thin sections | Porphyroblastic Phases |
|---|---|---|---|---|---|
| 71998 | CH2 | 35° 0.82' N | 84° 17.02' W | 0,10,20,30,40,60,90,120,130, 140,150,160,170 | gt, st, chl |
| 71999 | CH4 | 35° 0.64' N | 84° 15.92' W | 0,10,20,60,90,120,160,170 | gt,chl |
| 72000 | CH7 | 35° 9.19' N | 83° 39.18' W | 0,20,60,90,100,110,120,130 160 | gt, plag |
| 72001 | CH11 | 35° 24.86' N | 83° 33.42' W | 0,20,40,50,60,80,100,120, 140,150,160 | gt, st, plag, chl |
| 72002 | CH13 | 35° 24.86' N | 83° 33.42' W | 0,10,20,30,40,50,60,70,80,90 100,110,120,130,140,150, 160,170 | gt, bi, st |
| 72003 | CH14 | 35° 24.91' N | 83° 33.55' W | 0,10,20,30,60,80,100,120 130,150,160,170 | gt |
| 72004 | CH17 | 35° 25.43' N | 83° 33.63' W | 0,10,20,40,50,60,90,120, 130,140,150,160,170 | gt |
| 72005 | CH20 | 35° 24.81' N | 83° 34.06' W | 0,20,30,40, 50,60,90,120, 150,160 | gt, st |
| 72006 | CH21 | 35° 24.85' N | 83° 34.18' W | 0,30,60,70,80,90,100,110, 120,140 | gt |
| 72007 | CH22 | 35° 24.91' N | 83° 32.94' W | 0,0p10,20,30,30p,40,50,60, 70,80,90,100,110,120,130, 140,140p,150,160,170 | gt, bi, plag, st |
| 72008 | CH23 | 35° 24.78' N | 83° 33.29' W | 0,20,60,80,90,100,120,140 | gt |
| 72009 | CH24 | 35° 26.52' N | 83° 32.64' W | 0,30,60,70,80,90,100,110, 120,130,140,160 | gt, plag, chl |
| 72010 | CH25 | 35° 26.54' N | 83° 32.61' W | 0,20,40,60,70,80,90,100, 120,150 | gt |
| 72011 | CH27 | 35° 20.11' N | 83° 30.24' W | 0,10,20,20p,30p,40,50p,,60, 70p,80,80,100,120 | gt |
| 72012 | CH30 | 35° 26.24' N | 83° 33.70' W | 0,10,20,30,60,90,120,140, 160,170 | gt,chl |
| 72013 | CH32 | 35° 26.39' N | 83° 33.46' W | 0,20,40,60,80,100,120,140, 160 | gt |
| 72014 | CH35 | 35° 21.85' N | 83° 32.77' W | 0,0p,10,20,40,50p,60,80,90, 100,110,110p,120,130,140, 150,160,170 | gt, plag, bi, ky, st |
| 72015 | CH38 | 35° 23.80' N | 83° 31.34' W | 0,10,20,30,60,80,90,100,110, 120,150,160,170 | gt, ky |
| 72016 | CH40 | 35° 18.79' N | 83° 36.05' W | 0,30,60,90,120,120,150,160, | gt |
| 72017 | CH41 | 35° 16.46' N | 83° 39.82' W | 0,10,30,60,90,100,110.120, 130,140,150,160,170 | gt, bi |
| 72018 | CH42 | 35° 11.50' N | 83° 38.50' W | 0,20,10,60,90,120,150,160, 170 | gt |
| 72019 | CH43 | 35° 11.44' N | 83° 38.61' W | 0,20,40,60,80,100,120,130, 140,150,160 | gt, bi |
| 72020 | CH48 | 35° 16.73' N | 83° 41.51' W | 0,0,30,60,70,80,90,100,110, 120,150 | gt, bi |
| 72021 | CH49 | 35° 17.45' N | 83° 46.22' W | 0,20,40,60,70,80,80,90,90, 100,110,120,140,160 | gt, bi |
| 72022 | CH50 | 35° 18.27' N | 83° 47.75' W | 0,20,40,60,70,70,80,90,100, 110,120,130,140,160 | gt, st, plag |
| 72023 | CH51 | 35° 16.94' N | 83° 49.11' W | 0,30,60,90,120,140,160,170 | gt |
| 72024 | CH52 | 35° 15.50' N | 83° 49.21' W | 0,30,60,100,110,120,130, 140,160 | gt, st, chl |
| 72025 | CH53 | 35° 14.46' N | 83° 49.07' W | 0,30,60,70,80,90,100,110, 120,140,160 | gt |
| 72026 | CH56 | 35° 22.17' N | 83° 37.62' W | 0,10,20,30,60,70,80,90,100. 110,120,140,160 | gt |
| 72027 | CH57 | 35° 22.86' N | 83° 40.68' W | 0,30,60,80,90,100,110,120, 130,150,160,170 | gt |
| 72028 | CH58 | 35° 26.36' N | 83° 48.43' W | 0,30,60,90,120,130,140,150, 160,170 | gt |
| 72029 | CH60 | 35° 22.87' N | 83° 51.85' W | 0,30,60,80,90,100,110,120, 140 | gt |
| 72030 | CH62 | 35° 17.01' N | 83° 52.49' W | 0,30,60,60p,90,100,110, 110p,120,130,130p,150, 150p160,170 | gt, st |

| JCU Collection Number | Sample Number | Latitude | Longitude | Thin sections* | Porphyroblastic Phases |
|---|---|---|---|---|---|
| 72031 | CH68 | 35° 9.07' N | 84° 1.88' W | 0,30,60,80,90,100,110,120, 130,140,150,160 | gt, plag |
| 72032 | CH70 | 35° 12.85' N | 84° 2.51' W | 0,20,30,40,40,50,60,70,80,10 0,120,150 | gt, st |
| 72033 | CH71 | 35° 11.08' N | 84° 3.10' W | 0,40,50,60,70,80,120,150 | gt |
| 72034 | CH72 | 35° 13.07' N | 84° 5.95' W | 0,30,60,70,80,80,90,100,100 120,150 | gt, chl |
| 72035 | CH73 | 35° 8.09' N | 83° 58.40' W | 0,20,60,70,90,120,130,140,1 50,160,170 | gt |

* Thin section orientation in degrees. Repeats represent multiple thin sections. Suffix p denotes polished thin sections.

## Sample V209

| JCU Collection Number | Sample Number | Latitude | Longitude | Thin sections/ Drill Cores | Porphyroblastic Phases |
|---|---|---|---|---|---|
| 72036 | V209 | 43° 11' 09.6" N | 72° 38' 30"W | Thin sections 360,10,20,30,40,50,60,70p, 80,90,100,110,120,130,140p, 150,160,170,181, Horizontal, 15→88, 45→88, 45→268, 15→268. Polished section of core V209-1.<br><br>Cores V209-1, V209-2, V209-3, V209-4 | gt |

Ken Hickey collected this sample. Data collected from it was published in Bell et al. (1998). Core V209-1 has been sectioned and is no longer intact.

# Appendix C: HRXCT Raw Data

Raw high resolution X-ray computed tomography (HRXCT) data for the four drill cores from sample V209. These data were used for chapters 1 and 2 of this thesis. Data is in 16-bit tiff format files with one file for each of the 918 slices imaged from each core. 8-bit jpeg versions are also included. See content.txt in the root directory of the disc for more details.